New methods for electrical injection and oxide aperture control in VCSELs

Natan Monvoisin

Université Fédérale
Toulouse Midi-Pyrénées

THÈSE

En vue de l'obtention du
DOCTORAT DE L'UNIVERSITÉ DE TOULOUSE

Délivré par l'Institut National des Sciences Appliquées de Toulouse

---

Présentée et soutenue par

Natan MONVOISIN

Le 20 octobre 2023

Nouvelles méthodes pour l'injection électrique et le contrôle du diaphragme d'oxyde dans les VCSELs

---

Ecole doctorale : **GEETS - Génie Electrique Electronique,Télécommunications et Santé : du système au nanosystème**

Spécialité : **Photonique et Systèmes Optoélectroniques**

Unité de recherche :
LAAS - Laboratoire d'Analyse et d'Architecture des Systèmes

Thèse dirigée par
Guilhem ALMUNEAU et Stéphane CALVEZ

Jury

M. Luiz POFFO, Rapporteur
M. Xavier LETARTRE, Rapporteur
Mme Béatrice DAGENS, Examinatrice
M. Tomasz CZYSZANOWSKI, Examinateur
M. Guilhem ALMUNEAU, Directeur de thèse
M. Stéphane CALVEZ, Co-directeur de thèse

New methods for electrical injection and oxide aperture control in VCSELs

Abstract

Vertical-cavity surface-emitting lasers (VCSEL) are micrometric coherent light sources that are already ubiquitous in datacom, 3D sensors, and LiDAR technologies and are becoming increasingly attractive for a wide variety of other applications. The most widespread VCSEL structures embed one or several oxide apertures together with a metallic ring contact for the electrical current injection from the top-surface of the device, thereby avoiding obstructing the emitted beam. This technique efficiently combines optical and electrical confinement, and offers the possibility of transverse optical mode distribution fine tuning in the cavity, and the achievement of very low threshold currents.

This thesis addresses two major issues of VCSELs : The first one deals with the device emission power limitation resulting from the non-uniformity in the electrical current injection when its active surface area becomes large. The second one is tied to the lateral confinement and the need to accurately control the confinement aperture dimensions during the oxidation process.

A new type of metallic electrodes, that are nanostructured, and transparent in the near infrared spectral region, is presented to address the first issue. These subwavelength structures have been fabricated and characterized both optically and electrically, and are promising for electrical current injection homogenization over large active areas, thereby paving the way towards an increase in the effective emission area and alleviating emission power limitations. The second issue is addressed with the development of a spectrally-shaped source and its integration in an optical microscopy system implemented over an oxidation furnace. The illumination spectrum optimization maximizing the discernability between the oxidized and unoxidized material improves this optical monitoring technique.

Nouvelles méthodes pour l'injection électrique et le contrôle du diaphragme d'oxyde dans les VCSELs

Résumé

Les lasers à cavité verticale émettant par la surface (VCSEL) sont des sources de lumière cohérente de taille micrométrique de plus en plus attractives pour une grande variété d'applications, et déployées à ce jour principalement sur des technologies de communications de courte portée, capteurs 3D, et LiDAR. La grande majorité de ces structures VCSELs sont basées sur l'intégration d'un ou plusieurs diaphragme(s) d'oxyde, couplé(s) à une électrode métallique annulaire pour l'injection du courant électrique par la surface sans obstruction du faisceau émis. Cela permet de combiner efficacement confinement optique et électronique, de manière à sélectionner finement les modes transverses excités tout en atteignant de faibles courants de seuil.

Cette thèse propose de traiter deux grandes problématiques sur les VCSELs : La première a trait à la limitation de puissance d'émission quand ces dispositifs atteignent de plus grandes surfaces actives du fait de l'injection électrique non-uniforme. La seconde est liée au confinement latéral et la nécessité du contrôle précis des dimensions du diaphragme de confinement pendant le procédé d'oxydation.

Afin de répondre à la première problématique, le développement d'un nouveau type d'électrodes métalliques, nanostructurées, et transparentes dans le proche infrarouge, est proposé. Ces structures sub-longueur d'onde ont été fabriquées puis caractérisées optiquement et électriquement, et sont prometteuses pour l'homogénéisation de l'injection du courant électrique sur de grandes surfaces actives, de manière à lever cette limitation de puissance optique du composant en maximisant la surface effective d'émission. Une solution à la seconde problématique est apportée par le développement d'une source structurée et par son intégration dans un système de microscopie optique implémenté sur un four d'oxydation. L'optimisation du spectre d'illumination maximisant la discernabilité de l'oxyde par rapport au matériau non oxydé a permis d'améliorer cette technique de suivi du procédé.

International peer reviewed journal

Natan Monvoisin, Elizabeth Hemsley, Lucas Laplanche, Guilhem Almuneau, Stéphane Calvez, and Antoine Monmayrant, "Spectrally-shaped illumination for improved optical inspection of lateral III-V-semiconductor oxidation," Opt. Express 31, 12955-12966 (2023).

International conference

Poster presentation at the *CLEO Europe* conference, Munich (Germany), Jul. 2023.
"Spectrally-shaped illumination for improved optical inspection of lateral III-V-semiconductor oxidation", Natan Monvoisin, Elizabeth Hemsley, Lucas Laplanche, Guilhem Almuneau, Stéphane Calvez, Antoine Monmayrant.

National conferences

Oral presentation at the *Optique Dijon* conference, Dijon (France), Jul. 2021.

Oral presentation at the *GDR ondes* CNRS conference, Paris (France), Apr. 2023.
"Transparent electrodes by subwavelength structuration for VCSELs", Natan Monvoisin, Franck Carcenac, Aurélie Lecestre, Benjamin Reig, Stéphane Calvez, Weronika Glowadzka, Tomasz Czyszanowski, Guilhem Almuneau.

Oral presentation at the *GEETS* conference, Toulouse (France), May 2021.

Remerciements

Avant d'entrer dans le coeur de ce travail de recherche, j'aimerais d'abord en souligner la dimension collective, et remercier les personnes qui, de diverses manières, y ont contribué.

Merci à Guilhem Almuneau, Stéphane Calvez, et Antoine Monmayrant pour leur confiance, leur soutien, et leurs précieuses contributions tout au long du projet, notamment durant les absurdes, angoissantes, et interminables péripéties d'avant-thèse. Des péripéties qui auront eu l'heureux effet de conduire à une collaboration avec Tomasz Czyszanowski, Weronika Glowadzka, et Marcin Gebski, que je remercie pour leur grande sympathie et le partage de leurs excellentes idées. Merci également à Elizabeth Hemsley, avec qui j'ai eu plaisir à travailler, pour sa contribution majeure au projet, et à Olivier Gauthier-Lafaye pour son implication sur les parties simulation numérique, fabrication, et caractérisation.

Je suis également très reconnaissant envers l'équipe TEAM du LAAS pour l'aide capitale apportée en salle blanche. En particulier, merci à Franck Carcenac, Aurélie Lecestre, Benjamin Reig, Guillaume Libaude, Pascal Dubreuil, Jean-Christophe Marrot, Alexandre Arnoult et Jean-Baptiste Doucet. Merci aussi à Julien Roul et à Nicolas Mauran pour leur aide en caractérisation optique et électrique.

Je remercie les membres de mon jury de thèse, Béatrice Dagens, Luiz Poffo, et Xavier Letartre, pour l'intérêt qu'ils ont porté à ces travaux, et l'accueil chaleureux qu'ils lui ont réservé.

Ces trois années de thèse ont aussi été marquées par de nombreux bons moments partagés avec Ines, Lucas, Antoine, Romain, Maxime, François, Sébastien, Lizzie, Léopold et Ivan, au laboratoire comme en dehors. Ces moments étaient essentiels, aussi bien pour recharger les batteries en retournant compulsivement des sabliers colorés sur le temps du midi, que pour grandir et prendre du recul sur la thèse, la recherche, la science, et notre rôle dans tout ça.

Enfin, je remercie mes parents pour leur soutien tout au long de mes études.

List of acronyms

AFM Atomic Force Microscopy

ARC Anti-Reflective Coating

CR Cavity Resonance

CW Continuous Wave

DBR Distributed Bragg Mirror

DMD Digital Micromirror Device

DMSO Dimethyl Sulfoxide

EBL Electron-Beam Lithography

EBPVD Electron-Beam Physical Vapor Deposition

EEL Edge-Emitting Laser

FDA Fisher Discriminant Analysis

FIB Focused Ion Beam

FP Fabry-Perot

FWHM Full Width at Half Maximum

HMDS Hexamethyldisilazane

ICP-RIE Inductively Coupled Plasma - Reactive Ion Etching

IPA Isopropyl alcohol

ITO Indium Tin Oxide

LED Light-Emitting Diode

MHCG Monolithic High-Contrast Grating

MS Metal-Semiconductor

NID Nonintentionally Doped

NIR Near Infrared

PCE Power Conversion Efficiency

PECVD Plasma-Enhanced Chemical Vapor Deposition

RCWA Rigorous Coupled-Wave Analysis

SEM Scanning Electron Microcope

SMDSG Semiconductor-Metal Deep-Subwavelength grating

SOC System On Chip

SPP Surface Plasmon Polariton

SWIR Short-wave Infrared

TCE Transparent Conductive Electrode

TCO Transparent Conductive Oxide

TE Transverse Electric

TLM Transfer Length Method

TM Transverse Magnetic

UV Ultraviolet

VCSEL Vertical-Cavity Surface-Emitting Laser

VIS Visible

Contents

Introduction **1**

1 The context of high-power VCSELs **7**
1.1 Introduction . . . 8
1.2 High power VCSELs: commercial solutions and challenges . . . 9
1.2.1 Bottom-emitting VCSELs . . . 9
1.2.2 The challenge of large active area . . . 10
1.2.3 VCSEL arrays . . . 12
1.2.4 Discussion . . . 14
1.3 Electrical contacts in VCSELs . . . 15
1.3.1 Contact electrical properties . . . 15
1.3.2 Ohmic contact fabrication techniques in GaAs-based optoelectronic devices . . . 17
1.3.3 Top electrode engineering . . . 19
1.4 Conclusion . . . 24

2 Novel metallic transparent conductive electrodes for improved electrical injection uniformity in VCSELs **29**
2.1 Introduction . . . 30
2.2 Light transmission through subwavelength grating . . . 30
2.2.1 From diffraction gratings to deep-subwavelength gratings . . . 30
2.2.2 Transmission through semiconductor monolithic high contrast grating 32
2.2.3 Transmission through subwavelength-aperture metallic grating . . . 33
2.3 Transmission mechanisms in SMDSG structures . . . 34
2.3.1 High transmission through SMDSG in B-TE configuration . . . 35
2.3.2 High transmission through SMDSG in T-TM configuration . . . 36
2.3.3 Conclusion . . . 37
2.4 Fabrication . . . 38
2.4.1 Presentation of the nano-structuration and the characterization techniques for the fabrication . . . 38
2.4.2 Optimization of SMDSG dimensions . . . 43
2.4.3 Developed fabrication processes . . . 47
2.4.4 Fabricated SMDSGs . . . 52
2.5 Characterizations . . . 58
2.5.1 Spectroscopy . . . 58
2.5.2 Sheet resistance . . . 63
2.5.3 Specific contact resistance . . . 65
2.6 Conclusion and perspectives . . . 67

3 Spectrally-shaped illumination for improved optical monitoring of VCSEL oxide aperture 71
3.1 Introduction . . . 73
3.2 AlGaAs wet thermal oxidation process in VCSEL fabrication . . . 73
3.2.1 Fabrication of oxide-confined VCSEL . . . 73
3.2.2 AlGaAs wet thermal oxidation physico-chemical mechanisms . . . 75
3.3 The control of wet thermal oxidation process . . . 79
3.3.1 Oxidation furnace general principle . . . 79
3.3.2 Oxide layer optical detection in VCSEL structures . . . 80
3.3.3 Optical in-situ monitoring systems . . . 85
3.3.4 Perspectives . . . 88
3.4 Interest and implementation of pylochromatic illumination for optical monitoring . . . 89
3.4.1 Hyperspectral imaging and wet thermal oxidation monitoring . . . 89
3.4.2 Spectrally-shaped source development . . . 91
3.4.3 Conclusion . . . 97
3.5 Experimental setup and results . . . 97
3.5.1 Methodology . . . 97
3.5.2 Hyperspectral cube acquisition . . . 98
3.5.3 Spectral shaping . . . 100
3.5.4 Acquisition of monitoring "views" . . . 101
3.5.5 Results and discussion . . . 101
3.6 Conlusion and perspectives . . . 107

Conclusions and perspectives 114

Résumé de la thèse en français 121

A Tomasz Czyszanowski, Adam K. Sokół, et al., "Transparent electrode employing deep–subwavelength monolithic high-contrast grating integrated with metal", Optics Express, 2020 145

B Spectrally-shaped source design and modelling 163
B.1 Presentation of the supercontinuum laser source . . . 164
B.2 Dimensioning of spectral dispersion subsystem . . . 164
B.3 DMD diffraction modelling . . . 166
B.4 Collection subsystem efficiency calculations . . . 166
B.5 Fiber coupling subsystem . . . 167

Introduction

Vertical-cavity surface-emitting laser (VCSEL), a micrometric solid-state laser source invented in 1977 by Kenichi Iga, has emerged in the years 1990s as a low-cost and highly-reliable semiconductor technology, enabled by the strong progress of its performances and large-scale manufacturing capabilities due to its vertical geometry. In 1996, the first commercialized VCSELs were integrated to optical transceivers used in short optical communication links and later on in data centers, playing a key role in the expansion of the Internet. Nowadays, VCSEL is one of the crucial tools behind the ubiquity of the information and sensing technologies. Between 2020 and 2025, the projection of the VCSEL market increase has been estimated at 450%, which would represent $40 billion, thus 50% of the total photonics market in 2025 [1]. This current fast-growing market includes four major areas [1]: datacom, 3D sensing mainly implemented in smartphones, 3D imaging LiDAR for the automotive industry, and industrial heating. In addition, a wide variety of smaller application fields are also part of this market [1], such as defense and aerospace, medical with the optical coherence tomography, gas sensing, gaming, virtual reality / augmented reality / mixed reality, surveillance, 3D printing, or laser printing. The VCSEL success for such a diversified demand is due to its scalability in terms of emitting wavelength and output power with 1D or 2D arrays, combined with its good performances in terms of wavelength stability in temperature and power consumption. Typically, datacom applications mainly rely on high fiber coupling efficiency, large frequency modulation bandwidth, wavelength tunability, and efficient heat dissipation, while sensing applications require high peak pulse powers, high power conversion efficiency, and high beam quality [1]. This illustrates the large range of requirements imposed by the various applications and operational environments. In addition, single-mode or multi-mode operation can be needed in both optical communications and optical sensing, depending on the application. Commercial VCSELs emitting wavelengths are typically between 650 and 1550 nm, while research and development of devices emitting at shorter and longer wavelength are underway. Direct bandgap III-V semiconductor materials are usually used for the fabrication, like GaAs, InP, GaSb, or GaN [1], and more prospectively for the integration of III-V on Ge or Si substrates.

VCSEL operation principle relies, as all types of lasers, on the positive feedback to an amplifier. Although several VCSEL designs exist, the most widespread structure, called the oxide-confined top-emitting VCSEL, is presented in figure 1. The amplification condition is enabled by placing an active region, made of quantum wells, in an optical cavity defined between two highly-reflective distributed Bragg mirrors (DBR). The device, comparable to a PIN diode, is typically electrically-pumped via a top p-type annular contact, in order to set the population inversion in the quantum wells and generate stimulated emission using the photons oscillating between the DBRs. In the top-emitting VCSEL, the vertical emission is achieved by slightly lowering the top-DBR reflectivity. The small thickness of the structure enables to easily reach single longitudinal mode emission, while the oxide aperture defines both the transverse mode distribution and the location of current injection in the active region. Epitaxial growth from a substrate enables to obtain the VCSEL layer stack. Then, microfabrication techniques like metallization, dry-etching, oxidation, or passivation are performed to create the component, which is finally tested and packaged. The efficient design of such a component relies on a multiphysics study, from where compromises between electrical, optical, and thermal properties must be decided.

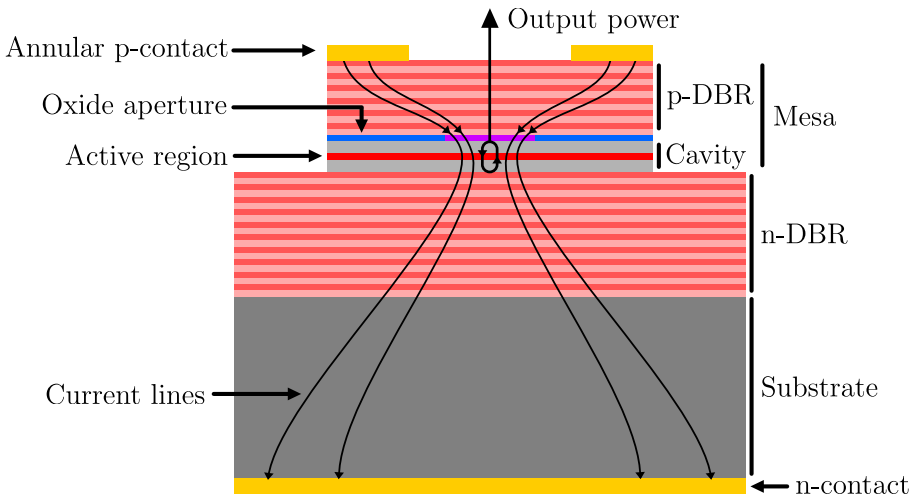

Figure 1: Cross-section of a standard oxide-confined top-emitting VCSEL.

Despite the recent maturity of VCSEL technology, some performance limitations still persist. This thesis work aims to contribute to the resolution of two of them:

- The first one is the current injection non-uniformity which limits the use of large active areas for higher output power. When the active area of oxide-confined top-emitting VCSELs becomes large, the current tends to flow at the edge of the oxide aperture, as shown in figure 1. The injection technique using annular top contact is responsible for this loss of effective emission area, which could be overcome by the use of a transparent conductive electrode (TCE) uniformizing the injected current distribution. While the implementation of several types of TCEs have already been reported for VCSELs, a new type of TCE reported in [2] in 2020 presents highly-transmittive structures made of metal and semiconductor, thus benefiting from the excellent eletrical properties of the metallic contacts. Based on the combination of a metal and a semiconductor subwavelength one-dimensional grating, these nanostructures theoretically outperform the ones previously reported. Chapter 1 describes the context of the use of TCEs for high power VCSELs. Then, chapter 2 presents the fabrication and the optical and electrical characterizations of the new TCE optimized for the near infrared spectral region.

- The second technological bottleneck addressed in this work is the difficult accurate control of the oxide aperture dimensions and shape fixed during the high-temperature oxidation process. Since the aperture geometry significantly impacts the VCSEL electro-optic performances, in-situ optical microscopy has been implemented to control it in real-time during the oxidation process. Prior to this work a strong expertise in this field has been developed at LAAS-CNRS [3]. However, the oxide aperture discernability below the top-DBR can drastically wane at high temperature, depending on the VCSEL stack. Chapter 3 demonstrates the use of hyperspectral imaging, for which the LAAS-CNRS has an expertise, to improve the oxide aperture detection. A spectrally-shaped source is presented and used, showing that shaping the illumination spectrum can lead to a more robust and accurate oxide aperture control in the fabrication of oxide-confined VCSELs.

Bibliography

[1] B. D. Padullaparthi, J. A. Tatum, and K. Iga, *VCSEL Industry: Communication and Sensing*. Wiley : IEEE Press, 2022.

[2] T. Czyszanowski, A. K. Sokól, M. Dems, and M. Wasiak, "Transparent Electrode Employing Deep– Subwavelength Monolithic High-Contrast Grating Integrated with Metal," *Optics Express*, vol. 28, no. 19, p. 28383, 2020.

[3] G. Almuneau, R. Bossuyt, P. Collière, L. Bouscayrol, M. Condé, I. Suarez, V. Bardinal, and C. Fontaine, "Real-Time in situ Monitoring of Wet Thermal Oxidation for Precise Confinement in VCSELs," *Semiconductor Science and Technology*, vol. 23, no. 10, p. 105021, 2008.

CHAPTER 1

The context of high-power VCSELs

The maturity of the VCSEL technology, from the design to the fabrication, associated with its attractive beam properties is the starting point of the fast-growing demand for high-power VCSELs as an alternative to the edge emitting lasers (EEL), for many applications in the medical, the industrial, or the military fields. Increasing the output power of a VCSEL requires to enlarge its effective emission area. However, the non-uniformity of the current injection in large-area standard oxide-confined VCSELs, in which the current is injected from the periphery of the active area, strongly limits this increase. Device structures like bottom-emitting VCSELs or VCSEL arrays have enabled the increase in the output power, but the output power of standard top-emitting VCSELs and the power density of VCSEL arrays is still limited. The use of a transparent conductive electrode (TCE) as top electrode, instead of the typical annular metallic contact, could drastically improve the current injection uniformity while being transparent to the emitted laser beam. In this chapter, the current commercial solutions for high power VCSELs and the use of a TCE in order to increase the top-emitting VCSEL output power are discussed in order to give a contextual overview of this thesis work presented in chapter 2.

Contents

1.1 Introduction 8
1.2 High power VCSELs: commercial solutions and challenges . . 9
1.2.1 Bottom-emitting VCSELs 9
1.2.2 The challenge of large active area 10
1.2.3 VCSEL arrays 12
1.2.4 Discussion 14
1.3 Electrical contacts in VCSELs 15
1.3.1 Contact electrical properties 15
1.3.2 Ohmic contact fabrication techniques in GaAs-based optoelectronic devices 17
1.3.3 Top electrode engineering 19
1.4 Conclusion 24

1.1 Introduction

High power lasers are employed in a wide variety of applications as direct beam or pump source for diode-pumped solid-state lasers or fiber-lasers. Skin-care or tissue welding in the medical field, industrial heating with cutting, welding, or marking technologies, time of flight measurement and LiDAR, as well as weapons or night vision in the military field, are exemples of these various applications. LiDAR is a fast-growing market, and causes a strong demand of compact high power laser sources. The power is crucial for probing at longer distances, as well as the power-conversion-efficiency (PCE) in order to limit the battery power consumption. Different power levels are required depending on the application. It can be a few watts, kilowatts for most applications, megawatts for very high power demands, and even gigawatts in nuclear fusion [1]. These lasers, with emission wavelengths usually comprised between 800 and 1500 nm, can be found as continuous-wave (CW) operation devices, or pulsed lasers for better thermal dissipation management or high energy output requirements.

Historically, the ubiquitous high power laser source is based on edge-emitting lasers (EELs), presented in figure 1.1, due to their high power-conversion-efficiency (PCE) up to 70% [1], while VCSEL PCE can be found around 50%. However, intrinsic characteristics and the maturity of VCSEL technology makes, nowadays, VCSEL more attractive than EELs for high power applications. While the EEL beam profile is elliptic, the VCSEL one is circular with a low divergence angle of about 20°, which is easier to manipulate in optical systems. The VCSEL emission spectrum has also better properties with the capability to accurately control longitudinal and transverse modes. With their high-reflectivity ($>$ 99.5%) Bragg mirrors, VCSELs are insensitive to optical feedback effects, avoiding the need of optical isolator or filter, in contrast to EELs. In high power lasers, high electrical power is involved, which causes strong device self-heating that reduces the PCE and increases the power consumption. The use of a chiller is required in the case of EELs caused by their low reliability when the device reaches higher operation temperatures, while passive heat-spreader elements can be employed for VCSEL, which do not suffer from catastrophic optical damage (COD) [2], saving power consumption in the overall device [3]. The better high temperature behavior of VCSELs compared to EELs can also be seen by the thermally-induced wavelength redshift rate, which is typically of 0.065 nm/K for VCSELs, and 5 times lower than for EELs.

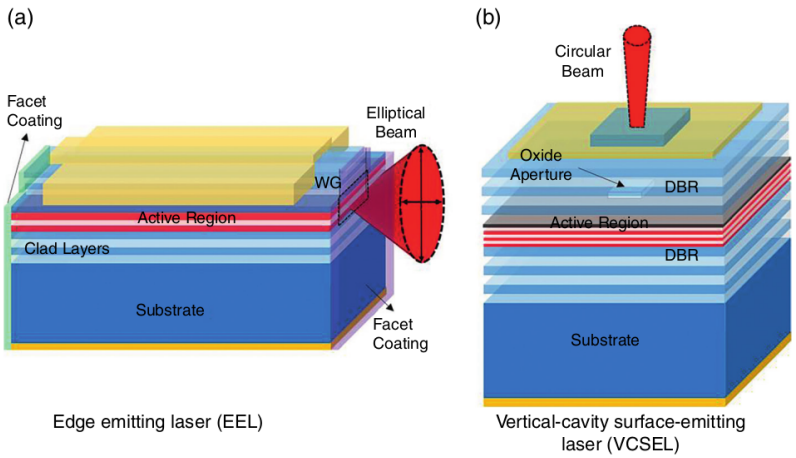

Figure 1.1: Schematic of (a) an edge-emitting laser (EEL), and (b) a VCSEL. Taken from [4].

Also, the larger is the active area of the device, the higher is the output power [5]. A

first part of this chapter focuses on the two methods employed to scale up output power. The first one, which is the main problematic of chapters 1 and 2 of this work, is the challenging increase of the active area of a single emitter. The bottom-emitting VCSEL solution is presented, and the use of bottom and top-emitting VCSELs as single high power sources is discussed. The second method consists in stacking emitters, with the final power defined as the sum of each individual emitter power. This is a convenient solution for VCSELs, much more than for EEL, since VCSELs are low-cost [6] and easy to fabricate side by side in the shape of 2D arrays on the wafer. Then, a second part of this chapter focuses on the top-electrode engineering in top-emitting VCSELs for the increase of the active area, which leads to the presentation of the use of transparent conductive electrodes (TCE). The standard metal-GaAs electrical contact modelling, properties, and fabrication is firstly described, and finally the state of the art of TCEs in top-emitting VCSELs is presented and discussed.

1.2 High power VCSELs: commercial solutions and challenges

1.2.1 Bottom-emitting VCSELs

Bottom-emitting VCSEL, presented in figure 1.2b, is a reversed version of conventional top-emitting structures reminded in figure 1.2a, where the beam is emitted from the substrate face instead of the top-DBR one. This geometry requires substrate thinning and polishing in order to minimize optical absorption losses. The presence of the substrate in the optical path limits the emission wavelength to energies below the GaAs substrate energy gap, because of strong absorption.

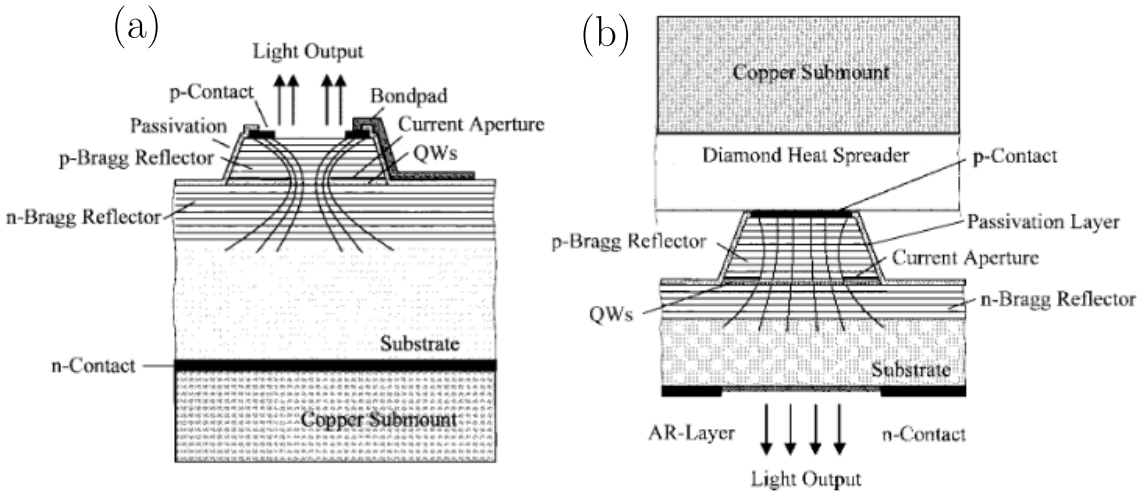

Figure 1.2: Schematic of (a) top-emitting, and (b) bottom-emitting VCSEL. Taken from [5].

The bottom emitting structure is employed for two reasons [1]:

1. It improves the current injection uniformity in the active area by switching from top-emitting structure annnular top-contact to a fully-covering top-contact, as suggested by current lines in figure 1.2. Moreover, since the electrons mobility is higher than the holes one, the annular contact on the n-type side of the device benefits from high conductivity to prevent strong current distribution inhomogeneity.

2. It reduces the thermal impedance between the active region and the heat-spreader, since the latter is placed in close proximity with the p-DBR, without high-thermal-impedance GaAs substrate in between. Furthermore, in this configuration, the heat-spreader is located on the p-type Bragg reflector side, which is the main heat source [5].

Thus, this configuration provides better conditions than top-emitting device for high power operation by the capability to extend the active area with improved heat removal, which requires a transparent substrate and a more complex fabrication. A continuous-wave room-temperature output power of 3 watts with a PCE of 25% has been reported by Princeton Optronics Inc in 2005 for such a structure containing an active diameter of 350 µm and emitting at 975 nm [7].

1.2.2 The challenge of large active area

In the quest to achieve large active area VCSEL for high output power operation, bottom-emitting device is more suitable than top-emitting one, as seen previously in section 1.2.1. However, it has been proven that this structure is well suited to medium power generation, but large active areas lead to a strong self-heating that decreases the PCE. The comparison between large active area top-emitting and bottom-emitting structures in terms of PCE, output power, and beam profile is the objective of this section.

Experimental data showing the impact of aperture diameter on PCE for top-emitting and bottom-emitting VCSELS are respectively presented in figures 1.3a and 1.3b. As one can see, the PCE decreases, in both device structure, with aperture diameter. However, this PCE drop is stronger in the case of bottom-emitting VCSEL, associated to higher threshold currents. In order to describe both behavior, the dependence of four parameters on the aperture diameter is studied in [5]. These parameters are:

- $R_{differential}$: the device intrinsic electrical resistance.
- $R_{thermal}$: the device intrinsic thermal resistance.
- $I_{threshold}$: the minimum current required to get a laser emission.
- $\Delta T_{threshold}$: the rise of the temperature when $I_{threshold}$ is applied.

The four parameters dependencies on the aperture diameter, extracted from [5], are summarized in table 1.1.

	Top-emitting VCSEL	Bottom-emitting VCSEL
$R_{differential}$	$\sim 1/D$	$\sim 1/D^2$
$R_{thermal}$	$\sim 1/D$	$\sim 1/D$
$I_{threshold}$	$\sim D$	$\sim D^2$
$\Delta T_{threshold}$	Independent of D	$\sim D$

Table 1.1: Dependance of device differential resistance $R_{electrical}$, thermal resistance $R_{thermal}$, threshold current $I_{threshold}$, and the rise of temperature at threshold $\Delta T_{threshold}$ on device active diameter D © 1998 IEEE [5]

The near field intensity distribution for top-emitting and bottom-emitting VCSEL with a 100-µm aperture diameter, respectively presented in figure 1.4a and 1.4b, gives a first important information about the current density distribution in both structures. While the bottom-emitting structure shows a relatively good current distribution homogeneity,

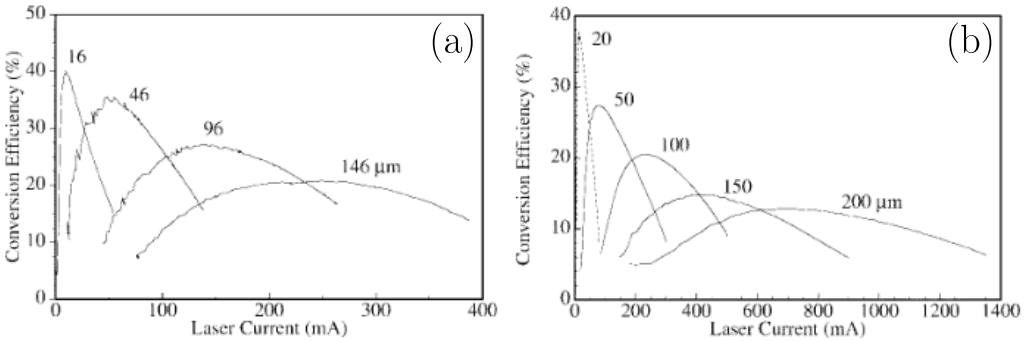

Figure 1.3: PCE as function of injected current and oxide aperture diameter for (a) top-emitting, and (b) bottom-emitting VCSEL. Taken from [5].

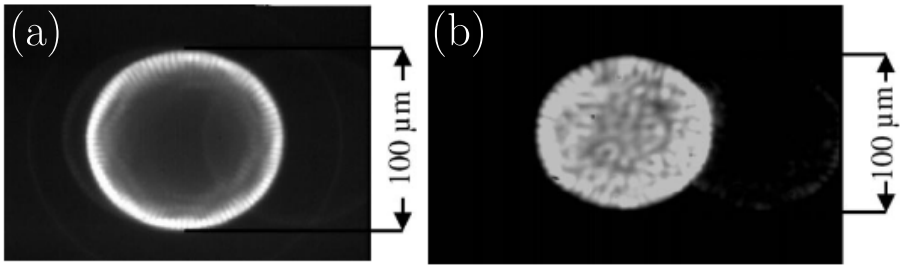

Figure 1.4: Near-field intensity distribution in a 100-µm oxide aperture (a) top-emitting VCSEL, and (b) bottom-emitting VCSEL. Taken from [5].

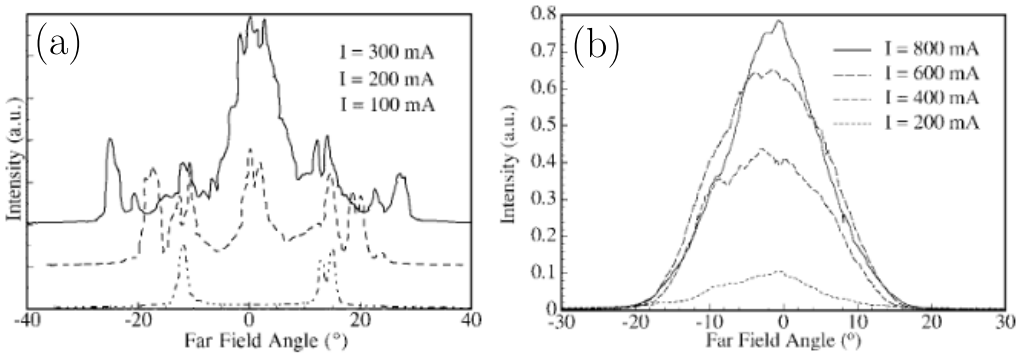

Figure 1.5: Angular distribution of far-field intensity from a 150-µm oxide aperture (a) top-emitting, and (b) bottom-emitting VCSEL. Taken from [5].

the annular top contact of the top-emitting configuration creates an effect called current crowding, where the current is concentrated at the edge of the aperture. The current follows the less resistive electrical path, thus minimizes the lateral resistance component of $R_{differential}$ [8] by flowing at the aperture edges. This effect appears for aperture diameters larger than 10 µm [9], and completely controls the behavior of $I_{threshold}$ above 50 µm [5]. In this case, instead of being proportional to the active area $\sim D^2$, $I_{threshold}$ is proportional to the perimeter $\sim D$. This results in lower threshold current compared to bottom-emitting devices due to the higher current density, at the cost of the loss of a large part of the active area. The lowered output power is then proportional to D, as seen in 1.6. This behavior is, as expected, also found for $R_{differential}$ behavior of top-emitting structures, which depends on $\sim 1/D$ instead of $\sim 1/D^2$ in bottom-emitting ones.

The current crowding effect is the origin of the differences between the behavior of each

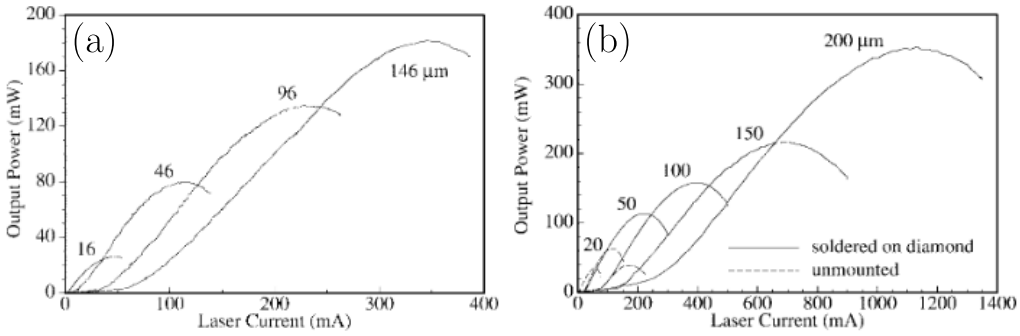

Figure 1.6: Output power as function of the device oxide aperture diameter for (a) top-emitting, and (b) bottom-emitting VCSEL. Taken from [5].

structure for the parameters $I_{threshold}$ and $R_{differential}$. The result of this difference is a dependence on $\sim D$ for the temperature increase at threshold current in bottom-emitting devices which doesn't exist in top-emitting ones [5]. Because the thermal resistance is proportional to $\sim 1/D$ in both cases, efficient heat-sinking is crucial for bottom-emitting VCSEL, and it is identified as the cause of the quick drop of PCE when aperture size increases.
Furthermore, the current crowding effect also impacts the far field beam profile, as shown in figure 1.5. The profile of top-emitting device beam appears to be ring-shaped, while the maximum intensity of the bottom-emitting device one is on the symmetry axis. Thus, the beam profile, in the latter case, is more convenient for device integration in optical systems.

Top-emitting VCSEL with conventional annular top contact have a strong limitation in terms of output power and beam quality because of the current crowding effect which prevent from taking advantage of large active areas. This effect doesn't occur in bottom-emitting devices, leading to higher output power and beam quality, but associated with stronger self-heating which increases with aperture diameter, and responsible for lower PCE. In order to find a compromise between output power, beam quality, and PCE, 2D arrays of top-emitting or bottom-emitting VCSELs have been developed, and are described in next section.

1.2.3 VCSEL arrays

2D VCSEL arrays can be composed of top-emitting or bottom-emitting VCSELs, made with square, hexagonal, or random geometrical arrangement, and driven under continuous wave or pulsed conditions. Compared to the fabrication of a single VCSEL, the production of arrays is almost similar, as one can see in figure 1.8. Care must be taken to the uniformity of the oxidation process that defines the confinement aperture inside each emitter, which is already known as sufficient for 5 mm chips fabrication and even larger ones [1]. An image of a commercial 2D top-emitting 940 nm VCSEL array is presented in figure 1.7.

The output power scales linearly, as the sum of each emitter. An important figure of merit of such arrays is the power density, and is defined by the dimensions of the chip and the emitter arrangement associated with the pitch between the devices. For exemple, in arrays containing 10-µm-aperture-diameter VCSELs, the power can vary from 1 mW to a few kW [4]. In terms of power density, a typical value of $4kW/cm^2$ is reached by these arrays, which is 8 times higher than the EELs typical value [4]. In such structures, the output power and PCE limitations of VCSELs for large active areas are overcome by grouping multiple smaller active area devices, with diameters generally comprised between

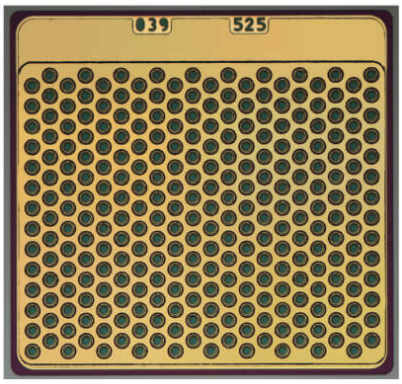

Figure 1.7: High power VCSEL array top view image. Taken from [10].

5 and 50 µm [4]. However, even if the active area is increased this way, the emitter density is limited since a certain distance must be kept between VCSELs, with the minimum one defined to suit both fabrication process (figure 1.8) and control of the thermal crosstalk between VCSELs. This thermal crosstalk is illustrated in figure 1.9, where the array thermal resistance decreases with increasing distance between emitters. Typically, the total active area of an array can reach 80 to 90% [1].

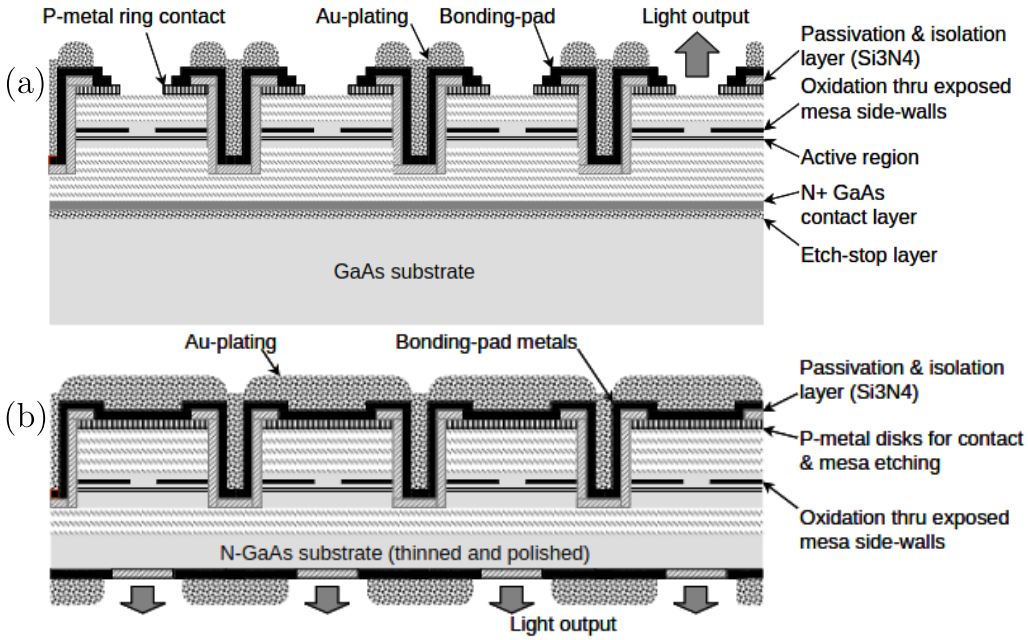

Figure 1.8: (a) Cross-section of a 2D VCSEL array of top-emitting devices, taken from [11]. (b) Cross-section of a 2D VCSEL array of bottom-emitting devices. Taken from [12].

Apart from thermal crosstalk, 2D VCSEL arrays keep the remarkable properties of a single emitter: circular beam, low divergence angle, narrow spectrum quantified by low FWHM of less than 1 nm and 4 to 6 times lower than EEL stacks [1] due to good chip-level uniformity, low thermally-induced wavelength redshift rate. Speckle-free emission is even achievable for arrays containing more than 100 emitters [1], which is an improvement compared to single emitters in imaging applications.

High brightness sources are fabricated by combining high power 2D VCSEL array with a matching micro lens array, for fiber coupling and small spots production, and achieve radiance $10MW.cm^2.sr$ [13].

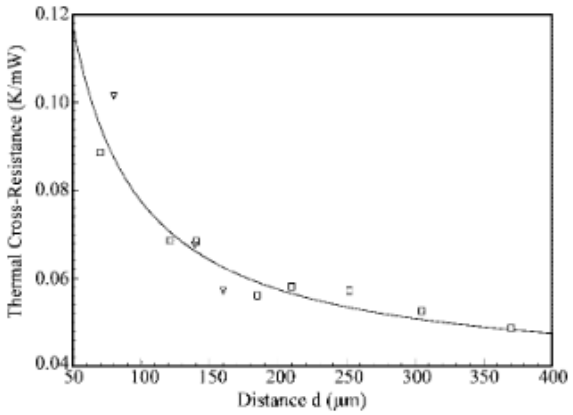

Figure 1.9: Thermal cross resistance of top-emitting VCSEL 2D array as a function of the distance between the emitters. Taken from [5].

Under CW operation at large current densities, self-heating increases optical losses which limits the emission output power. Higher optical peak powers can be generated using pulsed operation, with pulse width shorter than the time required for the VCSEL temperature to significantly increase, and low duty cycle for sufficient heat removal. The gain in power is about 10 times CW device performance [4]. An idea of the typical pulse widths can be found in figure 1.10.

Additionally, individual failure in 2D VCSEL arrays does not dramatically alter the emission quality nor impact adjacent devices [14].

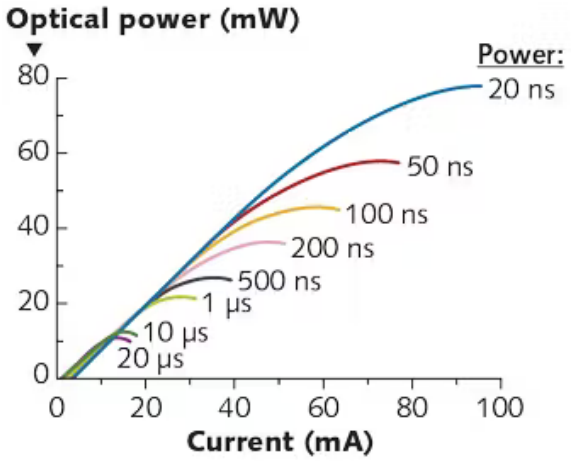

Figure 1.10: Optical power as a function of injected current of a typical VCSEL array under pulsed operation with different pulse widths. Taken from [15].

1.2.4 Discussion

The developement of high power VCSELs, which has become a more attractive solution than EELs, led to bottom-emitting devices and 2D arrays. Both aim the increase of the laser active area for power improvement, as well as high PCE to minimize the power consumption. Considering the current densities involved, the device self-heating is the main obstacle to a good PCE. Bottom-emitting devices are able to deliver higher output power than top-emitting ones, but are limited by the strong self-heating when the active area becomes large, leading to low PCE. Moreover, they are more difficult to fabricate than

top-emiting devices. 2D arrays of VCSELs take advantage of the remarkable properties of a single emitter, with an extention of the active area which is only limited by chip fabrication uniformity. However, the power density coming from these arrays is limited by the use of small or medium-size active area VCSELs, and by the minimum geometrical arrangement pitch value.

Since top-emitting VCSEL is the most straightforward structure to fabricate, the capability to produce large active area top-emitting devices is sought, in order to replace single bottom-emitting ones or to improve the power density of 2D arrays. The annular contact localized at the top these devices is responsible for the current distribution inhomogeneity when the active area diameter is typically larger than 50 µm. A transparent fully-covering contact might be employed as the top contact to overcome this limitation. This topic is presented in the next section.

1.3 Electrical contacts in VCSELs

Electrical contacts in VCSELs are crucial parts of VCSEL design for its performances in terms of PCE and output power. Like all electronic devices, both n and p-contact must be ohmic, and VCSEL devices require good electrode lateral and vertical current conduction. This section presents electrical contact modelling, properties, materials in GaAs-based optoelectronic devices, as well as techniques which have been developed to improve current injection uniformity. Particularly, the use of transparent conductive electrodes in top-emitting VCSELs will be presented.

1.3.1 Contact electrical properties

1.3.1.1 Ohmic contact

Ohmic contact is a specific qualification of the current flow behavior at a metal-semiconductor (MS) interface under forward and reverse bias voltage. The contact is defined as ohmic when the current can be conducted in both direction of the MS interface, which implies a non-rectifying junction that follow Ohm's law, represented by a linear I-V curve. It is opposed to the Schottky contact which is a diode, implying a rectifying behavior, and a certain energy threshold for the current to flow from the metal to the semiconductor. Thus, ohmic contact are important to ensure low contact resistance leading to improved PCE in the case of VCSELs.

The band diagram of the MS interface for n-type and p-type semiconductors is represented in figure 1.11. The semiconductor valence and conduction energy bands E_v and E_c are shown, as well as the Fermi level E_F which must be a constant throughout the semiconductor. Fermi level pinning causes E_v and E_c to bend at the interface because of the interface electronic states caused by unpaired electrons and crystal defects, creating an energy barrier when the junction reaches equilibrium. This barrier is called Schottky barrier, noted ϕ_B, and depends on the metal and semiconductor materials. Electrons that have sufficient thermal energy can cross the interface by a thermionic emission mechanism when ϕ_B is low enough, giving the current density described in equation 1.1.

$$J = J_s[exp(qV/nkT) - 1] \tag{1.1}$$

Where J_s is the saturation current density, q is the electron charge, k is the Boltzmann's constant, V is the applied voltage across the barrier, T is the temperature, and n the ideality factor.

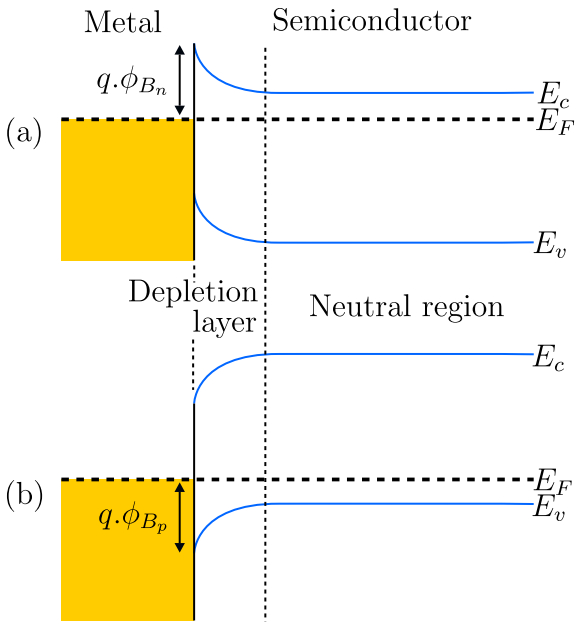

Figure 1.11: Energy band diagram of a metal–semiconductor contact, without bias voltage applied, where E_F is the Fermi level energy, E_c the conduction band energy, and E_v the valence band energy. (a) ϕ_{B_n} is the barrier against the electron flow between the metal and the N-type semiconductor, and (b) ϕ_{B_p} is the barrier against the hole flow between the metal and the P-type semiconductor.

In addition, the band bending can be narrow enough to enable current flow based on electron tunnelling called field emission, which results in a current density described in equation 1.2.

$$J = exp(-q\phi_B/E_{00}) \tag{1.2}$$

Where

$$E_{00} = q\hbar(N/\epsilon m^*)^{1/2}/2 \tag{1.3}$$

Where $\hbar$ is the Planck's constant divided by 2π, ϵ is the dielectric constant, N is the doping concentration, and * is the electron effective mass. In practice, both thermionic and field emission occur at room temperature, by tunnelling of thermally excited electrons through that barrier. This shows that an ohmic contact can be obtained by lowering ϕ_B, or by increasing the doping concentration. In the case of GaAs, the interface state densities are relatively high, which contrains a lot the lowering of ϕ_B [16]. Metallurgical approaches are employed to create a third material at the interface to lower the barrier, and will be briefly mentioned in section 1.3.2. Considering the doping level, in VCSELs or others optoelectronic devices, a compromise must be found between a high doping concentration at the semiconductor interface which causes light absorption, and a low one which would degrade the current injection efficiency.

1.3.1.2 Specific contact resistance

In VCSELs, and laser diodes in general, the contact area is large, and the current flow is vertical. Thus, an important figure of merit of the contact quality is the specific contact resistance ρ_c, generally expressed in $\Omega.cm^2$. As written in equation 1.4, it is defined by the contact resistance R_c in Ω, which is the resistance seen by the current when crossing the MS interface, multiplied by the effective contact area A in cm^2.

$$\rho_c = R_c \times A \tag{1.4}$$

This is a useful number to quantify the current injection efficiency in the device. While the fabrication of an ohmic contact is required, the minimization of ρ_c is also wanted for good device PCE.

1.3.1.3 Sheet resistance

Sheet resistance, noted R_{sh} and expressed in $\Omega.sq^{-1}$, is another important figure of merit to compare electrodes. It quantifies the ability of charge carriers to flow in the plane of a film with uniform thickness, by measuring the lateral resistance per square. It is used to characterize films of semiconducting and conducting materials [17]. Equations 1.5 and 1.6 give the two definitions of R_{sh}:

$$R_{sh} = R \times \frac{W}{L} \tag{1.5}$$

$$R_{sh} = \frac{\rho}{t} \tag{1.6}$$

With R the measured resistance in Ω, W, L, and t as defined in figure 1.12, and ρ the material bulk resistivity in $\Omega.m$. It can be seen in equation 1.5 that the square is an area unit, corresponding to the aspect ratio of W/L. The sheet resistance also corresponds to the bulk resistivity normalized by the film thickness, as seen in equation 1.6.

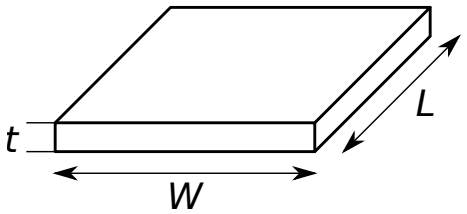

Figure 1.12: Schematic of a thin film defined by its three dimensions: L (length), W (width), and t (thickness). Taken from [18].

In the case of devices where current is injected vertically, like in VCSELs, a low R_{sh} is sought to ensure a good current homogenization in the plane of the electrode. This property, combined with a transparent electrode, could lead to better current injection homogeneity in the device.

1.3.2 Ohmic contact fabrication techniques in GaAs-based optoelectronic devices

Techniques have been developed to fabricate n-type and p-type GaAs devices with ohmic electrical contacts, involving various metals, in the forms of alloys or non-alloys. This work aims to fabricated and characterize metallic transparent electrodes based on gold, since it provides the desired optical properties, as will be explained in section 2.3. Thus, only usual gold-based contact techniques will be mentioned in this section. Table 1.2 presents values of Schottky barriers and specific contact resistivities found in litterature for n and p-type GaAs contacts, associated with doping concentration, for the main relevant gold-based materials for this work: Au, TiAu, TiPtAu, and GeAuNi. Since the VCSEL top electrode is usually a p-type contact, p-type contacts are the more relevant for this study, while n-type ones can be interesting as VCSEL inverted designs can also be used.

The fabrication of an ohmic contact usually consists in three steps:

1. Substrate surface cleaning: removal of both organic residues from previous fabrication steps by immersion in an organic solvent, and GaAs surface native oxide by wet-chemical etching in acidic solution (usually HCl or NH_4OH solutions). Indeed, both organic residues and native oxide would act as insulating materials. The native oxide is the result of a self-limited reaction of the GaAs surface with oxygen, and remains within a maximum depth of 2-3 nm [19] after long term air-exposure. It is composed of various stable compounds such as Ga_2O_3, As_2O3, and As_2O_5 [20]. After native oxide removal, the oxidation reaction starts again as soon as the surface is exposed to air. Since the re-oxidation is inevitable, minimizing the exposure time before metallic contact deposition or using in-chamber deoxidation can prevent the degradation of the electrical properties of the contact.

2. Metal deposition: different Physical Vapor Deposition (PVD) techniques are available for metal deposition, such as electron-beam, described in section 2.4.1, or sputter deposition.

3. Metal alloying: by annealing the deposited metallic layer, with control of temperature and time, to favor interdiffusion and lower the Schottky barrier.

Contact material	Au	TiAu	TiPtAu	GeAuNi
$\phi_{B_p}(eV)$	0.7 (doping $5.10^{16}cm^{-3}$) [21]	0.6 (doping $3.65.10^{17}cm^{-3}$) [22]		
$\phi_{B_n}(eV)$	0.92 (doping $10^{16}cm^{-3}$) [23]		0.8 (doping $1.5.10^{17}cm^{-3}$) [24]	0.4 (doping $5.10^{18}cm^{-3}$) [25]
$\rho_{c_p}(\Omega.cm^2)$		$2.7.10^{-7}$ (doping $5.10^{19}cm^{-3}$) [26]	$2.75.10^{-6}$ (doping $10^{19}cm^{-3}$) [27]	
$\rho_{c_n}(\Omega.cm^2)$		$4.5.10^{-7}$ (doping $10^{20}cm^{-3}$) [26]		$< 10^{-6}$ [16]

Table 1.2: Gold alloyed and non-alloyed p-GaAs and n-GaAs contact properties: ϕ_{B_p} the Schottky barrier on p-GaAs, ϕ_{B_p} the Schottky barrier on n-GaAs, ρ_{c_p} the specific contact resistance on p-GaAs, ρ_{c_n} the specific contact resistance on n-GaAs.

In all the presented contacts, Au is employed for its excellent electrical conductivity, and because it doesn't oxidize when exposed to air.
Alternatively, a GeAuNi contact is a widely-used alloyed contact for both n and p-type GaAs. In this contact, Ni reacts with the GaAs native oxide and facilitates the interdiffusion of others elements between contact and GaAs. Ge acts as a GaAs dopant by diffusion at the interface, that is facilitated by the presence of Ni. Au participates to the alloy by forming the AuGa compound when Ga diffuses in the contact when the temperature exceeds 250°C [16]. The formation of AuGa is known as the limiting factor of the contact thermal stability, as it degrades the contact [16].
P-type GaAs contacts have lower Schottky barrier height [16], which enabled the development of non-alloyed contacts. An important one is the TiPtAu structure, where Ti is used

as a stable adhesion layer on the GaAs, Pt acts as diffusion barrier, preventing from Au and Ga interdiffusion at high temperatures, improving the contact thermal stability.
TiAu contacts are also employed, without the feature of diffusion barrier, when the fabrication process and operation temperature are not considered high enough to degrade the contact.
In practice, Au is never used on its own as a contact, because of its poor adhesion on GaAs surface and its ability to diffuse in it. Nevertheless, its Schottky barrier values are presented since this configuration concerns some of the structures fabricated and presented in this work.

1.3.3 Top electrode engineering

This work focuses on the development of a new transparent electrode for improved top-emitting VCSEL current injection uniformity, using conventional top-emitting VCSEL designs. In the litterature, several methods implying significant VCSEL structure and process modifications to localize the current injection have been reported, and won't be mentioned in the following state of art, but a summary may be found in [28]. This part presents the state of art of solutions for VCSEL top-electrodes, with a first part dedicated to the opaque metallic electrodes, and a second one dedicated to the transparent conductive electrodes (TCE).

1.3.3.1 Opaque metallic electrodes

Metallic electrodes are desired to take advantage of the excellent electrical conductivity, and the widespread metalurgical techniques to get ohmic contacts on GaAs devices. Optically, metal mainly reflects or absorbs light, leading to contact geometry optimization to prevent these optical losses in the case of emitting devices.
The most widely used top-electrode scheme in top-emitting VCSEL structures is the metallic annular contact, which is associated with a buried oxide aperture to guide the injected current through the active region while avoiding emission beam interaction with the metal, forming the well-known oxide-confined VCSEL. It is explained in section 1.2.2 that this design limits the device active area by a current crowding effect at the aperture edges.
In order to improve current injection homogeneity over large areas, while keeping the metal electrical properties, metal grid electrodes have been developed as in [29]. A schematic of the idea is presented in 1.13a. The study reports metal grids with a periodicity of 4 µm, with 1-µm-width metal lines composed of a ∼120-nm-thick PtTiPtAu contact. Figure 1.13b show the measured near-field emission of the device. As one can see, the emission is uniform through the grid windows for a $40 \times 40 \mu m^2$ VCSEL, as a consequence of a uniform current density distribution, while the metal lines block the emission at their locations. This technique improves the capability to extend the active area, while the presence of metal remains a limiting factor. In addition, the current is injected where the emission is blocked, creating shadow losses that could lower the device PCE.

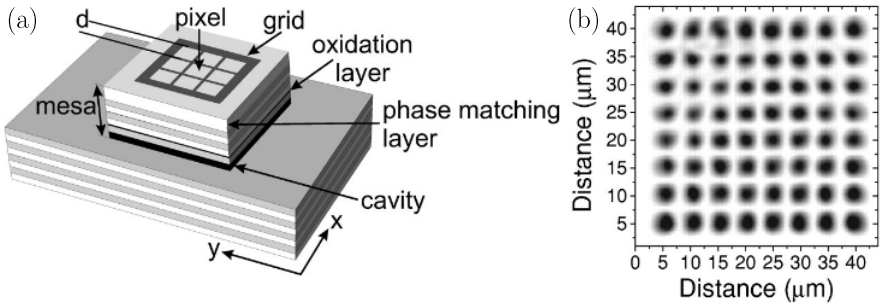

Figure 1.13: (a) Schematic of the metal grid electrode implemented on top of VCSEL structure (b) corresponding near field emission (c) corresponding far field emission. Taken from [29].

1.3.3.2 Transparent conductive electrodes

Transparent conductive electrode (TCE) is a crucial element in information and energy technologies, that include liquid cristal displays, touchscreens, OLEDs, LEDs, solar cells, or smart windows. Historically, the employed TCE were transparent conductive oxides (TCO), such as the well-known and widely spread Indium Tin Oxide (ITO). New types of TCE are emerging in the shape of nano or/and 2D-structured materials, such as metal nanowire networks or graphene. In addition, hybrid approaches are being studied combining TCO or dielectric materials with nanowires, metal grids, or ultrathin metal films [30].

Employing TCE appears to be the ideal way to achieve uniform current injection over broad areas in VCSELs, since the solution that consists in increasing the top Bragg reflector doping to enhance the current lateral spreading would strongly increase the free carrier absorption. The most important TCE properties are high electrical conductivity and high optical transparency in the targeted spectral window. The electrical conductivity, which can be expressed by the Drude-Boltzmann relation presented in equation 1.7,

$$\sigma = e.N.\mu \tag{1.7}$$

where σ is the conductivity, e is the elementary charge, N the carrier density, and μ the carrier mobility, is high in the case of high carrier density and high carrier mobility.
However, a high carrier density induces various absorption processes such as free carrier absorption, which increases the total absorption coefficient α, thus deteriorating the optical transparency. This is a challenging aspect in TCE design, which has to be specific to the targeted application requirements. This optimization is typically performed by the use of a figure of merits involving the σ/α ratio with the adequate ponderation σ and α to suit the targetted properties [31].

In the case of VCSELs, good electrical conductivity must be ensured in both lateral and vertical directions, meaning that respectively a low sheet resistance and a low specific contact resistance are required. Since the latter depends on both the electrode and the substrate materials, not all existing TCE are compatible with GaAs-based devices. In addition, long device lifetime requires a chemically and thermally stable TCE.

The use of TCE as VCSEL top electrode has been reported in the litterature to fabricate large active area single emitters, to increase the density of emitters, so the density of active area in 2D arrays, or to simplify the top contact deposition process compared to the usual approach. The main material that has been studied for VCSEL technology is ITO, while rare alternatives using emerging TCE like graphene or metal nanowires are also reported as detailed hereafter.

1.3.3.2.1 ITO

ITO, chemically described as $In_2O_3 - SnO_2$, is the most ubiquitous TCE used in industry primarily for liquid crystal displays and more recently for thin film solar cells. It has the advantage of a good transparency in the visible range and a relatively low sheet resistance which can approach a minimal value of 10 $\Omega.sq^{-1}$ [31]. In addition, deposited ITO on GaAs substrate can result in good ohmic contact using appropriate thermal annealing [32]. On the other hand, among its limitations, which depend on the targeted application, the scarcity of indium has led to the research of new alternatives. Both the electrical conductivity and the optical transparency limitations will be discussed in the context of their implementation on VCSELs.

The first top-emitting VCSEL employing ITO as top transparent electrode has been reported in 1997 in [32]. This is an interesting study to quantify the differences between the properties of ITO/p-GaAs and standard metal/p-GaAs contacts. The sheet resistance, specific contact resistance, and power transmission spectrum are measured from a 200-nm-thick ITO layer deposited on a p-GaAs cap layer with a doping concentration of $5.10^{18}cm^{-3}$, as a function of the contact annealing temperature. The results are respectively presented in figures 1.14b, 1.14a, 1.14c. The measured sheet resistance without annealing is $70\Omega.sq^{-1}$, and drops with the increase of the annealing temperature to a value of $12.5\Omega.sq^{-1}$ at 600°C. Similarly, it shows that the specific contact resistance for a low temperature process equals $\sim 10^{-3} - 10^{-2}\Omega.cm^2$, while it drops to $\sim 10^{-5}\Omega.cm^2$ above 600°C. In terms of power transmission spectrum through ITO, the unannealed ITO presents the best transmission, around 90%, in the 800-900 nm spectral region, which is the one targeted in most VCSELs applications, as well as in this work.

The 200-nm-thick ITO electrical properties can be compared to metal ones. In terms of sheet resistance, a gold thin film can typically give values lower than $1\Omega.sq^{-1}$. Thus, the lowest measured value for ITO remains more than ten times higher than that of gold. Specific contact resistances must be compared considering the same level of p-GaAs cap layer doping. Available values for a doping level of $5.10^{18}cm^{-3}$ are lacking, but the ITO value of $\sim 10^{-5}\Omega.cm^2$ reached with a high temperature annealing of 600°C is between one and two orders of magnitude higher than reported values for a doping concentration of $10^{19}cm^{-3}$ (see table 1.2).

Metal contacts are clearly electrically more advantageous, but the issue of current injection inhomogeneity motivated comparative studies between charateristics of typical oxide-confined VCSELs with annular metallic and ITO top-contacts. Such quantitative analysis has been reported in [33] and [34]. For 850-nm VCSELs, these studies respectively show an output power improvement of 27% and 18% at same driving currents for 10-µm-aperture devices. It is also reported in [33] that the device differential resistance is slightly higher using ITO, due to the higher specific contact resistance of the ITO/GaAs contact, which is in good agreement with the ITO/p-GaAs specific contact resistance value presented in [32]. Figure 1.15 presents the near-field emission of two broad-area 100-µm-aperture oxide-confined VCSELs: one using standard annular metallic top-contact, and one using ITO top-contact. It clearly shows a strong improvement of current injection uniformity using ITO.

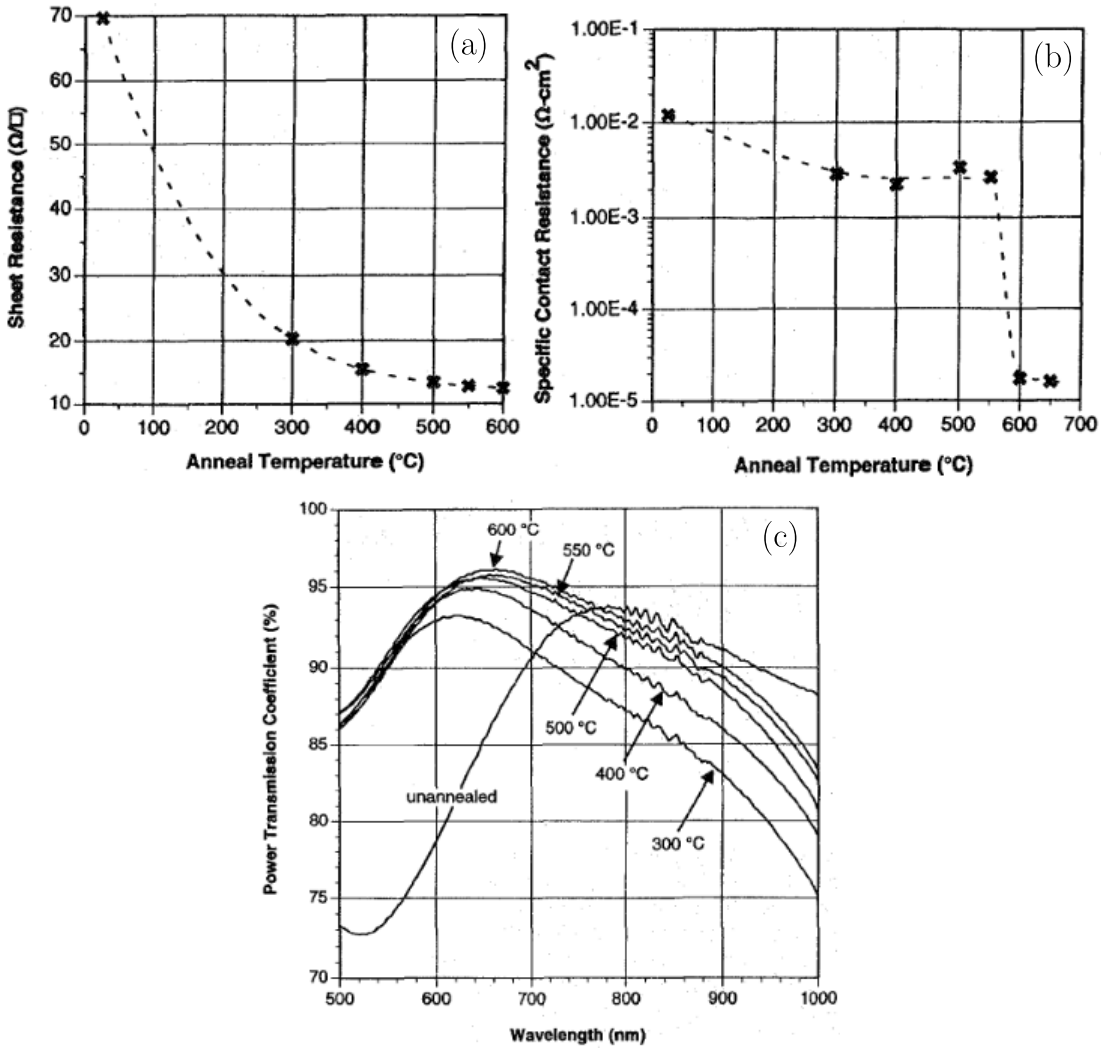

Figure 1.14: (a) Specific contact resistance of ITO on p-GaAs with a doping concentration of $5.10^{18} cm^{-3}$, (b) sheet resistance of a 200-nm-thick ITO layer, and (c) power transmission spectrum of a 200-nm-thick ITO layer, as a function of annealing temperature. Taken from [32]

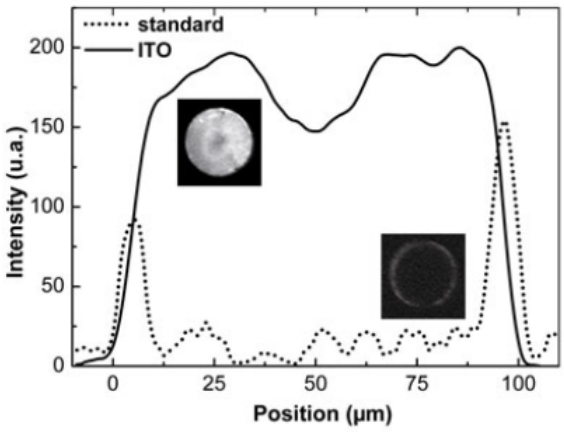

Figure 1.15: Near-field emission profiles of a 100-µm-aperture VCSEL with (a) an annular metallic contact, and (b) an ITO fully-covering contact. Taken from [9].

1.3.3.2.2 Graphene

Graphene is considered as a promising candidate to become a TCE in many applications. The atomic monolayer thickness allows high transmittance in the visible and NIR spectral regions [35], while the low carrier density ($< 10^{13} cm^{-3}$ [30]) is responsible for a quite low conductivity despite its extremely high carrier mobility ($10^3 - 10^4 cm^2.V^{-1}.s^{-1}$ in practice [31]). Thus, graphene needs to be doped and/or stacked in order to compete with ITO in terms of sheet resistance, increasing the optical absorption, and complicating the fabrication. Sheet resistances between 20 and 1000 $\Omega.sq^{-1}$ have been experimentally achieved [31], with transmittance around 90% in the NIR spectral region reported in [36]. The main advantage of graphene over ITO is its mechanical capability to bend, which is not sought in the case of VCSELs. Even so, graphene has been introduced as TCE in VCSELs in [37, 38, 39]. A 35-µm-aperture proton implanted VCSEL has been shown to allow a good current injection uniformity in [37].

1.3.3.2.3 Metallic nanostructured materials

Metallic nanostructured materials is a promising approach for the next generation of TCE, and appears to be relevant for VCSEL technology as they enable the use of metals, taking advantage of their excellent electrical properties, with the added benefit of high transparency. A wide variety of structures such as subwavelength 1D or 2D metal periodic gratings [40, 41], as well as patterned or randomely distributed nanoparticule/nanowire networks [42, 43] have been studied.

Among these techniques, the use of silver nanowire film as VCSEL transparent top electrode has been reported in [44]. Silver nanowires are dispersed in liquid solution and spin-coated on the wafer surface. This technique is promising for industry since it is already compatible with large-scale production without the need for vacuum deposition and high temperature processing. Both the silver nanowires concentration in the solution and the spin-coating speed define the number of nanowires in the film. The contact between the nanowires provides percolation paths that result in high electrical conductivity. Thus, the higher the number of nanowires, the higher the conductivity. This can be seen by comparing figures 1.16a and 1.16b, where the nanowire density lowers the film sheet resistance. Sheet resistance can be in the range of 10 to 1000 $\Omega.sq^{-1}$ [31]. Figure 1.16c shows that the lower is the sheet resistance of the silver nanowire film, the lower is the transmittance spectrum. Light transmission through silver nanowire film is enabled by the gaps between the nanowires. The lower is the nanowire density, the higher is the transmission, thus the lower is the sheet resistance. Once again, this TCE relies on the balance between high conductivity and high transparency. In addition, figure 1.16c shows that the silver nanowire film transmittance spectrum can be not only as high but also broader than the ITO one for comparable sheet resistance value. A sheet resistance of $28.4\Omega.sq^{-1}$ associated with a transmittance of 94.8% at 850 nm is reported in [44]. It also demonstrates a slightly higher output power, due to the more uniform current distribution, and a lower device differential resistance for a 42-µm-aperture oxide-confined VCSEL with the silver nanowire film top electrode than with a standard annular metallic one.

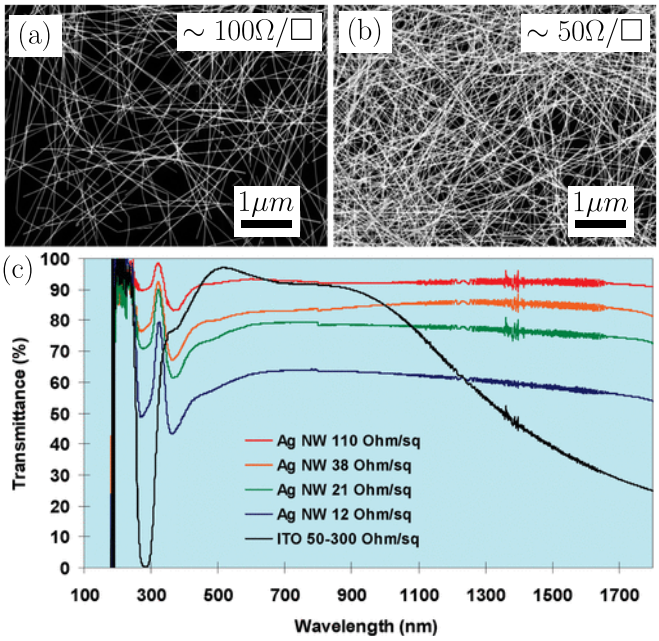

Figure 1.16: (a) SEM image of silver nanowire film resulting in a sheet resistance of $\sim 100\Omega.sq^{-1}$ (b) SEM image of silver nanowire film resulting in a sheet resistance of $\sim 50\Omega.sq^{-1}$ (c) silver nanowire film transmittance spectrum as a function of the corresponding network sheet resistance, and comparison with ITO transmittance spectrum. Taken from [43].

1.4 Conclusion

The issue of the current injection uniformity in standard top-emitting VCSELs, and the induced limitations on the output power of single emitters and on the power density of 2D VCSEL arrays have been presented. This is caused by the top electrode annular shape, which can be replaced by a fully-covering contact located above the VCSEL emission area in top-emitting devices using a TCE. The development of this idea is very attractive since the top-emitting VCSELs are the most straightforward structures to fabricate. Among the many TCEs reported in the litterature, three have been studied for their use in VCSELs: ITO, graphene, and silver nanowire film. ITO is the most commonly reported, and is used in a lot of applications, which explains the availability of a more comprehensive set of electrical and optical characterizations, while the specific contact resistance on GaAs substrate has not been reported yet for graphene or silver nanowire film. The silver nanowire film can compete with ITO in terms of transparency and sheet resistance, but for both solutions, the achievement of a low sheet resistance ($\sim 10\Omega.sq^{-1}$) comes at the expense of an increase of the optical absorption or of a high temperature processing in the case of ITO. This compromise limits the TCE sheet resistance to values at least ten times higher than that of the metal thin film ($< 1\Omega.sq^{-1}$). Also, the reported ITO specific contact resistance remains at least one order of magnitude below then one reported for gold-based contacts on p-GaAs. The emerging field of metallic nanostructured material brings some new interesting structures to combine standard metallic contact compositions presented in section 1.3.2, which should enable a low specific contact resistance, with the high optical transparency required for TCEs. This is the case of 1D subwavelength metal line gratings, known as plasmonic gratings, which show high transmission with polarization selectivity. A new type of TCE, whose structure is also a 1D subwavelength metal grating, is a promising VCSEL top electrode and is presented in the next chapter, where its fabrication as well as its optical and electrical properties are demonstrated.

Bibliography

[1] R. Michalzik, "VCSEL Fundamentals," in *VCSELs* (R. Michalzik, ed.), vol. 166, pp. 19–75, Berlin, Heidelberg: Springer Berlin Heidelberg, 2013.

[2] A. Moser and E. E. Latta, "Arrhenius Parameters for the Rate Process Leading to Catastrophic Damage of AlGaAs-GaAs Laser Facets," *Journal of Applied Physics*, vol. 71, no. 10, pp. 4848–4853, 1992.

[3] L. D'Asaro, J. Seurin, and C. Ghosh, "VCSELs: Powerful VCSEL Arrays Beat the Heat," *Laser Focus World*, 2007.

[4] B. D. Padullaparthi, J. A. Tatum, and K. Iga, *VCSEL Industry: Communication and Sensing*. Wiley : IEEE Press, 2022.

[5] M. Grabherr, M. Miller, R. Jager, R. Michalzik, U. Martin, H. Unold, and K. Ebeling, "High-Power VCSELs: Single Devices and Densely Packed 2-D-arrays," *IEEE Journal of Selected Topics in Quantum Electronics*, vol. 5, no. 3, pp. 495–502, 1999.

[6] K. Choquette and H. Hou, "Vertical-Cavity Surface Emitting Lasers: Moving from Research to Manufacturing," *Proceedings of the IEEE*, vol. 85, no. 11, pp. 1730–1739, 1997.

[7] L. D'Asaro, J. Seurin, and J. D. Wynn, "High-Power, High-Efficiency VCSELs Pursue the Goal," *Photonics media*, 2005.

[8] K. Lear, S. Kilcoyne, and S. Chalmers, "High Power Conversion Efficiencies and Scaling Issues for Multimode Vertical-Cavity Top-Surface-Emitting Lasers," *IEEE Photonics Technology Letters*, vol. 6, no. 7, pp. 778–781, 1994.

[9] T. Camps, V. Bardinal, E. Havard, M. Condé, C. Fontaine, G. Almuneau, L. Salvagnac, S. Pinaud, and J. B. Doucet, "Management of the Electrical Injection Uniformity in Broad-Area Top-Emitting VCSELs," *The European Physical Journal D*, vol. 59, no. 1, pp. 53–57, 2010.

[10] "High Power VCSEL Array, https://ii-vi.com/product/high-power-vcsel-array/."

[11] J.-F. Seurin, G. Xu, V. Khalfin, A. Miglo, J. D. Wynn, P. Pradhan, C. L. Ghosh, and L. A. D'Asaro, "Progress in High-Power High-Efficiency VCSEL Arrays," in *SPIE OPTO*, p. 722903, Feb. 2009.

[12] J.-F. Seurin, C. L. Ghosh, V. Khalfin, A. Miglo, G. Xu, J. D. Wynn, P. Pradhan, and L. A. D'Asaro, "High-Power High-Efficiency 2D VCSEL Arrays," in *Integrated Optoelectronic Devices 2008*, p. 690808, 2008.

[13] J.-F. Seurin, G. Xu, Q. Wang, B. Guo, R. Van Leeuwen, A. Miglo, P. Pradhan, J. D. Wynn, V. Khalfin, and C. Ghosh, "High-Brightness Pump Sources Using 2D VCSEL Arrays," in *SPIE OPTO*, p. 76150F, 2010.

[14] H. Moench, R. Conrads, C. Deppe, G. Derra, S. Gronenborn, X. Gu, G. Heusler, J. Kolb, M. Miller, P. Pekarski, J. Pollmann-Retsch, A. Pruijmboom, and U. Weichmann, "High-Power VCSEL Systems and Applications," in *SPIE LASE*, p. 93480W, 2015.

[15] H. Mönch, "Vertical-Cavity Surface-emitting Lasers: VCSEL Arrays Provide Leading-Edge Illumination for 3D Sensing," *Laser Focus World*, 2017.

[16] A. Baca and C. Ashby, *Fabrication of GaAs Devices*. Institution of Engineering and Technology, 2005.

[17] M. Naftaly, S. Das, J. Gallop, K. Pan, F. Alkhalil, D. Kariyapperuma, S. Constant, C. Ramsdale, and L. Hao, "Sheet Resistance Measurements of Conductive Thin Films: A Comparison of Techniques," *Electronics*, vol. 10, no. 8, p. 960, 2021.

[18] M. Ryazanov, "https://commons.wikimedia.org/w/index.php?curid=48912949."

[19] B. Tanner, D. Allwood, and N. Mason, "Kinetics of Native Oxide Film Growth on Epiready GaAs," *Materials Science and Engineering: B*, vol. 80, no. 1-3, pp. 99–103, 2001.

[20] G. Hollinger, R. Skheyta-Kabbani, and M. Gendry, "Oxides on GaAs and InAs Surfaces: An x-Ray-Photoelectron-Spectroscopy Study of Reference Compounds and Thin Oxide Layers," *Physical Review B*, vol. 49, no. 16, pp. 11159–11167, 1994.

[21] T. Okumura and K. N. Tu, "Electrical Characterization of Schottky Contacts of Au, Al, Gd, and Pt on \emphn -Type and \emphp -Type GaAs," *Journal of Applied Physics*, vol. 61, no. 8, pp. 2955–2961, 1987.

[22] D. R. Lovell, T. Yamamoto, M. Inai, T. T. Toshihiko Takebe, and K. K. Kikuo Kobayashi, "Titanium/Gold Schottky Contacts on P-Type GaAs Grown on (111)A and (100) GaAs Substrates Using Molecular Beam Epitaxy," *Japanese Journal of Applied Physics*, vol. 31, no. 7B, p. L924, 1992.

[23] G. Myburg, F. Auret, W. Meyer, C. Louw, and M. Van Staden, "Summary of Schottky Barrier Height Data on Epitaxially Grown n- and p-GaAs," *Thin Solid Films*, vol. 325, no. 1-2, pp. 181–186, 1998.

[24] B. Sehgal, R. Gulati, A. Naik, S. Vinayak, D. Rawal, and H. Sharma, "(N)GaAs/Ti/Pt/Au Schottky Contacts and Their Effect on MESFET's Dc Parameters," *Materials Science and Engineering: B*, vol. 48, no. 3, pp. 229–233, 1997.

[25] R. Gupta and W. Khokle, "Specific Resistivity of a Metal-n GaAs OHMIC Contact with an Intermediate N+ Layer," *Microelectronics Reliability*, vol. 25, no. 5, pp. 837–840, 1985.

[26] M. P. Patkar, T. P. Chin, J. M. Woodall, M. S. Lundstrom, and M. R. Melloch, "Very Low Resistance Nonalloyed Ohmic Contacts Using Low-Temperature Molecular Beam Epitaxy of GaAs," *Applied Physics Letters*, vol. 66, no. 11, pp. 1412–1414, 1995.

[27] S. S. Mahajan, A. Sharma, D. Jain, H. Saini, B. Yadav, A. Naik, and A. Jain, "A Comparative Study of Ti and Cr Based P-Ohmic Contacts on High Power GaAs Laser Diodes," *Vacuum*, vol. 152, pp. 128–131, 2018.

[28] E. Havard, *Contribution à l'étude de l'injection Électrique Dans Les VCSEL de Grandes Dimensions*. PhD Thesis, Université Toulouse 3, 2008.

[29] F. Monti Di Sopra, M. Brunner, H.-P. Gauggel, H. P. Zappe, M. Moser, R. Hövel, and E. Kapon, "Continuous-Wave Operation of Phase-Coupled Vertical-Cavity Surface-Emitting Laser Arrays," *Applied Physics Letters*, vol. 77, no. 15, pp. 2283–2285, 2000.

[30] M. Morales-Masis, S. De Wolf, R. Woods-Robinson, J. W. Ager, and C. Ballif, "Transparent Electrodes for Efficient Optoelectronics," *Advanced Electronic Materials*, vol. 3, no. 5, p. 1600529, 2017.

[31] A. D. Andrés, F. Jiménez-Villacorta, and C. Prieto, "The Compromise Between Conductivity and Transparency," in *Transparent Conductive Materials*, pp. 1–30, 2018.

[32] C. Chua, R. Thornton, D. Treat, V. Yang, and C. Dunnrowicz, "Indium Tin Oxide Transparent Electrodes for Broad-Area Top-Emitting Vertical-Cavity Lasers Fabricated Using a Single Lithography Step," *IEEE Photonics Technology Letters*, vol. 9, no. 5, pp. 551–553, 1997.

[33] W.-J. Jiang, M.-C. Wu, H.-C. Yu, C.-Y. Huang, C.-P. Sung, and J.-Y. Chi, "The Effect of Indium Tin Oxide as an Ohmic Contact for the 850 Nm GaAs Oxide-Confined VCSELs," *Solid-State Electronics*, vol. 46, no. 11, pp. 1945–1948, 2002.

[34] X. Meng, X. Chen, W. Jun, L. Jie, X. Kun, M. M. Ming, and Z. Y. Xu, "The Effect of Indium Tin Oxide as Transparent Conductive Layer for Oxide-Confined VCSELs," in *International Photonics and OptoElectronics Meetings*, p. OTh4C.5, OSA, 2014.

[35] R. R. Nair, P. Blake, A. N. Grigorenko, K. S. Novoselov, T. J. Booth, T. Stauber, N. M. R. Peres, and A. K. Geim, "Fine Structure Constant Defines Visual Transparency of Graphene," *Science*, vol. 320, no. 5881, pp. 1308–1308, 2008.

[36] S. Bae, H. Kim, Y. Lee, X. Xu, J.-S. Park, Y. Zheng, J. Balakrishnan, T. Lei, H. Ri Kim, Y. I. Song, Y.-J. Kim, K. S. Kim, B. Özyilmaz, J.-H. Ahn, B. H. Hong, and S. Iijima, "Roll-to-Roll Production of 30-Inch Graphene Films for Transparent Electrodes," *Nature Nanotechnology*, vol. 5, no. 8, pp. 574–578, 2010.

[37] L. Jie, X. Chen, X. Meng, W. Jun, and M. M. Ming, "The Effect of Graphene for Large Aperture Vertical Cavity Surface Emitting Laser," in *International Photonics and OptoElectronics Meetings*, p. OF5A.1, OSA, 2014.

[38] H. Ding, H. Li, B. Guan, and L. Liu, "Research on Graphene as Transparent Electrode of VCSEL Arrays," in *2021 4th International Conference on Electron Device and Mechanical Engineering*, (Guangzhou, China), pp. 130–134, IEEE, 2021.

[39] B. Guan, P. Li, S. Arafin, Y. Alaskar, and K. L. Wang, "Investigation of Single-Mode Vertical-Cavity Surface-Emitting Lasers with Graphene-Bubble Dielectric DBR," *Photonics and Nanostructures - Fundamentals and Applications*, vol. 28, pp. 56–60, 2018.

[40] J. Van De Groep, P. Spinelli, and A. Polman, "Transparent Conducting Silver Nanowire Networks," *Nano Letters*, vol. 12, no. 6, pp. 3138–3144, 2012.

[41] P. B. Catrysse and S. Fan, "Nanopatterned Metallic Films for Use As Transparent Conductive Electrodes in Optoelectronic Devices," *Nano Letters*, vol. 10, no. 8, pp. 2944–2949, 2010.

[42] M. Layani, A. Kamyshny, and S. Magdassi, "Transparent Conductors Composed of Nanomaterials," *Nanoscale*, vol. 6, no. 11, pp. 5581–5591, 2014.

[43] L. Hu, H. S. Kim, J.-Y. Lee, P. Peumans, and Y. Cui, "Scalable Coating and Properties of Transparent, Flexible, Silver Nanowire Electrodes," *ACS Nano*, vol. 4, no. 5, pp. 2955–2963, 2010.

[44] X. Guo, L. Shi, C. Li, J. Dong, B. Liu, S. Hu, and Y. He, "Research of the Use of Silver Nanowires as a Current Spreading Layer on Vertical-Cavity Surface-Emitting Lasers," *Chinese Physics B*, vol. 25, no. 11, p. 114208, 2016.

CHAPTER 2

Novel metallic transparent conductive electrodes for improved electrical injection uniformity in VCSELs

This chapter presents the fabrication and the optical and electrical characterizations of a new TCE, composed of a combination of subwavelength line gratings made of gold-based metallic contact and GaAs. Several configurations of polarization-selective highly-transmittive TCE are demonstrated, for both transverse electric (TE) and transverse magnetic (TM) polarizations, associated with the excellent electrical properties of metal. Such structures are also very promising for other optoelectronic devices like surface-emitting LEDs or photodetectors.

Contents

2.1 Introduction 30
2.2 Light transmission through subwavelength grating 30
2.2.1 From diffraction gratings to deep-subwavelength gratings 30
2.2.2 Transmission through semiconductor monolithic high contrast grating 32
2.2.3 Transmission through subwavelength-aperture metallic grating . 33
2.3 Transmission mechanisms in SMDSG structures 34
2.3.1 High transmission through SMDSG in B-TE configuration 35
2.3.2 High transmission through SMDSG in T-TM configuration . . . 36
2.3.3 Conclusion 37
2.4 Fabrication 38
2.4.1 Presentation of the nano-structuration and the characterization techniques for the fabrication 38
2.4.2 Optimization of SMDSG dimensions 43
2.4.3 Developed fabrication processes 47
2.4.4 Fabricated SMDSGs 52
2.5 Characterizations 58
2.5.1 Spectroscopy 58
2.5.2 Sheet resistance 63
2.5.3 Specific contact resistance 65
2.6 Conclusion and perspectives 67

2.1 Introduction

A new concept of TCE has been introduced in [1] by Tomasz Czyszanowski et al. in 2020, a fundamental study for this work which is presented in appendix A. It consists in a combination of a 1D subwavelength grating made of semiconductor interleaved with another one made of metal, and is called semiconductor-metal deep-subwavelength grating (SMDSG). The understanding of the possible structures allowed by this type of TCE, and the corresponding physical principles that explain the high transmission is the aim of the first part of this chapter. For this purpose, the light propagation in subwavelength line gratings, and the possibility to transmit light through a 1D semiconductor subwavelength grating, as well as through a 1D metallic grating with subwavelength apertures are presented. Then, the two TCE structures combined together are introduced, explaining how high transmission can be achieved through SMDSGs under transverse-electric (TE) or transverse-electric (TM) polarized light. TE polarization is defined as the electric field vector being parallel to the grating stripes, while TM corresponds to the magnetic field vector being parallel to the grating stripes. Then, the calculation of the optimal parameters for the SMDSG high transmission in the near infrared (NIR) spectral region, and more precisely for a wavelength of 940 nm and normal incidence, are presented. The demonstration of the fabrication of these structures as well as their optical and electrical properties constitutes the final section of this chapter.

2.2 Light transmission through subwavelength grating

Among the wide variety of periodic structures, one-dimensional diffraction gratings are employed in many applications such as optical filtering, spectral beam combiner, optical coupling, or pulse shaping. The improvement of fabrication techniques has led to the achievement of line gratings with a periodicity comparable to the wavelength and even lower, considering the visible and NIR spectral ranges. A grating with a periodicity Λ lower than the free space wavelength of the incident light λ_0 is called a subwavelength grating, while it is refered as a deep-subwavelength grating when $\Lambda < \lambda_0/n$ with n the grating material refractive index. The Λ/λ_0 ratio defines different regimes associated to different grating properties. Deep-subwavelength regime is the one of interest in this section, since it enables high transmission. After a short introduction to 1D diffraction grating modelling, the transmission mechanisms through 1D semiconductor subwavelength grating and 1D metal subwavelength grating will be presented for both TE and TM polarizations, since these structures are polarization sensitive by their nature of one-dimensional periodicity. This will be used subsequently to explain which transmission mechanisms can be considered when the two gratings are combined to give the TCE experimentally studied in this work.

2.2.1 From diffraction gratings to deep-subwavelength gratings

When the grating period becomes comparable to the incident beam free space wavelength, the optical response is governed by diffraction. The incident beam is broken down into diffracted reflected and transmitted beams due to constructive and destructive interferences. For a monochromatic light interacting with a diffraction grating, the main grating properties are: the number of reflected and transmitted diffraction orders, their corresponding angle, and their corresponding power. While the calculation of the power transported in each order requires the resolution of Maxwell's equations, the knowledge of the number of propagating orders and their angle is given by the grating equation 2.1. Figure 2.1 defines the important parameters to understand the grating equation. In this schematic, a

monochromatic light beam defined by it free space wavelength λ_0, wave vector $\vec{k_0}$ associated with its wavenumber $k_0 = 2\pi/\lambda_0$, is incident on the grating at angle θ_i. The propagation goes from a medium of refractive index n_0 toward a medium of refractive index n_1. The reflected m-order angle is written θ_m^r, while the transmitted m-order angle is written θ_m^t. Last, grating period is written Λ.

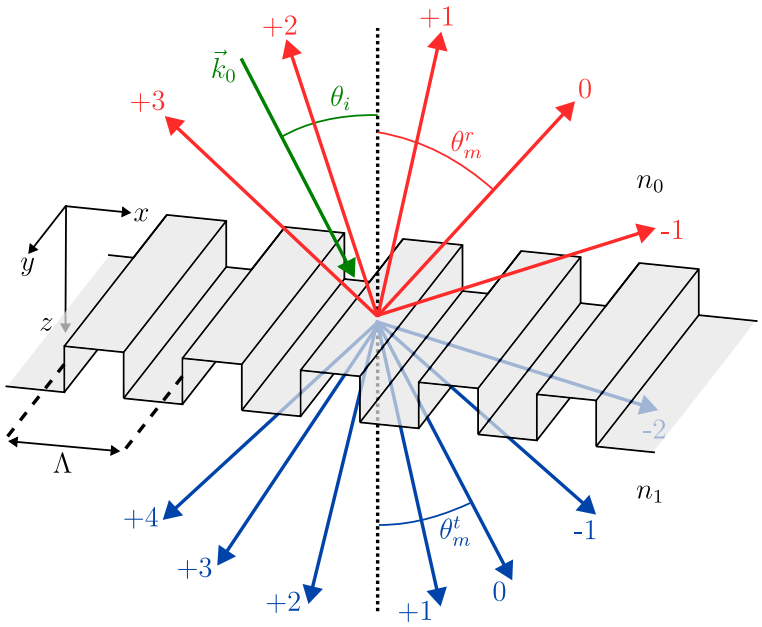

Figure 2.1: Schematic cross-section of a grating structure with its parameter definitions.

The grating equation enables to calculate the tangential component $k_{x,m}$ of the diffracted m-order as a function of grating period and angle of incidence, and is written as:

$$k_{x,m} = k_{x,i} - mK, \qquad m = 0, \pm1, \pm2, ..., \tag{2.1}$$

Where m is an integer giving the diffraction order, $k_{x,m}$ is the tangential component of the m-order wave vector, $k_{x,i}$ is the tangential component of $\vec{k_0}$ and defined as $k_{x,i} = n_0 k_0 sin(\theta_i)$, and K is the grating wavenumber $K = 2\pi/\Lambda$. Using $k_{x,m} = n_0 k_0 sin(\theta_m^r)$ and $k_{x,m} = n_1 k_0 sin(\theta_m^t)$ respectively for the reflected and transmitted m-order, equation 2.1 becomes:

$$n_0 sin(\theta_m^r) = n_0 sin(\theta_i) - m\frac{\lambda_0}{\Lambda}, \qquad m = 0, \pm1, \pm2, ..., \tag{2.2}$$

$$n_1 sin(\theta_m^t) = n_0 sin(\theta_i) - m\frac{\lambda_0}{\Lambda}, \qquad m = 0, \pm1, \pm2, ..., \tag{2.3}$$

Equations 2.2 and 2.3 give access to respectively θ_m^r and θ_m^t. Considering a given diffraction order m, this order propagates if $sin(\theta_m^r)$ or $sin(\theta_m^t)$ is between -1 and 1. Otherwise, the beam cannot propagate in the z-direction and is called evanescent. The larger the grating period is compared to the wavelength, the larger is the number of diffracted orders. Similarly, considering normal incidence $\theta_i = 0°$ since it is the angle of interest in the case of VCSEL top electrode, a grating with $\Lambda < \lambda_0/max(n_0, n_1)$ only supports the propagation of the 0-th order diffracted mode. Thus, interferences between modes cannot occur in the grating, preventing the possibility of high reflection, but enabling the broadband high transmission sought for TCE. This condition defines the deep-subwavelength grating regime, where the grating is seen as an homogeneous and anisotropic slab by the

incident beam [1]. The anisotropy comes from the difference of refractive index between x or y directions, thus depending on the polarization, giving rise to an artificial birefringence. The propagating modes supported by a periodic structures refer as Bloch modes. The regime where several Bloch modes are coexisting is called multi-mode. Otherwise, the regime is called single-mode.

2.2.2 Transmission through semiconductor monolithic high contrast grating

Monolithic high contrast gratings (MHCG) have been investigated in the litterature to work as reflectors [2, 3, 4], in particular in order to replace the top Bragg mirror in VCSELs. Such a grating consists in simple 1D grating etched at a material surface, which is a configuration that corresponds to the semiconductor grating contained in SMDSGs. Instead of reflectivity, this part aims to understand the transmission of TE and TM polarizations through this type of grating in the deep-subwavelength regime.

Figure 2.2 shows a schematic of a MHCG, while figures 2.3a and 2.3b respectively present the theoretical transmittance map of TE and TM-polarized light propagating through a MHCG [1] made of GaAs in the surface-normal direction going from the GaAs to the air. The x-axis of these maps is the ratio of the grating period over the wavelength, and the y-axis is the grating's teeth height normalized by the grating period. For both TE and TM polarizations, high transmission is enabled in the single-mode regime as well as in the multi-mode one which shows a pattern of low and high tranmission caused by interferences. In the single-mode regime, or deep-subwavelength regime, the transmission mechanism looks like the one of a Fabry-Perot (FP) cavity, the grating behaving as a quasi-uniform slab between the semiconductor and the air. It has also been reported that TE-polarized light is confined in the semiconductor stripes when high transmission occurs through MHCG, while TM-polarized light is confined between the stripes in that same high transmission case. This is an important mechanism to understand SMDSG high transmission in section 2.3.

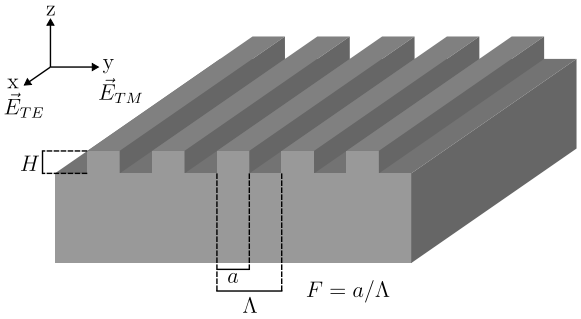

Figure 2.2: Schematic of a MHCG with Λ the grating period, a the stripe width, F the grating fill-factor, and H the stripe height.

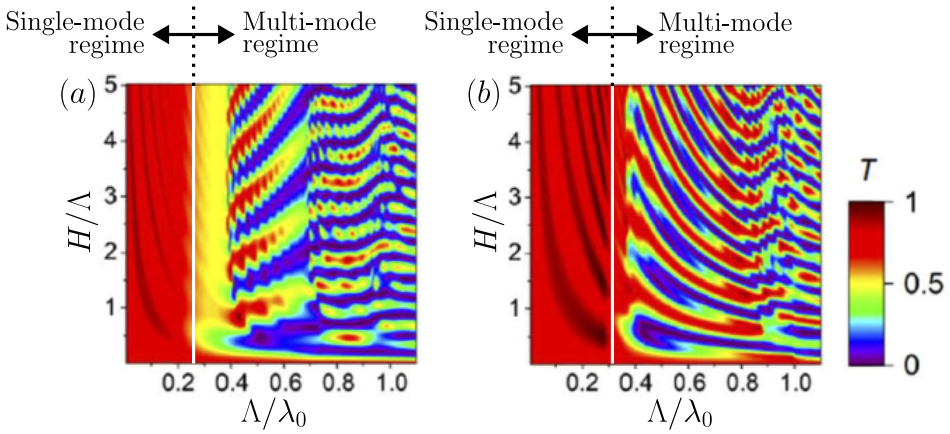

Figure 2.3: Transmittance maps at normal incidence of a MHCG made of GaAs under (a) TE-polarized light, and (b) TM-polarized light. These maps are taken from [1].

2.2.3 Transmission through subwavelength-aperture metallic grating

Unexpected high transmission, called extraordinary optical transmission, of TM-polarized light through a 2D periodic array of subwavelength holes in metal have first been reported in [5]. It describes a phenomenon where, for certain wavelengths, the optical transmission through the array of holes is higher than the one that could occur through a large macroscopic hole with an area being the effective area of the array of holes. This paved the way to many studies of TM-polarized light transmission through metal gratings with subwavelength apertures, including 1D gratings, shown in figure 2.4. Two mechanisms of high transmission through this type of grating have been reported in [6]. The first mechanism, for which the TM polarization electric field intensity is presented in 2.5a, is the excitation of surface plasmon polariton (SPP) modes on both surfaces of the grating. The second mechanism, for which the TM polarization electric field intensity is presented in figure 2.5b, is the coupling of the TM-polarized light with cavity resonances (CR) between the metal stripes. This mechanism is the one which enables high transmission in TM-polarized SMDSG.

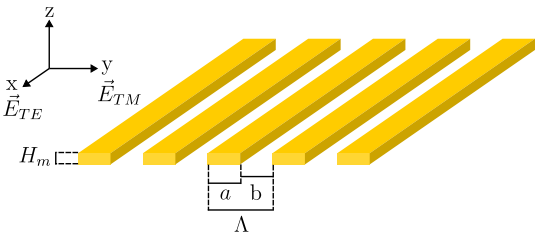

Figure 2.4: Schematic of a metal grating with Λ the grating period, a the metal stripe width, b the slit width, F the grating fill-factor, and H_m the metal stripe height

This type of metallic grating has been investigated as TCE in [7], where high transmission of TE-polarized light is also reported.

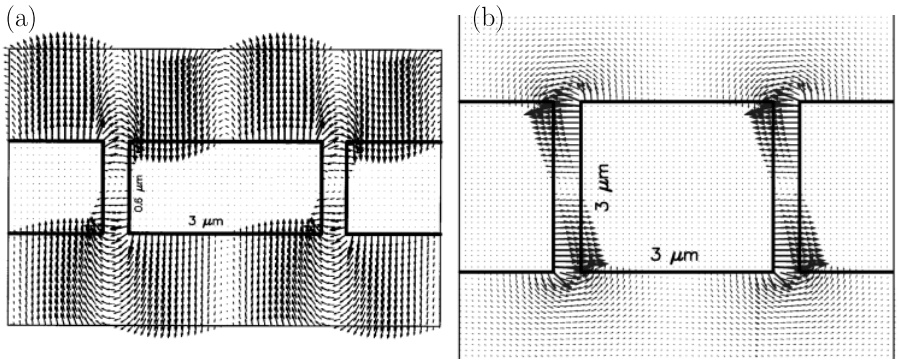

Figure 2.5: Maps of TM-polarized light electric field transmitted through a metal grating of period $\Lambda = 3.5\mu m$ in case of (a) coupling with surface plasmon polaritons (SPP) at wavelength $\lambda = 3.6\mu m$ and metal height $H_m = 0.6\mu m$, and (b) cavity resonances (CR) between metal stripes at wavelength $\lambda = 7.5\mu m$ and metal height $H_m = 3\mu m$. Taken from [6].

2.3 Transmission mechanisms in SMDSG structures

The semiconductor-metal deep-subwavelength gratings (SMDSG) which are studied as TCE in this work, can exist in two configurations: one with the metal stripes between the semiconductor stripes, called bottom configuration or B-TE, and presented in 4.2a, and one with the metal stripes at the top of the semiconductor stripes, called top configuration or T-TM and presented in 4.2b. As discussed below, The B-TE configuration can provide high transmission for TE-polarized light, while T-TM is highly transmittive for TM polarization. This section aims to explain the transmission mechanisms for both configurations.

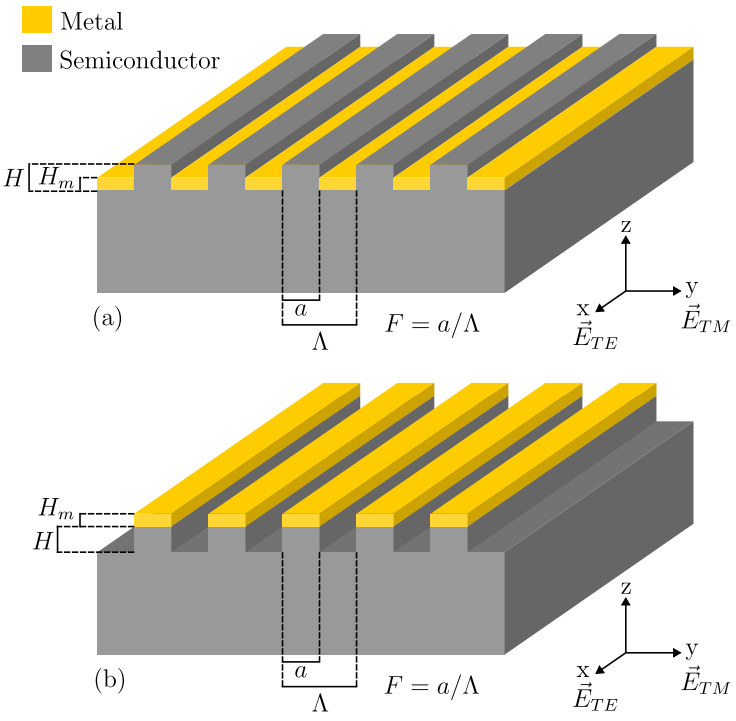

Figure 2.6: SMDSG configuration allowing high transmission of (a) TE polarization (B-TE), and (b) TM polarization (T-TM). Λ is the grating period, a the semiconductor stripe width, F the grating fill-factor, H the semiconductor stripe height, and H_m the metal stripe height.

2.3.1 High transmission through SMDSG in B-TE configuration

In the B-TE configuration, presented in 4.2a, the SMDSG can provide high optical transmission of TE-polarized light. This can be seen in figures 4.3a and 4.3b which respectively show the calculated transmittance map of TE and TM-polarized light propagating in the z direction through a B-TE configuration made of a GaAs substrate and 50-nm-thick stripes of gold [1].
Considering TE-polarized light in the single-mode regime, the transmission pattern appears similar to the one for MHCG presented in figure 2.3a, but with lower minima as a result of metal absorption. This suggests a similar transmission mechanism. Indeed, the TE electric field is confined in semiconductor stripes as previously mentioned in section 2.2.2, and as observed in the field intensity distribution shown in figure 2.8a, hereby preventing its interaction with the metal, and therefore its absorption and reflection. The nature of the metal is crucial since the lower is its real refractive index, the better is the electric field confinement in the semiconductor stripes. The influence of the imaginary part of the metal refractive index is also discussed in [1]. It is shown that a compromise must be found between a low value that ensures low absorption but weak confinement and a high value that provides the opposite. The operation principle also means that the metal thickness must be kept below $\sim 100nm$ in the NIR, since increasing the thickness necessarily increases the interaction with light.
For TM polarization, neither the cavity resonances, which are blocked by the high refractive index material between metal stripes, nor surface plasmon polaritons which are related to light absorption in the metal for an operation in the NIR spectral region, can provide high transmission.

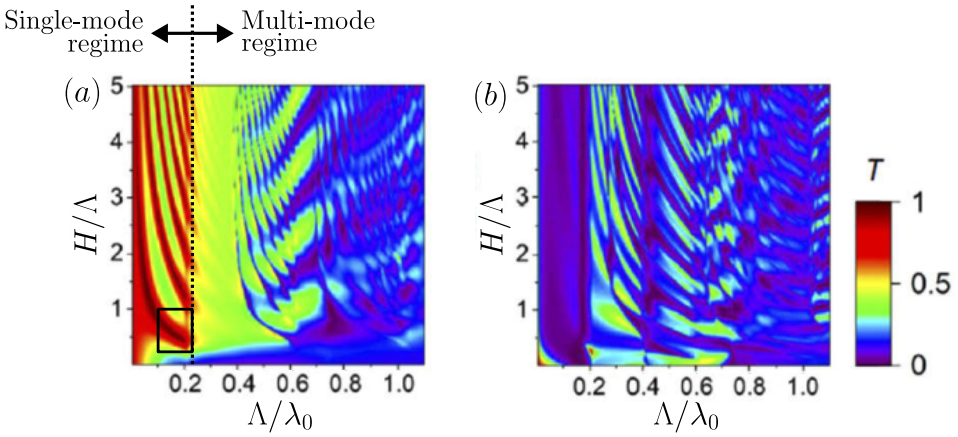

Figure 2.7: Transmittance maps at normal incidence of B-TE configuration made of a GaAs substrate and 50 nm of gold under (a) TE-polarized light, and (b) TM-polarized light. The black rectangle represents the range of periods and grating heights considered for B-TE structure optimization in this work. These maps are taken from [1].

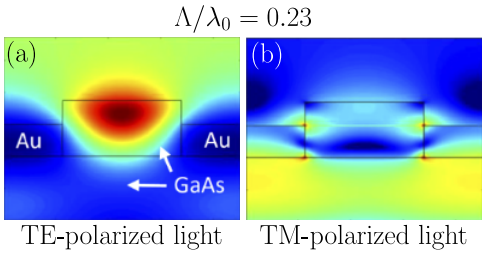

Figure 2.8: Distribution of optical field intensity within a single period of B-TE for (a) TE and (b) TM-polarized light at normal incidence and $\Lambda/\lambda_0 = 0.23$. These maps are taken from [1].

2.3.2 High transmission through SMDSG in T-TM configuration

In the T-TM configuration presented in 4.2b, the SMDSG can provide high optical transmission of TM-polarized light. This can be seen in figures 4.4a and 4.4b which respectively show the calculated transmittance map of TE and TM-polarized light propagating in the z direction through a T-TM configuration made of a GaAs substrate and 50-nm-thick stripes of gold [1].
Considering TE-polarized light, the electric field is confined in semiconductor stripes as previously mentioned in section 2.2.2, and gets reflected on the metal stripes, as observed in the field intensity distribution shown in figure 2.10a, preventing high transmission.
Looking at the TM-polarized light, high transmission is enabled by either of two mechanisms previously mentioned: the TM electric field confinement between the semiconductor stripes (section 2.2.2), and the cavity resonances between the metal stripes (section 2.2.3). This can be observed in the field intensity distribution shown in figure 2.10b. In figure 4.4b, one can see that high transmission is enabled when $\Lambda/\lambda_0 < 0.2$. The complex refractive index of metal impacts the cavity resonances. The transmission vanishes if the imaginary part is too low. In terms of metal thickness, transmission by cavity resonances enable to use metal thicknesses higher than for the B-TE configuration, but at the technological cost of a smaller grating period.

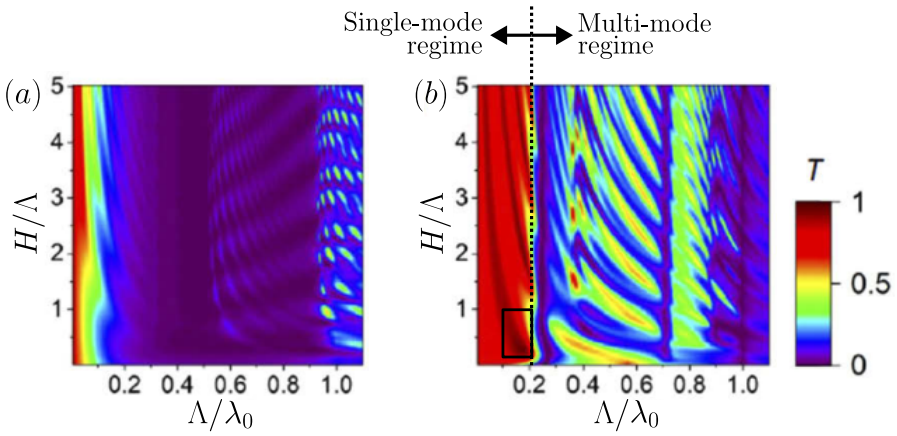

Figure 2.9: Transmittance maps at normal incidence of T-TM configuration made of a GaAs substrate and 50 nm of gold under (a) TE-polarized light, and (b) TM-polarized light. The black rectangle represents the range of periods and grating heights considered for T-TM structure optimization in this work. These maps are taken from [1].

A highly transmittive T-TM configuration has already been demonstrated in [8] for the infrared spectral region, using GaSb as semiconductor. Figure 2.11 presents the theoretical and measured transmission for TM and TE polarizations, as well as TM mode reflection.

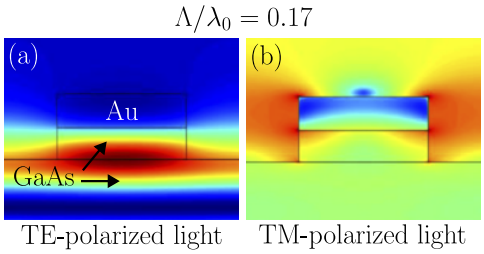

Figure 2.10: Distribution of optical field intensity within a single period of T-TM for (a) TE and (b) TM-polarized light at normal incidence and $\Lambda/\lambda_0 = 0.17$. These maps are taken from [1].

It shows a TM mode transmission maximum close to 90% at $\lambda = 4.64\mu m$ associated with a broadband high transmission which exceeds the Fresnel transmission at GaSb/air interface. In this work, the targeted spectral region is the NIR, which implies to reduce the grating period, challenging the fabrication.

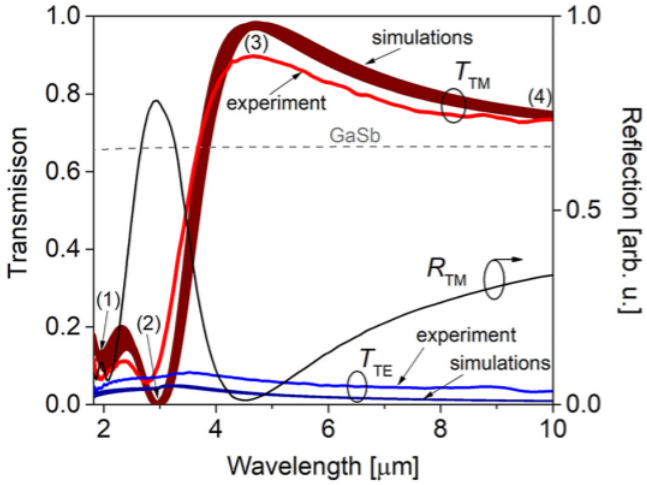

Figure 2.11: "Experimental spectra of transmittance for the SMDSG illuminated by TM (red) and TE (blue) polarizations; simulated spectra of transmittance for TM (dark red) and TE (dark blue) polarizations, multiple, overlapping lines represent combinations of errors in determining the SMDSG parameters; gray dashed line represents Fresnel transmission through the plane interface between the GaSb and air, based on GaSb refractive index dispersion. the black line and right axis represent the experimental spectrum of power reflectance determined in arbitrary units for TM polarization". Taken from [8].

2.3.3 Conclusion

The B-TE and T-TM configurations of SMDSGs enable high optical transmission for respectively TE and TM polarizations. Theoretical transmission levels above 95% have been calculated [1], while a value of 90% has been obtained experimentally in the mid infrared region [8]. These structures are tunable by adjusting Λ, H, H_m, and F (see figure 2.6) with a given high refractive index substrate and metal. Considering an interface GaAs/air, the Fresnel equation gives a transmission value of $\sim 70\%$ through the interface, which is much lower than the theoretical transmission through SMDSG. Thus, these structures offer on one side a metallic contact, and on the other side an optical impedance matching. In contrary to usual TCEs, it enables high transparency while keeping the high conductivity of metals. Each configuration has its own transmission mechanisms, which create important differences summarized hereafter.

In the B-TE configuration, the choice of the metallic contact composition is more flexible since the transmission mechanism limits the light-metal interaction. This is an advantage if ohmic contact is needed like in VCSELs. Also, the optimal periodicity is 35% larger than in the T-TM configuration [1], meaning larger metal line for better electrical conductivity, and easier fabrication. On the other hand, the transmission mechanism of the T-TM configuration offers a broader high transmission spectrum, as one can see in figures 4.3a and 4.4b. Also, the metal thickness is less constrained in this configuration.
Finally, a polarization-independent TCE using B-TE configuration has been theoretically investigated in [9]. It demonstrates that high transmission conditions for both TE and TM-polarized light can be found in a unique structure.
The objective of the chapter is to demonstrate the fabrication of both B-TE and T-TM configurations for NIR applications, and their optical and electrical properties.

2.4 Fabrication

Based on the theoretical calculations supplied by the photonics group of Łódź university in Poland, it has been decided to demonstrate the fabrication of SMDSGs as TCE for 940-nm emitting VCSELs. Both B-TE and T-TM structures have been optimized for transmission operation at normal incidence, considering firstly 50-nm-thick gold stripes as metallic contact on GaAs substrate, and secondly TiAu stripes in order to implement more realistic gold-based ohmic contact on GaAs. In the latter case, the titanium layer thickness has been set to 5 nm, while it has been set to 50 nm for the gold layer. Titanium was chosen since TiAu is a well-known ohmic contact on p-GaAs, and because its presence still enables high transmission implying achievable SMDSG dimensions in fabrication. However, all the structures have been fabricated on top side of nonintentionally doped (NID) GaAs substrate, without any doped cap layer that would enable an ohmic contact, since the first intention was to investigate the optical properties. Four types of SMDSGs have thus been made:

- B-TE configuration with gold as metallic contact, called "B-TE-Au".
- B-TE configuration with TiAu as metallic contact, called "B-TE-TiAu".
- T-TM configuration with gold as metallic contact, called "T-TM-Au".
- T-TM configuration with TiAu as metallic contact, called "T-TM-TiAu".

The objective of this section is to explain the nanofabrication process of B-TE and T-TM SMDSG configurations. A first part is dedicated to a brief presentation of the nano-structuration and characterization techniques that are employed in the fabrication. A second part describes the fabrication processes which have been developed, and discusses the related fabrication difficulties and possible solutions for improvements.

2.4.1 Presentation of the nano-structuration and the characterization techniques for the fabrication

The nano-structuration of B-TE and T-TM configurations requires specific techniques that are available in the LAAS laboratory clean room, which are:

- Electron-beam lithography (EBL):

  A lithography technique that enables to pattern gratings with the required nanometric periodicity and high resolution. This technique relies on an focused electron

beam which irradiates an electron-sensitive polymer resist in order to write shapes on its surface. The high energy of electrons enables to go far beyond optical resolution of standard photolithography techniques, while the use of a stage that moves under the beam allows custom patterning, without the need of a physical mask. The machine that was used is a RAITH 150. The EBL process requires a first step of resist spin-coating on the sample surface, followed by the exposure, and finally the resist development. The resist can be positive, when the irradiated area becomes soluble by the developer, or negative, when it becomes insoluble. Only positive resists are used in this work. In the case of nanometric grating fabrication, the mechanical stability of the resist lines can be delicate to obtain if the resist thickness is too high and/or adhesion on substrate too low, especially during resist drying after development. A drawing can be splited into several smaller exposure areas called write fields. In these areas, the stage doesn't move and the beam is deflected to write the pattern. The critical parameter is the amount of electrons per unit area of exposure, called the dose and expressed in $\mu C/cm^2$. The exact dose has to be found experimentally, since it depends on the substrate and the resist response to the exposure. The adjustment of sample planeness, focus, astigmatism, as well as write field alignment were all done manually. Table 2.1 summarizes the parameters which have been used for all fabricated structures.

Accelerating voltage (kV)	20
Aperture diameter (μm)	7.5
Resulting current (pA)	~ 20
Write field size (μm^2)	100×100
Scan direction	Grating line length

Table 2.1: Summary of EBL parameters used in this work.

- Inductively coupled plasma - reactive ion etching (ICP-RIE):

  A dry etching technique which allows to etch the semiconductor grating grooves in a precise and controlled way. The reactive ion etching (RIE) is a process where atoms from the substrate surface are physically removed by ions bombardment. The gas chemistry can be chosen to also react chemically with the substrate material, with the condition to form volatile etch products, increasing the etching rate and reducing the anisotropic nature of the physical bombardment. The inductively coupled plasma (ICP) part refers to the generation of a high-density plasma at low pressure caused by a radiofrequency (RF) source. The alternating RF magnetic field and induced RF electric fields energizes electrons, ionizing gas molecules and atoms of the gas mixture. ICP-RIE combines both physical etching and chemical reactions, and allows the decoupling of the plasma density, i.e. ion current, and ion kinetic energy, by separating the ICP power from the accelerating RF power. This makes the process more controllable and selective than for a capacitively coupled plasma (CCP) RIE system. The ICP-RIE systems used in this work were a Sentech SI 500 and a TRIKON OMEGA 201.

  For the ICP-RIE etching of GaAs, the Cl_2/N_2 chemistry was chosen, with a recipe that was optimized by the LAAS-CNRS photonics team to make GaAs-based photonic crystals [10]. Cl-based ions react chemically with the GaAs surface, while the use of N_2 as inert gas carrier is used for sidewall passivation, enabling highly

anisotropic etching [11]. The controllable parameters of an ICP-RIE recipe are: pressure, substrate temperature, gas flow, RF power, and ICP power. In addition, the susceptor material and the use of a high thermal conductivity material at the interface between the susceptor and the sample backside can be decided. Using a GaAs wafer instead of a Si wafer lowers the GaAs etching rate. Fomblin oil can be put between the sample and the susceptor to take advantage the oil high thermal conductivity to ensure good control of substrate temperature during the etching, especially for long etching times. Table 2.2 summarizes the GaAs etching recipe parameters used for each ICP-RIE machine.

	Sentech SI 500	TRIKON OMEGA 201
Pressure (mTorr)	3	3
Substrate temperature (°C)	25	25
Cl_2 flow (sccm)	9	9
N_2 flow (sccm)	11	11
RF power (W)	25	25
ICP power (W)	100	100
Susceptor material	Si	GaAs
Fomblin oil	No	Yes
GaAs etching rate (nm/s)	∼4.8 nm/s	∼1.8 nm/s
Selectivity with CSAR62 etching mask (etched material / etched mask)	∼ 2	Not available
Selectivity with gold etching mask (etched material / etched mask)	Not available	∼ 6

Table 2.2: Summary of ICP-RIE GaAs etching parameters used in Sentech SI 500 and TRIKON OMEGA 201 machines.

- Electron-beam physical vapor deposition (EBPVD):

  A physical vapor deposition technique that was used for gold and titanium thin film deposition, with deposition rates between 0.5 and 1 nm/s. The used evaporation machine that was the Alcatel EVA600. The material is introduced in the chamber in the form of an ingot, which is evaporated in vaccum by a concentrated high-energy electron beam. Then, the vapors condense on the substrate surface. The sample holder rotates in order to ensure a uniform deposition.

In addition, two other process steps are crucial in the SMDSG fabrication:

- Metal lift-off:

  The metal lift-off consists in creating the desired metal pattern at the substrate surface by removing the EBL-patterned resist on which the metal has previously been deposited. In such a process, a resist undercut profile is required to allow an easy and clean removal, since it prevents the deposition of the metal on the patterned resist sidewalls. Also, it is considered in this work that the resist thickness must be at least two times higher than the one of the metal. Table 2.3 describes the lift-off process. In this work, the chemical removal, presented in step 1, is not sufficient and must be completed with steps 2 and 3, which helps by mechanical removal.

Step number	Description
1	Resist dissolution in organic solvent: 8 hours of immersion in dimethyl sulfoxide (DMSO) heated at 80°C with stirring set at 60 rpm.
2	Ultrasonic bath: The beaker containing the sample in DMSO solution is placed in a 130-kHz-ultrasonic bath heated at 80°C. Process time: 5 minutes.
3	Acetone spray using syringe: Once the sample is in a beaker filled of acetone, a syringe spray enables to mechanically remove the metal. A strong spray at pattern locations is recommended since the adhesion of gold on GaAs or titanium on GaAs wasn't observed to be an issue.
4	Rincing in isopropanol (IPA).
5	Drying with nitrogen.

Table 2.3: Metal lift-off process.

- GaAs deoxidation:

  The removal of GaAs native oxide is done before metal deposition in order to enable ohmic contact, as described in 1.3.2. Also, this removal is done before ICP-RIE process as a surface cleaning step which reduces the roughness of the bottom of GaAs grating grooves after etching, and which ensure reproducibility since the surface is always the same before etching. Table 2.4 describes the deoxidation process. It relies on the selective wet-chemical etching of GaAs native oxide by hydrochloric acid.

Step number	Description
1	Substrate surface wetting by immersion in deionized water: the transfer between wetting bath and wet-etching bath using the water menisc ensures a uniform acid attack.
2	Wet etching: immersion in acidic solution composed of 3 volumes of deionized water for 1 volume of hydrochloric acid (HCl) of 37% mass concentration. Etching time: 90 seconds.
3	Rincing: immersion in deionize water.
4	Drying with nitrogen.

Table 2.4: GaAs deoxidation process.

Finally, the main characterization techniques that were used between the fabrication steps are:

- Scanning electron microscope (SEM):

  This microscopy technique scans the sample surface with a focused beam of electrons

to produce an image, and is widely used for high resolution images of micrometric and nanometric objects. The SEM machine that was used in this work is a Helios Nanolab 600i from FEI. It includes a high resolution scanning electronic column and a ionic column. Focus and astigmatism have to be ajusted by the user, as well as the electron accelerating voltage and the current, both of which must be adapted to the sample response to the electron beam. This technique was used to probe the quality and dimensions of EBL patterning, the depth and profile of the ICP-RIE, and finally the dimensions, profile, and quality of the lifted metal lines. While the dimensions in the sample surface plane could be measured using a simple image of the surface, the vertical dimensions of the etching depth and metal thickness could be performed by imaging the SMDSM cross-section, made using the focused ion beam tool described in the following, or by sample cleaving.

- Focused ion beam (FIB):

  As part of the Helios Nanolab 600i, the FIB enabled to etch sample areas of a few square microns by physical bombardment. The ion beam, which is created from a gallium source, has to be adjusted just like the SEM: focus, astigmatism, ion accelerating voltage and current. The following describes the FIB etching procedure:

  1. Platinum deposition: a 500-nm-thick protective platinum cap is deposited at the etching location using the electron beam. It adds a contrast layer for a better visualization of the SMDSG, and limits the curtaining effect during the ion etching, in order to get a clean FIB-etched cross-section. This platinum layer is seen as the upper material in all FIB-etched cross-sections SEM images presented in this work.
  2. Sample tilting: as presented in 2.12, the FIB column is placed at 52° from SEM one, which is the reason why the sample must be tilted at this angle to be etched.
  3. FIB column adjustment.
  4. FIB etching with an accelerating voltage of 30 keV.

  The SEM imaging of the FIB-etched cross-section is presented in figure 2.12. Considering the tilt of the sample, the vertical dimension measurements must be recalculated using equation 2.4.

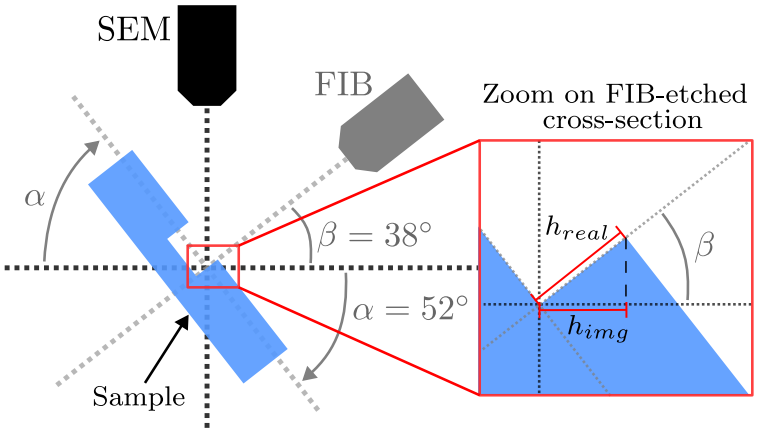

Figure 2.12: Schematic of the configuration of the SEM imaging with regard to the FIB-etched cross-section. The sample is 52°-tilted, the real vertical dimension is noted h_{real}, while the vertical dimension seen in SEM images is noted h_{img}. The relation between h_{real} and h_{img} is given by equation 2.4.

$$h_{real} = \frac{h_{img}}{cos(\beta)} = \frac{h_{img}}{cos(38)} \tag{2.4}$$

2.4.2 Optimization of SMDSG dimensions

The targeted SMDSG structures come from the optimal points in the transmission maps simulated using rigorous coupled-wave analysis (RCWA) method and presented in figure 2.13. RCWA has been performed using the scilab code developed by the group, with the number of harmonics set to 50. The maps show the transmission at 940 nm for normal incidence as a function of grating period Λ and semiconductor grating height H, setting gold height at 50 nm and titanium height at 5 nm in the case of TiAu contact. Grating fill-factors F of 0.4, 0.5, and 0.6 are presented, since it shows an important trade-off for the technological fabrication: whereas it is easier to achieve $F = 0.5$ when reaching such small periodicities, $F = 0.6$ enables larger periodicity for B-TE configuration high transmission, and $F = 0.4$ enables larger periodicity for B-TM configuration high transmission. From these maps, six structures have been targeted for this work, and are summarized in table 2.5, which gives their name, optimal parameters, and theoretical transmission for the relevant polarization at 940 nm. Figure 2.14 shows the calculated transmission and reflection spectra of these structures for TE and TM polarizations, plotted between 900 nm and 2000 nm, while the same plots are shown between 900 and 985 nm in figure 2.15. Although the high transmission is targeted at 940 nm, this large spectral range enables to visualize the higher high-transmission spectral window of T-TM with respect to B-TE configuration. That being said, the transmission behavior of B-TE also presents a relatively large window of about 200 nm with a transmission above 80%.

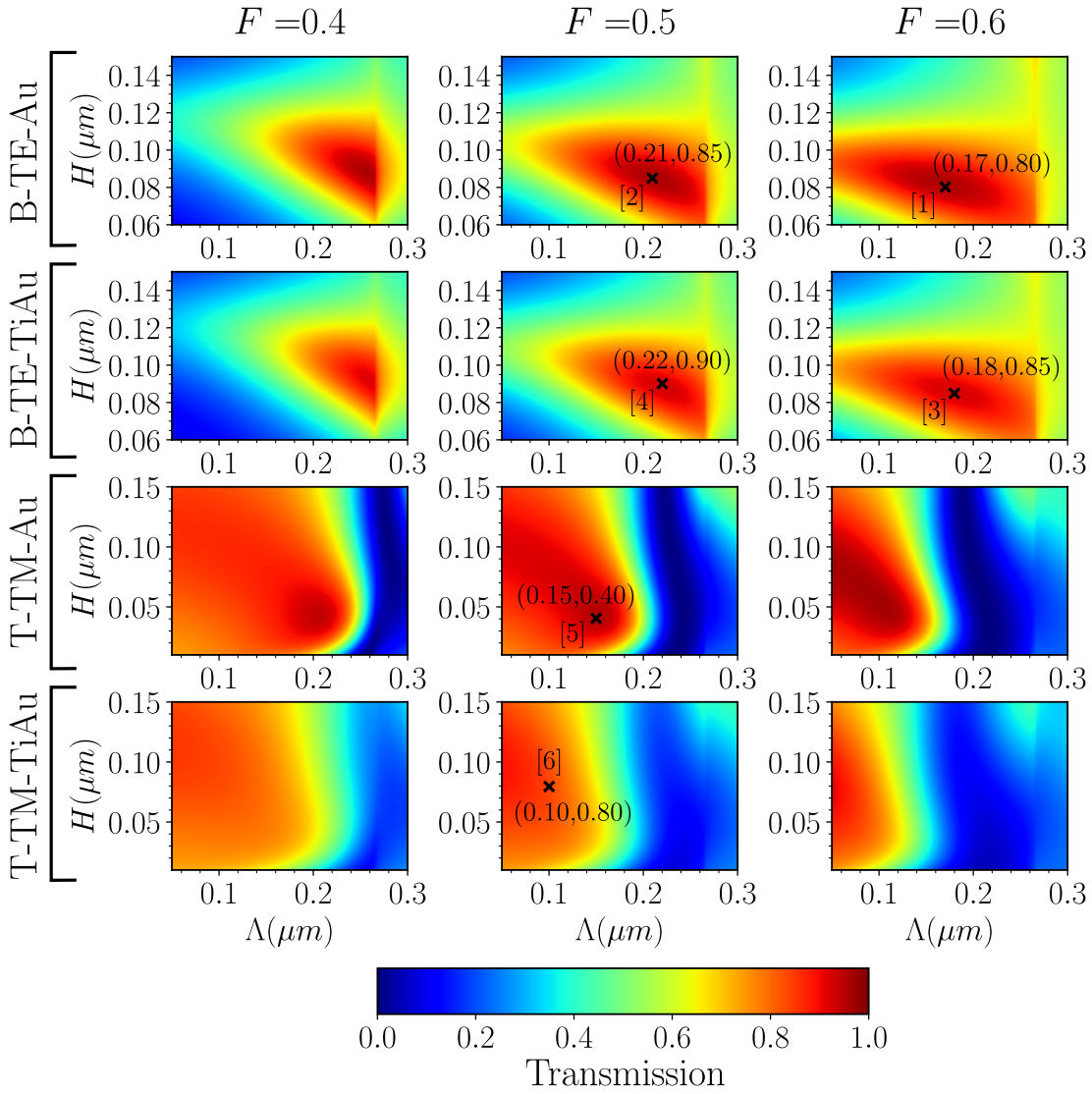

Figure 2.13: Theoretical transmission maps for a wavelength of 940 nm at normal incidence as a function of semiconductor teeth height H and grating period Λ. Each array line corresponds to one of the four structures fabricated in this work: B-TE-Au, B-TE-TiAu, T-TM-Au, T-TM-TiAu. The metal height is set at 50 nm for gold, and 5 nm for titanium in the case of a TiAu contact. Each column corresponds to the calculation made with a grating fill-factor value respectively of $F = 0.4$, $F = 0.5$, and $F = 0.6$. The theoretical calculation has been performed using the RCWA method. The six crosses corresponds to the six targeted structures for fabrication, labeled [1], [2], [3], [4], [5], and [6]. Their dimensions are detailed in table 2.5, and their spectra are presented in figure 2.14 and 2.15.

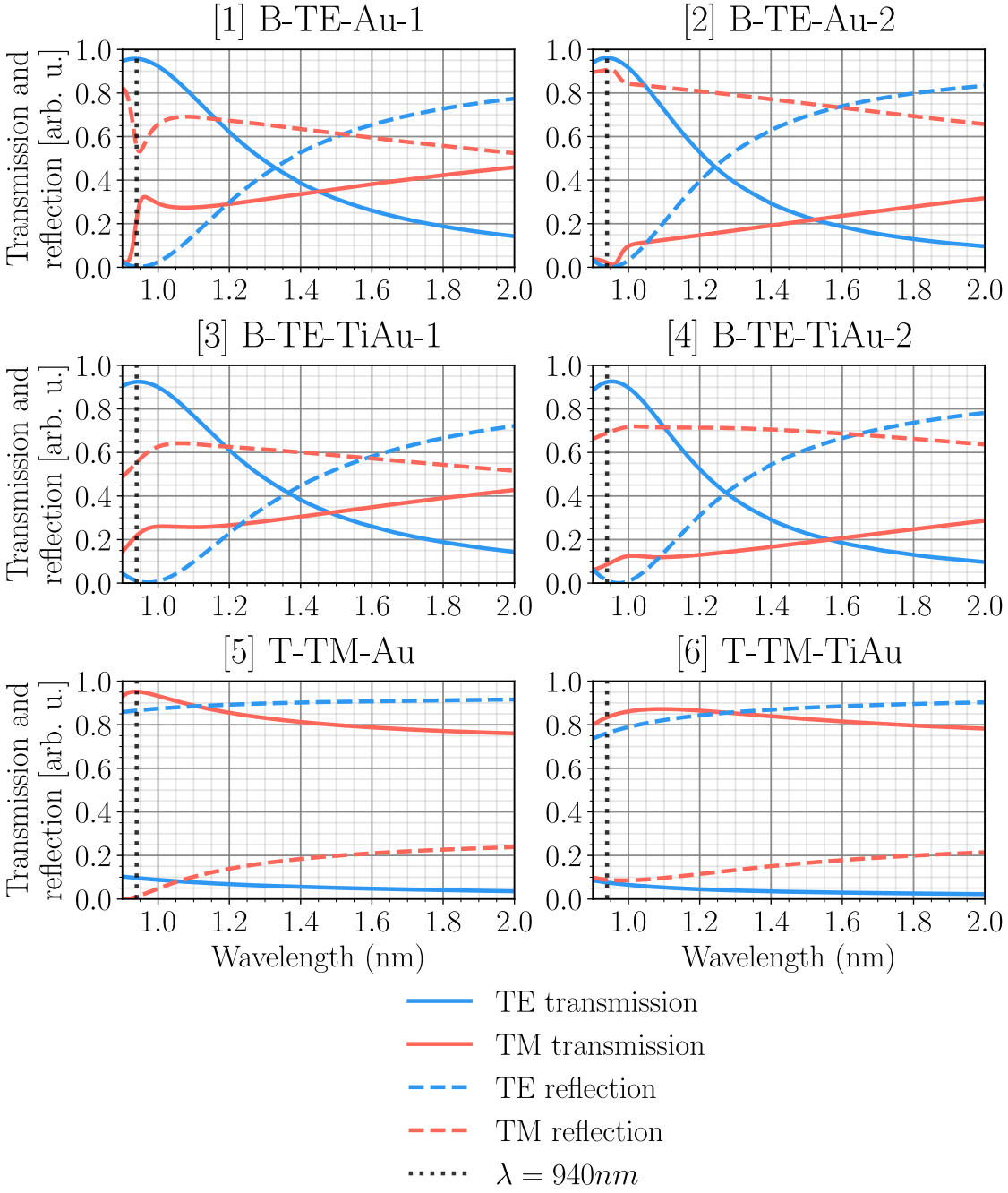

Figure 2.14: Theoretical spectra of targeted structures labeled [1], [2], [3], [4], [5], and [6] in figure 2.13. The spectra are calculated between 900 and 2000 nm at normal incidence, with gold height set at 50 nm and titanium height set at 5 nm in the case of a TiAu contact. Their dimensions are detailed in table 2.5. The theoretical calculation has been performed using the RCWA method.

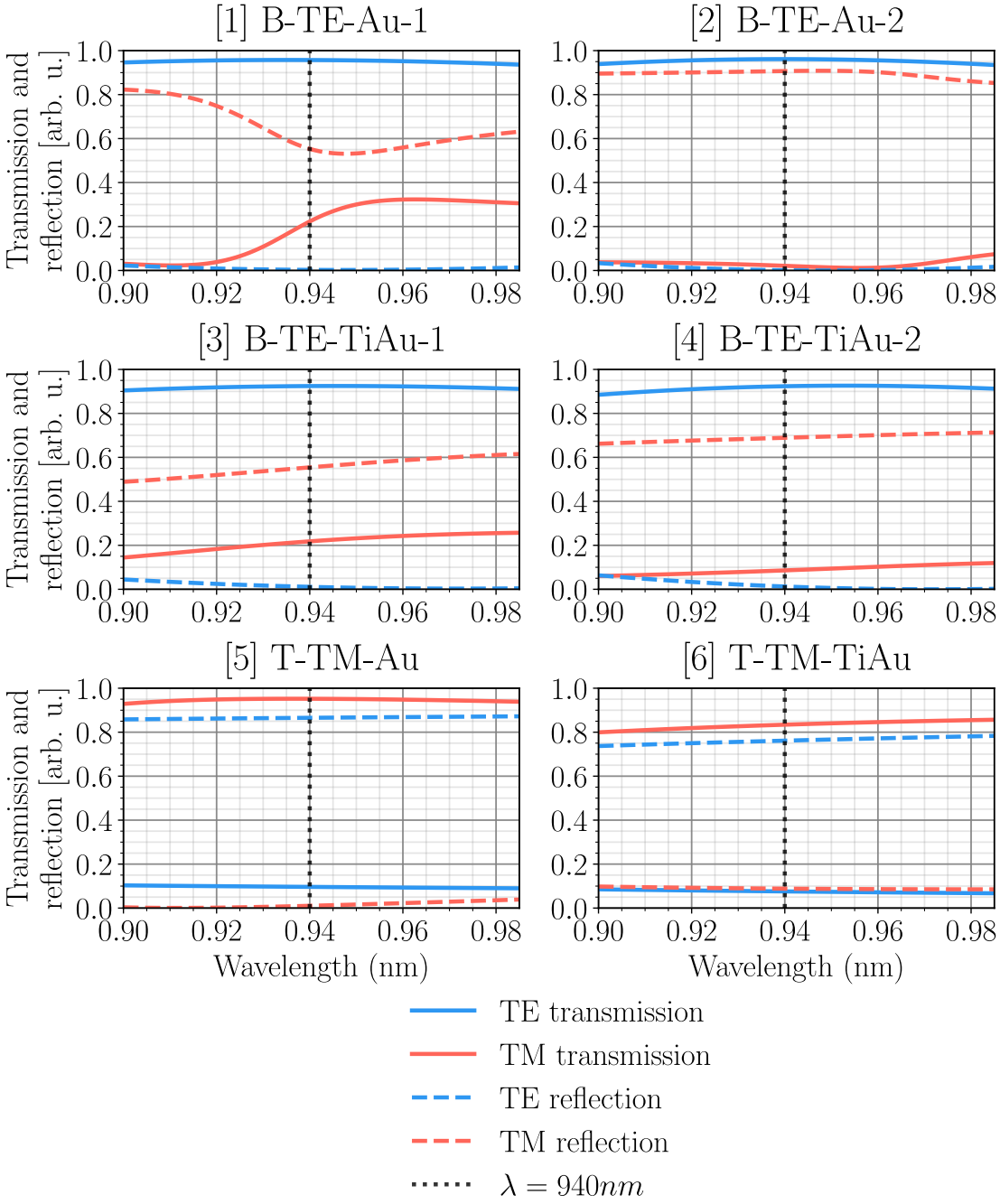

Figure 2.15: Theoretical spectra of targeted structures labeled [1], [2], [3], [4], [5], and [6] in figure 2.13. The spectra are calculated between 900 and 985 nm at normal incidence, with gold height set at 50 nm and titanium height set at 5 nm in the case of a TiAu contact. Their dimensions are detailed in table 2.5. The theoretical calculation has been performed using the RCWA method.

		SMDSG parameters					
Structure label	Structure name	Λ (nm)	F	H (nm)	H_{Au} (nm)	H_{Ti} (nm)	Theoretical transmission $(\lambda = 940nm)$
[1]	B-TE-Au-1	170	0.6	80	50		96% (TE)
[2]	B-TE-Au-2	210	0.5	85			96% (TE)
[3]	B-TE-TiAu-1	180	0.6	85		5	92% (TE)
[4]	B-TE-TiAu-2	220	0.5	90			92% (TE)
[5]	T-TM-Au	150	0.5	40			95% (TM)
[6]	T-TM-TiAu	100	0.5	80		5	83% (TM)

Table 2.5: SMDSG parameters of the targeted structures in fabrication. The dimensions are extracted from calculations in figure 2.13, and the theoretical level of transmission for a wavelength of 940 nm at normal incidence is taken from the theoretical spectra in figures 2.14 and 2.15.

2.4.3 Developed fabrication processes

Two processes have been developed in order to fabricate the B-TE and the T-TM configurations, and are described in this part. The main work was focused on the realization of all the required steps, while the ICP-RIE step is based on previous process used in the lab and wasn't optimized further. Table 2.6 summarizes the developed process for the fabrication of the B-TE and the T-TM configurations. The alignment of the GaAs and the metal grating is ensured by the self-aligned nature of these two processes.

B-TE step order	**T-TM step order**	**Step name**	**Description**	**Technique**
1	1	GaAs substrate preparation	Organic residues removal	Dissolution in organic solvent
			GaAs native oxide removal	Wet-chemical etching in acidic solution
2	2	Patterning	Resist deposition	Spin-coating
			Lithography	EBL
			Resist development	Selective wet-chemical etching
3	5	GaAs structuration	GaAs native oxide removal	Wet-chemical etching in acidic solution
			GaAs dry-etching using resist as etching mask	ICP-RIE
4	3	Metal deposition	GaAs native oxide removal	Wet-chemical etching in acidic solution
			Metal deposition	EBPVD

5	4	Metal lift-off	Resist chemical removal	Dissolution in organic solvent
			Resist mechanical removal	Ultrasonic bath
				Solvent syringe spray

Table 2.6: Summary of B-TE and T-TM configuration fabrication process.

2.4.3.1 The B-TE configuration fabrication process

The visual description of the B-TE configuration process is presented in figure 2.16.

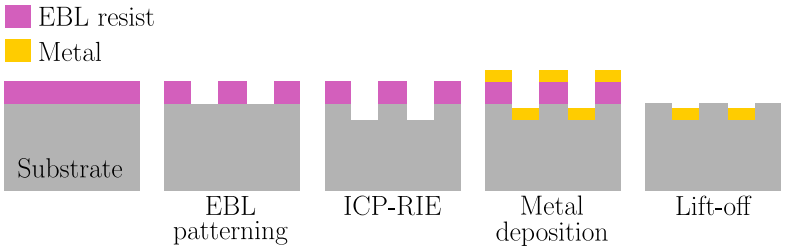

Figure 2.16: Schematic of B-TE configuration fabrication process.

Step 1 aims to clean the substrate surface before starting the process. This is done by immerging the sample in an organic solvent during 10 minutes to remove organic residues. The used solvent is DMSO and is heated at 80°C. Then, the sample is rinced in IPA solution and dried using nitrogen. Finally, the GaAs native oxide is removed using the deoxidation process described in table 2.4 to renew the surface.

Step 2 aims to transfer the grating pattern on a resist using EBL. The chosen EBL positive resist is the CSAR62 diluted at 9% (AR-P 6200.09). This resist has the advantage of high plasma etching resistance, which is crucial since the GaAs dry-etching is done prior to the metal deposition and lift-off processes. In addition, this resist enables high resolution patterning. Its drawback in the context of this process is it poor adhesion on GaAs surface, which is compensated by the deposition of an adhesion promoter, called hexamethyldisilazane (HMDS), at the substrate surface before resist deposition. HMDS monolayer can be deposited because it bonds to the oxygen of the surface native oxide. However, despite the use of HMDS, the adhesion wasn't perfect, and the mechanical stability of resist lines was difficult to achieve for a grating periodicity below 200 nm. The 9% dilution was chosen to enable a suitable resist thickness of $\sim 180nm$, which, once the etching done, results in a resist thickness of $\sim 140nm$. This is about 3 times the metal thickness of 50 nm which is a good ratio for lift-off process at nanoscale. The CSAR62 deposition is described in table 2.7. Then, the EBL process is performed using the parameters presented in table 2.1. A GDSII-type mask file gives the instructions to the machine. The encoded mask contains an array of $40 \times 40\mu m^2$ line gratings, with varying line width between 30 and 80 nm, and varying exposure dose. This grating size ensures the grating area to be large enough to perform the optical characterization. Each grating is located at the center of a $100 \times 100\mu m^2$ write field to limit the writing error. The exposure dose of CSAR62 on GaAs substrate using an accelerating voltage of 20 keV has been found to be about 60 $\mu C/cm^2$. Finally, the CSAR62 development is described in table 2.8.

Step number	Description
1	Sample dehydration: sample on hotplate heated at 150°C, 5 minutes.
2	HMDS monolayer deposition: 120°C, 60s.
3	CSAR62 spin-coating: 5000 rpm, 4000 rpm/s, 60s.
4	CSAR62 soft baking: sample on hotplate heated at 150°C, 60s.

Table 2.7: CSAR62 deposition process.

Step number	Description
1	Exposed resist wet-etching: 55s in amyl acetate.
2	Wet-etching stop / rincing: 60s in IPA
3	Drying: gentle nitrogen spray.

Table 2.8: CSAR62 development process.

Step 3 aims to etch the GaAs substrate, using the patterned EBL resist as etching mask, to obtain GaAs teeth of the targeted height. Firstly, the GaAs native oxide is removed for sake of roughness minimization and process reproducibility as previously described in section 2.4.1. The native oxide is wet-etched using the process described in table 2.4. Then, the GaAs etching is performed in the ICP-RIE Sentech SI 500 chamber using the process described in table 2.2. The etching time is short, typically between 10 and 20 seconds. With this recent machine, the plasma quickly reaches its steady state, within an insignificant time compared to the etching one. For such a short etching duration, the sample was laying on the susceptor without the use of fomblin oil. It has the advantage of preventing the delicate task of oil removal using solvent that could damage the resist, which still has to be used as sacrificial layer in the metal lift-off process.

Step 4 is the deposition of the metallic contact by EBPVD, which is preceded by GaAs native oxide removal to enable ohmic contact.

Step 5 is the metal lift-off process described in table 2.3. This step is particularly delicate for two reasons:

- The resist undercut profile that exists after the development is etched during ICP-RIE process, resulting in a rounded profile as seen in figure 2.17a. Thus, the metal can be deposited on resist and GaAs sidewalls, as seen in figure 2.17b, making the metal at the top of the resist harder to remove. Fortunately, the GaAs sidewalls are partially protected by the accumulated metal on the resist, which tends to create an undercut profile during metal deposition. This explains why the B-TE structures could be fabricated using this process, while "metal ears" at GaAs teeth top corners remain after lift-off.

- Because the resist has been exposed to the plasma during the etching process, its dissolution in organic solvent solution becomes harder. For this reason, the heating of the DMSO solution is important.

These two facts explain that the metal must be removed using mechanical techniques after resist dissolution, using ultrasonic bath and syringe spray. In addition, adding a rectangular delimitation area around each gratings in the EBL mask made the lift-off easier, since the metal lifting starting point was located in close proximity to each pattern.

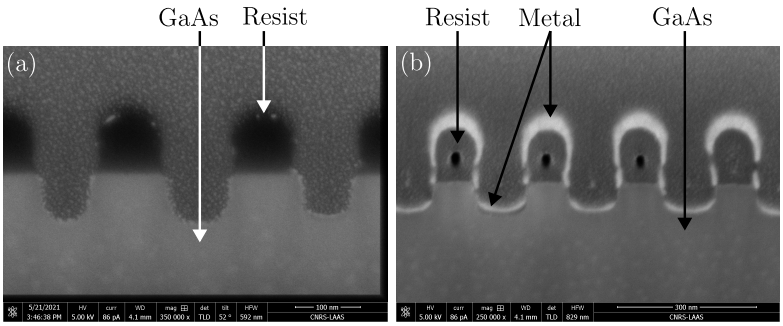

Figure 2.17: SEM image of the FIB-etched cross-section of B-TE configuration after (a) ICP-RIE process and (b) metal deposition.

Alternative processes could facilitate the metal lift-off. A room temperature wet-chemical digital etching technique of GaAs is proposed in [12], using the diffusion-limited 15-Å-thick native oxide layer as the etching increment. By alternatively oxidizing the GaAs surface in a hydrogen peroxide solution, and etching this layer of repeatable thickness in a hydrochloric acid solution, it is possible to get undercut profile by etching the GaAs under the resist with a resolution of 15 Å per etching step. This would prevent the metal from deposition on GaAs sidewalls. Also, the use of one or two other material layer(s) under the resist could be studied, in order to improve dry-etched GaAs profile, the sacrificial layer undercut after etching, and the efficiency of sacrificial layer removal during lift-off.

In this work, metal lift-off attempts have been performed using a SiO_2 or a germanium layer under the resist, respectively wet-etched using a hydrofluoric acid solution and a hydrogen peroxide solution. While the GaAs grating stripes have been partially etched in the hydrofluoric acid solution, the dissolution of germanium in the hydrogen peroxide solution left a very high surface roughness. The reasons of these unexpected results have not been studied. In addition, a digital etching process have been attempted using a SiO_2 or a Si_3N_4 hard mask layer under the resist. In both cases, the digital etching process has led to a loss of adhesion of the hard mask grating lines caused by the induced deoxidation at its interface with GaAs. The solution consisting in performing a digital etching of GaAs with only the EBL resist as mask hasn't been attempted in this work, but it could lead to an easier lift-off process.

2.4.3.2 The T-TM configuration fabrication process

The visual description of the B-TE configuration process is presented in figure 2.18.

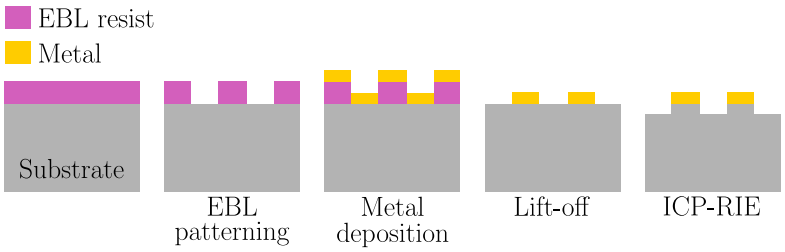

Figure 2.18: Schematic of T-TM configuration fabrication process.

Step 1 aim is the same as in B-TE fabrication process.

Step 2 aims to transfer the grating pattern on a resist using EBL. The chosen EBL positive resist is the PMMA diluted at 38 g/L in anisole. Its good adhesion on GaAs and the achievable thickness as small as $\sim 110nm$ ensures its good mechanical stability with regard to the small periodicity of the T-TM structures, which enables high resolution patterning. This resist wasn't chosen for the B-TE configuration since its resistance to plasma exposure is poor, but can be used in the context of the T-TM configuration fabrication since the GaAs dry etching step takes place after the metal lift-off. In addition, a thickness of $\sim 110nm$ is about 2 times the metal thickness of 50 nm, which is still a sufficient ratio for lift-off process at nanoscale. The PMMA deposition is described in table 2.9. Then, EBL process is performed using the parameters presented in table 2.1. A GDSII-type mask file gives the instructions to the machine. The encoded mask contains an array of $40 \times 40\mu m^2$ line gratings, with varying line width between 10 and 60 nm, and varying exposure dose. This grating size ensures the grating area to be large enough to perform the optical characterization. Each grating is located at the center of a $100 \times 100\mu m^2$ write field to limit the writing error. The exposure dose of PMMA on GaAs substrate using an accelerating voltage of 20 keV has been found to be about between 225 and 250 $\mu C/cm^2$ depending on the wanted T-TM pattern. Finally, the PMMA development is described in table 2.10.

Step number	Description
1	Sample dehydration: sample on hotplate heated at 170°C, 5 minutes.
3	PMMA spin-coating: 5000 rpm, 4000 rpm/s, 60s.
4	PMMA soft baking: sample on hotplate heated at 170°C, 60s.

Table 2.9: PMMA deposition process.

Step number	Description
1	Exposed resist wet-etching: 35s in MIBK:IPA (1:3) solution
2	Wet-etching stop / rincing: 60s in IPA
3	Drying: gentle nitrogen spray.

Table 2.10: PMMA development process.

Step 3 is the deposition of the metallic contact by EBPVD, which is preceded by GaAs native oxide removal to enable ohmic contact.

Step 4 is the metal lift-off process described in table 2.3. This step is easier than for the B-TE structures fabrication, as the resist hasn't been exposed to plasma. However, the use of mechanical step during the metal lift-off process is still required, which could be caused by the relatively low ratio between the resist thickness and the deposited metal thickness.

Step 5 aims to etch the GaAs substrate, using the patterned metal as etching mask, to obtain GaAs teeth of the targeted height. Firstly, the GaAs native oxide is removed

for sake of roughness minimization and process reproducibility as previously described in section 2.4.1. The native oxide is wet-etched using the process described in table 2.4. Then, the GaAs etching is performed in the TRIKON OMEGA 201 chamber using the process described in table 2.2, preventing metal contamination in the Sentech SI 500 chamber. Because this machine is older than the Sentech SI 500, the plasma steady state is reached in several seconds, while this time is reduced to the second in the Sentech SI 500. A GaAs susceptor is used in order to slower the etching rate and make the plasma stabilization time insignificant compared to the etching time. Giving this etching time about three times longer than the one when the Sentech SI 500 system is used, the sample is glued on the susceptor using fomblin oil to enable good thermal control during the process. After the process, the fomblin oil is diluted in a specific solvent called perfluoropolyether (PF2), which is itself diluted in a solution of hydrofluoroether (HFE). Next, the sample is rinced in acetone, then in IPA, and finally dried with nitrogen. This etching mask solution that directly uses metal stripes is convenient as it allows self-alignment of GaAs and metal gratings, but rounds the metal stripes profile. In [8], the T-TM configuration is fabricated in two EBL patterning steps: one for the semiconductor grating, on which a second patterning is aligned for the metal grating. This solution is not possible for the small periodicities considered in this work, with regards to the realignment errors.

2.4.4 Fabricated SMDSGs

Based on the structure designs summarized in table 2.5, seven structures have been fabricated using the processes described in section 2.4.3 and are described in table 2.11. This table presents their measured dimensions and the associated uncertainties that are explained below. Figures 2.19, 2.20, 2.21, 2.22, 2.23, and 2.24 correspond to SEM images of SMDSG top-views and cross-sections, on which the measurements could be realized. The fill-factor F is calculated using top-view images. The measurement of H and H_{Au} can be made either from FIB-etched or cleaved substrate cross-section SEM images. The substrate cleaving method, which can be seen in figure 2.23b, is less blurry than the FIB-etching one that is used in this work. The latter can be seen in 2.23c. This better image quality is at the cost of a delicate and destructive cutting technique, which is why FIB-etched cross-sections have been preferred in this work. Also, in order to preserve the to-be-characterized patterns, the presented FIB-etched cross-sections were performed on other patterns located on the same sample. Even if the FIB-etched structures are close to the ones of interest, it adds an uncertainty on the measured dimensions. H_{Ti} is difficult to distinguish in FIB cross-section SEM images, and no substrate cleaving were attempted to try to improve its discernibility, so this height could not be measured and is assumed to correspond to the targeted deposited thickness.

The sources of error for the distances measured on SEM views depends on the nature of the view, which can be top-view, top-view of the edge of a cleaved substrate, or 52°-tilted view of a FIB-etched cross-section. Three error causes that SEM images have in common are: the operator-dependent SEM beam alignment, which affects the resolution, distortion, and the uncertainty of 5% of the SEM magnification. Considering the cleaved substrate, the plane of the substrate edge has to be in the SEM image plane, requiring to place precisely the sample at an angle of 90° on a specific sample holder. If the sample isn't put exactly at this angle, the depth of field is large enough to make appear almost focused the objects that are slightly off-plane, and create blur along the grating edges. This can be observed in figure 2.23b. For FIB-etched cross-section, blurriness can appear in SEM images. When this doesn't come from SEM beam alignment, it can be caused by

	SMDSG parameters				
Structure name	Λ (nm)	F	H (nm)	H_{Au} (nm)	H_{Ti} (nm)
B-TE-Au-1	170	0.49 ± 0.01	84 ± 5	40 ± 3	
B-TE-Au-2a	210	0.53 ± 0.01	85 ± 5	36 ± 3	
B-TE-Au-2b	210	0.39 ± 0.01	85 ± 5	36 ± 3	
B-TE-TiAu-1	180	0.53 ± 0.01	89 ± 6	33 ± 5	5 ± 1
B-TE-TiAu-2	220	0.47 ± 0.01	107 ± 7	35 ± 4	
T-TM-Au	150	0.55 ± 0.01	Clived cross-section: 29 ± 2 FIB-etched cross-section: 31 ± 4	Clived cross-section: 56 ± 3 FIB-etched cross-section: 49 ± 5	
T-TM-TiAu	100	0.57 ± 0.01	88 ± 6	27 ± 4	5 ± 1

Table 2.11: Summary of SMDSG measured parameters of the fabricated structures. The dimensions are extracted from the SEM images in figures 2.19, 2.20, 2.21, 2.22, 2.23, and 2.24.

two things. The first one is the quality of the ion etching, which depends on the chosen current, the FIB beam alignment, and the chosen etching scan procedure. The second one is the electron interaction depth, which is responsible for the blurry metal stripes top. Because the sample is 52°-tilted for SEM imaging, as presented in figure 2.12, the signal coming from the metal stripes behind the focal plane reaches the detector. This effect magnifies with the electron accelerating voltage.

The uncertainty assessment method depends on the measured parameter, and only the errors that are quantifiable are considered, ignoring most of sources of error previously described:

- Λ: the uncertainty is not taken into account since the EBL writing accuracy is considered higher than the dimensions extracted from SEM images.

- F: $F = a/\Lambda$ is a relative measurement performed in the corresponding SEM top-view image. The uncertainty is the standard deviation of the several F measured in the image, while the value of F is the mean.

- H, H_{Au}: using equation 2.4, the measured height h in the 52°-tilted SEM image of the grating cross-section can be expressed as:
  $h = \frac{h_{img}}{cos(38)} \times \frac{1}{\gamma}$ with h_{img} the mean of the height measurements in pixels in the image, and γ the pixel-to-nm relationship in pixel/nm.
  The several height measurements give a standard deviation σ_h, while the magnification error of the SEM is estimated at 5%, giving a scaling error $\Delta\gamma/\gamma = 0.05$. Combining these two errors, the final uncertainty of h is calculated as $\Delta h = \sigma_h + h \times \frac{\Delta\gamma}{\gamma}$.
  In the case of structures with TiAu metallic contact the titanium height couldn't be measured. Hence, the ideal titanium height, which equals 5 nm, is substracted to the measured height to get the gold one. Therefore, the uncertainty becomes

$\Delta h = \sigma_h + h \times \frac{\Delta\gamma}{\gamma} + \Delta h_{Ti}$ with Δh_{Ti} the uncertainty of titanium height measurement described below.

- H_{Ti}: because the measurement in not possible using FIB-etched cross-section SEM images, only the measurement uncertainty coming from the EBPVD process itself is considered. The deposition rate uncertainty ΔV is estimated at 0.05 nm/s for titanium. The minimum deposition rate being 0.5 nm/s, a layer of thickness $e = 5nm$ of titanium can have a maximum deposition time t_{max} of 10 seconds. Then, the maximized process uncertainty Δe can be calculated as follow: $\Delta e = t_{max} \times \Delta V = 0.5 \sim 1nm$. Another uncertainty that comes from the fact that the deposition rate is slower in the grating groove, depending on the aspect ratio of the groove and evaporation solid angle, is not known and not considered.

The fabricated SMDSG have dimension errors higher than 10% in most cases with respect to the targeted structures. Filling factors far from 0.5 were difficult to achieve by EBL. The GaAs height errors come from the process repeatability, as well as the aspect ratio dependent etching (ARDE) effect, which refers to the change of etch rates for features that have different aspect ratios. The highest differences between the targeted and fabricated dimensions is on the metal height. For the B-TE configuration fabrication, the deposition depends on the aspect ratio of the structure, and the deposition rate as a function of aspect ratio should be measured to reduce the error. In the T-TM configuration, the metal stripes act as a mask in the GaAs etching process. Since gold is slightly etched during plasma exposure, the deposited metal thickness must be adjusted to compensate this height reduction.

In addition to the periodicity, fill-factor, and the various heights, the grating profile itself has a crucial impact on the spectral response of the structure. One can see in cross-section images that neither the semiconductor stripes nor the metal stripes have rectangular profile shape. The fabrication process of the B-TE configuration, with Au or TiAu metallic contact, leads to several changes with respect to the theoretical profile. In figures 2.19b, 2.20c, 2.21b, and 2.22b, the GaAs tooth bottom corners are rounded. In figure 2.22a and 2.22b, metal shadowing from the right grating tooth seems to happen during metal deposition, characterized by the small gap between the right top corner of the metal stripe and the GaAs stripe in the cross-section image, and by the darks lines in the top-view image. This causes the presence of "metal ears" on GaAs stripes right top corner that remains after the metal lift-off, as proved by the bright lines in top-view image. This shadowing effect is thought to come from the sample tilt with respect to the source combined with higher etched depth than in 2.19b, 2.20c, and 2.21b. "Metal ears" are observed in all the B-TE fabricated structures, but at more random spatial locations. The ears are caused by the lack of undercut in the resist profile, since the resist is etched and its profile rounded during the GaAs dry-etching process that is performed before metal deposition, as explained in 2.4.3.1.

In the case of the T-TM configuration, observing figures 2.23b, 2.23c, and 2.24b, the metal stripes appear rounded, and the GaAs stripes sidewalls are not completely vertical. The shape of the metal stripes is caused by the use of these stripes as a mask in the GaAs ICP-RIE etching process. During this process, the gold is slightly etched, especially the stripes top corners. The non-vertical GaAs sidewalls could be caused by the gold mask erosion during the etching, or by etching conditions, as the recipe hasn't been studied and optimized to make it more vertical.

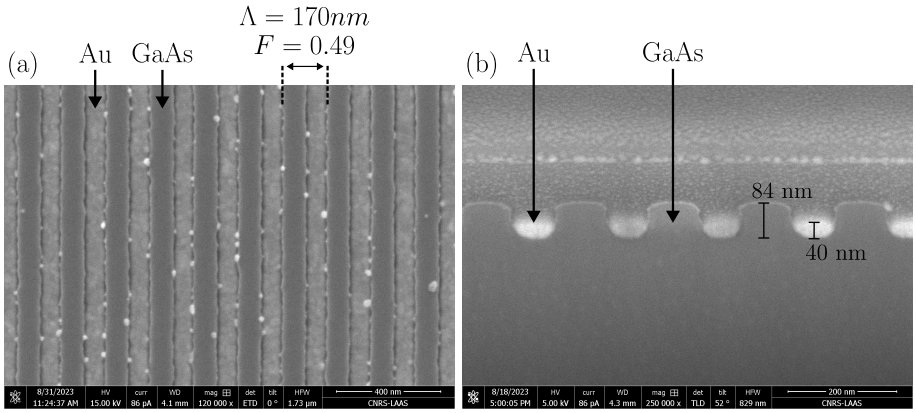

Figure 2.19: SEM images of the fabricated B-TE-Au-1 configuration: (a) top view from where grating period Λ and grating fill-factor F are measured, and (b) 52°-tilted view of the FIB-etched cross-section from where the GaAs teeth height H and the gold height H_{Au} are measured using vertical dimension scaling presented in figure 2.12 and equation 2.4. The pattern on which the FIB-etched has been performed is not the same as the one shown in (a). The spectroscopy measurement of the pattern shown in (a) is presented in figure 4.8a.

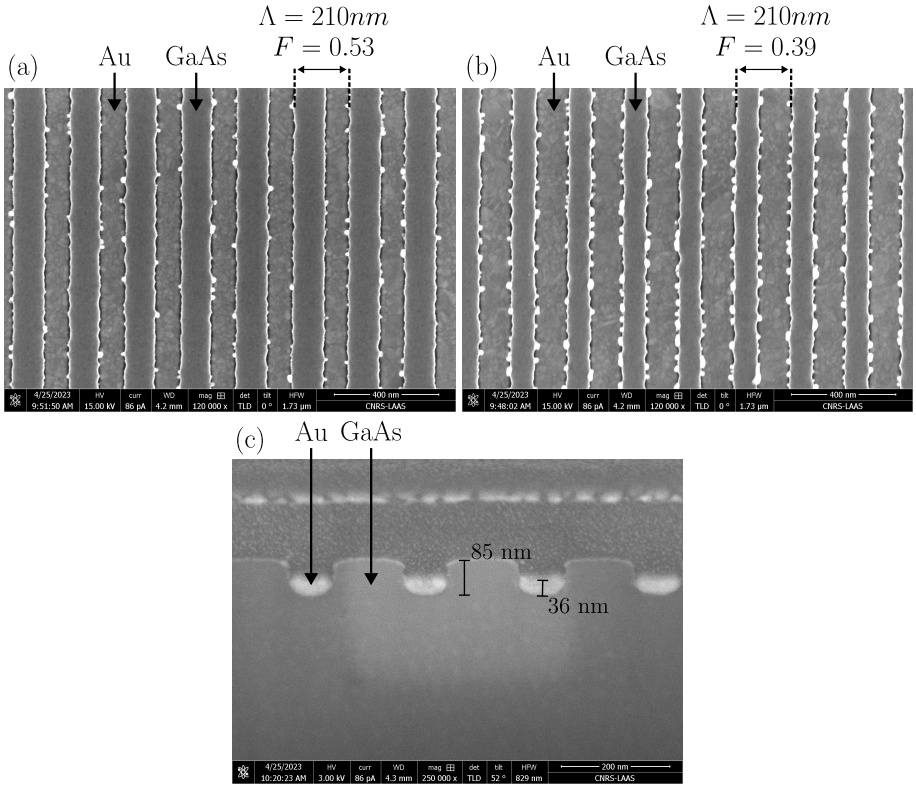

Figure 2.20: SEM images of the fabricated B-TE-Au-2 configuration. Top views of (a) B-TE-Au-2a, and (b) B-TE-Au-2b, from where grating period Λ and grating fill-factor F are measured. (c) shows the 52°-tilted view of the FIB-etched cross-section from where the GaAs teeth height H and the gold height H_{Au} are measured using vertical dimension scaling presented in figure 2.12 and equation 2.4. The pattern on which the FIB-etched has been performed is neither the pattern shown in (a) nor the one shown in (b). The spectroscopy measurement of the pattern shown in (a) is presented in figure 4.8b, and the one from the pattern shown in (b) is presented in 4.8c.

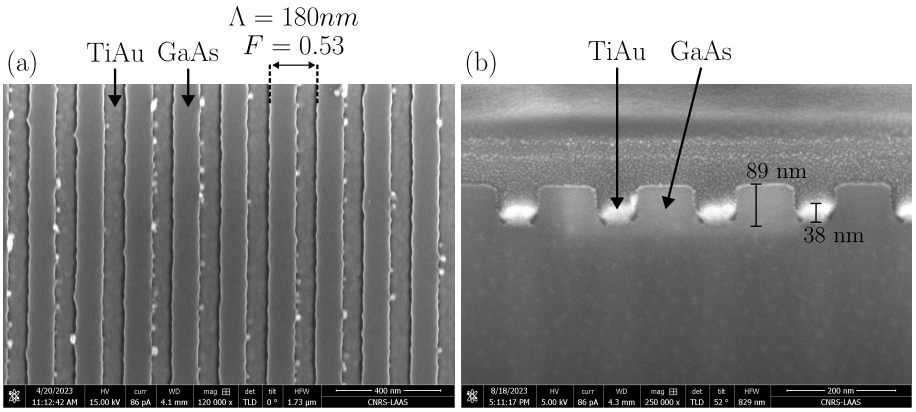

Figure 2.21: SEM images of the fabricated B-TE-TiAu-1 configuration: (a) top view from where grating period Λ and grating fill-factor F are measured, and (b) 52°-tilted view of the FIB-etched cross-section from where the GaAs teeth height H, the gold height H_{Au}, and the titanium height H_{Ti} are measured using vertical dimension scaling presented in figure 2.12 and equation 2.4. The pattern on which the FIB-etched has been performed is not the same as the one shown in (a). The spectroscopy measurement of the pattern shown in (a) is presented in figure 4.8d.

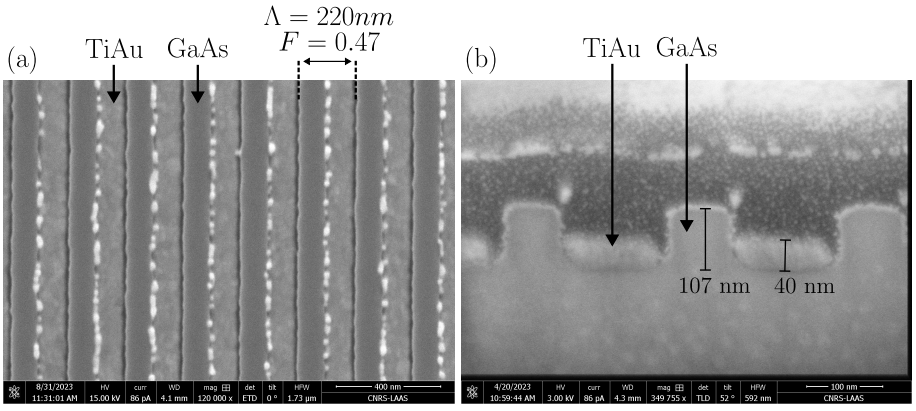

Figure 2.22: SEM images of the fabricated B-TE-TiAu-2 configuration: (a) top view from where grating period Λ and grating fill-factor F are measured, and (b) 52°-tilted view of the FIB-etched cross-section from where the GaAs teeth height H, the gold height H_{Au}, and the titanium height H_{Ti} are measured using vertical dimension scaling presented in figure 2.12 and equation 2.4. The pattern on which the FIB-etched has been performed is not the same as the one shown in (a). The spectroscopy measurement of the pattern shown in (a) is presented in figure 4.8e.

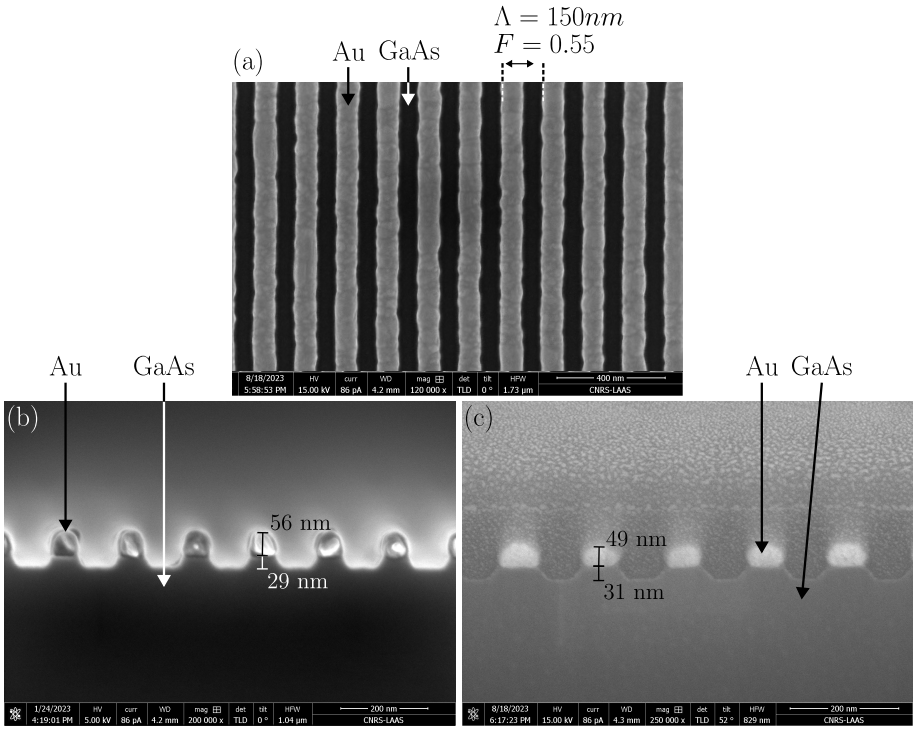

Figure 2.23: SEM images of the fabricated T-TM-Au configuration: (a) top view from where grating period Λ and grating fill-factor F are measured, (b) profile top view from a cleaved pattern, and (c) 52°-tilted view of the FIB-etched cross-section from where the GaAs teeth height H and the gold height H_{Au} are measured using vertical dimension scaling presented in figure 2.12 and equation 2.4. The pattern shown in (a) and (b) are the same, while the one shown in (c) is a different one. The spectroscopy measurement of the pattern shown in (a) is presented in figure 4.9a.

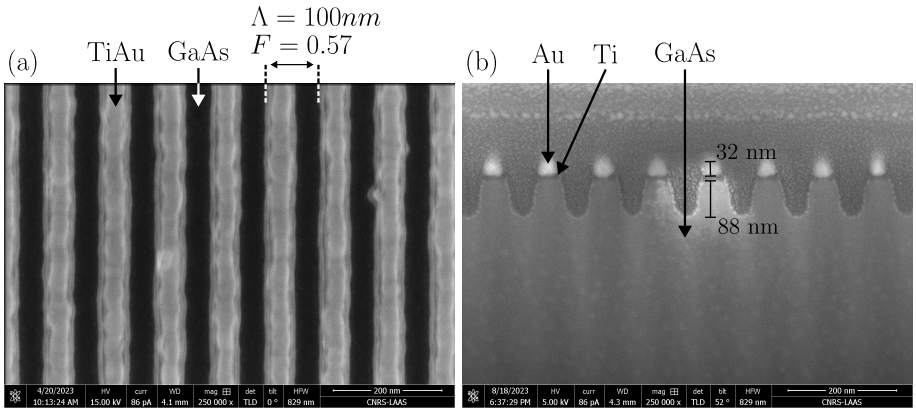

Figure 2.24: SEM images of the fabricated T-TM-TiAu configuration: (a) top view from where grating period Λ and grating fill-factor F are measured, and (b) 52°-tilted view of the FIB-etched cross-section from where the GaAs teeth height H, the gold height H_{Au}, and the titanium height H_{Ti} are measured using vertical dimension scaling presented in figure 2.12 and equation 2.4. The pattern on which the FIB-etched has been performed is not the same as the one shown in (a). The spectroscopy measurement of the pattern shown in (a) is presented in figure 4.9b.

2.5 Characterizations

The fabricated SMDSG structures summarized in table 2.11 were characterized optically using a dedicated spectroscopy setup, developed by the photonics team. This setup enables the sample illumination with TE or TM-polarized light, at quasi-normal incidence, as well as the reflected and transmitted signals collection. From these measurements, transmission and reflection of the air/SMDSG/GaAs interface could be extracted. A transmission equal or higher than the one afforded by the air/GaAs interface have been demonstrated for TE polarization in the case of the B-TE configuration, and under TM polarization in the case of the T-TM configuration.

2.5.1 Spectroscopy

2.5.1.1 Experimental setup

The spectroscopy experimental setup is presented in figure 2.25. It relies on a tunable laser whose wavelength can be scanned between 880 and 995 nm, and two photodiodes for reflected and transmitted signals measurement. The acquisition is synchronized with the laser spectral sweep using laser trigger out signal. The laser beam is focused on the sample surface with a beam waist estimated to $\sim 10\mu m$, which is compatible with $40 \times 40\mu m^2$ fabricated structure size. The pattern alignment is realized using a 940-nm LED illumination, a camera, and the sample XYZ stage. The angle of the linear polarization is tuned using a half-wave plate. Because this component is optimized for a wavelength of 850 nm, the incident TE and TM polarizations are slightly elliptical. Between 880 and 995 nm, this results in a mean ellipticity of 2.5° for the TE polarization, which means $\sim$ 4% of the TM component, and of 7.0° for the TM polarization, which means $\sim$ 12% of the TE component. The ellipticity η is calculate as $\eta = arctan(b/a)$ with b the semi-minor and a the semi-major axis dimension of the ellipse. The is the main source of error of the spectroscopy setup, which may lead to a lower measured transmission, and a higher measured reflection than for a perfectly linearly polarized incident light. It has more impact on the measurements based on TM-polarized light, with an assessed error of $\sim$ 12% compared to $\sim$ 4% under TE-polarized light. The measurement configurations and extraction of transmission and reflection at air/SMDSG/GaAs interface are described in the following section. The notations are summarized in table 2.12. Because oscillations were observed in the measured signals, coming from the Fabry-Perot cavity formed inside the GaAs slab, an anti-reflective coating (ARC) was deposited on the sample backside. This ARC is a quarter-wave-thick Si_3N_4 layer deposited by plasma-enhanced chemical vapor deposition (PECVD). The refractive index of this material of about 2 theoretically enables a reflection coefficient below 1% at normal incidence between 900 and 1000 nm.

The measurement procedure involves five steps:

1. The measurement of the signals that are transmitted and reflected by the SMDSG, illuminating from the sample top side.

2. The measurement of the signals that are transmitted and reflected by the GaAs substrate, illuminating from the sample top side.

3. The measurement of the reference signal in transmission by removing the sample from the stage.

4. The measurement of the reference signal in reflection using a gold mirror on silicon substrate whose reflectivity is assumed to be 98%. The final reference is corrected using this value.

5. The measurement of the zero of each photodiode signal by putting an absorber at the sample location.

The first two steps are described below, showing how the SMDSG transmission and reflection spectra are extracted from these measurements.

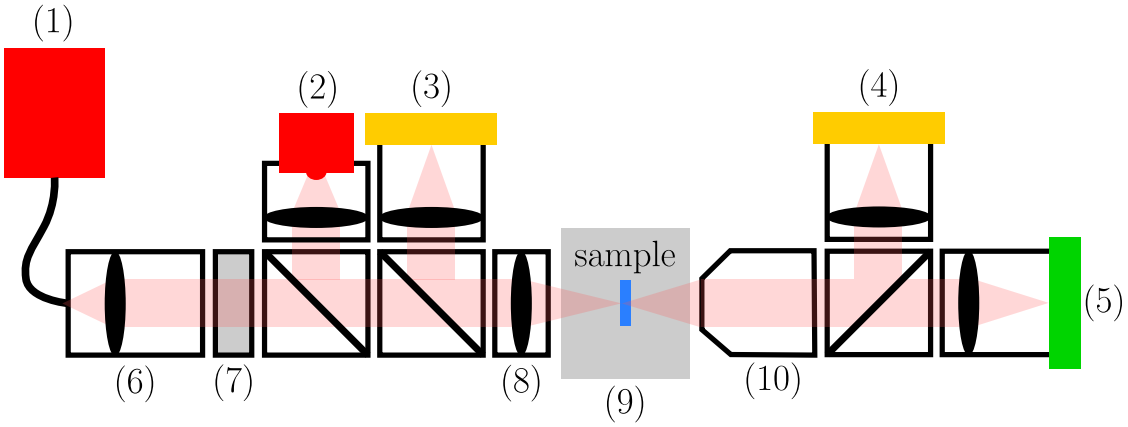

Figure 2.25: Experimental spectroscopy setup with the following components: (1) Tunable laser (superlum BS-930-1-OEM) of 880 - 995 nm spectral range and linewidth of 0.05 nm (2) 940-nm LED for sample visualization in transmission on camera (3) Photodiode for reflected signal measurement (4) Photodiode for transmitted signal measurement (5) CMOS camera to visualize the sample surface in transmission and target the center of the pattern of interest with the focused laser beam (6) Zoom fiber collimator (Thorlabs ZC618APC-B) (7) Half-wave plate (8) laser beam focusing lens (9) XYZ stage (10) Collection objective.

Notation	Definition
f	Incident beam focal point
ARC	Anti-reflective coating (quarter-wave layer of SiN)
n_0	Refractive index of medium 0 (air)
n_1	Refractive index of medium 1 (GaAs)
k_1	Extinction coefficient of medium 1 (GaAs)
I_0	Incident beam intensity
I_{r_i}	Reflected beam intensity of measurement i
I_{t_i}	Transmitted beam intensity of measurement i
I_{r_0}	Reference signal in reflection
I_{t_0}	Reference signal in transmission
$I_{r_{dark}}$	Zero of the photodiode signal in reflection
$I_{t_{dark}}$	Zero of the photodiode signal in transmission
T_{sub}	Transmission through 625-µm-thick GaAs NID substrate
T_{01}	Transmission through air/GaAs and GaAs/air interfaces
R_{01}	Reflection at air/GaAs and GaAs/air interfaces
T_{ARC}	Transmission through air/ARC/GaAs interface

R_{ARC}	Reflection at air/ARC/GaAs interface
T_{SMDSG}	Transmission through air/SMDSG/GaAs interface
R_{SMDSG}	Reflection at air/SMDSG/GaAs interface
T_i	Measured transmission in measurement i
R_i	Measured reflection in measurement i

Table 2.12: Formalism notations for the calculation of the SMDSG transmission and reflection from spectroscopy measurements.

- Measurement at normal incidence of the sample with SMDSG from the substrate top side:

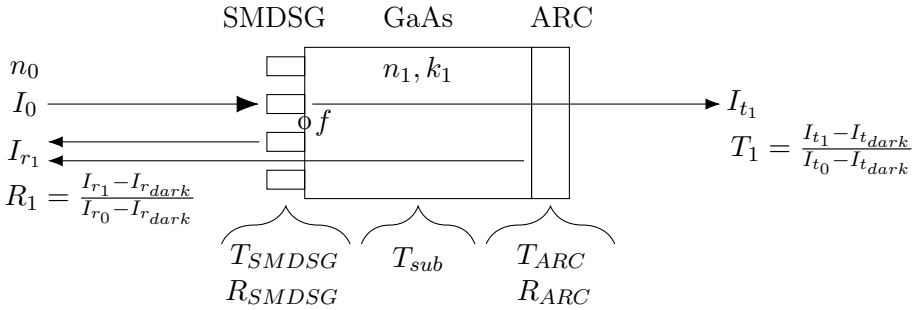

Figure 2.26: Schematic of the spectroscopy measurement from the SMDSG top side at normal incidence.

$$T_1 = T_{SMDSG} \times T_{sub} \times T_{ARC} \tag{2.5}$$

$$R_1 = R_{SMDSG} + T_{SMDSG}^2 \times T_{sub}^2 \times R_{ARC} \tag{2.6}$$

- Measurement at normal incidence of the GaAs reference from the substrate top side:

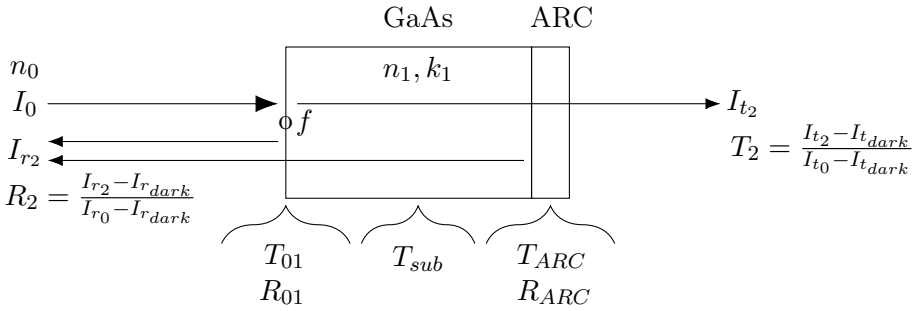

Figure 2.27: Schematic of the spectroscopy measurement of the GaAs substrate reference from the substrate top side at normal incidence.

$$T_2 = T_{01} \times T_{sub} \times T_{ARC} \tag{2.7}$$

$$R_2 = R_{01} + T_{01}^2 \times T_{sub}^2 \times R_{ARC} \tag{2.8}$$

- Calculation of T_{SMDSG} and R_{SMDSG} from the measurements:

  Equation 2.5 gives:

$$T_{SMDSG} = \frac{T_1}{T_{sub} \times T_{ARC}} \tag{2.9}$$

Equation 2.7 gives:

$$T_{sub} \times T_{ARC} = \frac{T_2}{T_{01}} \tag{2.10}$$

Hence:

$$\boxed{T_{SMDSG} = \frac{T_1}{T_2} \times T_{01}} \tag{2.11}$$

Equation 2.6 gives:

$$R_{SMDSG} = R_1 - T_{SMDSG}^2 \times T_{sub}^2 \times R_{ARC} \tag{2.12}$$

Equations 2.8 gives:

$$T_{sub}^2 \times R_{ARC} = \frac{R_2 - R_{01}}{T_{01}^2} \tag{2.13}$$

Injecting the expression of T_{SMDSG} given in equation 2.11, expression of R_{SMDSG} becomes:

$$\boxed{R_{SMDSG} = R_1 - \frac{T_1^2}{T_2^2} \times (R_2 - R_{01})} \tag{2.14}$$

T_{01} can be theoretically calculated from Fresnel intensity coefficient expression by $T_{01} = 1 - \left(\frac{n_0 - n_1}{n_0 + n_1}\right)^2$, which enables the calculation of T_{SMDSG} and R_{SMDSG} from the measurements.

2.5.1.2 Measurement results

The fabricated SMDSG transmission and reflection spectra, extracted from the measurements performed using the previously described spectroscopy setup, are presented in figure 2.28 for the B-TE structures, and figure 2.29 for the T-TM structures. Spectra are plotted in the 900-985 nm spectral range. The use of an anti-reflective coating enabled to damp oscillations in the measured signals. However, this coating was not perfect and reflection and transmission curves have been post-processed using Fourier filtering to remove the remaining tiny oscillations by cutting the 100 first harmonics of the signal in the Fourier space. Considering a wavelength of 940 nm, measured transmission, reflection, and losses, which are considered to be the sum of absorption and uncollected scattering, are summarized in table 2.13, with losses $= 1 - R - T$. Those results demonstrate the polarization-selective nature of the optical response, with the B-TE structures which mainly transmit TE polarization, and the T-TM structures which mainly transmit the TM one. For both the B-TE and the T-TM structures, and both Au and TiAu metallic contacts, transmission levels higher than the Fresnel transmission at GaAs/air interface are observed when considering the appropriate transmitted polarization. The change from Au to TiAu contact doesn't impact the losses of the highly transmitted polarization. Also, the amount of losses is

observed to be the lowest in the T-TM configuration. The structure called B-TE-TiAu-2 presents the largest losses, which could be caused by the metal ears described in section 2.4.4, or by the grating dimensions and profile. Figures 4.8b and 4.8c enable the comparison of two similar structures but with a different fill-factor of respectively 0.53 and 0.39. As expected, reducing the fill-factor blue-shifts the high transmission window.

As explained in section 1.3.2, ohmic contact requires a doped cap layer to lower the Schottky barrier height. The measured structures have been fabricated on GaAs NID substrate, thus free carrier absorption from the doped cap layer isn't taken into account. In [13], an absorption coefficient of $\sim 100 cm^{-3}$ is reported for p-GaAs doping level of $1.6{\times}10^{19} cm^{-3}$. Considering a doped cap layer thickness of 100 nm, it results in a theoretical absorption of $\sim 0.1\%$ in the layer, which is low enough to be confident about the high transmission of SMDSG with ohmic contact. As presented in section 2.4.4, the structure dimensions and profile are not perfect. Despite this, the demonstrated high transmission of several structures shows the robustness of the SMDSG optimized in transmission for the NIR spectral range with regard to fabrication induced flaws.

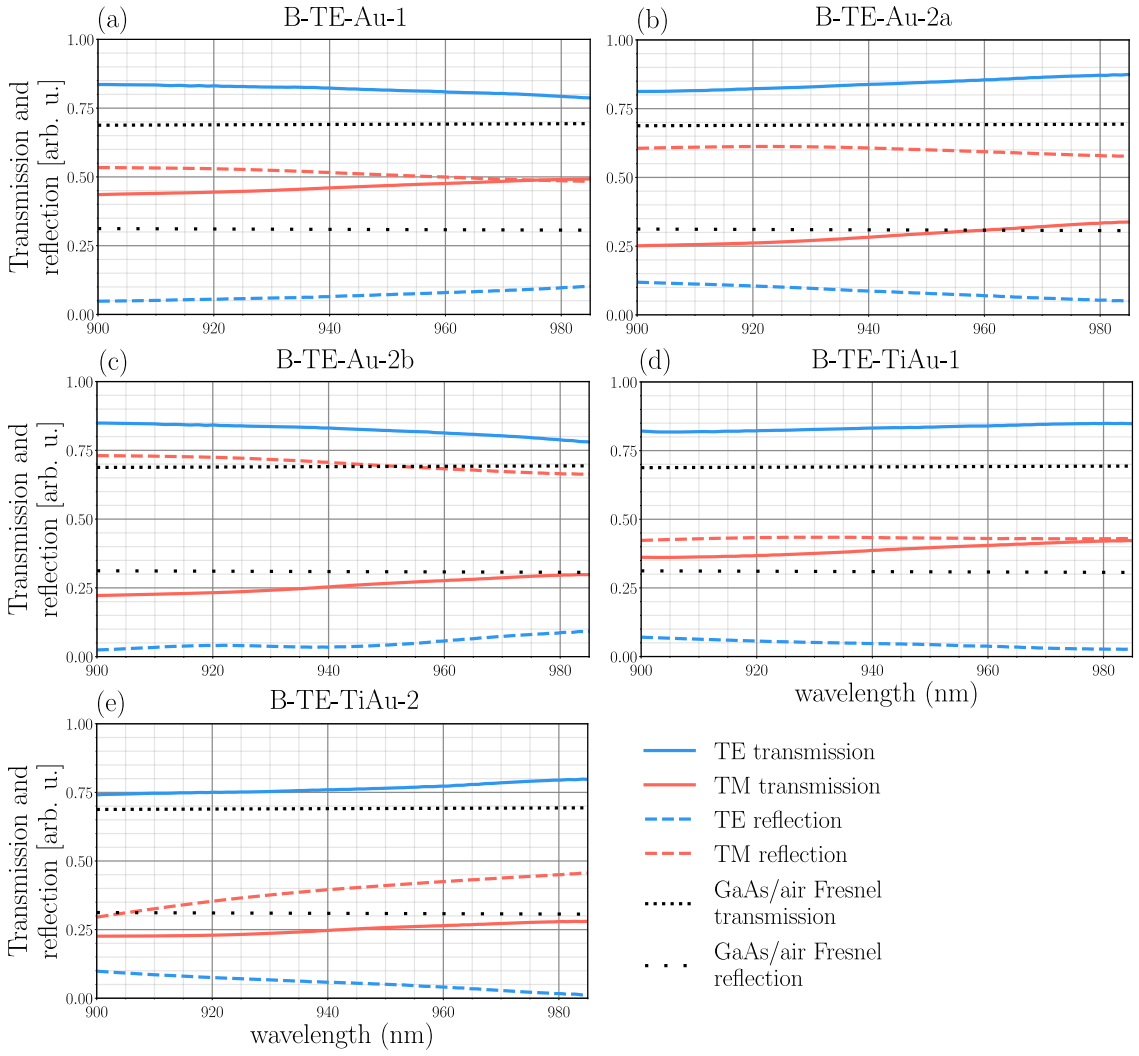

Figure 2.28: Spectroscopy measurements of fabricated B-TE configurations at normal incidence between 900 and 985 nm.

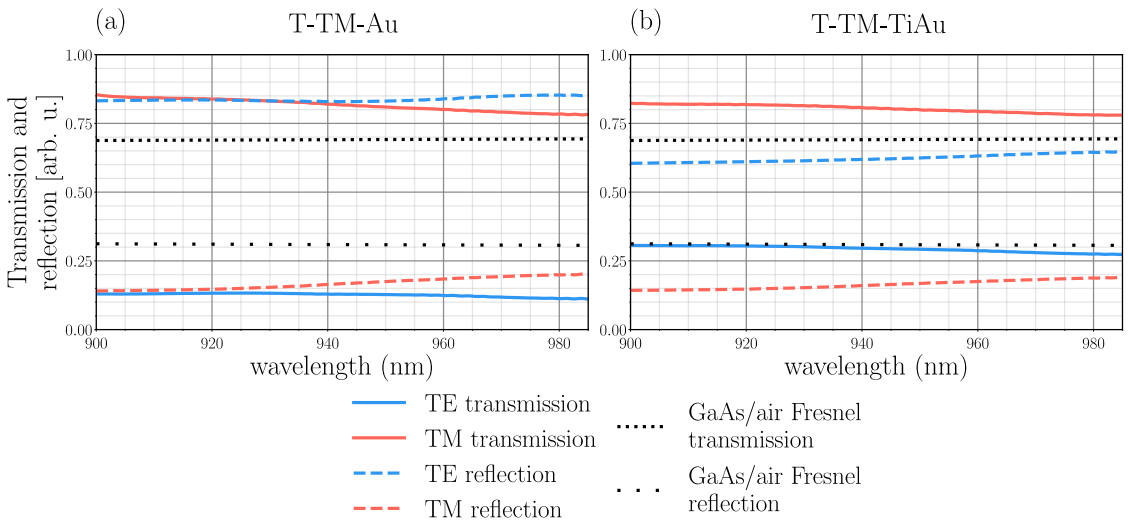

Figure 2.29: Spectroscopy measurements of fabricated T-TM configurations at normal incidence between 900 and 985 nm.

	T (940 nm)		R (940 nm)		Losses (940 nm): absorption and scattering	
	TE	TM	TE	TM	TE	TM
B-TE-Au-1	0.82	0.46	0.06	0.51	0.12	0.03
B-TE-Au-2a	0.84	0.28	0.09	0.61	0.07	0.11
B-TE-Au-2b	0.83	0.25	0.03	0.7	0.14	0.05
B-TE-TiAu-1	0.83	0.38	0.05	0.43	0.12	0.19
B-TE-TiAu-2	0.76	0.25	0.06	0.39	0.18	0.36
T-TM-Au	0.13	0.82	0.83	0.16	0.04	0.02
T-TM-TiAu	0.29	0.81	0.62	0.16	0.09	0.03

Table 2.13: Summary of transmission (T), reflection (R), and losses $= 1-R-T$ from measurements in figures 2.28 and 2.29.

2.5.2 Sheet resistance

In addition to optical characterization, the sheet resistance of a gold nanowire with dimensions close to the ones required in the B-TE and the T-TM configurations have been measured using a two-probes setup. In this experiment, the resistance of a set of one or several nanowire(s) is measured, and the sheet resistance R_{sh} is calculated using equation 4.2:

$$R_{sh} = (R - R_p).N.\frac{W}{L} \tag{2.15}$$

Where R is the measured resistance, R_p the parasitic contacts and probes resistance measured in short circuit configuration, N the number of nanowire, W the nanowire width, and L their length.
Sets of 1, 2, 5, and 10 48-nm-thick gold nanowire have been deposited on GaAs NID substrate using EBL patterning and EBPVD. The fabricated nanowires length are 20 and 40 µm, with width of 60 nm, and a periodicity of 150 nm in sets of multiple nanowires. The extremities of each set have been connected to TiAu contact pads for the two-probes

measurement, as presented in figure 2.30. As shown in figures 2.31a, 2.31b, and 2.31c, the gold height was measured with atomic force microscopy (AFM), while W and L were measured using SEM.
Figure 2.32 shows the measured R_{sh} with respect to the number of nanowire, including 20-µm-long and 40-µm-long sets. This results in a measured mean value of $R_{sh} = 1.4 \pm 0.1$ $\Omega.sq^{-1}$ for one nanowire, equivalent to a resistivity of $\rho = 6.7.10^{-8} \pm 0.5.10^{-8}$ $\Omega.m$. This is less than 3 times the gold bulk resistivity of $2.44.10^{-8}$ $\Omega.m$. This demonstrates the excellent electrical conductivity of gold, even in the shape of nanowires, which, combined with high optical transmission results, makes SMDSG structures very promising for their implementation as electrodes. The last required characterization is the specific contact resistance, which is the topic of the next section.

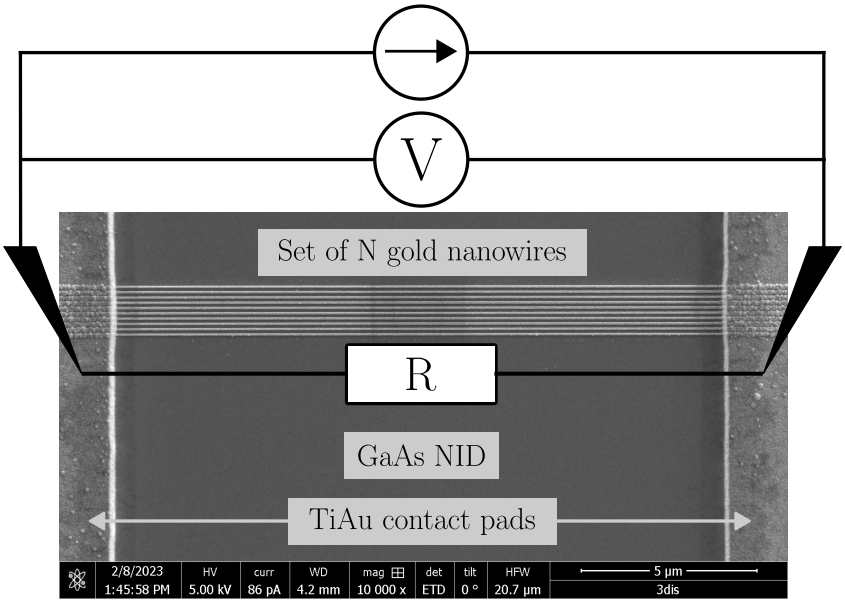

Figure 2.30: Schematic of the two-probes measurement principle of the resistance of a nanowire set.

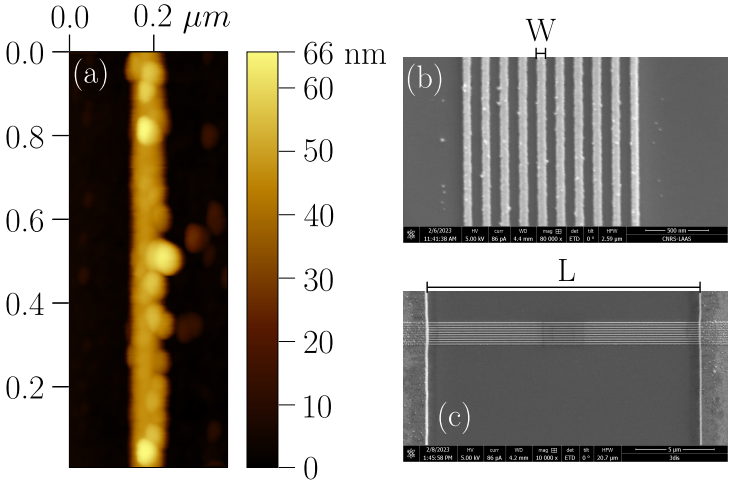

Figure 2.31: (a) Nanowire AFM height measurement, (b) SEM top-view image used for nanowire width measurement, and (c) SEM top-view image used for the measurement of the length between the contact pads.

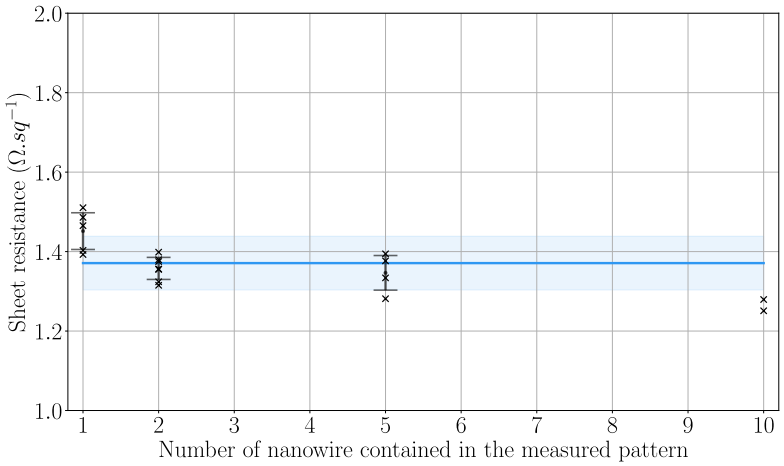

Figure 2.32: Sheet resistance measurement results as a function of the number of nanowire. The blue line is the mean value, and the light blue rectangle shows the standard deviation around the mean value.

2.5.3 Specific contact resistance

As mentioned in the section 1.3.1.2, the specific contact resistance ρ_c enables to quantify the efficiency of the vertical current injection from the metallic subwavelength grating to the doped GaAs cap layer. Transfer length method (TLM) is a typical way to measure this value. Thus, TLM patterns have been designed and fabricated, but not completely finished by lack of time. This part relates the design and the fabrication process of these patterns although no specific contact resistance could be measured.

The principle of the TLM is to measure the resistance between contacts separated by various distances d. The fabricated measurement structure is presented in figure 2.33a. In this design, metal subwavelength gratings are in contact with a 500-nm-thick doped GaAs cap layer previously grown by molecular beam epitaxy (MBE). A 50-nm-thick SiO_2 layer deposited using PECVD acts as an insulator to connect gratings with contact pads preventing current injection from the pads (see figure 2.33b). Thus, metal gratings are patterned on SiO_2 openings defined by W and L dimensions, as shown in figure 2.33a. In addition, this structure allows current to flow in the y direction only, since doped cap layer limited thickness confines in the z direction while a doped cap layer etched mesa of width Z confines in the x direction, as shown in figure 2.33b. Figure 2.33c presents the several resistances which are measured between two pads, which is formalized by equation 2.16:

$$\begin{aligned} R &= R_{cap} + 2R_c \\ &= R_{sh,cap}.\frac{d}{W} + 2R_c \end{aligned} \tag{2.16}$$

With R the measured resistance, R_{cap} the resistance coming from the cap layer, R_c the resistance coming from the contact between the metal grating and cap layer, $R_{sh,cap}$ the sheet resistance of the cap layer, d the distance between contacts, and W the contact width illustrated in figure 2.33a. Using this equation, the measurement of R for various d results in the knowledge of the specific contact ressitance ρ_c using equation 2.17:

$$\rho_c = \frac{R(d=0)}{2}.W.L_T \tag{2.17}$$

Where $W.L_T$ corresponds to the effective contact area, which is different from $W.L$ because the current doesn't flow uniformly in the contact. In this current crowding, where the

current mainly flows at the contact edge, the transfer length L_T is the characteristic length of the exponential drop of current from the contact edge. L_T is illustrated in figure 2.33d and can be found thanks to the TLM measurement, as shown by equation 2.18:

$$L_T = -\frac{d(R=0)}{2} \tag{2.18}$$

Good TLM measurement conditions are enabled by current confinement in the direction of interest, and by a transfer length L_T which is not too short compared to L. Thus, the encoded photolithography mask contains patterns with various L and various W, since L_T increases with W as reported in [14]. In addition, SiO_2 openings with an area equivalent to metal effective area in gratings are encoded in the photolithography mask, in order to ensure a fair comparison between a fully-covering contact and a grating contact specific contact resistance. Table 2.14 presents the developed fabrication process of the test structures presented in figure 2.33a. This process can be used for the integration of the SMDSGs on devices.

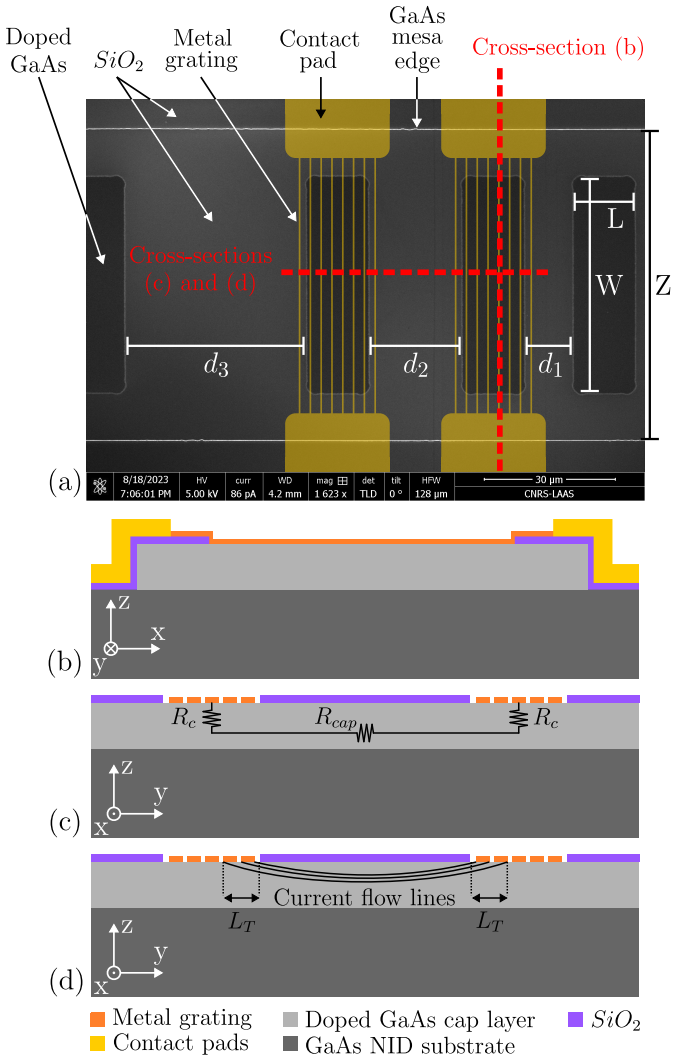

Figure 2.33: (a) SEM top-view of a part of a fabricated TLM pattern before metal deposition with locations of metal drawn on top of it, (b) a schematic of the cross-section corresponding to the vertical red dashed line in (a), (c)-(d) schematics of the cross-section corresponding to the horizontal red dashed line in (a). (c) shows the different electrical resistances seen by the current between the two contacts, and (d) shows the origin of the transfer length L_T.

Step order	Description	Technique
1	Growth of 500-nm-thick doped GaAs cap layer on GaAs substrate	Molecular beam epitaxy (MBE)
2	Deposition of EBL gold alignment marks	Photolithography
		Gold deposition: EBPVD
		Lift-off
3	Dry etching of 500-nm-high doped cap layer mesas	photolithography
		ICP-RIE: Cl_2/N_2 chemistry
		Resist removal
4	50-nm-thick SiO_2 layer deposition	PECVD
5	SiO_2 opening	photolithography
		RIE: CHF_3/O_2 chemistry
		Resist removal
6	Subwavelength gratings patterning	EBL resist deposition (PMMA)
		EBL patterning with alignment on structures using previously deposited gold alignment marks
		Resist development
7	Subwavelength gratings TiAu contact deposition	GaAs native oxide removal
		EBPVD
		Lift-off
8	TiAu contact pads deposition	Photolithography
		EBPVD
		Lift-off

Table 2.14: Summary of TLM test pattern fabrication process.

2.6 Conclusion and perspectives

In this chapter, the issue of the injection uniformity in VCSELs simultaneously with high optical transmission has been presented. While transparent conductive electrodes like ITO, graphene, or silver nanowires have been reported as VCSEL top electrode, their engineering is based on a compromise between conductivity and transparency. Moreover, the efficiency of the vertical injection is degraded with respect to metallic contact in the case of ITO, and unknown for graphene and silver nanowires. SMDSG structures have been presented, enabling highly transmittive metallic electrodes for TM or TE polarization. These designs benefit from both the excellent electrical properties of metal and the high transmission coming from the nano-structuration. This works aimed to demonstrate the fabrication of SMDSGs optimized for the NIR spectral region, and their optical and electrical properties. The fabrication process of the B-TE and the T-TM configurations has been developed and

realized successfully, while dry-etching, metal deposition, and lift-off process steps could be optimized further or changed by following the suggestions given in this chapter. Despite the smaller periodicity required for the T-TM configuration, its fabrication is easier compared to the B-TE structures. Optical transmission above 80% has been demonstrated between 900 and 985nm, which is above 14% higher than the Fresnel transmission at the GaAs/air interface. This demonstration has been made for TE and TM-polarized light, using both Au and TiAu metallic contact and GaAs NID substrate. Complementary measurements over a larger spectral window would enable to quantify the width of high transmission window, since spectra measured between 900 and 985nm are relatively flat. If the T-TM configuration is easier to fabricate, spectroscopy measurements show that they also show less optical losses. A low sheet resistance of 1.4 $\Omega.sq^{-1}$ have been measured for such structures made of gold, which is at least one order of magnitude lower than ITO, graphene, and silver nanowires. The specific contact resistance of SMDSG structures made of TiAu contacts on p-GaAs is the last required characterization to conclude about the potential of such structures for high efficiency vertical electrical injection.

That being said, the presented structures are optimized with regards to the transmitted mode, which is not a perfect solution for VCSEL or devices based on a resonant cavity, since this work experimentally demonstrates that the mode that is not transmitted is mainly reflected. This reflected mode will exhibit the highest net gain in the cavity, so the laser will lase on a mode for which the losses in SMDSG hasn't been minimized. A better solution would therefore be to maximize the mode reflectivity while minimizing the absorption to ensure an efficient transmission when not reflected. This leads to longer required periodicity, since at least two propagating modes are needed to induce interferences. The presented fabrication and characterization techniques remain completely relevant for such structures given their similarity in nature. The applications of the fabricated structures of this work can be found in devices which are not based on resonant cavity, like surface-emitting LEDs or photodetectors. They would benefit from the optical impedance matching at the high-refractive-index semiconductor / air interface.

Bibliography

[1] T. Czyszanowski, A. K. Sokól, M. Dems, and M. Wasiak, "Transparent Electrode Employing Deep– Subwavelength Monolithic High-Contrast Grating Integrated with Metal," *Optics Express*, vol. 28, no. 19, p. 28383, 2020.

[2] M. Gębski, M. Dems, A. Szerling, M. Motyka, L. Marona, R. Kruszka, D. Urbańczyk, M. Walczakowski, N. Palka, A. Wójcik-Jedlińska, Q. J. Wang, D. H. Zhang, M. Bugajski, M. Wasiak, and T. Czyszanowski, "Monolithic High-Index Contrast Grating: A Material Independent High-Reflectance VCSEL Mirror," *Optics Express*, vol. 23, no. 9, p. 11674, 2015.

[3] M. Marciniak, M. Gębski, M. Dems, E. Haglund, A. Larsson, M. Riaziat, J. A. Lott, and T. Czyszanowski, "Optimal Parameters of Monolithic High-Contrast Grating Mirrors," *Optics Letters*, vol. 41, no. 15, p. 3495, 2016.

[4] M. Dems, "Monolithic High-Contrast Gratings: Why Do They Not Scatter Light?," *Journal of Lightwave Technology*, vol. 35, no. 2, pp. 159–165, 2017.

[5] T. W. Ebbesen, H. J. Lezec, H. F. Ghaemi, T. Thio, and P. A. Wolff, "Extraordinary Optical Transmission through Sub-Wavelength Hole Arrays," *Nature*, vol. 391, no. 6668, pp. 667–669, 1998.

[6] J. Porto, F. J. Garcia-Vidal, and J. B. Pendry, "Transmission Resonances on Metallic Gratings with Very Narrow Slits," *Physical Review Letters*, vol. 83, no. 14, pp. 2845–2848, 1999.

[7] P. B. Catrysse and S. Fan, "Nanopatterned Metallic Films for Use As Transparent Conductive Electrodes in Optoelectronic Devices," *Nano Letters*, vol. 10, no. 8, pp. 2944–2949, 2010.

[8] L. Y. M. Tobing, M. Wasiak, D. H. Zhang, W. Fan, and T. Czyszanowski, "Nearly Total Optical Transmission of Linearly Polarized Light through Transparent Electrode Composed of GaSb Monolithic High-Contrast Grating Integrated with Gold," *Nanophotonics*, vol. 10, no. 15, pp. 3823–3830, 2021.

[9] A. K. Sokól and T. Czyszanowski, "Nearly Perfect Transmission of Unpolarized Infrared Radiation through a One-Dimensional Metal Grating Embedded in a Monolithic High-Contrast Grating," *Optics Express*, vol. 28, no. 26, p. 38857, 2020.

[10] S. I. Flores Esparza, *CALAM : Cavités Actives Laser à Autocollimation Mésoscopique*. PhD Thesis, Université Toulouse 3, 2022.

[11] L. Jalabert, P. Dubreuil, F. Carcenac, S. Pinaud, L. Salvagnac, H. Granier, and C. Fontaine, "High Aspect Ratio GaAs Nanowires Made by ICP-RIE Etching Using

Cl2/N2 Chemistry," *Microelectronic Engineering*, vol. 85, no. 5-6, pp. 1173–1178, 2008.

[12] G. C. DeSalvo, C. A. Bozada, J. L. Ebel, D. C. Look, J. P. Barrette, C. L. A. Cerny, R. W. Dettmer, J. K. Gillespie, C. K. Havasy, T. J. Jenkins, K. Nakano, C. I. Pettiford, T. K. Quach, J. S. Sewell, and G. D. Via, "Wet Chemical Digital Etching of GaAs at Room Temperature," *Journal of The Electrochemical Society*, vol. 143, no. 11, pp. 3652–3656, 1996.

[13] B. Ullrich, S. R. Munshi, and G. J. Brown, "Photoluminescence Analysis of P-Doped GaAs Using the Roosbroeck–Shockley Relation," *Semiconductor Science and Technology*, vol. 22, no. 10, pp. 1174–1177, 2007.

[14] S. Grover, "Optimization of Transmission Line Measurement (TLM) Structures for Specific Contact Resistivity Determination.," in *Microelectronic Engineering Conference*, vol. 22, p. 18, 2016.

CHAPTER 3

Spectrally-shaped illumination for improved optical monitoring of VCSEL oxide aperture

Good electro-optic performances of oxide-confined VCSEL devices require the accurate control of the oxide aperture(s) diameter. In-situ real-time monitoring of Al-based III-V semiconductors wet thermal oxidation process have been developed at LAAS-CNRS prior to this work by using narrow-band illumination with an optical microscope. However, the discernability of the oxide has been found to be challenging for some VCSEL structures. This work presents the implementation and the use of a spectrally-shaped illumination which has been developed to enhance the in-situ inspection of this oxide aperture. This source exploits a digital micromirror device (DMD) to arbitrarily tailor its emission spectrum. When combined to a microscope, the ability to detect small surface reflectance contrasts on any VCSEL or AlOx-based photonic structure and, in turn, the improvement of the in-situ inspection of the oxide aperture shapes and dimensions are demonstrated in this chapter.

Contents

3.1 Introduction 73
3.2 AlGaAs wet thermal oxidation process in VCSEL fabrication . 73
3.2.1 Fabrication of oxide-confined VCSEL 73
3.2.2 AlGaAs wet thermal oxidation physico-chemical mechanisms . . 75
3.3 The control of wet thermal oxidation process 79
3.3.1 Oxidation furnace general principle 79
3.3.2 Oxide layer optical detection in VCSEL structures 80
3.3.3 Optical in-situ monitoring systems 85
3.3.4 Perspectives 88
3.4 Interest and implementation of pylochromatic illumination for optical monitoring 89
3.4.1 Hyperspectral imaging and wet thermal oxidation monitoring . . 89
3.4.2 Spectrally-shaped source development 91
3.4.3 Conclusion 97
3.5 Experimental setup and results 97
3.5.1 Methodology 97
3.5.2 Hyperspectral cube acquisition 98
3.5.3 Spectral shaping 100

3.5.4 Acquisition of monitoring "views" 101
3.5.5 Results and discussion 101
3.6 Conlusion and perspectives 107

3.1 Introduction

Oxide-confined VCSELs, which have become the ubiquitous light sources for high-speed data transmission in datacenters and in LiDAR applications, rely on the selective oxidation of a thin buried semiconducting AlGaAs layer into an insulating oxide (AlOx), to define their electrical and optical aperture and, in turn, control their performances [1]. Single-mode VCSEL devices, for which this aperture diameter must be small, usually below 5 µm, are employed in many technologies as optical mices, laser printers, gas sensors, atomic clocks and magnetometers, or optical coherence tomography [2]. Since the geometric features of this lateral semiconductor/oxide aperture set the beam modal distribution, act on the modulation response bandwidth and may also be the source of dislocation defects causing device failure, in-situ real-time imaging of the wet thermal oxidation process is a valuable asset to reach the required control accuracy in fabrication.

The capability to monitor the wet thermal oxidation of Al-based III-V semiconductors has been proven to be a valuable tool especially for the fabrication of VCSELs [3, 4, 5]. These monitoring techniques exploit the spectral changes in the VCSEL reflectivity between the oxidized and unoxidized areas to visualize the oxide aperture. This detection is challenging and of limited spatial resolution. Moreover it is highly dependant on the particular vertical stack of each VCSEL batch.

This chapter presents the methodology and the results of a versatile solution, based on hyperspectral imaging, to shape the illumination spectrum for the application of in-situ imaging of the VCSEL oxide aperture. The role and the fabrication of the oxide aperture in VCSEL devices are explained, just like the state of art of the aperture real-time in-situ monitoring. From this knowledge, the possible improvement of the wet thermal oxidation process control through hyperspectral imaging and spectrally-shaped illumination is discussed and experimented. The proposed spectrally-shaped source enables weighting the spectral bands to increase the distinctness between regions of very close reflectivities. In addition, this source can be harnessed to acquire in-situ hyperspectral cube of the sample under study. A quantitative analysis of the distinctness improvement of oxide aperture is presented in the specific case of room temperature conditions on an already-oxidized 850 nm VCSEL, called static conditions.

3.2 AlGaAs wet thermal oxidation process in VCSEL fabrication

3.2.1 Fabrication of oxide-confined VCSEL

The first commercialized VCSELs, supplied by the Honeywell company in 1996 for datacom applications, was based on proton implantation confinement technique. In the early 2000s, the speed modulation of those devices reached its limit and couldn't follow the requirements of ethernet technology. Oxide-confined devices, firstly introduced in 1990 [1], was more suitable to the datacom market specifications, and became the most widespread confinement technique for VCSELs. From this nascent period to the nowadays information high technologies, its expansion is due to its many advantageous properties, that include the best results in terms of threshold current and power conversion efficiency [6]. Typical threshold current is in the order of magnitude of 1 mA with a driving voltage below 2 V. A modulation rate of 25 Gbps is widely available, while advanced modulation technology developments, dedicated to ultra-high-speed data transmission, are underway. The highest reported power conversion efficiencies are above 50% [7]. VCSEL designs, based on compromises between optical, electrical, and thermal properties, benefit from various ap-

proaches to use oxide aperture, playing with aperture position in the stack, shape, profile, thickness, aperture number, as well as hybridation with complementary carrier and photon guiding methods. This section aims to give a general comprehension of the impact of oxide aperture on VCSEL characteristics.

Figure 3.1 shows the oxide-confined VCSEL cross-section, and highlights the both electrical and optical confinement feature of the oxide aperture. The optical confinement, described by the effective index model for VCSEL [8], relies on the lateral position dependency of the Fabry-Perot resonnance frequency. Indeed, the introduction of the low refractive index oxide in a portion of the cavity lowers the effective index in this oxidized region, which produces a local blue shift of the resonnance wavelength. This transverse optical confinement is completed with a charge carriers confinement in the central region of the VCSEL, based on the high resistivity of the oxidized material. An etched mesa, also presented in figure 3.1, is necessary for the high aluminium content layer ($Al_xGa_{1-x}As$ with x>0.97) to be exposed to the oxidation environment, described in section 3.3.1.

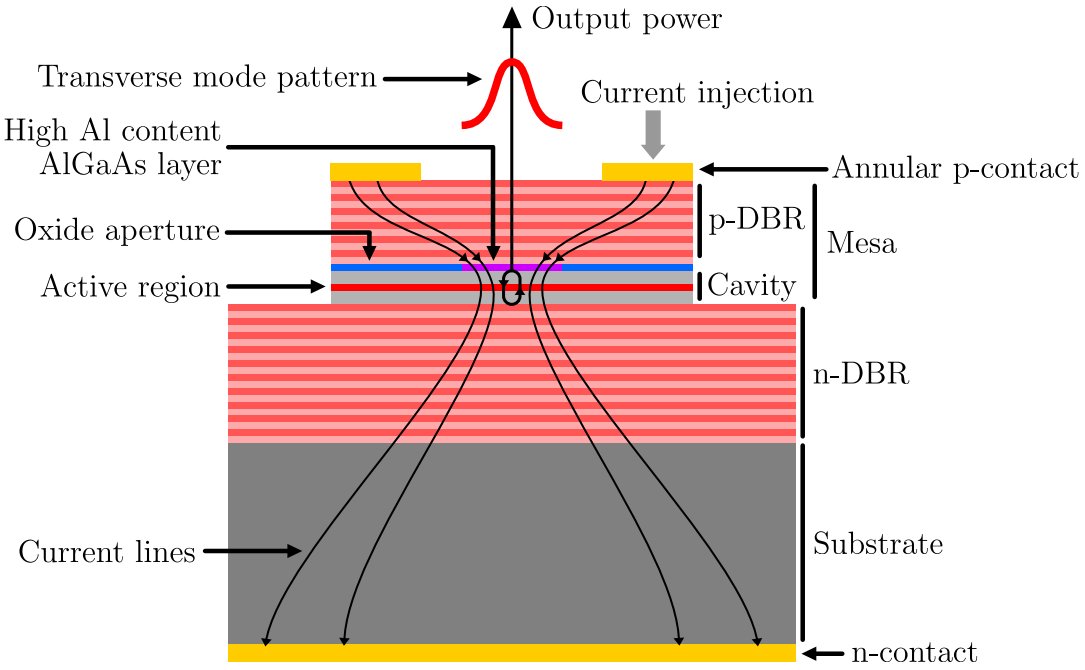

Figure 3.1: Oxide-confined VCSEL cross-section.

The oxide aperture is generally located just above the cavity, between the electromagnetic field node and antinode positions. This is the result of a compromise between the antinode position that provides the best optical confinement enabling low theshold current, and the node position that advantgeously enhances the fundamental mode stability by decreasing the confinement of higher-order modes at the cost of a larger threshold current [9]. The oxide aperture thickness layer, typically around 30 nm [10], affects the VCSEL capacitance, a key parameter for modulation speed, as well as the effective index change, respectively inversely proportional and proportional to it.

The influences of single circular oxide aperture dimension on VCSEL performances have been studied in [11, 12]. Electrically, the decrease of the oxide aperture diameter decreases the threshold current of the device, while it increases the current density in the active region. In order to avoid VCSEL reliability issues, the maximum usable current density, estimated at 10 kA/cm^2 [13], limits the applied bias current in case of low apertures. The smaller is the aperture diameter, the broader is the small signal modulation bandwidth,

making small aperture devices suitable for high-speed data transmission. Optically, such small diameter ensures a narrow spectral width of the emission, which limits the chromatic dispersion in optical fibers for the benefit of longer distance data transmission. Also, while the wavelength of each mode is blue-shifted, the adjacent modes become spectrally more distant, and directly affects the far-field emission angle of the fundamental mode that tends to increase. Thermally, the aperture diameter reduction increases the device thermal resistance, as well as the device differential electrical resistance which is responsible for self-heating, both of which are responsible for the more complex thermal management in the case of small aperture VCSELs.

Optimized VCSEL structures based on several oxide layers have also been reported in litterature. These multiple layers are used for better current distribution homogeneity in VCSEL cavity in [14, 9], which offers single-mode devices with higher output power, resulting in structures employing one or several oxide aperture above the cavity, and one below. Multiple oxide apertures are also used in [15] to lower the device capacitance which is inversely proportional to the insulator thickness, and enable higher modulation speed while keeping the small oxide layer thickness required for good optical performances. In addition, the use of multiple oxide apertures is reported in [10] to enable the single-mode operation of VCSELs with a larger aperture, typically with a diameter of about 10 µm. Those layers are larger than the fundamental mode, but smaller than higher-order modes which causes strong scattering losses for those modes.

Scattering losses increase as the oxide aperture diameter is reduced, which limits the performances of small aperture devices. For this reason, tapered oxide profile is explored in [16], where the oxide thickness is gradually lowered at its extremity. The taper oxide tip can extend to a few microns [15], and approximates the parabolic refractive index profile of a "perfect lens". Compared to a sharp taper, this design reduces the optical scattering losses that occur at the aperture, as well as the mode confinement.

Finally, noncircular aperture, which can be obtained as a result of the anisotropy of the oxidation process, or asymmetric mesas, has an strong impact on the VCSEL emission properties. It can stabilize the polarisation [17], with the drawback of changing the tranverse mode distribution compared to a circular aperture shape [18].

Because the VCSEL optical, electrical, and thermal behaviors are very sensitive to the lateral confining oxide layer(s) parameters, the oxidation process must be made highly controllable. This control can benefit from the deep understanding of the phenomenon, as well as the development of real-time monitoring solutions.

3.2.2 AlGaAs wet thermal oxidation physico-chemical mechanisms

The AlGaAs wet thermal oxidation has been discovered in 1990 by researchers at the University of Illinois [1]. This oxide is stable, amorphous, and appears to be a good electrical insulator, with a low optical refractive index, around 1.6 in visible and near-infrared spectral regions [19], that creates a large refractive index difference with the unoxidised material. Similarly as silicon processes that take advantage of silicon native oxide, electrical and optical confinement fonctions in GaAs-based devices, as discussed in the previous section (3.2.1), have become achievable. These confinement properties led to the uptake of this technique for VCSELs, LEDs, waveguides, optical microcavities, as well as for nonlinear optical components. A wide variety of Al-based III-V semiconductors as AlGaAs, AlGaSb, InAlP, InAlSb, InAlAs, AlGaP, or InAlGaP can be oxidised using this process. The basic understanding of the fundamental chemical and physical properties of the AlGaAs alloys wet thermal oxidation, which was encouraged by the strong development of

oxide-confined VCSELs, is summarized in this section. Specific mechanisms of reaction and diffusion of AlGaAs wet thermal oxidation, as well as the associated oxidation conditions and final oxide structure will be described.
The oxidation of AlGaAs occurs when high Al-content AlGaAs is exposed to high temperature, aound 400°C, combined with either O_2, in the dry thermal oxidation, or H_2O vapor, in the wet thermal oxidation. The following chemical reactions approximate the AlGaAs alloy as AlAs. The role of Ga content in the AlGaAs alloy will be explained further in the section.

The dry thermal oxidation, described in equation (3.1), results in a non-porous As oxide, As_2O_3, that limits the oxide progression [20]. Thus, this reaction must be avoided.

$$2AlAs + 3O_2 = Al_2O_3 + As_2O3 \tag{3.1}$$

The wet thermal oxidation is a more complex process described by the following equations [21]:

$$2AlAs + 3H_2O(g) = Al_2O_3 + 2AsH_3 \tag{3.2}$$

$$2AlAs + 4H_2O(g) = 2AlO(OH) + 2AsH_3 \tag{3.3}$$

$$2AsH_3 = 2As + 3H_2 \tag{3.4}$$

$$2AsH_3 + 3H_20(g) = As_2O_3(l) + 6H_2 \tag{3.5}$$

$$As_20_3(l) + 3H_2 = 2As + 3H_2O(g) \tag{3.6}$$

$$2AlAs + 3H_20(g) = Al_2O_3 + 2As + 3H_2 \tag{3.7}$$

$$2AlAs + 4H_20(g) = 2AlO(OH) + 2As + 3H_2 \tag{3.8}$$

Equations (3.7) and (3.8) show the formation of elemental As, which is the main difference with dry oxidation. It comes from the production of AsH_3 during the Al oxidation (equations (3.2) and (3.3)), which can dissociates either in elemental As (equations (3.4)) or in As oxide As_2O_3 (equations (3.5)). This oxide can itself reduce in elemental As (equations (3.6)). This is the balance between As oxide and elemental As production that controls the oxidation rate. The more elemental As is produced, the higher is the oxidation rate. This is caused by its easy volatility and removal, that results in a porous oxide enhancing the transport of reactants and products. For this reason, the oxide can progress up to several tens of microns in the case of wet oxidation, whereas the dry oxidation progression is limited to hundreds of nanometers. At last, this explains why the final oxide has been found as porous, skrinked, and relatively As-free [21].

The oxide front progression versus time, as described in figures 3.2 and 3.3, must be understood to guarantee a controllable process. It relies on two phenomena: the diffusion of water vapor through the oxide to reach the oxide/AlGaAs interface, and the oxidation reaction at this interface [21]. For the oxidation of a planar surface, the oxide progress versus time is linear when the oxidation is reaction-rate limited, which results in a few nanometers wide dense amorphous oxide/AlGaAs interface mainly composed of AlO_xH_x and As_2O_3. After a certain oxide penetration depth in the structure, the water vapor diffusion slows down, shifting the oxidation to a diffusion-limited regime. In this case, the

oxide front progression versus time tends to a parabolic behavior, while the oxide/AlGaAs interface width increases as the oxide front moves deeper into the layer. Indeed, the lack of hydrogen decreases the reduction rate of As_2O_3 to As, which favours the formation of As_2O_3 relative to As loss. The competition between linear and parabolic regime is well described by the Deal and Grove model [22], which is used to fit the data points in figure 3.3. This model has been developed for silicon wet thermal oxidation, and must be employed only as a predictive tool in the case of AlGaAs. Just like the oxide penetration length, the rise of the temperature is known to favour the formation of As_20_3 versus its reduction to As, which slows down the diffusion of water vapor and shifts the oxidation rate toward parabolic behavior [23], as seen in figure 3.3.

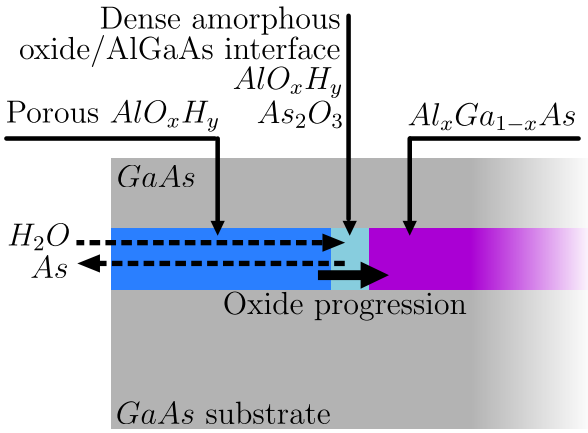

Figure 3.2: Schematic of AlGaAs wet thermal oxidation reaction.

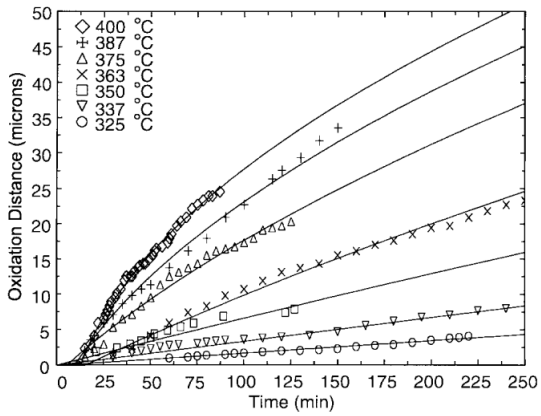

Figure 3.3: AlAs oxide penetration depth as a function of time for various temperatures at a pressure of 5 torr. Taken from [3].

Typical oxidation conditions of $Al_{0.98}Ga_{0.02}As$ layer at 440°C during 30 minutes approximates linear oxide front progression over time. The insertion of the Ga content into the AlAs alloy impacts deeply the oxidation rate, as well as the final oxide structure [24, 21]. Figure 3.4 illustrates the oxidation rate decrease when $Al_xGa_{1-x}As$ alloy Ga mole fraction increases. This slower oxidation rate favours the loss of As, which guarantees the porosity of the oxide, therefore the good transport of reactants and products. Thus, the linearity of the AlGaAs oxide progression over time is observed for higher temperatures and longer process time than in the case of AlAs. Typically, an initial oxidation rate below 0.2 µm/min allows a stable linear regime at long process time, while a parabolic behavior

is predominant when the the rate exceeds 1.3 µm/min [21]. The strong dependance of the oxidation rate of the Ga content requires either a high accuracy of the to-be-oxidized layer composition during the VCSEL epitaxy, the use of an oxidation calibration run, or the use of a monitoring system to get devices of reproducible aperture dimensions.

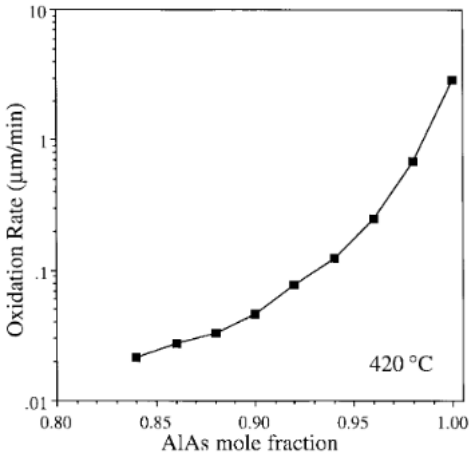

Figure 3.4: $Al_xGa_{1-x}As$ oxidation rate as a function of $AlAs$ mole fraction. Taken from [24].

The thickness of AlGaAs layer also impacts the oxidation rate, as presented in figure 3.5. The thicker is the layer, the easier is the diffusive transport of reactants and oxidation products. For AlAs, the influence of the thickness becomes negligible for values above 80 nm [24].

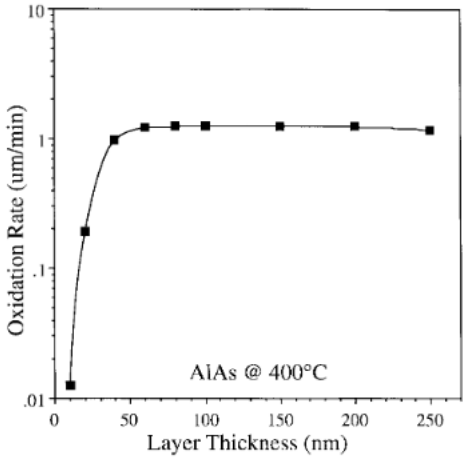

Figure 3.5: $AlAs$ oxidation rate as a function of layer thickness. Taken from [24].

The oxidation rate of the lower Al-content material can be enhanced when two layers of AlGaAs with different Al contents are placed close together [25]. This proximity enhancement effect is a phenomenon that gets weaker the further apart two materials are, as illustrated in figure 3.6. In this case, an inter-layer vertical diffusion completes the standard lateral diffusion. This vertical diffusion is made even more effective by the strain that exists in neighboring layers of a being-oxidized layer. Practically, taking into account this phenomenon is essential for managing the tapered-oxide profile used to optimize the performance of oxide-confined VCSELs. Figure 3.6 shows an oxide aperture with a relatively sharp tip profile, achieved with only three AlGaAs layers exploiting this effect.

Another important parameter to consider when describing the oxidation rate is the

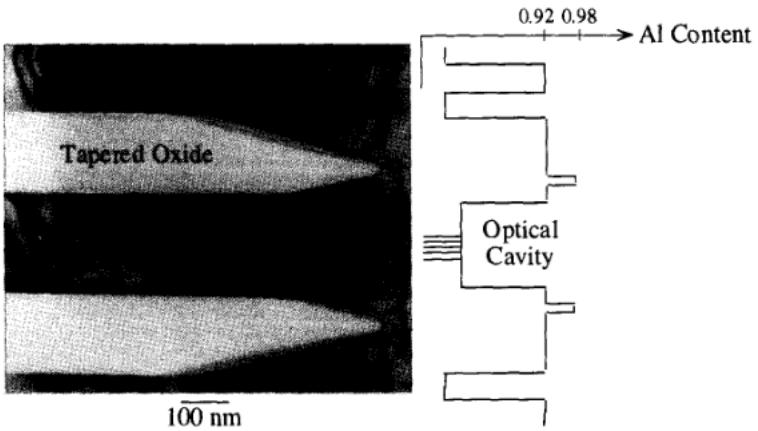

Figure 3.6: "Cross section TEM image of two tapered oxides (adjacent to optical cavity) produced from 14 nm thick $Al_{0.98}Ga_{0.02}As$ embedded within a 160 nm thick $Al_{0.92}Ga_{0.08}As$ layer". Taken from [26].

crystalline nature of the AlGaAs layer which is responsible for oxidation rate anisotropy [27, 28], as mentioned in section 3.2.1.

Finally, the shape of the mesa impacts the oxide progression. This result is presented in [29], where the progression of the oxide front as a function of the mesa diameter r is found to be proportional to $1/r^2$. Thus, in the case of oxide-confined VCSELs, which are typically circular, an acceleration of the oxide progression occurs near the aperture closure.

In terms of structural properties, the oxide resulting from AlGaAs oxidation is known to be mechanically more robust compared to the AlAs oxide, since the layer shrinkage observed after oxidation is approximately two times less, respectively by 6.7% for AlGaAs and 13% for AlAs [24].

In conclusion, the principles and important parameters of AlGaAs wet thermal oxidation have been described in order to understand the phenomena that could be relevant for the process monitoring, including optical imaging, which is the focus of this work. The demand for high accuracy and reproducibility for oxide aperture diameter in VCSEL production is a challenge given the number of factors that strongly impact the oxidation rate and their own repeatability limitations. These factors can be linked to the process conditions as the temperature and water vapor pressure, or come from the material preparation like the AlAs mole fraction and its uniformity on the wafer, the AlGaAs layer thickness, or the proximity enhancement effect. In addition, AlGaAs wet thermal oxidation process generally cannot be restarted because of changes in the chemical or structural nature of the oxide/AlGaAs interface [20]. Costly repetitive calibrations are required to reach the high level of accuracy and reproducibility when the process is not monitored in-situ in real-time.

3.3 The control of wet thermal oxidation process

3.3.1 Oxidation furnace general principle

Wet thermal oxidation for Al-based III-V alloys is typically performed using an inert gas source, a moisture-generating source injecting in a furnace, as described in figure 3.7 [20].

The water vapor is carried by an inert gaz flow. Then, the gas mixture is injected to

Figure 3.7: Schematic of basic wet thermal oxidation system.

the heated furnace. A pressure controller regulates the furnace pressure while mass flow controllers manage the gas flows. The equilibrium vapor pressure of water in the flowing gas, which determines the water concentration in contact with the sample, depends on the water temperature. For this reason, the injector must operate in stable conditions during the process to guarantee the uniformity of the formed oxide characteristics. The used inert gaz can be either N_2, H_2N_2, or Ar, as long as it doesn't introduce O_2 to prevent dry oxidation reaction that would reduce the oxidation chemical selectivity [30] or even stop the oxide in-depth progression, as discussed in section 3.2.2. The uniformity of the temperature and the gas flow inside the furnace are required to achieve wafer-scale uniformity since the process is very sensitive to these parameters, as shown in figure 3.3 for the temperature. To end the process and limit the oxidation inertia, the wet gas is substituted for the dry one.

Commercial wet thermal oxidation furnace can be horizontal (tubular) for multi-wafer oxidation with high temperature uniformity, or vertical (chamber) where in-situ monitoring solutions can be more easily implemented, at the cost of a smaller production scale and temperature uniformity [2]. These suppliers are Aloxtec (France), Koyo Thermos Systems (Japan), and CSL (USA).

3.3.2 Oxide layer optical detection in VCSEL structures

The optical monitoring of AlGaAs oxide progression during the wet thermal oxidation process is made possible thanks to the high refractive index contrast between the AlGaAs and its AlOx. Typically, the refractive index at 300K of a to-be-oxidised $Al_{0.98}Ga_{0.02}As$ material is approximately 3 [31] while it is 1.6 for its oxide, giving a strong refractive index difference of 1.4. This results in a significant difference in the reflectivity spectrum of the two materials. However, oxide-confined VCSEL structure challenges the oxide optical observation, for several reasons that are discussed in this section.

In these specific VCSEL structures, the 30-nm-thick AlGaAs layer is buried under the 2 to 3-µm-thick top distributed Bragg mirror, as shown in figure 3.8. Figures 3.9, 3.10, 3.11 show the reflectivity spectra of the oxidised and unoxidised areas, simulated from, respectively, a 850 nm, a 940 nm, and a 1300 nm VCSEL structure, at 25 and 400°C. These figures also show the difference of spectral distribution of contrast between the reflectivity spectra at 25 and 400°C. The reflectivity spectra from oxidized and unoxidized areas contain a highly reflecting spectral region, called "stop band", spread over several tens of nanometer around the VCSEL emission wavelength, surrounded by damped reflectivity oscillations. The spectral distribution of contrast, defined as the difference between the reflectivity spectrum of the oxidized and the unoxidized area, oscillates between positive and negative values. Because positive and negative contrasts would partially cancel each other in case of broadband illumination, only narrow spectral windows should be used. Thus, large available spectral range and high spectral resolution are required be able to target the spectral regions giving the best contrast, which depend on the VCSEL stack design. Also, one can clearly see that the highest differences in reflectivity are found at the edges of the stop band.

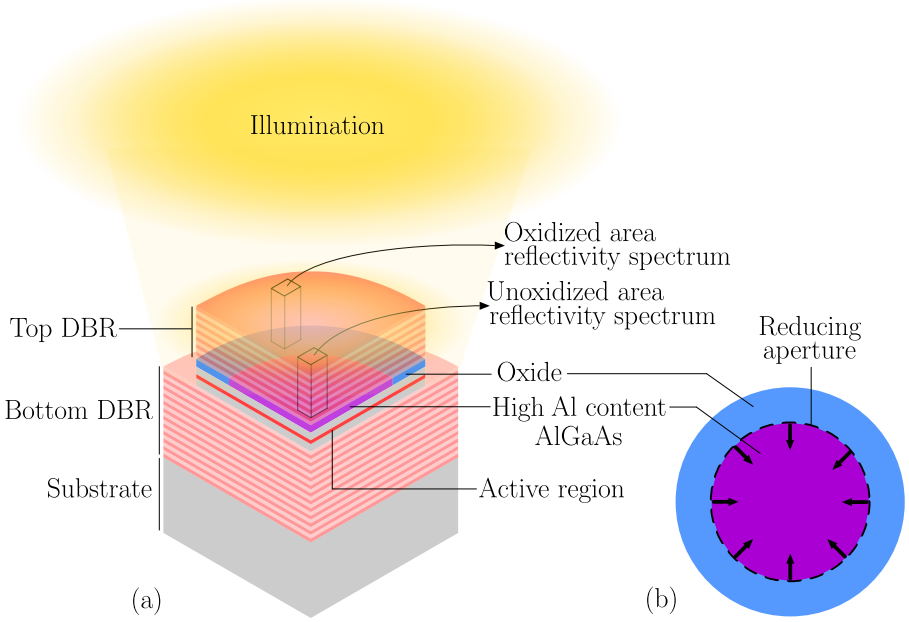

Figure 3.8: Schematic of optical reflectometry principle over a (a) VCSEL cross-section, and (b) VCSEL top view.

In addition, these figures show that this contrast is redshifted at high temperature, while the contrast in the visible spectral range is strongly reduced due to the redshifted absorption edge of $Al_xGa_{1-x}As$. Typically, a 850 nm VCSEL top distributed Bragg mirror is composed of around 20 periods of $Al_{0.15}Ga_{0.85}As/Al_{0.85}Ga_{0.15}As$ quarter-wave layers. Figure 3.12 presents the bandgap wavelength as a function of aluminium content in the $Al_xGa_{1-x}As$ layer at 25 and 400°C. It shows that $Al_{0.15}Ga_{0.85}As$ absorbs below 760 nm at 25°C and 870 nm at 400°C, while $Al_{0.85}Ga_{0.15}As$ does so below 590 nm at 25°C and 640 nm at 400°C. At the temperature required for the oxidation process, typically 400°C, the real and imaginary parts of the $Al_xGa_{1-x}As$ complex refractive index are redshifted. This explains the redshift of the VCSEL stack reflectivity and absorption spectra. The edge of the DBR absorption spectrum is different between 850 nm, 940 nm, and 1300 nm VCSEL, since the low and high refractive index DBR materials are not the same.

While the optical monitoring of the buried oxide layer is challenging in the visible spectral range in the oxidation process temperature condition, and prevented in the stop band, near-infrared and longer wavelengths appear advantageous. This statement will be discussed in section 3.3.4.

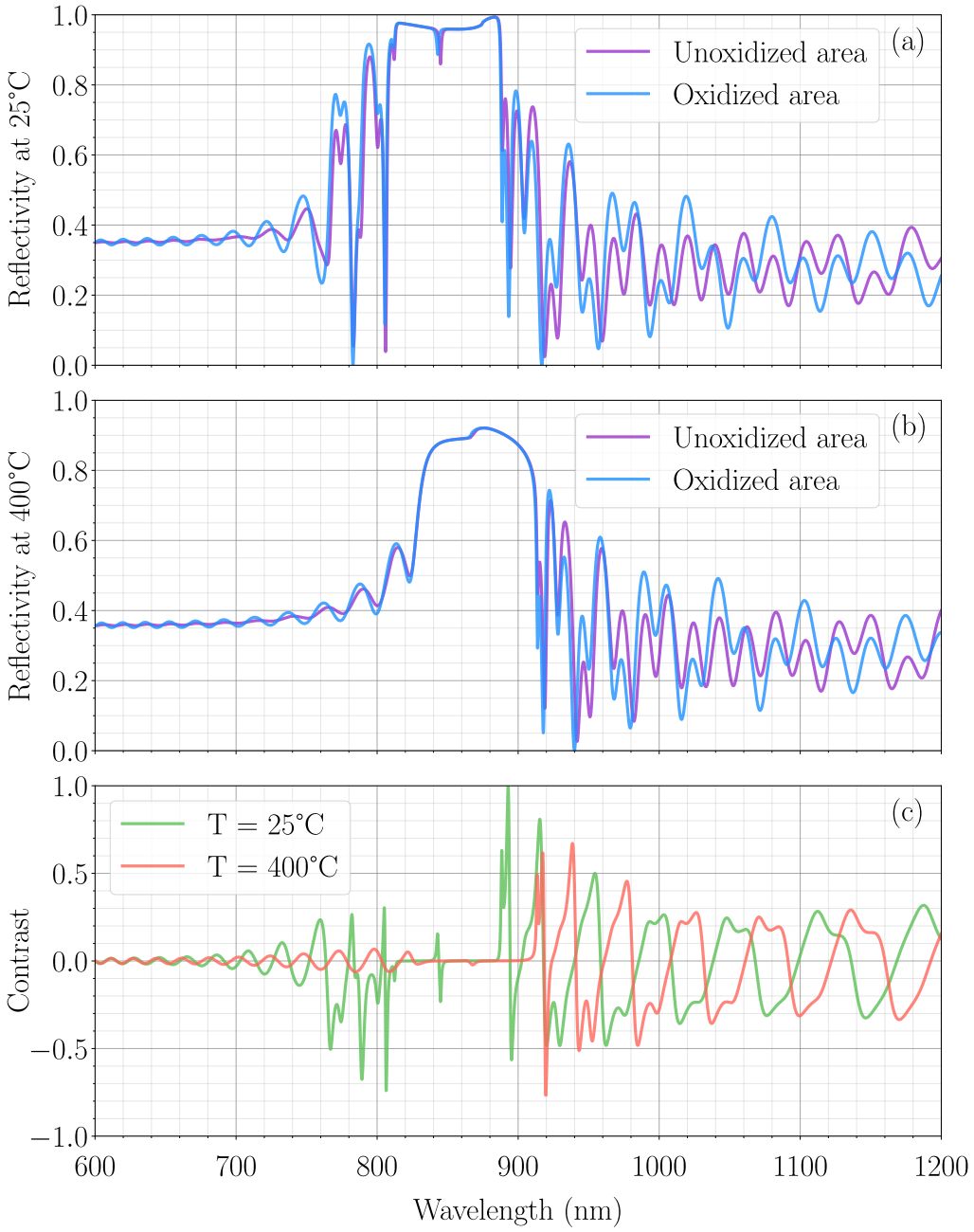

Figure 3.9: Unoxidized and oxidized areas simulated top reflectivity spectra for a 850 nm VCSEL at (a) 25°C, (b) 400°C, and (c) the associated spectral distribution of contrast at 25°C and 400°C.

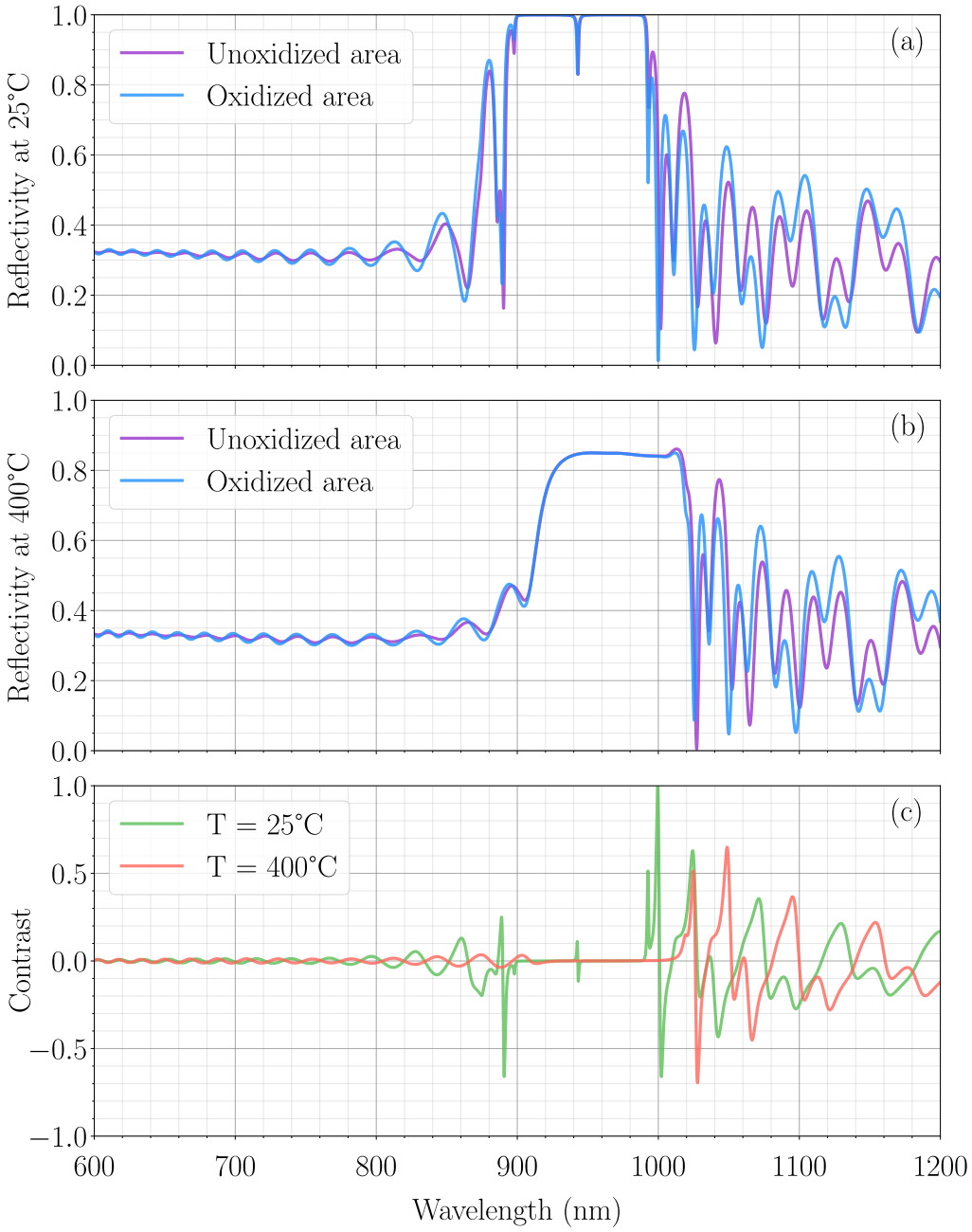

Figure 3.10: Unoxidized and oxidized areas simulated top reflectivity spectra for a 940 nm VCSEL at (a) 25°C, (b) 400°C, and (c) the associated spectral distribution of contrast at 25°C and 400°C.

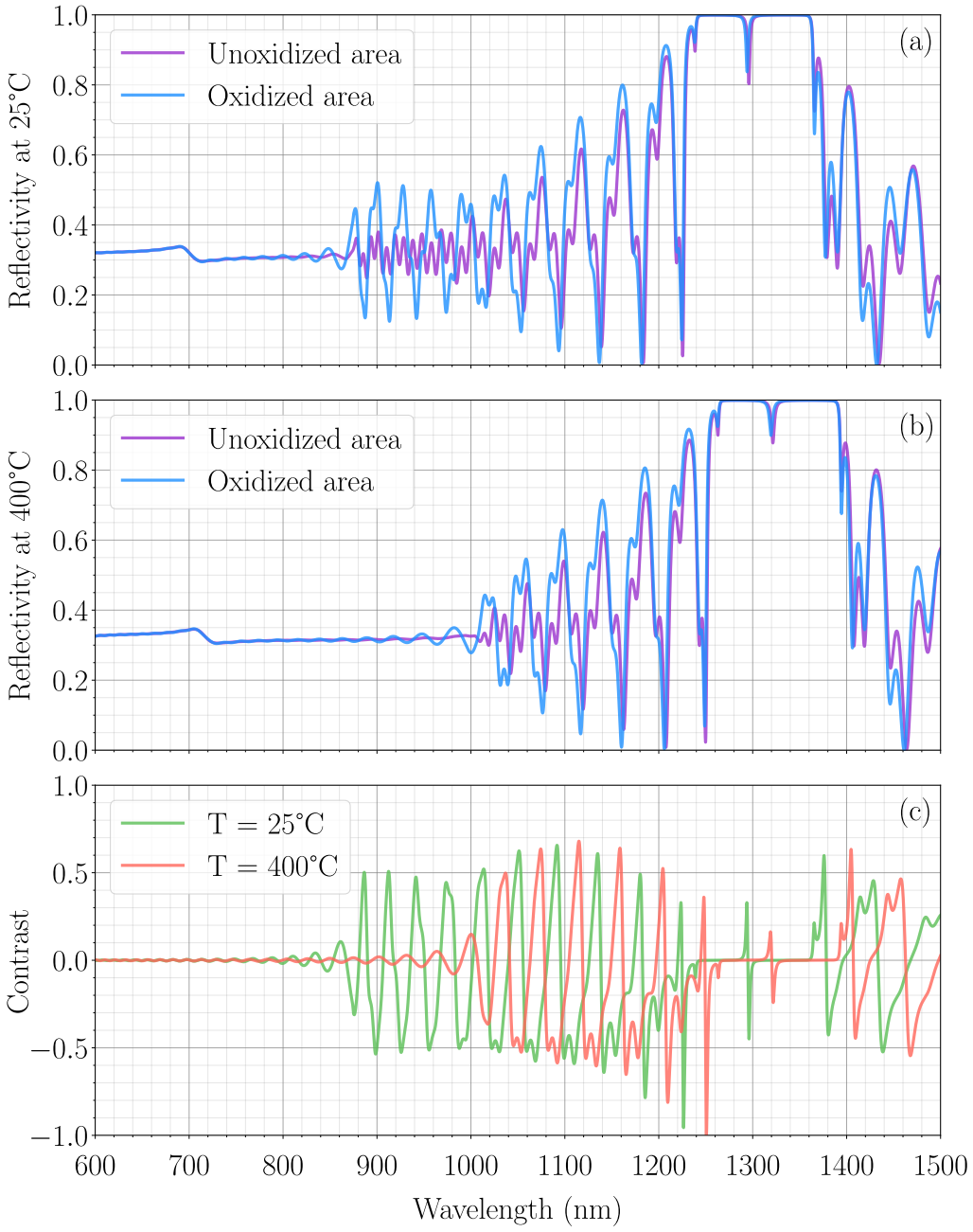

Figure 3.11: Unoxidized and oxidized areas simulated top reflectivity spectra for a 1300 nm VCSEL (GaAs/$Al_{0.9}Ga_{0.1}As$ DBR) at (a) 25°C, (b) 400°C, and (c) the associated spectral distribution of contrast at 25°C and 400°C.

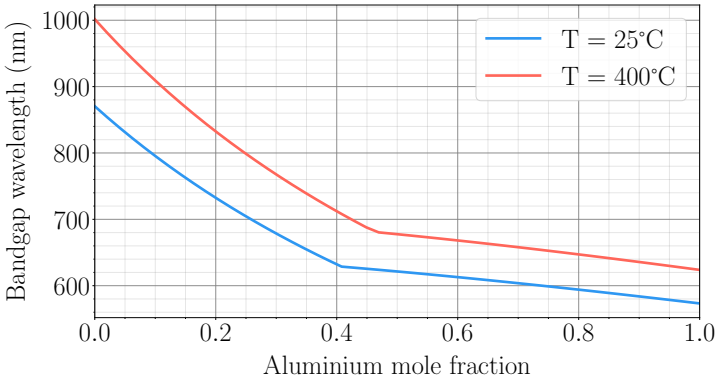

Figure 3.12: Bandgap wavelength as a function of aluminium mole fraction in $Al_xGa_{1-x}As$ layer at 25 and 400°C.

3.3.3 Optical in-situ monitoring systems

For the control of the wet thermal oxidation process, a number of optical in-situ monitoring systems have been developed and fitted to tube or chamber furnaces. This section focuses on those systems, to establish the state of art and discuss new perspectives.

An optical probing system for large-scale production tube furnace has been reported in [4] in 2002. This technique, called OPTALO (Optical Probing Technique of AlAs Lateral Oxidation), doesn't require the use of a microscope, which makes it suitable for monitoring under atmospheric pressure ambient. In fact, using a microscope at this pressure would require to install a glass window in the furnace where water vapor could condense. The change in reflectivity between the unoxidised and the oxidised zones is exploited by measuring the averaged reflectivity of a being-oxidised large pattern area over time. As presented in figure 3.13, an halogen lamp illuminates the wafer via an optical fiber, while another optical fiber, placed several millimeters or centimeters from the wafer, collects the reflected signal. A spectrometer analyses the signal between 700 and 950 nm. Since VCSEL aperture oxidation requires the etching of a mesa, the oxide area to unoxide area ratio versus time is parabolic, while it is linear in the case of stripe structures. Whether it is linear or parabolic, the oxide area coverage is directly linked to the averaged reflectivity versus time curve. This technique requires a calibration step in order to know the relation between the averaged reflectivity level of signal and oxide penetration depth. Once this relation is known, a specific oxidation depth can be targeted based on the real-time optical probing. The accuracy of this technique is adequate for the fabrication of large-aperture multi-mode VCSELs, but is insufficient for the production of small-aperture single-mode VCSELs, since signal variation decreases for low aperture sizes, as described by the parabolic behavior.

Real-time in-situ monitoring systems have also been developed for horizontal furnace, as reported in [3] and [5]. Both systems rely on the chamber with an integrated window, which allows for the use of an optical system from the outside. Low pressure ambient, in the 2-500mbar range [27], is required to prevent the water vapor from condensing on the cold window.

The first study of such a system has been reported in 1998 [3]. Figure 3.14 illustrates the experimental setup. This study relates the widefield microscopy in-situ real-time monitoring of being-oxidized distributed Bragg reflector structures composed of alternating

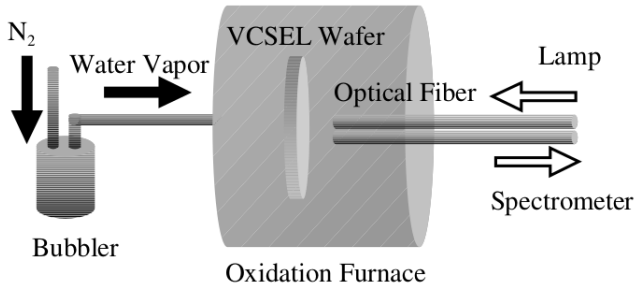

Figure 3.13: Schematic of the OPTALO system implemented in wet thermal oxidation tube furnace. Taken from [4].

GaAs and AlAs layers. Near-infrared light with a cutoff wavelength of 750 nm is obtained using long-pass filter and is used to illuminate the sample through the viewport. The reflected signal is collected by the long working distance objective and measured with a silicon CCD camera, with a spatial resolution of approximately 1 µm. The significant contrast between each zone at 325°C makes it easy to detect the difference between low refractive index oxidized and high refractive index unoxidized areas. This study enlights the efficient use of near-infrared microscopy for wet thermal oxidation in-situ real-time monitoring of a relatively simple structure. The oxide reflectivity spectrum in this structure differs significantly from the AlGaAs spectrum, as presented in figure 3.15. This is not the case for a VCSEL stack, where the reflectivity spectrum of the two areas are close, as explained in section 3.3.2, which leads to a lower contrast. While the exploitable information for the visualization of the oxide layer in a VCSEL stack is strongly reduced, the use of a broadband near-infrared illumination spectrum is not sufficient anymore to detect the oxide front. Indeed, it would average the alternating positive and negative contrasts of a typical contrast spectral distribution which would result in contrast cancelation, as explained in section 3.3.2.

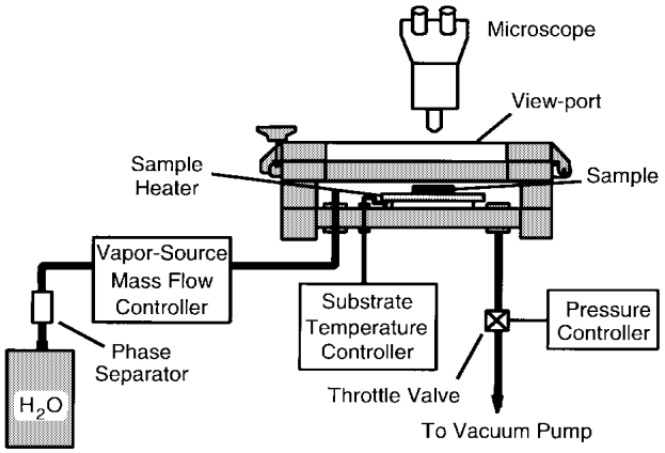

Figure 3.14: Schematic of the experimental setup reported in [3].

The challenging real-time optical monitoring of the oxide progression in VCSEL structures has been made easier by the development of a more spectrally-selective widefield microscopy system reported in 2008 [5] by the photonics group of LAAS-CNRS laboratory. It introduces the use of a monochromator to filter a few nanometer wide spectral band from a white light source. A near-infrared sensitive camera acquires the signal collected by the long working distance microscope. As a first step, the reflectance spectrum of the

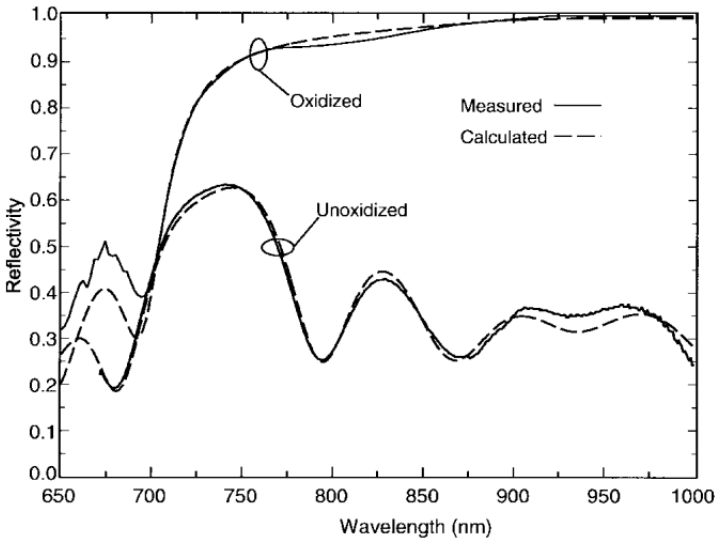

Figure 3.15: Measured and calculated reflectivity spectra of oxidized and unoxidized regions of the distributed Bragg reflector reported in [3].

oxidized and unoxidized materials are measured by scanning the illumination wavelength with the monochromator, and measuring the signal at each iteration on the camera. Then, from this knowledge, the narrow spectral band that gives the best contrast is chosen for the monitoring. This study focuses on the high-magnification observation of a 850 nm VCSEL sample composed of a to-be-oxidized $Al_{0.98}Ga_{0.02}As$ layer buried under a 26-period distributed Bragg reflector. A good discernability of the two areas was observed for an oxidizing sample heated to 420°C and illuminated with this specific spectral band. This flexible technique doesn't require any calibration step, and ensure reproducible fabrication of optimized oxide aperture size of single-mode VCSELs, regardless of its emission wavelength. An upgraded version of the system is presented in figure 3.16, and used in [27]. It enables 5 nm wide spectral band illumination for improved contrast but lower amount of collected signal, automated VCSEL oxide aperture edge detection via image numerical processing, as well as wafer-scale monitoring via a XYZ stage holding the microscope. The spatial resolution has been estimated below 1 µm. This system is the basis of the optical monitoring development described in this chapter, which add to the photonics group process monitoring knowledge some computer vision concepts developed by the robotics group.

The approach of narrow-spectral-band illumination for enhanced discernability between oxidised and unoxidised areas has been pushed forward in 2013 [32]. This method relies on the use of a Nd:YAG laser source emitting at 1064 nm with a typical full width at half maximum (FWHM) that can be estimated around 0.2 nm [33]. Previously discussed widefield microscopy technique is replaced by laser scanning microscopy, where a sharply focused diffraction-limited laser beam spatially scans the sample surface over the targeted field of view. The visualization of a being-oxidised thin AlAs layer embedded between two distributed Bragg mirrors has been demonstrated, using a long working distance objective and a CCD camera. The laser wavelength was chosen to be on the long-wavelength side of the distributed Bragg mirror stopband to avoid its absorption in the visible spectral range. This sample, close to a VCSEL structure, could be monitored during its 420°C oxidation with good contrast between the AlAs material and its oxide, but with a relatively low frame rate as the laser scanning takes 90 seconds to complete an image. Compared to the technique employing widefield microscopy with a monochromator, the ability to perform

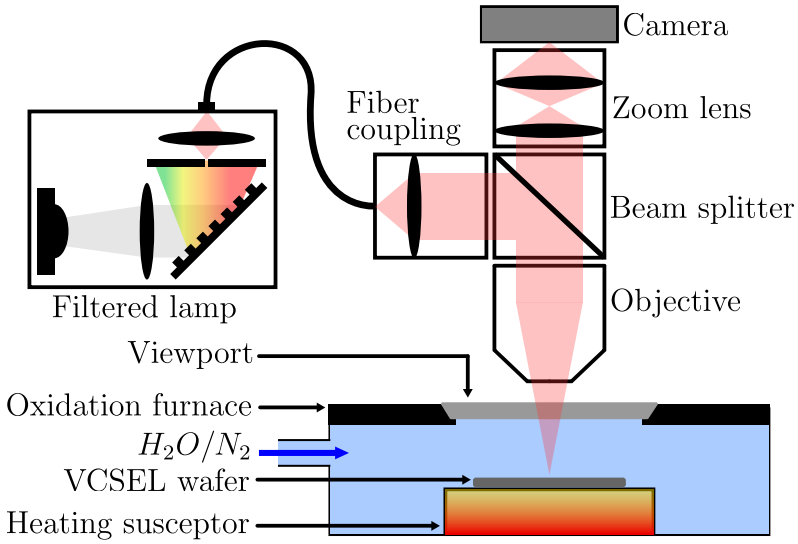

Figure 3.16: Upgraded wet thermal oxidation system with in-situ monitoring based on the work reported in [5].

real-time monitoring as well as the illumination spectrum adaptation to a specific sample are lost.

3.3.4 Perspectives

From large-scale production tube furnaces without in-situ monitoring, to spectrally-selective optical microscopy systems implemented on chamber furnaces, solutions have been found to improve the control of the III-V semiconductors wet thermal oxidation process. The demand of reproducibility in the fabrication of more and more complex device structures, mainly represented by oxide-confined VCSELs that have been spread in a wide variety of technologies, encouraged this development. The state of art shows that real-time monitoring of VCSEL aperture oxidation has been facilitated by the integration of a microscope on a chamber furnace, combined with a suitable illumination spectrum. The illumination narrow spectral band that can be employed to achieve the best contrast is determined by the calculation of the contrast spectral distribution, which is based on the difference between the reflectivity spectra of AlGaAs and its oxide.

Highly reflecting distributed Bragg mirror stopband forbids any measurable signal of the buried oxide layer in this spectral region, while the best contrast wavelengths are generally found at the side lobes of the stopband, either in short or long-wavelength side. $Al_xGa_{1-x}As$-based distributed Bragg mirror absorbs a fraction of the visible light, that increases at high temperature, which strongly attenuates the contrast over the whole visible spectral region as shown in [5]. For this reason, the use of the short-wave infrared (SWIR) spectral region, defined from 900 to 1700 nm, seems advantageous. Unfortunately, silicon CCD or CMOS camera sensor quantum efficiency is usually less than 10% for wavelengths longer than 1000 nm and quickly falls to zero after that. In addition, with regard to the strong impact of aperture diameter on VCSEL performances, the spatial resolution of the imaging system is important to limit aperture detection incertainty. InGaAs SWIR sensors are not enough spatially resolved yet, with pixel size at least 3 times larger than for CMOS sensors. SWIR CMOS sensor technology is currently emerging in the market, from companies like Sony or TriEye with its "raven" sensor, and might offer a solution in the near futur.

The poor exploitable information in the reflectivity spectra of AlGaAs and its oxide

in the visible range at high temperature, and the to-date impossible combination of high sensitivity and high spatial resolution in the SWIR spectral range, make the optical wet thermal oxidation real-time monitoring difficult for some complex VCSEL structures. The lack of sensitivity of a silicon sensor in the 900-1100 nm wavelength range can be overcome by a powerful source in that range, like a tunable or a supercontinuum laser. However, another way of improving the monitoring can be drawn out based on the following observation: when the illumination narrow spectral band giving the best contrast is chosen, the rest of the information contained in the reflectivity spectra remains unexploited. Typically, the weak but existing level of contrast in the visible spectral window seems underexploited, while sticking to this range would minimize the diffraction limit and make the choice of optical components easier. This statement opens the way to the optimization of the sample image spectral content, based on the selection of the useful information contained in the reflectivity spectrum of AlGaAs unoxidized area and of the oxidized area.

3.4 Interest and implementation of pylochromatic illumination for optical monitoring

3.4.1 Hyperspectral imaging and wet thermal oxidation monitoring

The idea of sample image spectral content optimization to improve optical monitoring, based on the assessment of spectral information usefulness considering the criterion of discernability between two different materials in the same field of view, refers to a both spectrally and spatially-resolved imaging technique known as hyperspectral imaging. A general overview of this technology and its interest in the context of AlGaAs wet thermal in-situ real-time monitoring, as well as the choice of an imaging system based on a spectrally-shaped illumination source, are presented in this section.

3.4.1.1 General principle of hyperspectral imaging

Spectral imaging is a general name for all kind of optical imaging systems which, in addition to the acquisition of the two-dimentionnal spatial information of a scene, gives access to one-dimentionnal spectral information of each spatial element. The amount of spectral information defines two main categories of spectral imaging: multispectral imaging when the number of acquired spectral bands is low with regard to the whole spectral range, and hyperspectral imaging when this number is typically higher than 30. In this case, advanced spectroscopy techniques enable measurement in UV, visible, and SWIR spectral regions. Once acquired, the hyperspectral image, commonly called "hyperspectral cube", stores spatial information in the first 2 dimensions, and spectra along the third one, as shown in figure 3.17.
The large quantity of data makes this technique very attractive and powerful for computer vision applications, where classification of elements from a scene is aimed, but challenging in terms of data acquisition and fast processing. Earth observation, that uses multispectral imaging since late 1960s, takes now advantage of hyperspectral imaging [35, 36], just like biology [37, 38], pharmaceutics [39, 40], defence and security [41], archeology and art conservation [42], food quality assessment [43], semiconductor material [44, 45] and device metrology [46, 47, 48].
The field of 3D data encoding using a 2D imaging sensor has given birth to various techniques that have different performances in terms of spatial and spectral resolution, spectral range, acquisition time, processing time and energy consumption, optical system complexity, measurement noise, or amount and types of errors in the data. Figure 3.18 presents

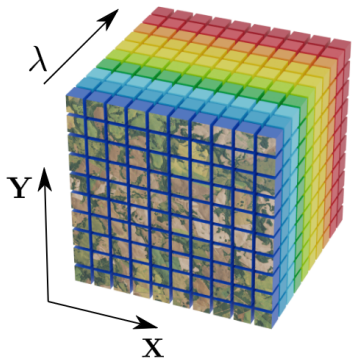

Figure 3.17: Schematic of an "hyperspectral cube", where each location on the scene has its measured spectrum stored along the λ direction. Taken from [34].

5 approaches that were developed to acquire the hyperspectral cube: point-scanning (or whiskbroom) and line-scanning (or pushbroom) that refer to a spatial scan of the scene, spectral scanning, spatio-spectral scanning, and snapshot imaging that eliminates the need of a scan. While point-scanning uses a 1D detector array that measures the spectrum of

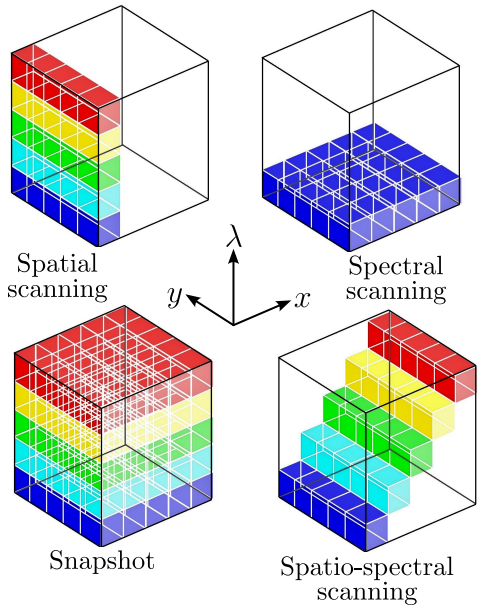

Figure 3.18: Schematics of hyperspectral cube acquisition techniques. Taken from [49].

each individual spatial point one after the other, line-scanning takes advantage of a 2D sensor to spread the spectra of one spatial line over the second dimension of the sensor. In spectral scanning, images of the scene are sequentially taken at each targeted spectral band. Both spatial and spectral scanning is realized using a linear gradient spectral filter that is translated along the gradient direction in front of a 2D detector. Finally, snapshot imaging employs compressed sensing techniques to acquire the minimum amount of data needed for the numerical reconstruction of the hyperspectral cube.

3.4.1.2 Context of the wet thermal oxidation monitoring

In the case of the wet thermal oxidation polychromatic monitoring, the hyperspectral cube acquisition represents a first step that enables to access to the scene spectral information.

As previously discussed, several methods can be employed in this aim. A second step can be described as the real-time production of a spectrally-selective image based on the usefulness assessment of the spectral bands considering a given criterion. It could be done once the cube acquired, by summing it up with an adequate ponderation of each spectral band, or by spectral filtering of the light reaching the detector or filtering the light illuminating the sample. Real-time imaging using the cube weighted sum solution would be possible with a commercial snapshot hyperspectral camera, but this approach is too limited in terms of spectral resolution, spectral range, and spectral flexibility for this application. On the other side, spectral filtering can reach high spectral resolution over UV, visible, NIR, and SWIR spectral regions, thanks to spatial light modulators (SLM) like nematic liquid crystal (LC) or digital micromirror device (DMD), on which the intensity of the spread spectral components from a light source can be finely modulated. Spectral filtering of the illumination is prefered to the before-detector approach, as the manipulation of the sample image would introduce artifacts in the final image. Hence, this work relates the development of such a spectrally-shaped source and its implementation on an imaging system for wet thermal oxidation monitoring. It will be used for both hyperspectral cube acquisition by wavelength scanning, and illumination spectrum shaping for improved oxide discernability.

3.4.2 Spectrally-shaped source development

3.4.2.1 Technological context

The ability to arbitrarily tailor the illumination spectrum of a given scene with high spectral resolution paved the way to the development of new optical imaging and characterization techniques based on spectral optimization. Fluorescence imaging is one obvious example of strong improvement based on this technology [50, 51], but more general features like spectral high dynamic range capture and glare removal, or contrast enhancement [52] between several scene components for enhanced image segmentation efficiency has been made possible. In addition, new standard spectra, closer to the realistic to-be-measured ones, have been established to test, calibrate, and characterize optical instruments [53]. Material and optical device characterization has also been largely impacted, including for example surface roughness mesurements [47], or solar cells illumination with simulated solar spectrum [54].
In the wide variety of applications, the global architecture of this type of highly resolved spectrally-shaped source remains approximately the same, and was first presented in [51, 53, 55, 56]. It is composed by a broadband light source, an optical element that spatially disperses the spectral bands along one direction, and a third element, called spatial light modulator (SLM), which modulates each band at the desired intensity. In order to cover visible, NIR, and SWIR spectral regions, cheap incoherent filament lamps like tungsten-halogen bulbs can be chosen. However, the more expensive but powerful and spectrally broadened pulsed laser source, called supercontinuum laser, is the most attractive solution. For the spectral dispersion, prism or grating can be employed. A simple prism offers a broad spectral range at the cost of a nonlinear spectral dispersion, while common diffraction gratings have more restricted spectral range, but give compacity and linear and generally stronger spectral dispersion. Finally, grayscale amplitude modulation can be realized using LC-SLM or DMD. The high modulation rate of DMD [57] compared to LC-SLM fits the requirement of fast hyperspectral cube acquisition for real time monitoring in the frame of this work. The development of a spectrally-shaped source employing a supercontinuum laser source, a grating, and a DMD as spatial light modulator is the focus of the following section.

3.4.2.2 Spectrally-shaped source optical design

The photograph of the spectrally-shaped source (S^3), designed by Elizabeth Hemsley, PDRA in the group, is presented in figure 4.14a together with a simplified diagram showing all the key components in figure 4.14b. The spectrum of a supercontinuum source is dispersed, via a grating, on the DMD. The latter selectively reflects desired wavelength bands into an optical fibre whose output end serves as the illumination source of the in-situ inspection imaging system described in section 3.4.2.3.

This hardware configuration was designed to allow flexibility in terms of spectral range, and can be easily modified, by rotating the grating and changing the edge filters, to match the spectral region of interest of the oxided-confined devices to be monitored. Moreover, for a larger spectral tuning, the hardware configuration could be easily modified, by change of gratings and optics with different coatings.

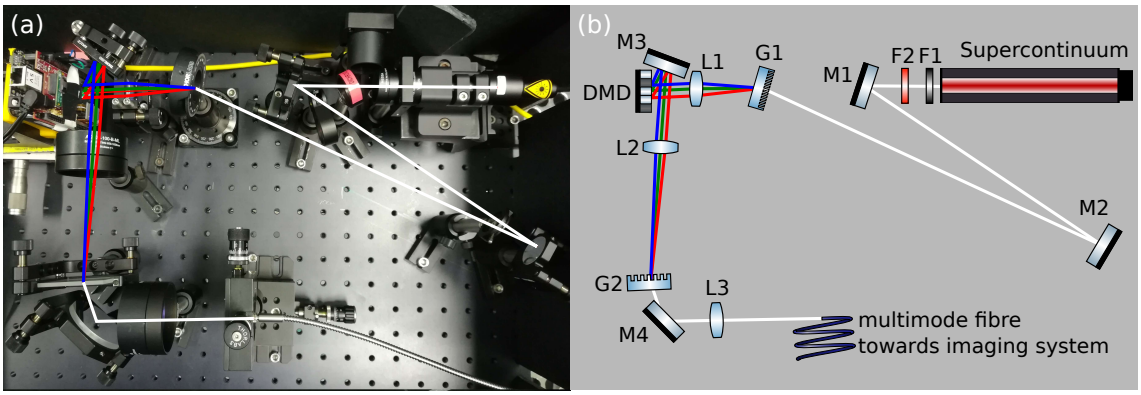

Figure 3.19: Spectrally-Shaped Source: (a) photograph ; (b) schematic. Optical components: F1, F2 filters; M1 to M4 mirrors; G1, G2 gratings; L1 to L3 lenses; DMD digital micromirror device. Taken from [58].

The DMD is a DLPDLCR2000EVM acting as a projector for a System On Chip (SOC) computer (BeagleBone). It consists of an array of 640×360 square mirrors with a 7.6μm pitch for a physical dimension of 4864×2736 μm^2, as shown in figure 3.20. The mirrors are in a square configuration, with a 12-degrees-tilt axis along their diagonal, shown in figure 3.21, so the DMD itself is tilted vertically by 8.73° so the reflected light remains on the horizontal plane of the optical table. The light is spectrally dispersed along the width of the DMD, which enables to use each DMD mirror column as an homogeneous slit that modulates the intensity of its associated spectral band, while the FWHM of this spectral band is defined by the spectral resolution measured in section 3.4.2.5.2. The transmitted intensity per band is modified by adapting the [0-255] gray level of each DMD column using pulse width modulation (PWM). The light transmission as a function of encoded gray level is characterized in section 3.4.2.5.1. Gray level encoding of mirrors is realized by displaying 640×360-pixel 8-bit-grayscale masks on the DMD.

A complementary description and modelling of the optical design can be found in appendix B, which includes information about the laser source, spectral dispersion subsystem, DMD modelling, filtered light collection subsystem, and fiber coupling into the imaging system.

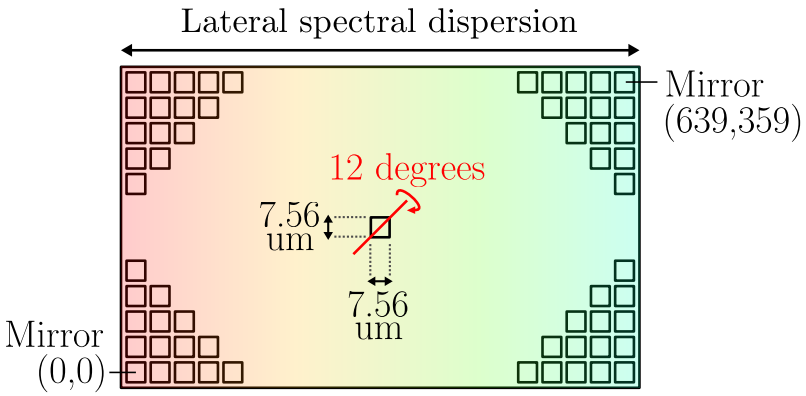

Figure 3.20: DMD schematic front view.

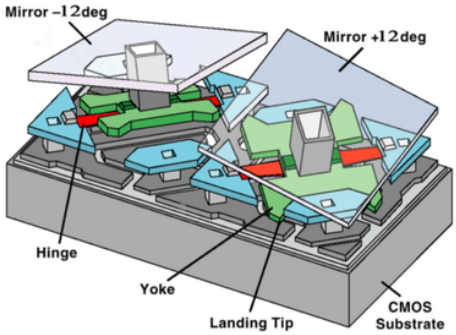

Figure 3.21: Simplified description of the DMD structure [59].

3.4.2.3 Imaging system

The output of the optical fibre is used as the illumination source for the microscope described in figure 3.22. As a result of a quite sensitive coupling distribution over the different fibre modes, a mechanical vibrator (Pasco Scientific, model SF-9324) attached to the fibre can be used to homogenise the spectrum, avoiding spikes that change over time.

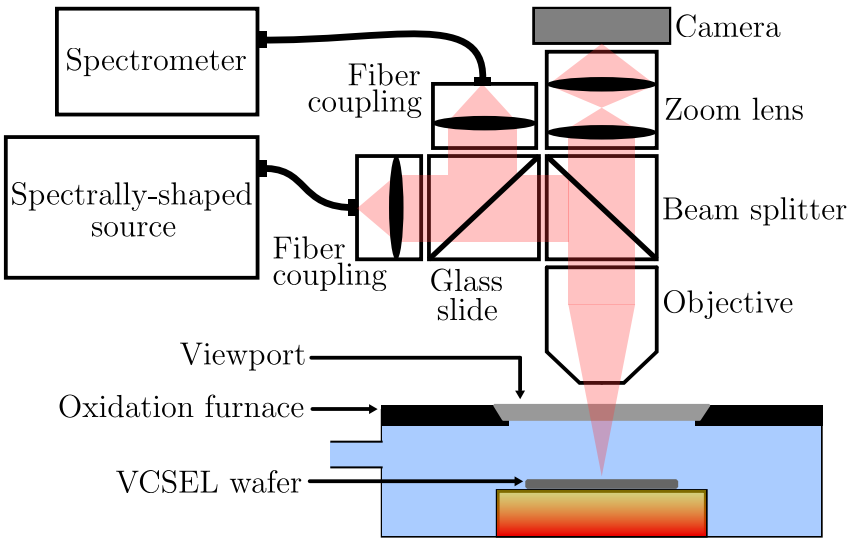

Figure 3.22: Schematic of the imaging system located over the oxidation furnace.

This imaging system is based on a long-working-distance microscopy setup that al-

lows the acquisition of images of the surface of a particular VCSEL device located in the furnace. Practically, a XYZ motorized micro-positioned microscope with a x20 objective (Mitutoyo G Plan APO), a x12 relay lens (Navitar ultra zoom) allows the recording of x17-magnification images using a VIS-NIR CMOS camera (Basler acA2000-165um). In order to measure the illumination spectrum coming from the spectrally-shaped source, and perform the calibrations described in section 3.4.2.5, a glass slide pickup is inserted in the system to send $\simeq 5\%$ of the incoming light to a spectrometer (VIS-NIR Flame Ocean Optics spectrometer).

3.4.2.4 Instrumentation

This instrumentation part relies on the communication between the DMD, the camera, and the spectrometer. This synchronisation between the 3 components is implemented at a software level using a PC as central piece for command management. The PC communicates with the SOC computer by USB over SSH. It uses the Basler python wrapper interface "pypylon" to communicate with the camera, and the "SeaBreeze" python package to control the spectrometer. The communication relies on a semaphore file that informs the SOC computer and the PC of the last action that was completed among the following three: (1) display of a mask on the DMD, (2) acquisition of an image by the camera or (3) the whole acquisition sequence is over.

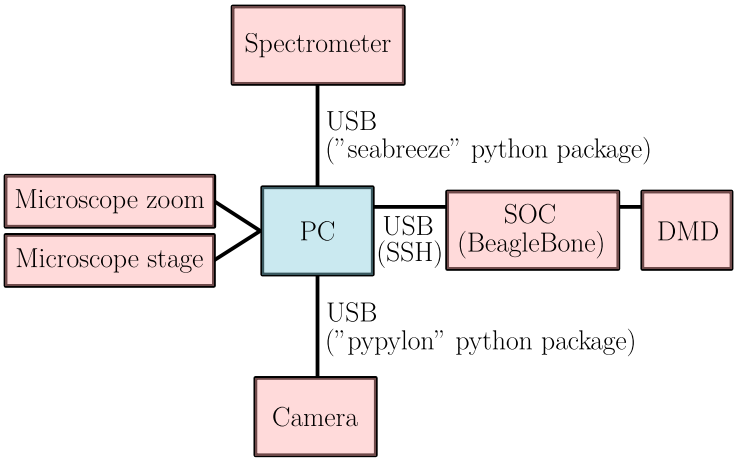

Figure 3.23: Schematic of the communications between PC, DMD, camera, spectrometer, and microscope stage and zoom.

An embedded system oriented synchronisation solution, which uses hardware triggering between DMD and camera is also possible, but wasn't implemented for this work. In this configuration, a voltage is applied to the SOC computer analog output when a mask is being displayed on the DMD, and read by the camera to start the image acquisition. Once the image acquired, the camera applies a voltage to SOC computer analog input port. The spectrometer is also compatible with that kind of communication system. This is an important configuration to consider in order to reach fast hyperspectral cube acquisition and thus real-time monitoring.

3.4.2.5 Spectrally-shaped source characterization

Two prior knowledges are required for the spectral shaping to be performed. The first one is the measurement of the source spectrum when all mirrors are set to gray level value of 255, which corresponds to a fully white mask applied to the DMD. The second one

is the measurement of the light intensity transmitted in the final spectrum by the DMD as a function of the encoded gray level. Because the DMD serves initially as a projector for the SOC computer, it contains internal gamma correction curves, leading to a non-linear relation between gray level and transmitted intensity that need to be taken into account for an accurate control of the transmitted spectrum. These two measurements allow to calculate the right gray level to apply to each mirror column to reach the targeted spectrum.

Two other characterizations can also be performed to complete the knowledge of the source: the measurement of the spectral dispersion on the DMD and the spectral resolution. While these information are not mandatory for the spectral shaping itself, the spectral dispersion is measured in order to show the data associated with its spectral information, and the knowledge of the spectral resolution indicates the ability to reproduce the possible high frequencies contained in the targeted spectra envelop.

All of these 4 calibrations are performed using the spectrometer implemented between the spectrally-shaped source and the imaging system, as seen in figure 3.22.

3.4.2.5.1 Grayscale calibration

In order to calibrate the transmitted intensity as a function of the applied gray level on the mask, one could apply a constant gray level to the whole DMD, measure the resulting spectrum and repeat for each of the 256 accessible gray levels. However, as the calibration is not really dependent on the wavelength, various gray levels for each of the measurements have been displayed to speed up the process by displaying . For this work, 1D calibration masks of the form $G(p) = 255[\sin(2\pi p/p_0)/2 + 1/2]$ have been displayed, with p the index of the column in the DMD and p_0 the pattern period. Then, the spectra resulting from 11 periods ranging from $p_0 \sim 40$ mirrors to $p_0 \sim 440$ mirrors have been recorded. Typical masks are shown in figure 3.24.

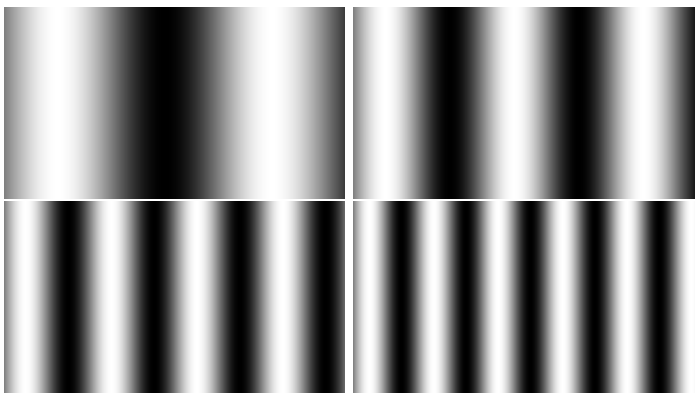

Figure 3.24: Four typical grayscale calibration masks, with varying periodicity p_0. Taken from [58].

Using these masks, many datapoints are measured across the transmitted spectrum to represent the dependence of the transmission on the applied gray level. These datapoints are plotted in figure 3.25 (blue dots). After averaging all the datapoints for each gray level (orange dots), the relationship is found to be nonlinear. An erf(.) function, shown as a gray line in figure 3.25, is then used to fit the latter relationship and used as a simplified intensity coding.

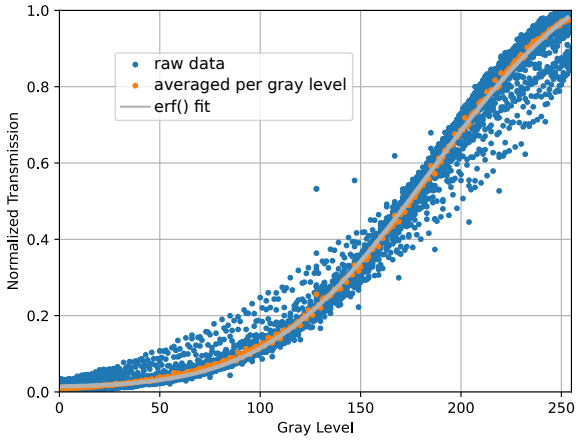

Figure 3.25: Transmission efficiency as a function of the gray level on the DMD: raw transmission efficiency with different sinusoidal pattern applied to the DMD for the same gray level (blue); averaged transmission efficiency at each applied gray level (orange); error function fit of the averaged transmission efficiency (gray). Taken from [58].

3.4.2.5.2 Spectral dispersion and resolution

The spectral resolution and dispersion of the spectrally-shaped source is quantified by applying a black/white Heaviside step function mask across the 640 columns of the DMD, and fitting the measured transmission spectral response by a Gaussian error function (erf(.)). The fitted mean and standard deviation respectively gives the cutoff wavelength and the spectral resolution. The wavelength is swept over the whole accessible spectral range by scanning the step edge across the column number (labelled p). The wavelength dispersion as a function of p is shown in figure 3.26a, while the resolution versus p is represented in figure 3.26b.

The dispersion is seen to be strictly linear with a slope of $\Delta\lambda/\Delta p \simeq -0.24\,\text{nm}$ per DMD column, whereas the resolution is observed to be constant through the DMD columns at $\delta\lambda \simeq 0.89\,\text{nm}$. Given the spatial spreading onto the DMD array, this resolution corresponds to $\simeq 3.7$ mirrors. Rounding up to 4 mirrors per band, the illumination is thus shaped into 160 independent bands over the full spectral range of $640 \times 0.24 \sim 153\,\text{nm}$.

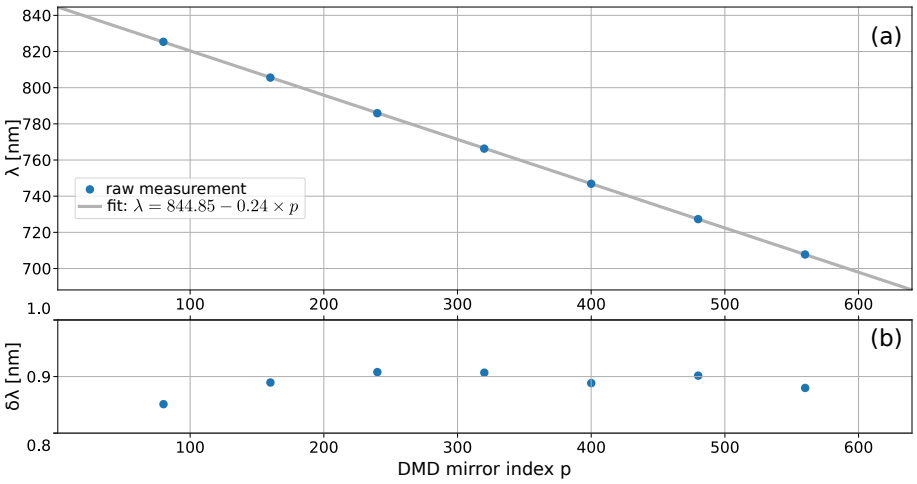

Figure 3.26: Spectral calibration: (a) Wavelength and (b) spectral resolution as a function of the DMD mirror index p. Taken from [58].

3.4.3 Conclusion

From the study of spectral imaging technical solutions, the spectral shaping of the microscope illumination has been chosen as the best candidate to take advantage of the AlGaAs and oxide reflectivity spectra characteristics in order to improve their discernability. It fits the needs of flexibility in terms spectral range and band selection, good spectral resolution, and compatibility with CMOS camera that offers high spatial resolution. Thus, a spectrally-shaped source has been developed to be used for both hyperspectral cube acquisition by wavelength scanning, and spectral shaping of the illumination to improve oxide discernability based on hyperspectral cube information. This source is powerful, and largely attenuated using filters in this work, versatile, and easy to spectrally tune by moving or changing some optical components. It is based on a DMD device where each mirror can be encoded with 256 accessible gray levels, and offers, in the configuration chosen for this work, 160 independant spectral bands over a 153 nm wide spectral range. Its implementation in the context of in-situ static inspection of VCSEL aperture, and its advantage compared to narrow-band illumination are presented in the next section.

3.5 Experimental setup and results

Once the spectrally-shaped source developed and connected to the imaging system placed over the wet thermal oxidation furnace, the next step is to assess its performances in the context of VCSEL aperture detection. In this aim, a comparison between different types of illumination spectra is realized. This section presents the experiment methodology that ensures a fair comparison between these different types of illumination spectra and the results of this comparison, as well as the hyperspectral cube acquisition and the spectral shaping methods. All the measurements reported hereafter were carried for an already-oxidized commercial 850 nm VCSEL sample, with the VCSEL wafer maintained at room temperature and under inert atmosphere. These static conditions, where oxidation doesn't occur, is a first step toward the long-term intention of this work that is to implement an in-situ, real-time monitoring of the lateral oxidation of III-V semiconductor devices. For this reason, the observation setup, the source spectral coverage and the data acquisition and treatments were selected to be compatible with in-situ real-time tracking.

3.5.1 Methodology

The experiment consists in the comparison of three different illumination spectra:

1. The panchromatic illumination: it corresponds to the supercontinuum source spectrum as transmitted by the spectrally-shaped source applying a fully white mask on the DMD.

2. The monochromatic illumination: it corresponds to the method used previously at the laboratory, described in figure 3.16, for which a lamp-source is filtered through a monochromator. The spectrally-shaped source is used to reproduce this narrow band illumination at the wavelength that gives the highest contrast between AlGaAs and oxide.

3. The shaped illumination: it corresponds to the polychromatic illumination that has been tailored based on the assessment of each spectral band usefulness for oxide edge discernability.

The first step of the experiment is to calibrate the source, as described in section 3.4.2.5, to know the transmitted intensity as a function of the applied gray level on the mask, the measurement of the output spectrum for a fully white mask on the DMD, the spectral dispersion on the DMD, and the spectral resolution.
Since AlGaAs and oxide spectral information are required to calculate the targeted spectra for monochromatic and shaped illuminations, the second step of the experiment is the the hyperspectral cube acquisition.
Then, the masks corresponding to the monochromatic and shaped illuminations can be calculated using calibration and spectral data.
For each illumination, the corresponding mask is applied on the DMD, and the integration time is tuned to take advantage of the full dynamic range of the camera. In order to make a fair comparison despite the different acquisition times, acquired "views" are generated for each illumination as the sum of all the images acquired during a fixed time of $T = 2\,\text{seconds}$, which, as already highlighted above, is fully compatible with the requirements of future real-time tracking as it ensures the recording of successive oxide profiles with a $< 40\,\text{nm}$ process-induced accuracy, with respect to a typical oxidation rate of $\simeq 1\,\mu\text{m/min}$.
Finally, the acquired view are investigated to quantify the impact of the illumination on the oxide edge detection.

3.5.2 Hyperspectral cube acquisition

3.5.2.1 Hadamard spectral imaging method

The hyperspectral cube acquisition could be performed using a classical wavelength scan, transmitting a single spectral band and recording each monochromatic image in a sequence. However, for high spectral resolution it requires very long integration times as the illumination in each band is low, and can induce speckle distortion as the coherence length is high. A more efficient approach is the Hadamard scan method [60], where each image corresponds to a linear combination of spectral bands, improving simultaneously upon both limitations. In particular, the gain in acquisition time between a wavelength scan and an Hadamard scan scales with the number of combined bands. This method also benefits from the Fellgett's advantage [60], that refers to a gain in the signal to noise ratio compared to the classical measurement.

Hadamard spectral imaging using S^3 was implemented by applying a sequence of N masks on the DMD, where each mask represents a unique wavelength combination of the N spectral bands to acquire. In our current implementation of the Hadamard scan, we restrict ourselves to 127 5-column-wide bands and for each measurement in the scan, we combine 64 of these bands, resulting in a 64-fold improvement. This method requires a data post-processing step, in order to extract each wavelength contribution from these multiplexed measurements, that can be performed in a time and with a computational power compatible with future real-time oxidation monitoring. Thus, each measured spectrum of the hyperspectral cube is reconstructed using:

$$S_\lambda = M^{-1} \times S_H \tag{3.9}$$

Where S_λ is the reconstructed spectrum, S_H the acquired signal, and M is the measurement matrix that is closely related to Hadamard matrices [60] . In order to benefit from Fellgett advantage the measurement matrix needs to fulfil certain requirements. To ensure this, as in [60], we build M as follow:

- M is a square $N \times N$ matrix with $N = 2^n - 1$ for fast computation. We chose $n = 7$, limiting the total number of spectral bands to $N = 127$. As the DMD has

640 columns, we combined the columns into groups of 5 per band, ignoring the final 5. The width of each spectral band in this case is therefore $\sim 5 \times 0.24 = 1.20\,\text{nm}$. It is possible to increase N and to use the full resolution of the DMD, but it requires a slower and more complex construction for the matrix M.

- M coefficients are 0 or 1: we can either block (0) or transmit the light (1).
- M is cyclic: only the first row is needed to generate the whole matrix, each subsequent row derived by cyclic permutation.
- The rows of M should ensure measurement diversity (the combination of bands appearing in the N measurements should be as dissimilar as possible).

In order to guarantee this last point, we generate the first row as a 127-element pseudo-noise sequence where each element e_{m+n} is calculated as the modulo 2 of the following polynomial [60]:

$$e_{m+n} = \sum_{i=0}^{n-1} a_i \times e_{m+i} \tag{3.10}$$

With $0 \leq m \leq N - n - 1$ and $a = [1, 1, 0, 0, 0, 0, 0]$ the coefficients of the 7-order primitive polynomial. The first 7 elements of the sequence are arbitrarily set as $e_0 = 1$, $e_1 = 0$, $e_2 = 1$, $e_3 = 0$, $e_4 = 1$, $e_5 = 0$, $e_6 = 1$.

Figure 3.27 shows the 3 consecutive Hadamard masks used during the acquisition sequence. Note that apart from the last 5 black columns that are fixed, each subsequent mask is obtained by cyclic shifting by one spectral band (i.e. by 5 pixel).

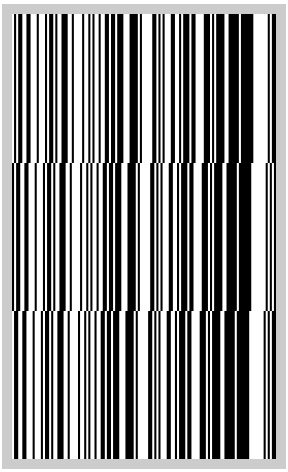

Figure 3.27: Three consecutive Hadamard masks used during the acquisition. Taken from [58].

3.5.2.2 Acquisition and data extraction

Hyperspectral cube acquisition using Hadamard method has been performed by capturing the image corresponding to each of the 127 Hadamard-mask-based illuminations. After data cube reconstruction, reflectivity spectra of oxidized and unoxidized areas have been extracted from the data cube, as shown in figure 3.28. The figure 3.28a presents the image under panchromatic illumination of the VCSEL mesa, where the two regions to be detected are identified: the central dark area (and in particular the blue highlighted zone) corresponding to the unoxidized part and the peripheral oxidized area (especially in orange

donut). The blue circle and the orange donut correspond to the areas where pixel value have been averaged to give the final intensity level for each each spectral band of the cube, which gives respectively the reflectivity spectra of unoxidized and oxidized areas presented in figure 3.28b.

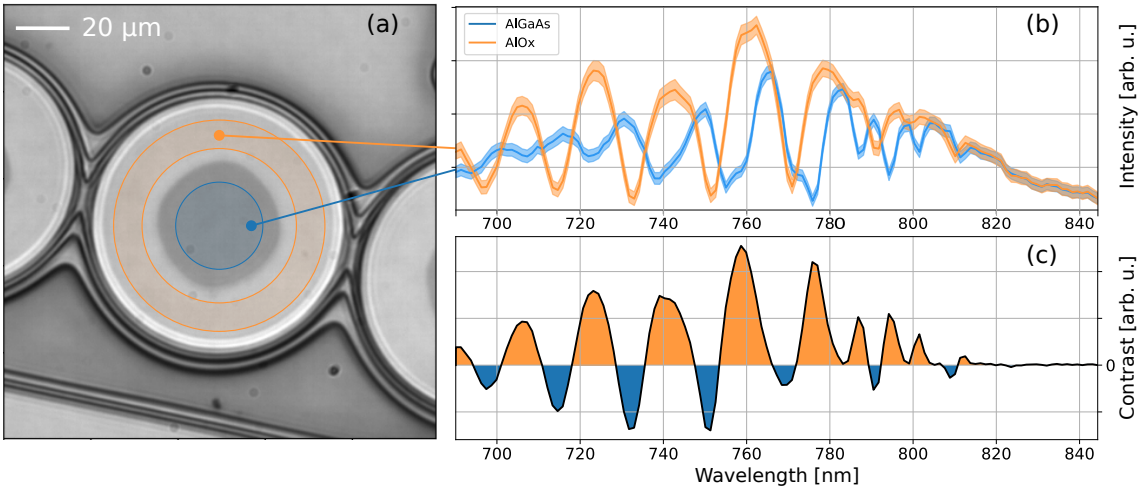

Figure 3.28: (a) Top view of the sample under panchromatic illumination with AlOx (orange) and AlGaAs (blue) regions-of-interest, the etched mesa is delimited by three thin black lines outside of which is the bottom of the etch; (b) mean reflectivity spectrum in each region (central line) surrounded by the variance (pale color area); (c) Spectrally-resolved reflectivity contrast between AlOx and AlGaAs regions. Taken from [58].

The figure 3.28c shows the spectral distribution of contrast resulting in the difference between oxidized and unoxidized areas reflectivity spectra.

3.5.3 Spectral shaping

While the panchromatic illumination only requires a fully white mask to apply to the DMD, monochromatic and shaped illumination are determined from the contrast spectral distribution presented in figure 3.28c.
The monochromatic illumination spectrum corresponds to the spectral band where the highest contrast between oxidized and unoxidized is reached. This results in a 15-pixel-column-wide spectral band ($\simeq 3.75\,\text{nm}$) centered at $\lambda = 758.66\,\text{nm}$.
In the case of the shaped illumination spectrum, the spectral band ponderation result from an optimization process that aims the discernability improvement between the two areas of interest, and can be realized in various ways. The Fisher discriminant analysis (FDA) could be relevant and efficiently applied [61]. With this method, the band weights w to be applied are chosen to maximize the ratio of "inter-region variance" to "intra-region variance", using the equation 3.11:

$$w = \frac{(\mu_{ox} - \mu_{unox})^2}{v_{ox}^2 + v_{unox}^2} \tag{3.11}$$

Where μ_{ox} and μ_{unox} are respectively the mean of the oxidized and of the unoxidized area, and v_{ox} and v_{unox} the corresponding variance. As such, this method optimizes the separability by increasing the contrast between the two regions while minimizing the noise in each region. As a first step, the noise is considered to be constant across the spectral range, as observed in figure 3.28b, which allows to directly set the spectral band

weights to the reflectivity contrast between the two regions (figure 3.28c). In order to simplify the acquisition and make it faster by applying a single mask, only the positive part of the contrast distribution is chosen for the spectral band ponderation in the shaped illumination spectrum, which includes the highest cumulated contrast (filled orange curve in figure 3.28c).

In the case of monochromatic or shaped illumination, the gray level mask is created as follows: the targeted spectrum is normalized by the full spectrum of the source previously measured using a fully white mask on DMD. This quantity, which is the level of signal, for each spectral band, that must be transmitted by the DMD, is then normalized to 1 and transformed to the equivalent gray level distribution by interpolating the transmitted intensity versus gray level curve previously measured and shown in figure 3.25.

Figure 3.29 shows the spectrometer measurement of panchromatic (in gray), monochromatic (in blue), and shaped spectra (in orange), resulting from the display of the created masks on the DMD.

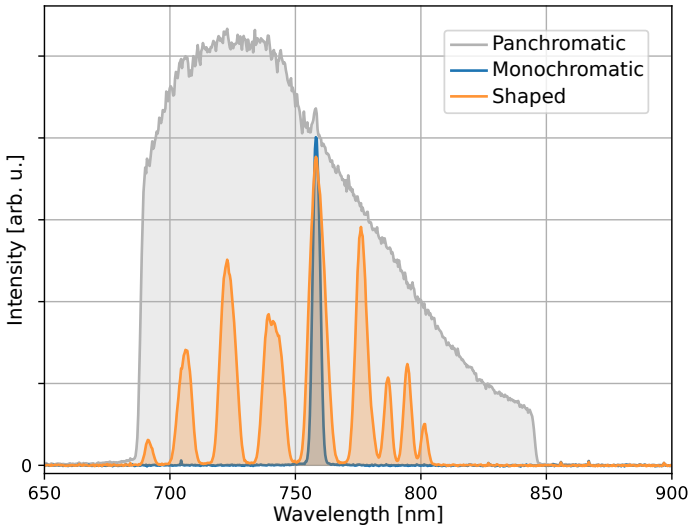

Figure 3.29: The three illumination spectra generated with S^3: panchromatic spectrum (gray), monochromatic spectrum offering maximum contrast between AlOx and AlGaAs (blue), shaped spectrum (orange) corresponding to all the bands with positive contrast (see figure 3.28c). Taken from [58].

3.5.4 Acquisition of monitoring "views"

In order to use the full dynamic range of the camera, the integration times of the image acquisition are set to 95 ms, 2000 ms and 400 ms respectively for the panchromatic, monochromatic and shaped illumination. As previously explained, the signal coming from the sample is recorded during a fixed time of 2 seconds, keeping these integration times, for each illumination. This corresponds to 21, 1, and 5 images taken in 2 seconds respectively for the panchromatic, monochromatic and shaped illumination. For each set of images, the images are summed together to produce a single monitoring "view" that represents the entire signal acquired in 2 seconds, and that contitutes the raw material of quantitative analysis presented in next section.

3.5.5 Results and discussion

The discernability quantitative analysis of the monitoring "views" of an already-oxidized VCSEL in static conditions relies on two steps that this section aims to present:

1. The analysis of the signal level distribution in oxidized and unoxidized areas.
2. The oxide edge detection

3.5.5.1 Histogram analysis

The figure 3.30 presents the impact of the illumination spectrum on the discernability of the AlGaAs and AlOx regions in the monitoring views. The discernability D is defined as follows :

$$D = \frac{\mu_{ox} - \mu_{ox}}{\sigma_{ox} + \sigma_{unox}} \tag{3.12}$$

Where μ_{ox} and μ_{unox} are respectively the histogram mean value of the oxidized and the unoxidized area, and σ_{ox} and σ_{unox} are respectively the variance of the pixel value in the oxidized and the unoxidized area. The three spectral illuminations are represented: panchromatic (figures 3.30a, 3.30b), monochromatic (figures 3.30c, 3.30d), and shaped (figures 3.30e, 3.30f) showing respectively the monitoring view and the corresponding histograms for the oxidized region (blue) and unoxidized region (orange). The discernability between the two regions can be inferred by looking at the two peaks in the histograms of figure 3.30: it increases both with increasing distance between the peaks and decreasing width of both peaks.
The resulting view with the panchromatic illumination corresponds to the sum of 21 images, each one acquired at an integration time of 95 ms. We see in figure 3.30a and figure 3.30b that this method gives a discernability of 6 between AlGaAs and AlOx regions, characterized by a relative low contrast and sharp peaks. For the monochromatic illumination case, corresponding to a single image with an integration time of 2 s, a twice better separation between the pixel mean value of each the regions is obtained, with a discernability of 12. Albeit, in figure 3.30c, we observe the presence of grains, imputed to speckle patterns, inherent to the spectral coherence of the illumination. This can also be seen in figure 3.30d with the broadening of the histograms of both regions (speckle increasing the intra-region variance).
The view using the spectrally-shaped illumination, visible in figure 3.30e, is the sum of 5 images with an integration time of 400 ms. We see on its corresponding histogram, in figure 3.30f, that the spread of the pixel values of each regions has decreased compared to the monochromatic illumination, due to the disappearance of the speckle. It leads to a discernability of 18, which is an improvement of 300% compared to the panchromatic illumination, and of 50% compared to the monochromatic illumination. Although the contrast with spectrally-shaped illumination is slightly smaller than with monochromatic illumination, as the intra-region variance is reduced (ie the peaks in the histogram are narrower), the discernability remains larger and results in better oxide edge detection as discussed hereafter.

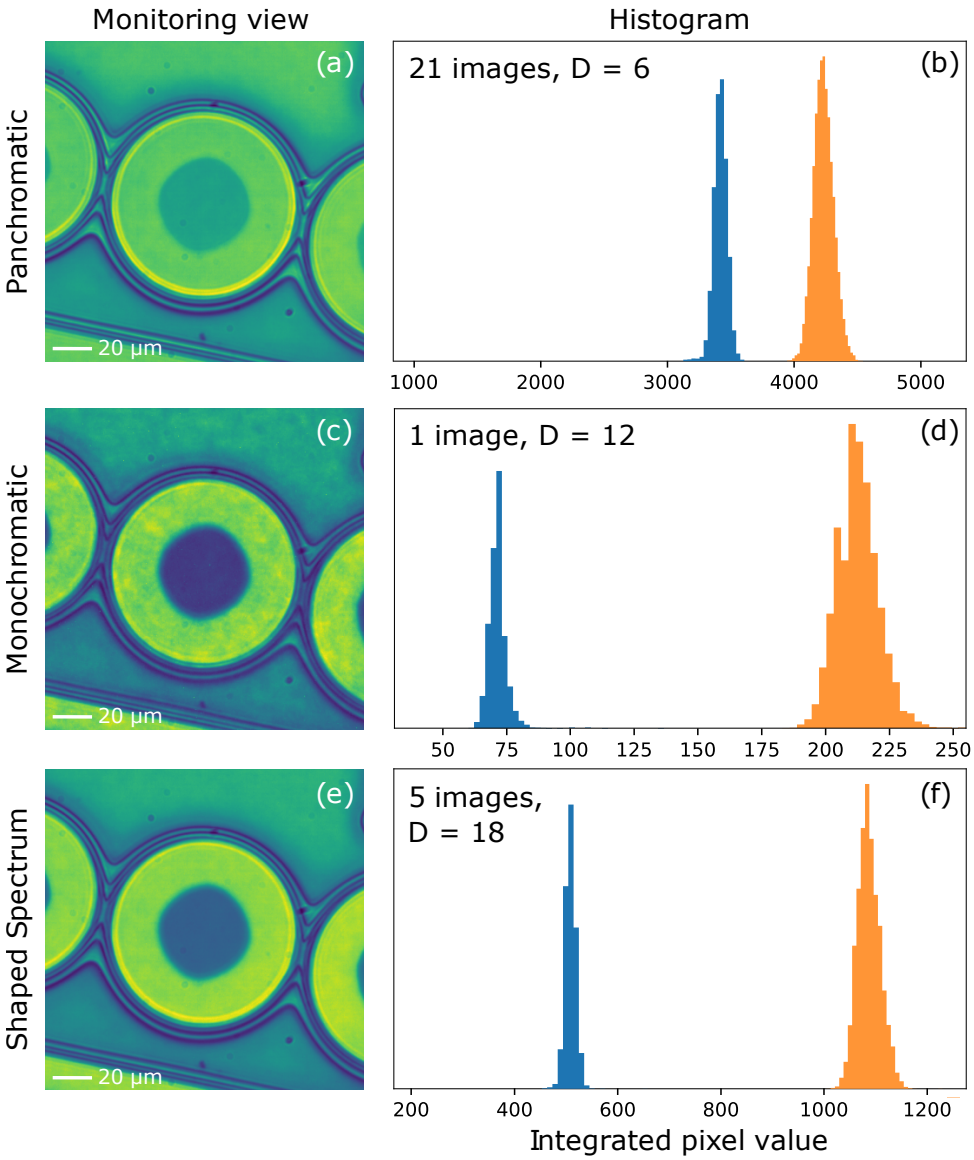

Figure 3.30: [(a), (c), (e)] Monitoring views and [(b), (d), (f)] associated histograms in the oxidized (blue) and unoxidized (orange) regions for three illumination spectra: [(a), (b)] panchromatic , [(c), (d)] monochromatic and [(e), (f)] shaped. A view corresponds to the sum of all the images acquired in $T = 2.0\,\mathrm{s}$. D corresponds to the calculated discernability using equation 3.12. Taken from [58].

3.5.5.2 Oxide edge detection

The oxide aperture dimensions are extracted from the detected contours in the monitoring views. The detection is performed all across the aperture circumference in steps of 2 degrees. At each step, a radial gray level curve is extracted from the view, which starts at the mesa centre and extends across the oxidised region up to the mesa edge. This curve is then fitted with a Gaussian error function whose mean value indicates the AlGaAs/AlO_x interface position. This function, noted erf(x), is defined as:

$$\mathrm{erf}(x) = A \times \frac{2}{\sqrt{\pi}} \int_0^x e^{-\left(\frac{p-x_0}{\sigma\sqrt{2}}\right)^2} dp + y_0 \tag{3.13}$$

Where A corresponds to the contrast step between the oxidized and unoxidised areas, y_0 is

the background offset (in the unoxidised area), x_0 the (mid contrast) radial coordinate of the oxide front boundary, and σ qualifies the abruptness of the aperture step. The fitted radius corresponds to the number x_0.
Figures 3.31, 3.32, and 3.33 show this fit respectively for the monochromatic, panchromatic, and shaped illumination views, at an arbitrary angle of 44°.

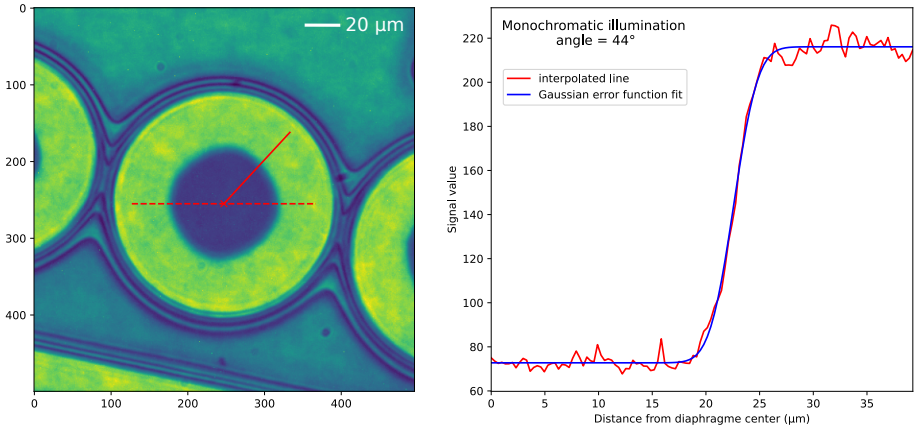

Figure 3.31: Oxide front fitting from the monochromatic view at 44° angle. Taken from [58].

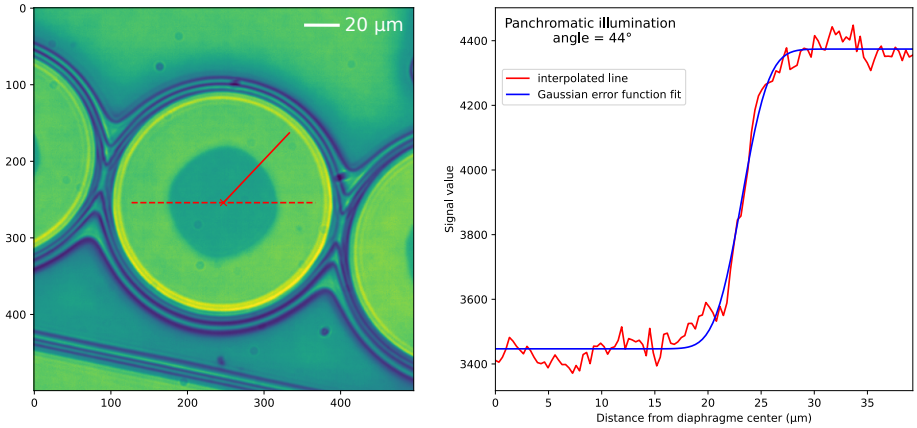

Figure 3.32: Oxide front fitting from the panchromatic view at 44° angle. Taken from [58].

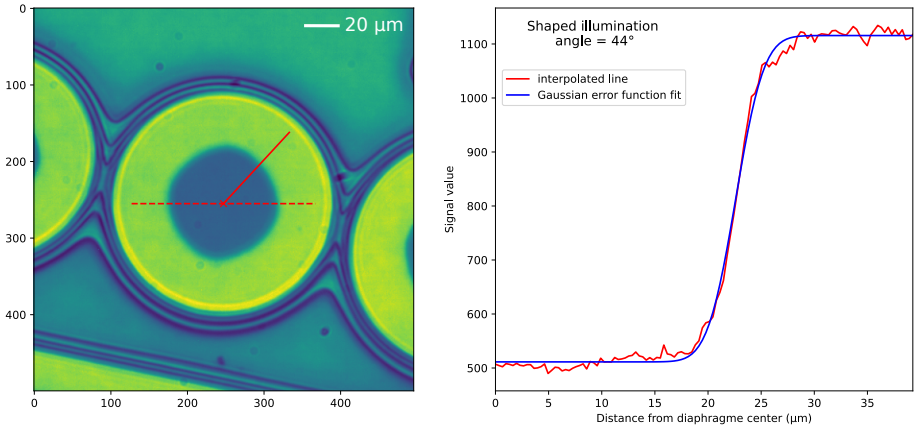

Figure 3.33: Oxide front fitting from the shaped illumination view at 44° angle. Taken from [58].

The figures 3.34a, 3.34b, and 3.34c show the view obtained during the inspection re-

spectively for panchromatic, monochromatic and spectrally-shaped illuminations, with a magnified view on the AlGaAs/AlO_x interface respectively in figures 3.34d, 3.34e, and 3.34f. In all cases, the red curve corresponds to the detected oxide edge.

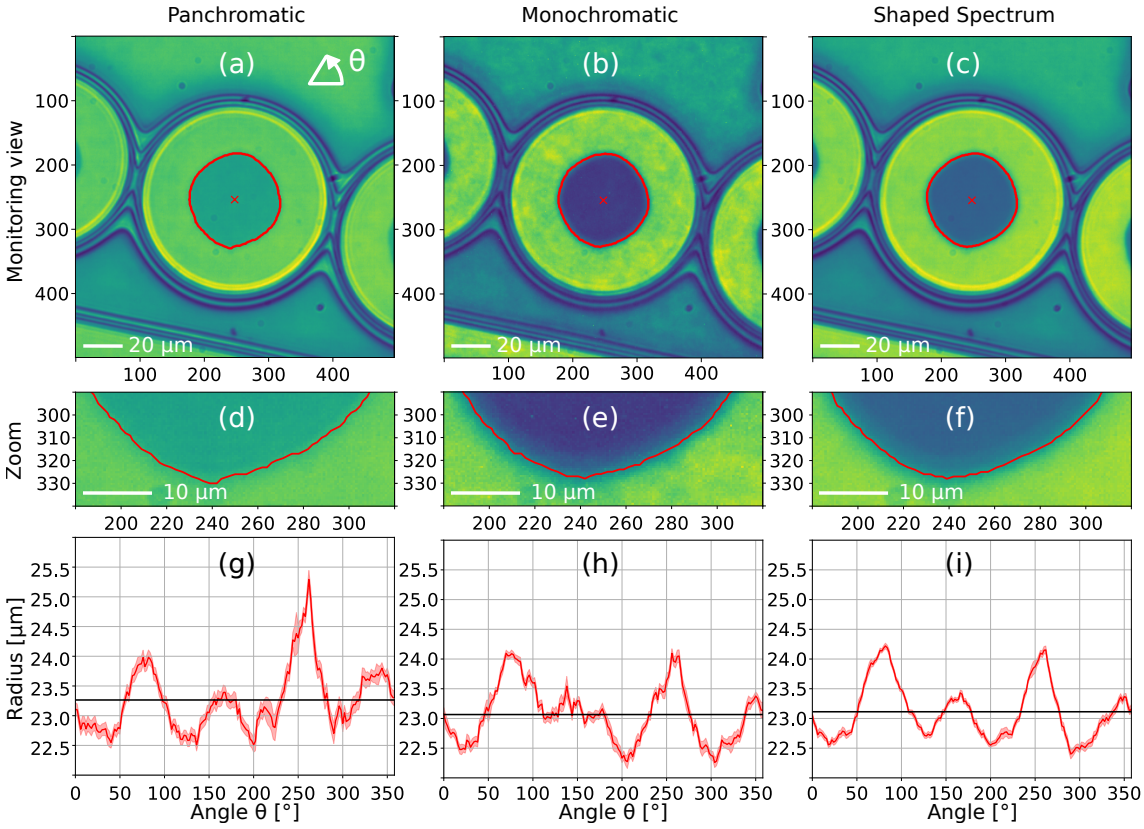

Figure 3.34: Oxidation front measurements for three illumination spectra: panchromatic [(a), (d), (g)], monochromatic [(b), (e), (h)], shaped [(c), (f), (i)]. From the monitoring view [(a)-(c)] an error function fit is used to determine the position of the oxide front (red line), presented in polar coordinate in [(g)-(i)] together with the confidence interval of the fit (pale red area) and the average radius (black line). Taken from [58].

As one can see, for all three illuminations (see black lines in figures 3.34g, 3.34h, and 3.34i), the average radius for the oxide aperture is similar, with values of 23.3, 23.1 and 23.1 µm for panchromatic, monochromatic and shaped illuminations respectively.

However, one can see that the fitted angular distributions are noticeably different. First, the confidence interval at 95 % of the fitted oxide radius (shown as a pale red area in figures 3.34g, 3.34h, and 3.34i), is reduced when going from panchromatic (127 nm) to monochromatic (90 nm) and to shaped-spectrum illumination (56 nm). This parameter quantifies the intrinsic uncertainty of the radius fitting and shows that the fit is the least noisy when illuminating with the shaped spectrum. In the latter case, the extracted oxide aperture angular distribution is observed to present four distinct maxima (at ∼81, 167, 261 and 351 degrees) and four minima (at ∼22, 130, 205 and 301 degrees) in agreement with the oxide aperture contour being a rounded diamond (squircle), as already observed in previous reports [27] and attributed to an anisotropic oxide progression [28]. For panchromatic and monochromatic illuminations, (figures 3.34g and 3.34h) these peaks and valleys are harder to distinguish.

Last, because of the diffusive nature of the lateral wet oxidation [62], we expect a smooth profile for the oxide front. For panchromatic and monochromatic illuminations

(figures 3.34g and 3.34h), one can observe a high angular frequency component, whereas the profile is smoother, and thus more realistic, for shaped illumination (figure 3.34i). This is a clear indication that shaped-spectrum illumination provides a better monitoring (figure 3.34c).

Additionally, it can also be noticed in figure 3.34i that the oxide aperture is a slightly deformed squircle (the radius at 81 and 261 degrees being longer than at 167 and 351 degrees), which may be due to the oxidation being impaired in the inter-mesa region (along the 167 and 351-degree direction) where the next mesas are in close proximity and the etching is not as deep. This kind of subtle observation is not achievable with panchromatic or monochromatic illuminations.

To further validate the above statements based on image analysis considerations and on oxidation physical insight, the above-studied VCSEL aperture (at the centre of figure 3.34c) was also imaged by Scanning Electron Microscopy (SEM). Given the aperture depth in the structure ($> 4\,\mu m$), a localized but destructive removal of the AlGaAs layers burying the oxide aperture by focussed ion beam (FIB) etching had to be performed to be able to make this observation. Practically, as shown in figure 3.35a, a $\simeq$80-µm-diameter disk area was etched away from the 90-µm-diameter VCSEL mesa. Figure 3.35a shows an

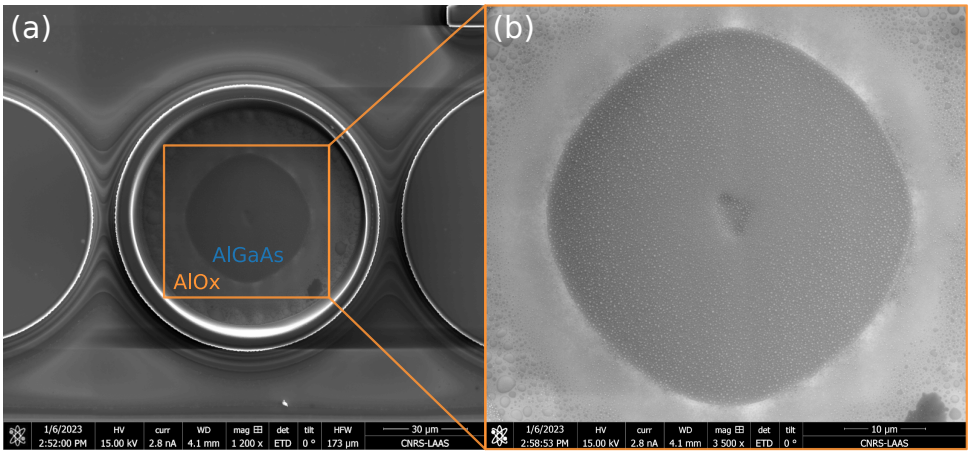

Figure 3.35: Scanning Electron Microscope images of the AlOx aperture after Focussed Ion Beam Etching of the top layers: (a) overview of the circular aperture on the central mesa; (b) zoomed view of the aperture. Taken from [58].

overview image of the etched sample where the oxide aperture of the central VCSEL can easily be identified (as the boundary between the central dark grey unoxidised area and the surrounding light grey oxidized region) in contrast to the apertures of the off-centre VCSELs which are oxidized (see figure 3.34c) but were left unetched. Despite the FIB etching artefacts (central etch dimple and $<$ 1-µm-diameter Gallium droplets lying on the etched surface), the zoomed SEM image of figure 3.35b clearly shows that the oxide aperture is indeed squircle-like and with a smooth profile as deduced from the optical image obtained under shaped-spectrum illumination.

Using (particle and mesa) features on the images, the composite image of figure 3.36, has been assembled based in figures 3.34c, 3.35a, 3.35b with the appropriate rescaling and rotation. As shown, the extracted aperture contour (red dashed line), obtained from the optical measurement in figure 3.34c, closely matches the oxide aperture observed on the SEM image.

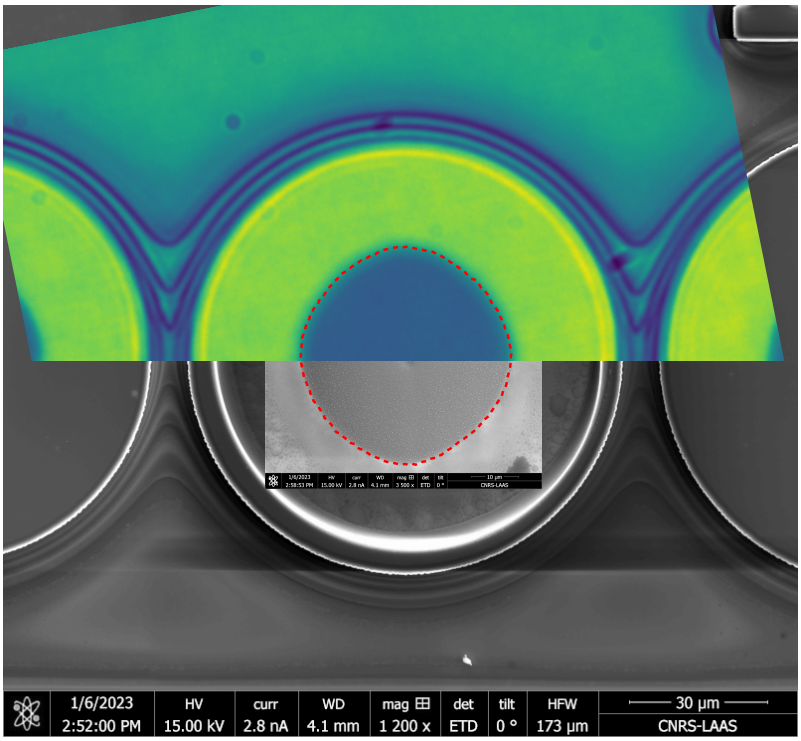

Figure 3.36: Composite image with top to bottom overlap of the in-situ inspection view obtained with shaped spectrum illumination (clipped, with green colormap), the zoomed FIB etching SEM image (light gray), the overview FIB etching SEM image (darker gray). The red dashed line corresponds to the aperture fitted using the shaped spectrum illumination. Taken from [58].

3.6 Conlusion and perspectives

The growing demand of oxide-confined VCSELs with controlled beam properties and electro-optic performances in telecommunications and sensing technologies requires an accurate control of the fabrication. With respect to the impact of oxide aperture dimensions on VCSEL performances, which have been presented in this chapter, its control during the wet thermal oxidation process is required, but the in-situ real-time monitoring can be challenged by the discernability of the oxide aperture in certain VCSEL structures. In order to improve its detection, a spectrally-shaped source based on a digital micromirror device has been set-up and used, providing a versatile illumination for in-situ inspection of VCSEL aperture at room temperature.

This work is the continuity of the research on wet thermal oxidation in-situ real-time monitoring driven by the LAAS-CNRS photonics team, and relies on the previous implementation of narrow-band illumination imaging setup above the oxidaton furnace. In addition, this work takes advantage of the previously designed spectrally-shaped source. The contribution presented in this chapter is about the combination of these two previous systems to improve the monitoring technique. It includes the instrumentation of the source, the developement of an efficient strategy, based on Hadamard patterns, to acquire the hyperspectral cube, as well as the hyperspectral data processing and spectral bands weighting methods implementation. Moreover, the experiment strategy for quantitative analysis of different illumination spectra have been developed and exploited. Images have been recorded under conventional white-light (panchromatic), monochromatic, and a shaped-spectrum illumination tailored on purpose to correspond to the differences observed in the reflected spectra of the oxidized and unoxidized regions. Quantitative analysis of the

quality of these images has revealed that the latter illumination scheme allows enhanced detection as a result of a compromise between the high-contrast but speckle-altered images of monochromatically-lit scenes and the high-fluence (hence high-speed) recordings usually obtained using white light illumination. In addition, the same source has been used to acquire in-situ the whole hyperspectral cube of the sample under study. A subsequent SEM image on a single FIB-etched oxidized VCSEL has also been made and has enabled both qualitative and quantitative validations of the optical measurements.

Further work will consist in implementing this technique for real-time in-situ monitoring of the wet thermal oxidation process, which implies taking into account the incidence of the real operating conditions on the aperture measurement such as high temperature environment, mechanical vibrations and other altering factors. The reasonably short integration times achievable associated with high flexibility in the targeted spectral range and spectral bands should enable the transfer from static inspection to dynamic tracking. Since the discernability of the oxide aperture in VCSELs tends to fade at high temperature in the visible spectral range, the parallel acquisition over multiple spectral bands will bring a significant gain to compensate for this lack of contrast.

The image recording system studied in this work, based on a spectrally-shaped source, is amenable to implement more advanced image processing techniques such as the Fisher Discriminant Analysis (FDA) or the Principal Component Analysis (PCA) to optimize the discernability between two or more areas in the field of view, and further enhance the quality of the images and to subsequently lead to improved process monitoring and characterisation. Also, the arrival of CMOS SWIR cameras on the market could be a breakthrough for high-yield oxide-confined VCSEL production, by bringing high sensitivity and high spatial resolution to the SWIR detection spectral range, that is beyond the VCSEL top Bragg mirror absorption spectral edge. The technique could also be used to improve the monitoring and control of other semiconductor processing steps where the distinguishability between side-by-side regions is key such as lithography and selective etching or deposition.

Bibliography

[1] J. M. Dallesasse, N. Holonyak, A. R. Sugg, T. A. Richard, and N. El-Zein, "Hydrolyzation Oxidation of Al \textsubscript \emphx Ga \textsubscript 1- \emphx As-AlAs-GaAs Quantum Well Heterostructures and Superlattices," *Applied Physics Letters*, vol. 57, no. 26, pp. 2844–2846, 1990.

[2] B. D. Padullaparthi, J. A. Tatum, and K. Iga, *VCSEL Industry: Communication and Sensing*. Wiley : IEEE Press, 2022.

[3] S. Feld, J. Loehr, R. Sherriff, J. Wiemeri, and R. Kaspi, "In Situ Optical Monitoring of AlAs Wet Oxidation Using a Novel Low-Temperature Low-Pressure Steam Furnace Design," *IEEE Photonics Technology Letters*, vol. 10, no. 2, pp. 197–199, 1998.

[4] A. Sakamoto, H. Nakayama, and T. Nakamura, "Fabrication Control during AlAs Oxidation of the VCSELs via Optical Probing Technique of AlAs Lateral Oxidation (OPTALO)," in *Symposium on Integrated Optoelectronic Devices*, p. 211, 2002.

[5] G. Almuneau, R. Bossuyt, P. Collière, L. Bouscayrol, M. Condé, I. Suarez, V. Bardinal, and C. Fontaine, "Real-Time in situ Monitoring of Wet Thermal Oxidation for Precise Confinement in VCSELs," *Semiconductor Science and Technology*, vol. 23, no. 10, p. 105021, 2008.

[6] F. Koyama, "Recent Advances of VCSEL Photonics," *Journal of Lightwave Technology*, vol. 24, no. 12, pp. 4502–4513, 2006.

[7] R. Michalzik, "VCSEL Fundamentals," in *VCSELs* (R. Michalzik, ed.), vol. 166, pp. 19–75, Berlin, Heidelberg: Springer Berlin Heidelberg, 2013.

[8] G. R. Hadley, "Effective Index Model for Vertical-Cavity Surface-Emitting Lasers," *Optics Letters*, vol. 20, no. 13, p. 1483, 1995.

[9] M. Yazdanypoor and A. Gholami, "Optimizing Optical Output Power of Single-Mode VCSELs Using Multiple Oxide Layers," *IEEE Journal of Selected Topics in Quantum Electronics*, vol. 19, no. 4, pp. 1701708–1701708, 2013.

[10] N. Nishiyama, M. Arai, S. Shinada, K. Suzuki, F. Koyama, and K. Iga, "Multi-Oxide Layer Structure for Single-Mode Operation in Vertical-Cavity Surface-Emitting Lasers," *IEEE Photonics Technology Letters*, vol. 12, no. 6, pp. 606–608, 2000.

[11] W.-Y. Liao, J. Li, C.-C. Li, X.-F. Guo, W.-T. Guo, W.-H. Liu, Y.-J. Zhang, X. Wei, and M.-Q. Tan, "Oxide-Aperture-Dependent Output Characteristics of Circularly Symmetric VCSEL Structure," *Chinese Physics B*, vol. 29, no. 2, p. 024201, 2020.

[12] F. Adel Ismael Chaqmaqchee and J. A. Lott, "Impact of Oxide Aperture Diameter on Optical Output Power, Spectral Emission, and Bandwidth for 980 Nm VCSELs," *OSA Continuum*, vol. 3, no. 9, p. 2602, 2020.

[13] B. Hawkins, R. Hawthorne, J. Guenter, J. Tatum, and J. Biard, "Reliability of Various Size Oxide Aperture VCSELs," in *52nd Electronic Components and Technology Conference 2002*, pp. 540–550, IEEE, 2002.

[14] L. Liu, H. Zhao, and H. Niu, "Influence of Double Oxide-Confined Regions on Electrical, Optical, and Thermal Field Distribution Characteristics of Vertical-Cavity Surface Emitting Laser," in *Photonics Asia 2004* (J.-q. Yao, Y. J. Chen, and S. Lee, eds.), p. 135, 2005.

[15] Y.-C. Chang and L. A. Coldren, "Efficient, High-Data-Rate, Tapered Oxide-Aperture Vertical-Cavity Surface-Emitting Lasers," *IEEE Journal of Selected Topics in Quantum Electronics*, vol. 15, no. 3, pp. 704–715, 2009.

[16] E. Hegblom, D. Babic, B. Thibeault, and L. Coldren, "Scattering Losses from Dielectric Apertures in Vertical-Cavity Lasers," *IEEE Journal of Selected Topics in Quantum Electronics*, vol. 3, no. 2, pp. 379–389, 1997.

[17] C. L. Chua, R. L. Thornton, D. W. Treat, and R. M. Donaldson, "Anisotropic Apertures for Polarization-Stable Laterally Oxidized Vertical-Cavity Lasers," *Applied Physics Letters*, vol. 73, no. 12, pp. 1631–1633, 1998.

[18] P. Debernardi, G. Bava, C. Degen, I. Fischer, and W. Elsasser, "Influence of Anisotropies on Transverse Modes in Oxide-Confined VCSELs," *IEEE Journal of Quantum Electronics*, vol. 38, no. 1, pp. 73–84, 2002.

[19] K. J. Knopp, R. P. Mirin, D. H. Christensen, K. A. Bertness, A. Roshko, and R. A. Synowicki, "Optical Constants of (Al0.98Ga0.02)xOy Native Oxides," *Applied Physics Letters*, vol. 73, no. 24, pp. 3512–3514, 1998.

[20] A. Baca and C. Ashby, *Fabrication of GaAs Devices*. Institution of Engineering and Technology, 2005.

[21] C. I. H. Ashby, M. M. Bridges, A. A. Allerman, B. E. Hammons, and H. Q. Hou, "Origin of the Time Dependence of Wet Oxidation of AlGaAs," *Applied Physics Letters*, vol. 75, no. 1, pp. 73–75, 1999.

[22] B. E. Deal and A. S. Grove, "General Relationship for the Thermal Oxidation of Silicon," *Journal of Applied Physics*, vol. 36, no. 12, pp. 3770–3778, 1965.

[23] M. Ochiai, G. E. Giudice, H. Temkin, J. W. Scott, and T. M. Cockerill, "Kinetics of Thermal Oxidation of AlAs in Water Vapor," *Applied Physics Letters*, vol. 68, no. 14, pp. 1898–1900, 1996.

[24] K. Choquette, K. Geib, C. Ashby, R. Twesten, O. Blum, H. Hou, D. Follstaedt, B. Hammons, D. Mathes, and R. Hull, "Advances in Selective Wet Oxidation of AlGaAs Alloys," *IEEE Journal of Selected Topics in Quantum Electronics*, vol. 3, no. 3, pp. 916–926, 1997.

[25] O. Blum, C. I. H. Ashby, and H. Q. Hou, "Barrier-Layer-Thickness Control of Selective Wet Oxidation of AlGaAs for Embedded Optical Elements," *Applied Physics Letters*, vol. 70, no. 21, pp. 2870–2872, 1997.

[26] K. Choquette, K. Geib, H. Hou, D. Mathes, and R. Hull, "The Technology and Applications of Selective Oxidation of AlGaAs," in *Proceedings of the 10th Conference on Semiconducting and Insulating Materials*, pp. 209–213, IEEE, 1998.

[27] G. Lafleur, G. Almuneau, A. Arnoult, H. Camon, and S. Calvez, "Anisotropy in the Wet Thermal Oxidation of AlGaAs: Influence of Process Parameters," *Optical Materials Express*, vol. 8, no. 7, p. 1788, 2018.

[28] S. Calvez, G. Lafleur, A. Arnoult, A. Monmayrant, H. Camon, and G. Almuneau, "Modelling Anisotropic Lateral Oxidation from Circular Mesas," *Optical Materials Express*, vol. 8, no. 7, p. 1762, 2018.

[29] G. Lafleur, *Nouvelles Architectures de Composants Photoniques Par l'ingénierie Du Confinement Électrique et Optique*. PhD Thesis, Université Toulouse 3 Paul Sabatier, 2016.

[30] Y. Luo and D. Hall, "Nonselective Wet Oxidation of AlGaAs Heterostructure Waveguides Through Controlled Addition of Oxygen," *IEEE Journal of Selected Topics in Quantum Electronics*, vol. 11, no. 6, pp. 1284–1291, 2005.

[31] S. Adachi, "GaAs, AlAs, and Al \textsubscript \emphx Ga \textsubscript 1- \emphx As: Material Parameters for Use in Research and Device Applications," *Journal of Applied Physics*, vol. 58, no. 3, pp. R1–R29, 1985.

[32] M. P. Bakker, D. J. Suntrup, H. Snijders, T.-A. Truong, P. M. Petroff, M. P. van Exter, and D. Bouwmeester, "Monitoring the Formation of Oxide Apertures in Micropillar Cavities," *Applied Physics Letters*, vol. 102, no. 10, p. 101109, 2013.

[33] Y. Salvadé, R. Dändliker, A. Courteville, and M. Zickar, "Air-Dispersion Measurement by Second-Harmonic Heterodyne Interferometry," *Optics Letters*, vol. 27, no. 16, p. 1424, 2002.

[34] A. Rouxel, *Étude d'un Imageur Hyperspectral Adaptatif Dans Un Contexte d'observation de La Terre*. PhD Thesis, Université de Toulouse, LAAS-CNRS, 2022.

[35] E. Adam, O. Mutanga, and D. Rugege, "Multispectral and Hyperspectral Remote Sensing for Identification and Mapping of Wetland Vegetation: A Review," *Wetlands Ecology and Management*, vol. 18, no. 3, pp. 281–296, 2010.

[36] M. Govender, K. Chetty, and H. Bulcock, "A Review of Hyperspectral Remote Sensing and Its Application in Vegetation and Water Resource Studies," *Water SA*, vol. 33, no. 2, 2009.

[37] \. L. Gao and R. T. Smith, "Optical Hyperspectral Imaging in Microscopy and Spectroscopy - a Review of Data Acquisition," *Journal of Biophotonics*, vol. 8, no. 6, pp. 441–456, 2015.

[38] S. Ortega, M. Halicek, H. Fabelo, G. M. Callico, and B. Fei, "Hyperspectral and Multispectral Imaging in Digital and Computational Pathology: A Systematic Review," *Biomedical Optics Express*, vol. 11, no. 6, p. 3195, 2020.

[39] L. M. Kandpal, J. Tewari, N. Gopinathan, P. Boulas, and B.-K. Cho, "In-Process Control Assay of Pharmaceutical Microtablets Using Hyperspectral Imaging Coupled with Multivariate Analysis," *Analytical Chemistry*, vol. 88, no. 22, pp. 11055–11061, 2016.

[40] X. Su, Y. Wang, J. Mao, Y. Chen, \. A. Yin, B. Zhao, H. Zhang, and M. Liu, "A Review of Pharmaceutical Robot Based on Hyperspectral Technology," *Journal of Intelligent & Robotic Systems*, vol. 105, p. 75, Aug. 2022.

[41] P. W. Yuen and M. Richardson, "An Introduction to Hyperspectral Imaging and Its Application for Security, Surveillance and Target Acquisition," *The Imaging Science Journal*, vol. 58, no. 5, pp. 241–253, 2010.

[42] H. Liang, "Advances in Multispectral and Hyperspectral Imaging for Archaeology and Art Conservation," *Applied Physics A*, vol. 106, no. 2, pp. 309–323, 2012.

[43] H. Pu, L. Lin, and D.-W. Sun, "Principles of Hyperspectral Microscope Imaging Techniques and Their Applications in Food Quality and Safety Detection: A Review," *Comprehensive Reviews in Food Science and Food Safety*, vol. 18, no. 4, pp. 853–866, 2019.

[44] X. Dong, A. K. Yetisen, J. Dong, K. Wang, P. Kienle, M. Jakobi, and A. W. Koch, "Hyperspectral Fingerprints for Atomic Layer Mapping of Two-Dimensional Materials with Single-Layer Accuracy," *The Journal of Physical Chemistry C*, vol. 125, no. 30, pp. 16583–16590, 2021.

[45] F. Chouchane, G. Almuneau, O. Gauthier-Lafaye, A. Monmayrant, A. Arnoult, G. Lacoste, and C. Fontaine, "Observation of Overstrain in the Coalescence Zone of AlAs/AlOx Oxidation Fronts," *Applied Physics Letters*, vol. 98, no. 26, p. 261921, 2011.

[46] B. Gawlik, C. Barrera, E. T. Yu, and S. V. Sreenivasan, "Hyperspectral Imaging for High-Throughput, Spatially Resolved Spectroscopic Scatterometry of Silicon Nanopillar Arrays," *Optics Express*, vol. 28, no. 10, p. 14209, 2020.

[47] X. Buet, M. Zerrad, M. Lequime, G. Soriano, J.-J. Godeme, J. Fadili, and C. Amra, "Immediate and One-Point Roughness Measurements Using Spectrally Shaped Light," *Optics Express*, vol. 30, no. 10, p. 16078, 2022.

[48] C. Yoon, G. Park, D. Han, S.-i. Im, S. Jo, J. Kim, W. Kim, C. Choi, and M. Lee, "Toward Realization of High-Throughput Hyperspectral Imaging Technique for Semiconductor Device Metrology," *Journal of Micro/Nanopatterning, Materials, and Metrology*, vol. 21, no. 02, 2022.

[49] S. Grusche, "https://en.wikipedia.org/wiki/Hyperspectral_imaging."

[50] G. McConnell, S. Poland, and J. M. Girkin, "Fast Wavelength Multiplexing of a White-Light Supercontinuum Using a Digital Micromirror Device for Improved Three-Dimensional Fluorescence Microscopy," *Review of Scientific Instruments*, vol. 77, no. 1, p. 013702, 2006.

[51] T. C. Wood and D. S. Elson, "A Tunable Supercontinuum Laser Using a Digital Micromirror Device," *Measurement Science and Technology*, vol. 23, no. 10, p. 105204, 2012.

[52] A. Mohan, R. Raskar, and J. Tumblin, "Agile Spectrum Imaging: Programmable Wavelength Modulation for Cameras and Projectors," *Computer Graphics Forum*, vol. 27, no. 2, pp. 709–717, 2008.

[53] J. P. Rice, S. W. Brown, B. C. Johnson, and J. E. Neira, "Hyperspectral Image Projectors for Radiometric Applications," *Metrologia*, vol. 43, no. 2, pp. S61–S65, 2006.

[54] M. Mühleis and J. Hohl-Ebinger, "Programmable Spectral Shaping Demonstrated at the Solar Spectral Irradiance Distribution," *Optics Express*, vol. 29, no. 6, p. 8223, 2021.

[55] Y. Gao, X. Chen, G. Chen, Z. Tan, Q. Chen, D. Dai, Q. Zhang, and C. Yu, "Programmable Spectral Filter in C-Band Based on Digital Micromirror Device," *Micromachines*, vol. 10, no. 3, p. 163, 2019.

[56] C. H. Chuang and Y. L. Lo, "Digital Programmable Light Spectrum Synthesis System Using a Digital Micromirror Device," *Applied Optics*, vol. 45, no. 32, p. 8308, 2006.

[57] S. Turtaev, I. T. Leite, K. J. Mitchell, M. J. Padgett, D. B. Phillips, and T. Čižmár, "Comparison of Nematic Liquid-Crystal and DMD Based Spatial Light Modulation in Complex Photonics," *Optics Express*, vol. 25, no. 24, p. 29874, 2017.

[58] N. Monvoisin, E. Hemsley, L. Laplanche, G. Almuneau, S. Calvez, and A. Monmayrant, "Spectrally-Shaped Illumination for Improved Optical Inspection of Lateral III-V-semiconductor Oxidation," *Optics Express*, vol. 31, no. 8, p. 12955, 2023.

[59] "Introduction to Texas Instrument DLP Device. http://satdream.tech/?introduction-aux-dlp-de-texas-instruments."

[60] E. D. Nelson and M. L. Fredman, "Hadamard Spectroscopy," *Journal of the Optical Society of America*, vol. 60, no. 12, p. 1664, 1970.

[61] R. A. Fisher, "The use of multiple measurements in taxonomic problems," *Annals of Eugenics*, vol. 7, no. 2, pp. 179–188, 1936.

[62] S. Calvez, P.-F. Calmon, A. Arnoult, O. Gauthier-Lafaye, C. Fontaine, and G. Almuneau, "Low-Loss Buried AlGaAs/AlOx Waveguides Using a Quasi-Planar Process," *Optics Express*, vol. 25, no. 16, p. 19275, 2017.

Conclusions and perspectives

This work is a contribution to two research axes aiming to the improvement of VCSEL performances, in the context of the fast-growing demand of VCSELs and diversification of their applications and operational requirements. High-power VCSELs and single-mode VCSELs are two significant parts of this demand, and are associated with the two challenges considered in this work:

1. The limited increase of the active area for standard top-emitting VCSELs, which prevents the rise of their output power.

2. The problematic control of the oxide aperture diameter in oxide-confined VCSELs fabrication, which is crucial for their electro-optic performances, especially when the single-mode operation is targeted.

In standard top-emitting oxide-confined VCSELs, a metallic annular top contact is employed to enable the current injection in the structure while preventing the metal to block the laser emission. This technique causes the current to be mainly injected preferentially at the edges of the oxide aperture when its diameter becomes large, leaving a significant part of the active area unused for the amplification process. The research path that has been followed to uniformize the current injection over large active areas was the replacement of the annular top contact with a fully-covering contact made of a transparent conductive electrode (TCE). This work specifically focuses on a new TCE, introduced in [1] in 2020 by Tomasz Czyszanowski et al., which consists in a combination of a one-dimentional subwavelength grating made of semiconductor interleaved with another one made of metal. This TCE, called semiconductor-metal deep-subwavelength grating (SMDSG), has the outstanding property of being highly transparent over a relatively large spectral region, which is tuned by optimizing the grating dimensions, for transverse-electric (TE) or transverse-magnetic (TM) polarized light, while taking the advantage of the excellent electrical properties of a metallic contact. In the case of a high transmission of TE-polarized light, the metal stripes are located in the grooves of the semiconductor grating, while they are located at the top of the semiconductor stripes for the high transmission of TM-polarized light. Each SMDSG configuration has its own transmission mechanism, leading to differences between their optimal dimensions and spectral signatures.

This work demonstrates the fabrication, and the high transmission and the excellent electrical properties of both SMDSG configurations made of GaAs and gold-based metallic contacts. This is the first experimental demonstration of this novel SMDSG concept on GaAs material system for near infrared spectral region. The dimensions of these fabricated and characterized SMDSGs have been optimized for the high transmission in the near infrared spectral region, and more specifically at 940 nm for the normal incidence. The SMDSG parameters that were optimized are the grating periodicity and fill factor, and the height of the semiconductor stripes, while the metal stripes height were fixed. For this spectral region, the required grating periodicity was between 100 and 220 nm depending on the type of the fabricated SMDSG configuration and on the metallic contact composition. The fabrication processes of the SMDSG for the high transmission of TE and TM-polarized light have been developed, which implies the use of nanostructuration techniques and the self-alignment of the semiconductor and the metal grating. SMDSGs made of Au and TiAu metallic contact have been fabricated, since the TiAu composition is typically used for the GaAs p-type ohmic contacts in VCSELs or other GaAs-based devices. For both contact composition, and for both SMDSG configurations, a transmission above 80% has been measured considering the adequate polarization between 900 and 985 nm, which is higher than the Fresnel transmission at the interface between GaAs and air. Concerning the characterization of the electrical properties, the lateral current conduction has been

quantified by the measurement of a sheet resistance of $1.4 \pm 0.1\Omega.sq^{-1}$ considering 48-nm-thick gold metal stripes. This is an excellent result for metal nanowires, which is at least ten times lower than for the other TCEs implemented in VCSELs until now. The specific contact resistance, which enables to quantify the current vetical injection efficiency, couldn't be measured by lack of time, even so information to perform this measurement can be found in this manuscript. However, since this work proves that both SMDSG configurations offer the possibility to use the standard TiAu/p-GaAs ohmic contact, an efficient current vertical injection is expected.

These results make the SMDSGs very promising for the improvement of top-emitting VCSELs output power in the near infrared region, by their implementation as top electrode in these devices. Nevertheless, in the case of a devices based on a resonant cavity like VCSELs, the use of SMDSGs optimized in transmission for one polarization leads to the other polarization to be mainly reflected. This results in a higher net gain for this reflected polarization, degrading the VCSEL power conversion efficiency. A better way to use SMDSGs could be to maximize the reflectivity of one polarization while minimizing the absorption to ensure an efficient transmission when the mode is not reflected. Therefore, there is still work to be done to demonstrate high power top-emitting VCSELs employing SMDSGs. The SMDSGs fabricated in this work could be efficient electrical contact solutions for optoelectronic devices without resonant cavity, like surface-emitting LEDs or photodetectors, which could benefit from the optical impedance matching between the semiconductor and the air offered by the SMDSGs.

The second research axis for VCSEL performances improvement targeted in this work also concerns the standard top-emitting oxide-confined VCSELs. The oxide aperture(s) shape and dimension define the modal distribution of the VCSEL emission. Typically, a small aperture diameter below 5 µm enables a single-mode emission. For this reason, optical in-situ real-time monitoring techniques of the Al-based III-V semiconductor wet thermal oxidation process have been used to control the aperture diameter. In particular, the photonic group of the LAAS-CNRS laboratory developed a spectrally-selective illumination coupled to a reflectometry imaging system placed above an oxidation furnace with a viewport [2]. It enables to select the illumination narrow spectral band which results in the best discernability between the oxidized and the unoxidized material in the image for a given VCSEL stack. However, this discernability can be low since the to-be-oxidized thin AlGaAs layer is buried under the top distributed Bragg mirror (DBR) stack of the VCSEL. At the high temperature required for the oxidation process, the absorption edge of the DBR is redshifted, drastically reducing the contrast in the visible spectral range. This range is employed for the narrow-band illumination system, since it is compatible with the use of a higly-spatially-resolved CMOS camera. The contrast at high temperature in this range also depends on the VCSEL stack design, and the oxide aperture detection can become very difficult in some cases as reported by some industrial manufacturers. Moreover, the DBR high reflectivity spectral window of typical 850-nm and 940-nm VCSELs prevent any observation in the near infrared spectral region. Despite the theoretical high oxide aperture discernability in the short-wave infrared (SWIR) spectral region, higly-spatially-resolved camera was lacking in this wavelength range until very recently. A high spatial resolution is crucial since a small aperture diameter is targeted in single-mode VCSELs.

In this work, the choice has been made to develop a customizable illumination technique which maximizes the exploitation of the contrast information contained in the visible range, to keep the advantage of conventionnal optical components including the CMOS camera. A versatile spectrally-shaped source has been developed and implemented as the illumination source in the reflectometry imaging system, with a spectral range that can be tuned to

suit the VCSEL reflectivity characteristics. This source, based on a supercontinuum laser and a digital micromirror device (DMD), enables to perform a quick acquisition of the hyperspectral data cube by multiplexed wavelength scanning, as well as to arbitrarily tailor the illumination spectrum with a spectral resolution below 1 nm over a 150-nm-wide spectral window. The spatial and spectral information contained in the data cube are used to weight the spectral bands to maximize the discernability between the oxidized and the unoxidized material. In this work, the weights were simply based on the spectral distribution of the contrast between the materials to separate. The advantage of such an illumination strategy for the oxide aperture detection has been demonstrated compared to a narrow-band and a white light illumination, in the case of a room-temperature in-situ static inspection of an already oxidized VCSEL. It enables a more robust and a more accurate detection of the oxide aperture, as a result of a compromise between the high-contrast but speckle-altered images from a narrow-band illumination, and the high-fluence, hence high-speed recording when a white light illumination is used.

This technique is compatible with real-time monitoring considering the reasonably short achievable integration times. Further work consists in its implementation for the real oxidation process conditions, including dynamic tracking of the oxide front and high temperature. In addition, more advanced processing techniques could be employed for the optimization between two or more areas in the field of view in order to improve the monitoring. The SWIR spectral region has been mentionned as very interesting for the monitoring of the buried aperture. The very recent availability of highly-spatially-resolved SWIR CMOS cameras is an outstanding opportunity to exploit this wavelength range, using the spectrally-shape source or a narrow-band illumination for a simpler optical system. Finally, such a use of spatial and reflectivity spectral information of a scene to shape an illumination spectrum which optimizes the discernability between several features could be an attractive solution for other semiconductor processing and characterization steps.

To conclude, this work brings new technological tools and methods for the improvement of VCSEL performances, in terms of output power and precise control of the oxide aperture, in response to the multi-purpose applicative context toward which the VCSEL market rapidly and constantly evolves.

Bibliography

[1] T. Czyszanowski, A. K. Sokól, M. Dems, and M. Wasiak, "Transparent Electrode Employing Deep– Subwavelength Monolithic High-Contrast Grating Integrated with Metal," *Optics Express*, vol. 28, no. 19, p. 28383, 2020.

[2] G. Almuneau, R. Bossuyt, P. Collière, L. Bouscayrol, M. Condé, I. Suarez, V. Bardinal, and C. Fontaine, "Real-Time in situ Monitoring of Wet Thermal Oxidation for Precise Confinement in VCSELs," *Semiconductor Science and Technology*, vol. 23, no. 10, p. 105021, 2008.

Résumé de la thèse en français

Sommaire

4.1 Introduction 122

4.2 Les VCSELs de forte puissance 124

4.3 Nouvelles électrodes transparentes métalliques pour l'amélioration de l'uniformité d'injection dans les VCSELs 126

4.4 Illumination à spectre structuré pour l'amélioration du suivi optique du diaphragme dans les VCSELs à diaphragme d'oxyde 135

4.5 Conclusions et perspectives 140

4.1 Introduction

Le laser à cavité verticale émettant par la surface (VCSEL) est un type de laser solide de taille micrométrique inventé en 1977 par Kenichi Iga. Il s'est récemment imposé comme une technologie à base de semiconducteurs peu coûteuse et très fiable, grâce aux progrès importants qui ont été réalisés pour sa fabrication à grande échelle. En 1996, le premier VCSEL commercialisé a été utilisé pour des communications à courte portée puis dans les centres de données, jouant ainsi un rôle clé dans l'expansion d'internet. Aujourd'hui, le VCSEL est l'un des outils essentiels au développement des technologies de l'information et de la détection. Pour les années 2020 à 2025, la croissance du marché des VCSEL a été estimée à 450%, ce qui représenterait 40 milliards de dollars, soit 50% du marché total de la photonique en 2025. Ce marché en pleine expansion comprend quatre grands domaines [1]: la datacom, la détection 3D principalement mise en œuvre dans les smartphones, l'imagerie 3D LiDAR pour l'industrie automobile ainsi que la découpe et le traitement thermique dans l'industrie. Une grande variété de domaines d'application plus restreints font également partie de ce marché [1], comme la défense et l'aérospatiale, la médecine avec la tomographie par cohérence optique, la détection de gaz, la réalité virtuelle / réalité augmentée / réalité mixte, la surveillance, l'impression 3D, ou encore l'impression laser. Le succès des VCSELs dans des domaines aussi diversifiés est dû à la grande gamme de longueurs d'onde d'émission et de puissances d'émission possibles, ainsi qu'à leurs bonnes performances en termes de stabilité spectrale en température et de consommation d'énergie. En règle générale, les applications datacom reposent principalement sur une grande efficacité de couplage dans les fibres optiques, une large bande passante, l'accordabilité de la longueur d'onde, ou encore une dissipation thermique efficace. Les applications de détection nécessitent de leur côté des puissances d'impulsion élevées, un rendement élevé ou une bonne qualité de faisceau [1]. Cela illustre le large éventail d'exigences techniques qu'impose le marché des VCSEL. De plus, un fonctionnement monomode ou multimode peut être nécessaire pour les communications et la détection optique, en fonction de l'application. Les longueurs d'onde d'émission des VCSELs commerciaux se situent généralement entre 650 et 1550 nm, tandis que la recherche de dispositifs émettant à des longueurs d'onde plus courtes et plus longues est en cours. Des matériaux semi-conducteurs III-V à gap directe sont généralement utilisés, comme le GaAs, l'InP, le GaSb ou encore le GaN [1], pour la fabrication et l'intégration sur substrats germanium ou silicium.

Le principe de fonctionnement des VCSELs repose, comme pour tous les types de lasers, sur la rétroaction positive d'un amplificateur. Bien qu'il existe plusieurs modèles de VCSELs, la structure la plus répandue est le VCSEL à diaphragme d'oxyde, présenté en figure 4.1. L'amplification est rendue possible par une zone active, constituée de puits quantiques, positionnée dans une cavité optique définie par deux miroirs de Bragg (DBR) hautement réfléchissants. Le dispositif, comparable à une jonction PIN, est généralement pompé électriquement via le contact supérieur de forme annulaire. Cela permet d'obtenir l'inversion de population dans les puits quantiques et de générer une émission stimulée. Dans un VCSEL standard, l'émission verticale est obtenue en abaissant légèrement la réflectivité du DBR supérieur. La faible épaisseur de la structure permet d'atteindre facilement une émission monomode longitudinale, tandis que le diaphragme d'oxyde définit à la fois la distribution des modes transversaux et l'emplacement de l'injection du courant dans la zone active. La croissance épitaxiale à partir d'un substrat permet d'obtenir l'empilement VCSEL. Ensuite, des techniques de microfabrication telles que la métallisation, la gravure sèche, l'oxydation ou la passivation sont utilisées pour créer le composant, qui est ensuite testé et conditionné. La conception efficace d'un tel composant repose sur une étude mul-

tiphysique, à partir de laquelle des compromis entre les propriétés électriques, optiques et thermiques doivent être décidés.

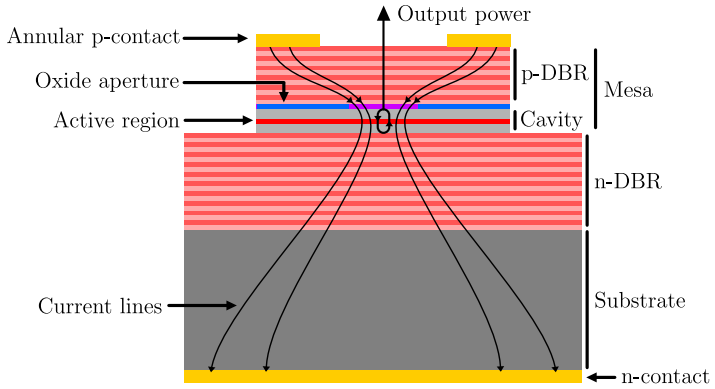

Figure 4.1: Vue en coupe d'un VCSEL à diaphragme d'oxyde standard.

Malgré la maturité récente de la technologie VCSEL, certaines limites liées aux performances electro-optiques de ces sources lasers persistent. Cette thèse vise à contribuer à la résolution de deux d'entre elles:

- La première est la non-uniformité de l'injection du courant électrique qui limite l'exploitation de grandes zones actives pour l'augmentation de la puissance d'émission. Lorsque la surface active devient importante, le chemin préférentiel du courant se situe au bord du diaphragme d'oxyde, comme le montre la figure 4.1. La technique d'injection utilisant le contact annulaire supérieur est responsable de cette perte de surface effective d'émission, qui pourrait être résolue par l'utilisation d'une électrode transparente uniformisant la distribution du courant injecté. Plusieurs types d'électrodes transparentes ont déjà été étudiées pour les VCSELs. Une nouvelle électrode présentée dans l'article [2] en 2020 présente des structures à haute transmission composées de métal et de semi-conducteur, bénéficiant ainsi des excellentes propriétés électriques des contacts métalliques. Basées sur la combinaison d'un réseau sub-longueur d'onde métallique unidimentionnel et d'un autre en semi-conducteur, ces structures sont théoriquement plus performantes que celles qui ont été étudiées précédemment. Le chapitre 1 décrit le contexte de l'utilisation des electrodes transparentes pour les VCSELs de haute puissance. Ensuite, le chapitre 2 présente la fabrication et les caractérisations optiques et électriques de la nouvelle électrode transparente optimisée pour le proche infrarouge.

- Le deuxième problème abordé dans ce travail est la difficulté du contrôle précis de la taille et de la forme du diaphragme d'oxyde pendant le procédé d'oxydation à haute température. Ces paramètres ayant un impact significatif sur les performances électro-optiques des VCSELs, une technique de microscopie optique in-situ a été developpée au LAAS-CNRS avant ce travail [3] afin de les contrôler. Cependant, la discernabilité du diaphragme situé sous le DBR supérieur peut fortement chuter à haute température, en fonction de la constitution de l'empilement VCSEL. Le chapitre 3 démontre l'utilisation de l'imagerie hyperspectrale, pour laquelle le LAAS-CNRS possède une expertise, pour l'amélioration de la détection du diaphragme d'oxyde. Une source structurable spectralement est présentée et utilisée, montrant que le façonnage du spectre d'illumination peut conduire à un contrôle plus robuste et plus précis du diaphragme dans la fabrication des VCSELs à diaphragme d'oxyde.

4.2 Les VCSELs de forte puissance

Les VCSELs de forte puissance tendent à remplacer les lasers à émission par la tranche, et leur développement a conduit à la création de dispositifs émettant par le substrat ainsi qu'à des matrices 1D ou 2D. Ces deux types de dispositifs visent à augmenter à la fois la surface active du laser pour accroitre sa puissance, ainsi que son rendement pour minimiser la consommation d'énergie. Les VCSELs à émission par le subtrat sont capables de fournir une puissance de sortie plus élevée que les structures standards qui émettent par leur face supérieure, mais sont limités par l'auto-échauffement lorsque la surface active devient importante, conduisant à un faible rendement. En outre, ils sont plus difficiles à fabriquer que les dispositifs standards. Les matrices de VCSELs permettent de conserver les excellentes propriétés de faisceau d'un émetteur unique, tout en étendant la zone active qui n'est limitée que par l'uniformité de fabrication sur la surface de la matrice. Cependant, ces matrices ont une densité de puissance limitée par la surface active relativement petite des VCSELs qui les composent, et par la valeur minimale du pas de l'arrangement géométrique.
Les VCSELs dont l'émission se fait par la face supérieure étant la structure la plus simple à fabriquer, la capacité de produire de tels composants avec une grande surface active est recherchée, afin de remplacer les dispositifs à émission par le substrat ou d'améliorer la densité de puissance des matrices. Le contact annulaire localisé au sommet des VCSELs standards est responsable de l'inhomogénéité de l'injection du courant dans ces structures lorsque le diamètre de la zone active est typiquement supérieur à 50 µm. Une électrode transparente pourrait être utilisée comme contact supérieur pour surmonter cette limitation.

L'électrode transparente est un élément crucial pour les technologies de l'information et de l'énergie, qui comprennent les écrans à cristaux liquides, les écrans tactiles, les OLEDs, les LEDs, les cellules solaires ou les fenêtres "intelligentes". Historiquement, les électrodes transparentes utilisées étaient des oxydes transparents conducteurs, tels que l'Indium Tin Oxide (ITO), bien connu et largement répandu. De nouvelles électrodes transparentes telles que les réseaux de nanofils métalliques ou le graphène présentent un intérêt croissant. De plus, des approches hybrides sont étudiées, combinant le oxydes conducteurs transparents ou des matériaux diélectriques avec des nanofils, des grilles métalliques, ou des couches minces métalliques [4].
Les propriétés recherchées pour une électrode transparente sont une conductivité électrique et une transparence élevée, pour une gamme spectrale visée. La conductivité électrique, qui peut être exprimée par la relation de Drude-Boltzmann présentée dans l'équation 4.1,

$$\sigma = e.N.\mu \tag{4.1}$$

où σ est la conductivité, e est la charge élémentaire, N la densité de porteurs, et μ la mobilité des porteurs, est élevée si à la fois la densité de porteurs et leur mobilité sont élevés.
Cependant, une forte densité de porteurs induit divers processus d'absorption tels que l'absorption par porteurs libres, ce qui augmente le coefficient d'absorption total α, détériorant ainsi la transparence. Ce compromis entre conductivité électrique et transparence optique est l'enjeu principal lors de la conception des électrodes transparentes, qui doit être spécifique aux exigences de l'application ciblée.

Dans le cas des VCSELs, une bonne conductivité électrique doit être assurée à la fois latéralement et verticalement, ce qui implique une faible résistance de couche mince et une

faible résistance spécifique de contact. Cette dernière dépend à la fois des matériaux de l'électrode et du substrat. Par conséquent, tous les types d'électrode transparentes ne sont pas compatibles avec les dispositifs à base de GaAs. De plus, la longue durée de vie des composants exige l'utilisation de matériaux stables au niveau chimique et thermique.
L'emploi d'une électrode transparente comme contact supérieur sur des VCSELs pour fabriquer des composants à grande surface active est un sujet de recherche qui a donné lieu à l'utilisation de plusieurs types de matériaux dans la littérature. Le principal matériau étudié est l'ITO [5]. De rares alternatives utilisant des matériaux émergents comme le graphène [6, 7] ou les nanofils d'argent [8] ont également données lieu à des publications. Que ce soit pour l'ITO, le graphene, ou les nanofils d'argent, une meilleure uniformité de l'injection du courant au sein de la zone active a été démontrée. Les niveaux de transparence et les résistances de couches minces sont rapportés dans les trois cas, tandis que la resistance spécifique de contact n'est connu que pour l'ITO, qui a l'avantage d'avoir été un matériau très étudié par le passé. Il a été démontré que cette résistance spécifique de contact de l'ITO reste au minimum un ordre de grandeur au-dessus de celle d'un contact métallique standard sur un substrat GaAs dopé p. Le contact fait de nanofils d'argent peut rivaliser avec l'ITO en terme de transparence et de résistance de couche mince. Cependant, l'obtention d'une faible résistance de couche mince ($\sim 10\Omega.sq^{-1}$) se fait au détriment d'une augmentation de l'absorption optique dans les deux cas, impliquant même un traitement thermique à très haute température pour l'ITO. Ce compromis limite la résistance de couche mince à des valeurs au moins dix fois supérieures à celle d'une couche mince métallique ($< 1\Omega.sq^{-1}$). Le domaine émergent des matériaux métalliques nanostructurés apporte de nouvelles structures intéressantes pour combiner des compositions de contact métalliques standards, qui permettent une faible résistance spécifique de contact et une faible résistance de couche mince, avec une transparence élevée. C'est le cas de la structure fabriquée et caractérisée lors de ce travail, qui est présentée dans le chapitre suivant.

4.3 Nouvelles électrodes transparentes métalliques pour l'amélioration de l'uniformité d'injection dans les VCSELs

Ce chapitre rapporte la fabrication et la caractérisation optique et électrique d'un nouveau type d'électrode transparente pour l'amélioration de l'uniformité d'injection du courant dans des structures VCSELs émettant dans le proche infrarouge. Cette nouvelle électrode transparente, appelée SMDSG (Semiconductor-Metal Deep-Subwavelength Grating) est le résultat d'une combinaison de deux réseaux unidimensionnels sub-longueur d'onde: un premier de semiconducteur et un second de métal. Comme le montre la figure 4.2, deux configurations sont possibles. Une première configuration, appelée B-TE, se caractérise par le placement du métal entre les dents de semi-conducteur, permettant la haute transmission de la polarisation TE. Une seconde permet la haute transmission de la polarisation TM en plaçant le métal au sommet des dents de semi-conducteur, et est appelée T-TM.

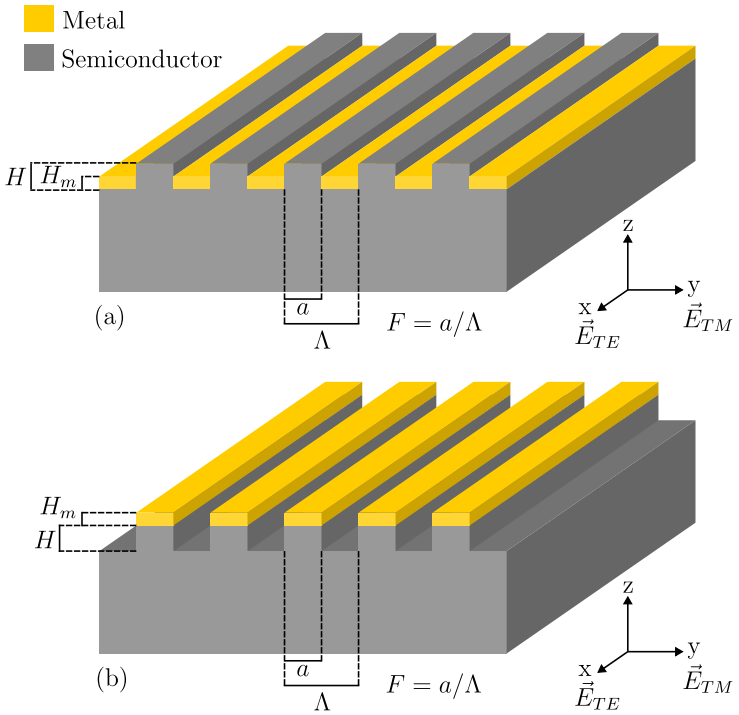

Figure 4.2: Configuration d'un SMDSG permettant la haute transmission de (a) la polarisation TE (B-TE), et (b) la polarisation TM (T-TM). Λ représente la période du réseau, a la largeure des dents de semi-conducteur, F le facteur de remplissage, H la hauteur des dents de semi-conducteur, et H_m la hauteur des dents de métal.

La variation de la transmission de ces structures en fonction de la période du réseau et de la hauteur des dents de semi-conduteur est donnée par les cartographies en figure 4.3 pour la configuration B-TE et ne figure 4.4 pour la configuration T-TM.
Pour la configuration B-TE en polarisation TE, la cartographie montre que lorsque la périodicité du réseau est assez petite devant la longueur d'onde pour que le réseau ne permette plus qu'un seul mode de Bloch, le réseau agit comme une cavité Fabry-Perot. Cet effet se caractérise par une oscillation de la transmission en fonction de la hauteur des dents de semi-conducteur. Les points de haute transmission sont permis par le guidage de l'onde incidente dans les dents de semi-conducteur, évitant ainsi l'intéraction avec le métal. En polarisation TM, le champ électrique est confiné entre les dents de semi-conducteur, ce qui engendre une réflection de l'onde incidente au niveau du métal, et donc l'impossibilité

d'une haute transmission.
Pour la configuration T-TM, toujours dans le régime où la structure ne permet qu'un seul mode de Bloch, la cartographie montre qu'une haute transmission n'est possible qu'en polarisation TM, où le champ électrique confiné entre les dents de semi-conducteur permets le couplage de l'onde entre les lignes de métal dans des cavités résonnantes. En polarisation TE, l'onde confinée entre les dents de semi-conducteur est réfléchie par le métal.

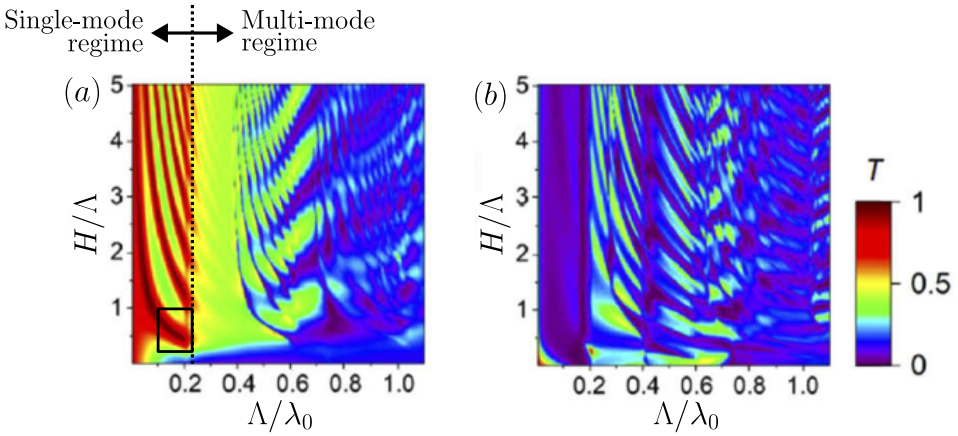

Figure 4.3: Cartographie théorique de la transmission en incidence normale de la configuration B-TE composée d'un substrat de GaAs et de 50 nm d'or, pour (a) la polarisation TE, et (b) la polarisation TM. Le rectangle noir représente la gamme de valeurs utilisées pour la période du réseau et la hauteur des dents de semi-conducteur lors de l'optimisation de la structure. Ces images proviennent de [2].

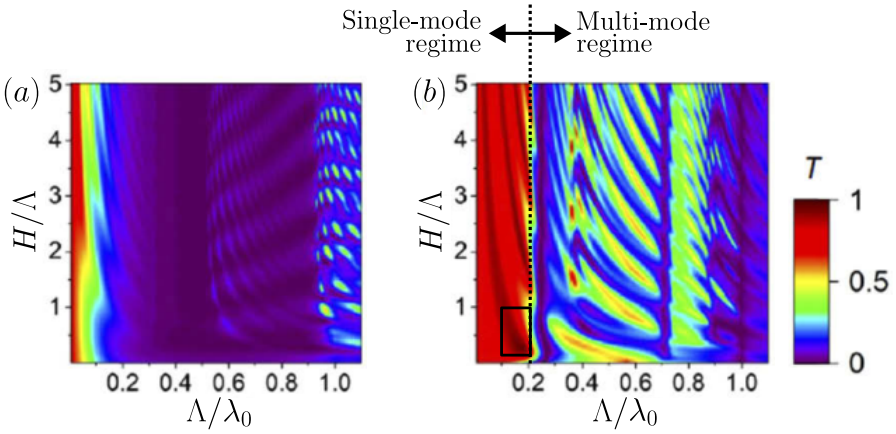

Figure 4.4: Cartographie théorique de la transmission en incidence normale de la configuration T-TM composée d'un substrat de GaAs et de 50 nm d'or, pour (a) la polarisation TE, et (b) la polarisation TM. Le rectangle noir représente la gamme de valeurs utilisées pour la période du réseau et la hauteur des dents de semi-conducteur lors de l'optimisation de la structure. Ces images proviennent de [2].

L'optimisation des dimensions des deux configurations de SMDSG composées d'un substrat de GaAs et d'un contact métallique en Au ou TiAu est présentée en figure 4.5. De ces cartographies sont extraits les points de hautes transmission visés pour la fabrication, qui dépendent de la période, de la hauteur des dents de semi-conducteur, du facteur de remplissage, et du type de contact métallique. Les dimensions des structures associées à ces points de fonctionnement sont résumées dans la table 4.1. La hauteur de l'or est fixée à 50 nm, et celle du titane à 5 nm dans le cas d'un contact TiAu. Le contact TiAu

est classique sur du GaAs dopé p, car il permet la réalisation d'un contact ohmique dans cette configuration, et donc une injection verticale efficace du courant électrique dans la structure. C'est donc un contact sur GaAs plus réaliste que celui composé d'or, qui adhère mal au GaAs et y diffuse, et qui est utilisé dans ce travail pour la caractérisation optique uniquement.

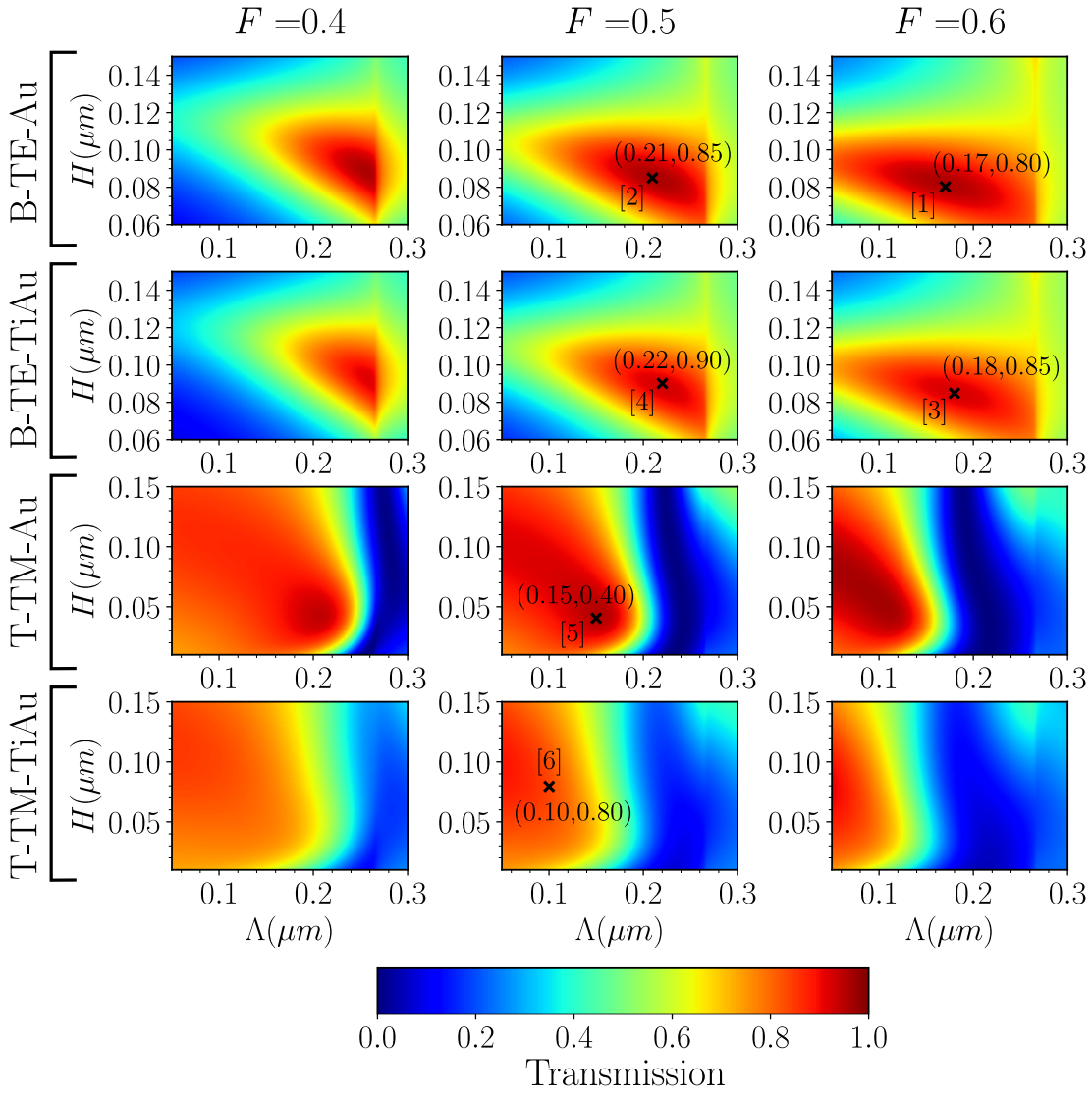

Figure 4.5: Cartographies théoriques de la transmission à 940 nm et en incidence normale en fonction de la hauteur des dents de semiconducteur H et de la période Λ. Chaque ligne correspond à une des quatre structure fabriquées dans ce travail: B-TE-Au, B-TE-TiAu, T-TM-Au, et T-TM-TiAu. La hauteur du métal est fixée à 50 nm pour l'or, et à 5 nm pour le titane dans le cas des contacts TiAu. Chaque colonne correspond à la prise en compte d'un facteur de remplissage différent dans le calcul, de gauche à droite respectivement $F = 0,4$, $F = 0,5$, et $F = 0,6$. Le calcul a été effectué en utilisant la méthode RCWA (Rigorous Coupled Wave Analysis). Les six croix correspondent aux six structures visées en fabrication, labellisées [1], [2], [3], [4], [5], et [6]. Leurs dimensions sont détaillées dans la table 4.1.

		Paramètres des SMDSGs					
Numéro de la structure	Nom de la structure	Λ (nm)	F	H (nm)	H_{Au} (nm)	H_{Ti} (nm)	Transmission théorique $(\lambda = 940nm)$
[1]	B-TE-Au-1	170	0,6	80	50		96% (TE)
[2]	B-TE-Au-2	210	0,5	85			96% (TE)
[3]	B-TE-TiAu-1	180	0,6	85		5	92% (TE)
[4]	B-TE-TiAu-2	220	0,5	90			92% (TE)
[5]	T-TM-Au	150	0,5	40			95% (TM)
[6]	T-TM-TiAu	100	0,5	80		5	83% (TM)

Table 4.1: Paramètres des SMDSGs visés en fabrication. Les dimensions sont extraites des calculs présentés en figure 4.5.

Les procédés de fabrication développés pendant ce travail pour fabriquer chaque configuration sont résumés dans la table 4.2. Dans chaque cas, le procédé assure l'auto-alignement des réseaux de semi-conducteur de métal. Les deux procédés comportent les mêmes étapes technologiques, mais dans un ordre différent, ce qui entraine des différences notables. Ces étapes sont la lithographie électronique (EBL pour Electron-Beam Lithography), qui permet de dessiner des motifs à l'échelle requise par les SMDSGs avec une excellente résolution, la gravure plasma en configuration ICP-RIE (Inductively Coupled Plasma - Reactive Ion Etching), le dépôt du métal par EBPVD (Electron beam physical vapor deposition), et le lift-off du métal.

La configuration B-TE, dont le schéma du procédé de fabrication est présenté en figure 4.6, requiert de graver le GaAs avant le dépôt du metal et le lift-off. Dans le cas ou la résine de lithographie électronique est utilisée comme masque de gravure, comme c'est le cas dans ce procédé, l'emploi d'une résine résistante à la gravure plasma est indispensable. C'est pourquoi la résine CSAR62 diluée à 9% a été utilisée malgré son problème d'adhésion à la surface du GaAs partiellement réglé par le dépôt préalable d'une couche de HMDS (hexamethyldisilazane). Après la gravure, et une fois le métal déposé, le lift-off de ce métal est rendu difficile par le fait que la résine ait été exposée au plasma pendant la gravure sèche. La dissolution de la résine nécessite l'immersion de l'échantillon pendant plusieurs heures dans du DMSO (diméthylsulfoxyde) chauffé à 80°C avec une agitation. Une fois cette dissolution effectuée, une action mécanique est nécessaire pour finir l'étape de lift-off. Cela est dû au profil de la résine sur laquelle est déposé le métal. Ce profil, érodé pendant la gravure plasma, est arrondi au lieu d'être plus large au sommet qu'à la base de la ligne de résine, comme l'exige la méthode classique du lift-off. Le métal est donc voué à se déposer en partie sur les flancs des lignes de résine et des lignes de semi-conducteur, ce qui lie le métal au semiconducteur et rend nécessaire cette action mécanique. Elle est réalisée en deux étapes, une première qui consiste en un bain d'ultrasons, et une seconde pour laquelle de l'acétone est projetée via une seringue à la surface de l'échantillon pour finir d'enlever le film métallique.

Bien que la configuration T-TM requiert une périodicité plus petite, elle est plus facile à fabriquer. Le schéma de son procédé de fabrication est présenté en figure 4.7. En effet, le dépôt du métal et le lift-off sont réalisés avant la gravure plasma du GaAs. Cela permet d'employer une résine qui adhère mieux au GaAs, appelée PMMA, qui permet de réduire plus facilement la périodicité des réseaux. Les lignes de métal liftées sont utilisées comme masque pour la gravure du GaAs, ce qui a pour effet d'éroder et d'arrondir le profil des

lignes métalliques.

Ordre des étapes B-TE	Ordre des étapes T-TM	Nom de l'étape	Description	Technique
1	1	Préparation du Substrat de GaAs	Nettoyage des résidus organiques	Dissolution dans un solvant organique
			Retrait de l'oxyde natif du GaAs	Gravure chimique sélective en solution acide
2	2	Mise en forme du réseau	Enduction de la résine	Spin-coating
			Lithographie	EBL
			Développement de la résine	Gravure chimique humide sélective
3	5	Structuration du GaAs	Retrait de l'oxyde natif du GaAs	Gravure chimique sélective en solution acide
			Gravure sèche du GaAs avec le masque de résine	ICP-RIE
4	3	Dépôt du métal	Retrait de l'oxyde natif du GaAs	Gravure chimique sélective en solution acide
			Dépôt	EBPVD
5	4	Lift-off du métal	Lift-off par voie chimique	Dissolution dans un solvant organique
			Lift-off par voie méchanique	Bain d'ultrasons
				Solvant en spray via une seringue

Table 4.2: Résumé des procédés de fabrication développés pour les configurations B-TE et T-TM.

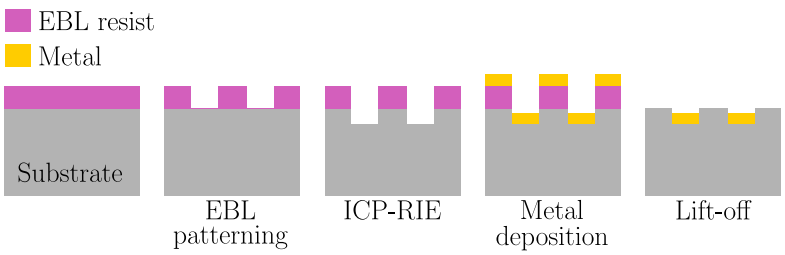

Figure 4.6: Schéma du procédé de fabrication de la configuration B-TE.

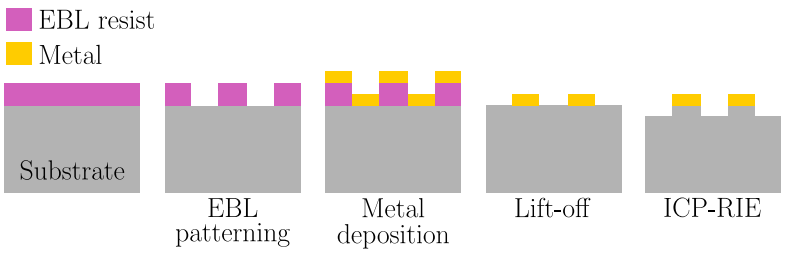

Figure 4.7: Schéma du procédé de fabrication de la configuration T-TL.

Les dimensions des différents SMDSGs fabriqués sont présentées dans la table 4.3. La valeur indiquée pour la période Λ est celle de la période encodée en lithography électronique, puisque la précision de la calibration du masqueur électronique est considérée plus élevée par rapport à la précision de la mesure sur une image MEB (Microscopie Electronique à Balayage). Le facteur de remplissage F est mesuré sur les images MEB en vue de dessus. Les hauteurs des dents de GaAs H et de l'or H_{Au} sont mesurées à partir des vues en coupe du profil des structures. Ces vues en coupe sont réalisées par clivage ou gravure ionique puis imagées par MEB. Enfin, la hauteur du titane H_{Ti}, dans le cas des contacts TiAu, n'est pas mesurable par MEB, et la valeur indiquée est la hauteur idéale déposée associée à l'incertitude du dépôt.

	Paramètre des SMDSGs				
Nom de la structure	Λ (nm)	F	H (nm)	H_{Au} (nm)	H_{Ti} (nm)
B-TE-Au-1	170	0,49 ± 0,01	84 ± 5	40 ± 3	
B-TE-Au-2a	210	0,53 ± 0,01	85 ± 5	36 ± 3	
B-TE-Au-2b	210	0,39 ± 0,01	85 ± 5	36 ± 3	
B-TE-TiAu-1	180	0,53 ± 0,01	89 ± 6	33 ± 5	5 ± 1
B-TE-TiAu-2	220	0,47 ± 0,01	107 ± 7	35 ± 4	
T-TM-Au	150	0,55 ± 0,01	Coupe par clivage: 29 ± 2 Coupe par gravure FIB: 31 ± 4	Coupe par clivage: 56 ± 3 Coupe par gravure FIB: 49 ± 5	
T-TM-TiAu	100	0,57 ± 0,01	88 ± 6	27 ± 4	5 ± 1

Table 4.3: Résumé des dimensions mesurées pour les SMDSGs fabriqués.

La figure 4.8 montre les résultats de caractérisation optique des structures B-TE fabriquées, et la figure 4.9 montrent ces résultats pour les structures T-TM. Les spectres en transmission et en réflection pour les polarisations TE et TM sont mesurés entre 900 nm et 985 nm à l'aide d'un laser accordable. Chaque structure a été mesurée en focalisant le faisceau laser sur sa face supérieure avec un waist estimé à 10 µm, pour des structures de 40 µm de côté. Le réglage de la polarisation est permis par une lame demie-onde. Bien que les erreurs sur les dimensions induitent par la fabrication soient dans certains cas assez importantes par rapport à la structure idéale visée, les mesures optiques montrent de haut niveaux de transmission pour toutes les structures en considérant la polarisation adéquate.

Cela démontre la robustesse des SMDSGs face aux erreurs de fabrication. Des transmissions allant de 75% à 85% sont mesurées, ce qui est supérieur à la transmission de Fresnel à l'interface GaAs/air qui est d'environ 70%. Ces résultats démontrent donc l'adaptation d'impédance optique qu'offrent ces structures métalliques. La table 4.4 résume les valeurs de transmission, de réflection, et de pertes mesurées à 940 nm. Les pertes, associées à l'absorption et à la diffusion, valent $1 - R - T$ avec R la réflection et T la transmission.

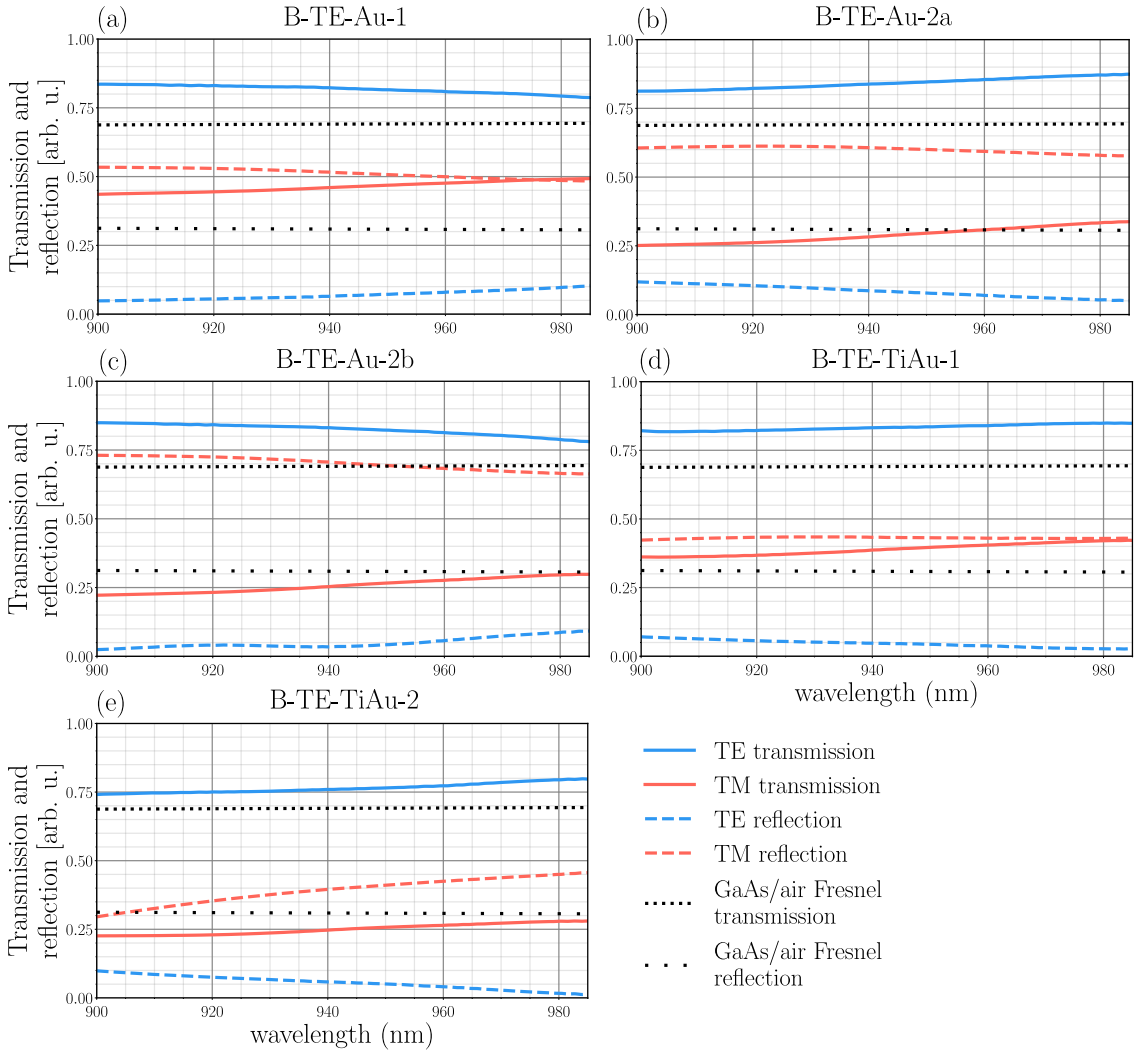

Figure 4.8: Mesure de la réflection et de la transmission en incidence normale entre 900 et 985 nm des structures B-TE fabriquées.

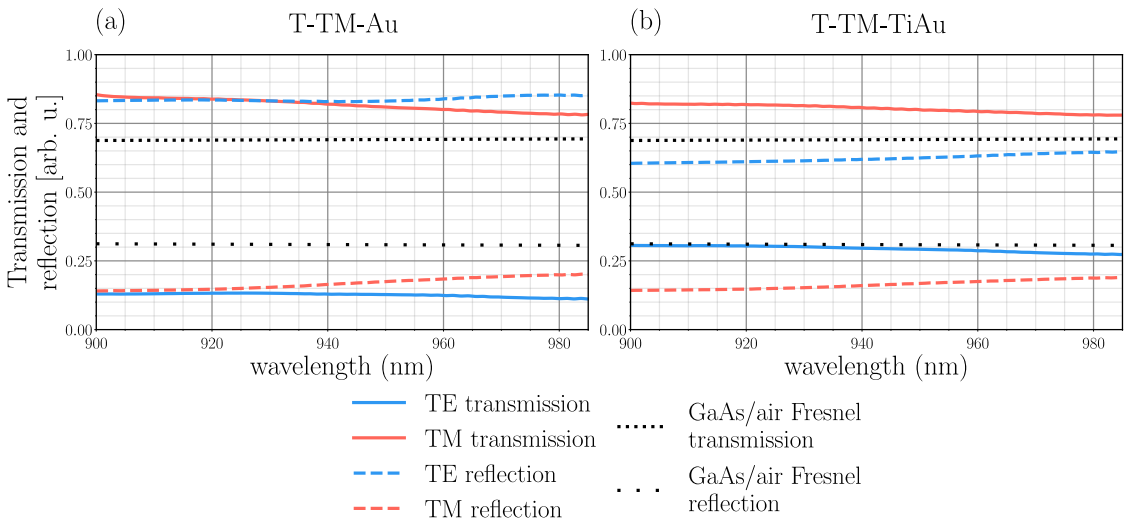

Figure 4.9: Mesure de la réflection et de la transmission en incidence normale entre 900 et 985 nm des structures T-TM fabriquées.

	T (940 nm)		R (940 nm)		Pertes (940 nm): absorption et diffusion	
	TE	TM	TE	TM	TE	TM
B-TE-Au-1	0.82	0.46	0.06	0.51	0.12	0.03
B-TE-Au-2a	0.84	0.28	0.09	0.61	0.07	0.11
B-TE-Au-2b	0.83	0.25	0.03	0.7	0.14	0.05
B-TE-TiAu-1	0.83	0.38	0.05	0.43	0.12	0.19
B-TE-TiAu-2	0.76	0.25	0.06	0.39	0.18	0.36
T-TM-Au	0.13	0.82	0.83	0.16	0.04	0.02
T-TM-TiAu	0.29	0.81	0.62	0.16	0.09	0.03

Table 4.4: Résumé de la transmission, la réflection, et les pertes $= 1 - R - T$ mesurées à 940 nm pour les SMDSGs fabriqués. Les valeurs sont extraites des mesures présentées en figures 4.8 et 4.9.

En plus de la caractérisation optique, la résistance électrique de couche mince, permettant de quantifer l'efficacité du transport latéral du courant électrique par l'électrode, a été mesurée. Pour cette mesure, des réseaux de lignes d'or ont été fabriqués en faisant varier leur longueur et le nombre de lignes, dont les dimensions sont similaires aux lignes métalliques dans les SMDSGs fabriqués dans ces travaux. Des pads de contact en TiAu ont été déposés à leurs extrémités. Ainsi, la résistance des réseaux a pu être mesurée dans une configuration deux pointes comme le montre la figure 4.10. De cette mesure, la résistance de couche mince R_{sh} a pu être calculée en appliquant l'équation suivante:

$$R_{sh} = (R - R_p).N.\frac{W}{L} \tag{4.2}$$

Où R est la résistance mesurée, R_p est la résistance parasite provenant des contacts et des pointes et mesurée en court-circuit, N est le nombre de lignes dans le réseau, W est la largeur des lignes mesurée à partir d'images MEB, et L est la longueur des lignes. La figure 4.11 montre le résultat des mesures, avec une résistance de couche mince moyenne mesurée à $1,4 \pm 0,1 \Omega.sq^{-1}$.

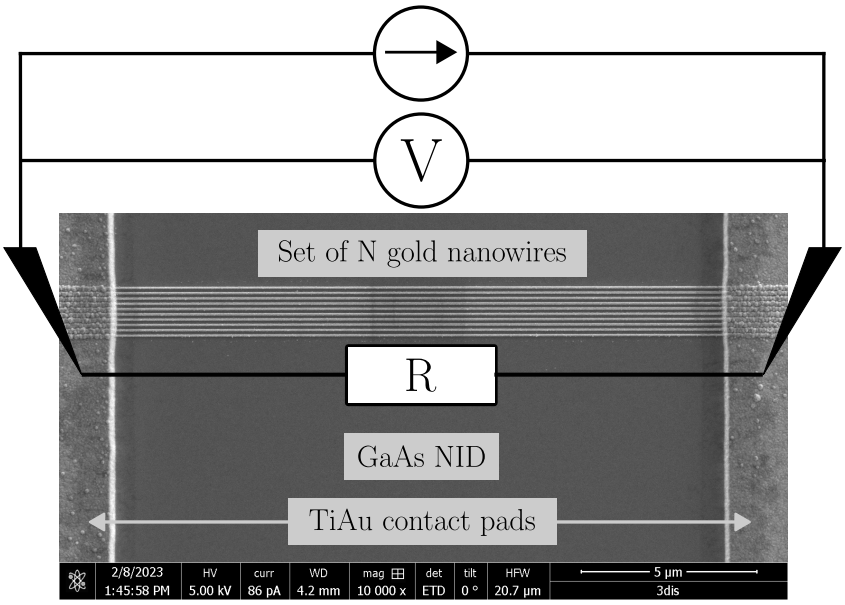

Figure 4.10: Schéma du principe de la mesure en configuration deux pointes de la résistance électrique d'un groupe de nanofils.

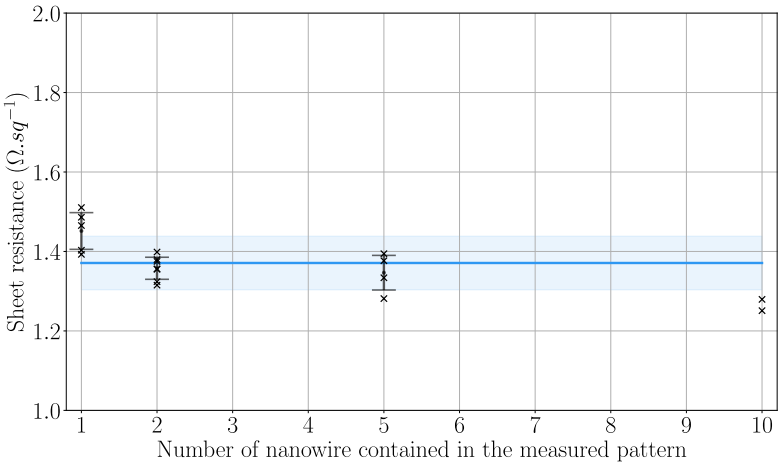

Figure 4.11: Mesure de la résistance de couche mince en fonction du nombre de nanofils d'or. La ligne bleue est la valeur moyenne sur la totalité des mesures, associée à la déviation standard marquée par la zone en bleu clair.

4.4 Illumination à spectre structuré pour l'amélioration du suivi optique du diaphragme dans les VCSELs à diaphragme d'oxyde

Ce chapitre rapporte l'utilisation d'une source à spectre structuré couplée à un système de microscopie en réflection pour l'amélioration du suivi optique du diaphragme dans les VCSELs à diaphragme d'oxyde. Ce diaphragme, élement crucial pour la majorités des VCSELs fabriqués aujourd'hui, est déterminant pour les performances électro-optiques de ces composants. Le principe du suivi optique est présenté en figure 4.12, et le système global composé de la source à spectre structuré, du système d'imagerie, et du four d'oxydation à hublot est présenté en figure 4.13. Le diaphragme d'oxyde, situé sous le miroir de Bragg supérieur du VCSEL, est difficile à détecter à 400°C, température typique du procédé d'oxydation par voie humide de semi-conducteurs III-V à base d'aluminium. A cette température, l'absorption par le DBR devient importante dans le spectre visible, et le contraste entre la zone oxydée et la zone non oxydée s'abaisse plus ou moins selon la composition de l'empilement VCSEL observé. Ces travaux visent à améliorer la méthode de suivi précédemment développée au LAAS-CNRS consistant en l'illumination du VCSEL par un spectre étroit sélectionné pour maximiser le contraste. Cette méthode n'exploite qu'une petite partie de l'information spectrale présente dans la gamme du visible. Lorsque cette information diminue à haute température, la restriction à une seule bande spectrale devient problématique. L'implémentation d'une source à spectre structuré permet d'exploiter au maximum les informations spectrales pour maximiser la discernabilité de l'oxyde, tout en restant dans la gamme spectrale du visible dans laquelle l'utilisation d'un capteur d'images CMOS à haute résolution spatiale est possible.

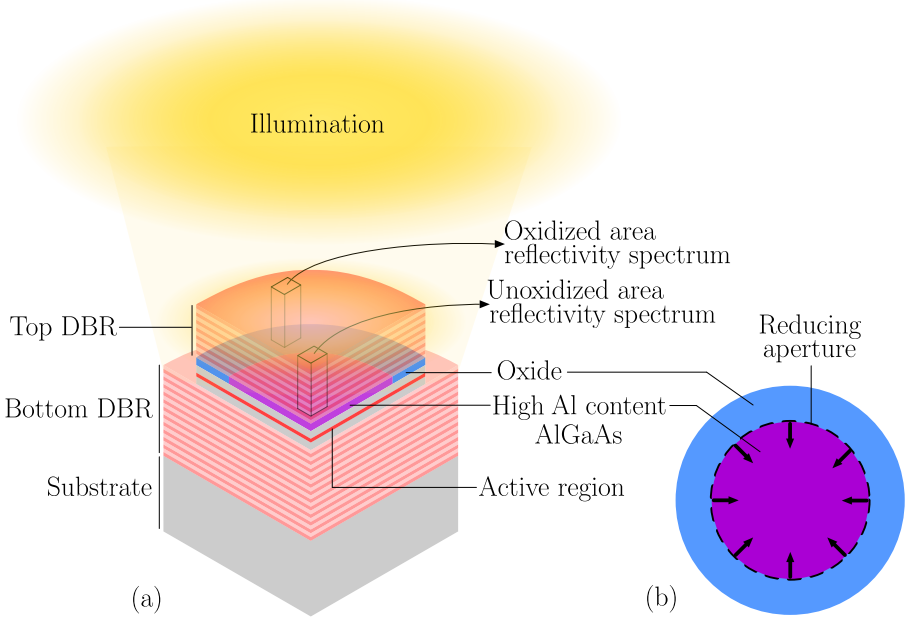

Figure 4.12: Schéma du principe du suivi du front d'oxyde situé sous le DBR supérieur par réflectométrie, avec (a) une vue en coupe, et (b) une vue de dessus.

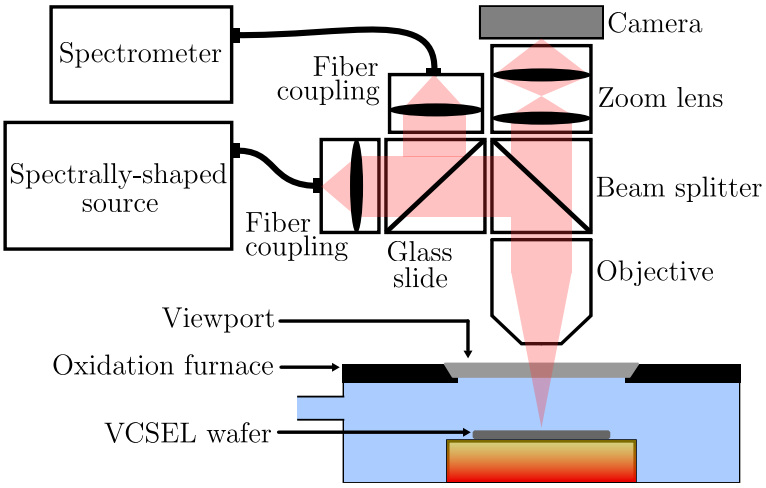

Figure 4.13: Schéma du système d'imagerie placé au dessus du four d'oxydation.

La source à spectre structuré est présentée en figure 4.14. Le faisceau puissant et large bande (450 - 2400 nm) d'un laser supercontinuum est envoyé sur un réseau de diffraction permettant de séparer spatialement, dans le plan horizontal, les bandes spectrales qui sont ensuite collimatées et envoyées sur le DMD. La modulation de largeur d'impulsions des micro-miroirs du DMD permet de moduler de manière indépendante l'intensité de chaque bande spectrale. Dans ces travaux, la modulation des bandes spectrales étalées dans le plan horizontal se fait en agissant sur les 640 colonnes de micro-miroirs. Le spectre structuré est ensuite collecté, recombiné à l'aide d'un second réseau de diffraction, et couplé dans une fibre optique pour être envoyé dans le système d'imagerie.

Une étape de calibration de la source est nécessaire pour mesurer à la fois le spectre panchromatique, qui correspond au spectre quand le DMD agit comme un miroir, la transmission en fonction de la largeur d'impulsion encodée, ainsi que la résolution de la structuration spectrale. Pour ces travaux, la distribution en longueur d'onde dans le plan horizontal du DMD est également mesurée afin de proposer une information supplémentaire, mais relier les données spectrales aux indices des colonnes de micro-miroirs est suffisant. La résolution de la source a été mesurée à environ 0,9 nm pour une plage spectrale disponible d'environ 150 nm.

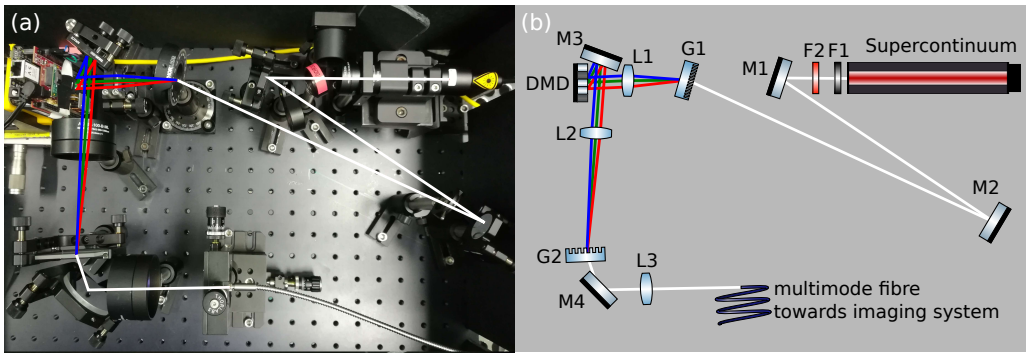

Figure 4.14: (a) Photographie, et (b) schéma de la source spectralement structurable. Composants optiques: filtres F1 et F2; miroirs M1 à M4; réseaux de diffraction G1 et G2, lentilles L1 à L3; matrice de micro-miroirs (DMD). Figure provenant de [9].

Après l'étape de calibration, la source à spectre structuré permet d'acquérir les données spatiales et spectrales de la scène observée, appelé cube hyperspectral, par balayage en

longueur d'onde. Pour cela, une acquisition multiplexée par l'application d'une séquence de masques de type Hadamard sur le DMD est préférée à une acquisition classique pour laquelle une séquence de fentes est utilisée. Cela permet d'acquérir le signal de plusieurs bandes spectrales à la fois, ce qui augmente le signal mesuré, augmentant le rapport signal à bruit et réduisant le temps d'acquisition. Une étape de reconstruction du cube hyperspectral est cependant nécessaire, mais n'est pas incompatible avec un système temps réel en optimisant le temps de calcul. La figure 4.15 présente l'extraction des données hyperspectrales pour le calcul des poids associés aux bandes spectrales. Ce calcul se fait avec comme critère d'optimisation la discernabilité entre la zone oxydée et la zone non oxydée. La figure 4.15a montre la vue d'un VCSEL émettant à 850 nm déjà oxidé sous illumination panchromatique. Les spectres en réflectivités associés à l'AlOx (oxide) et à l'AlGaAs (matériau non oxydé) sont tracés en figure 4.15b, et le contraste correspondant à la différence entre ces deux spectres est tracé en figure 4.15c. C'est la partie positive de ce contraste qui est retenue pour la pondération spectrale. C'est une méthode simple de pondération, qui découle d'une simplification de la méthode d'optimisation FDA (Fisher Discriminant Analysis), dans laquelle la séparation entre deux classes est optimisée en maximisant la moyenne entre les deux classes tout en minimisant la variance au sein de chaque classe. Dans le cas du suivi de l'oxyde, la figure 4.15b montre que la variance dans chaque classe peut être considérée comme constante. C'est donc la moyenne entre les classes, et donc le contraste, qui est la grandeur privilégiée pour la détermination des poids.

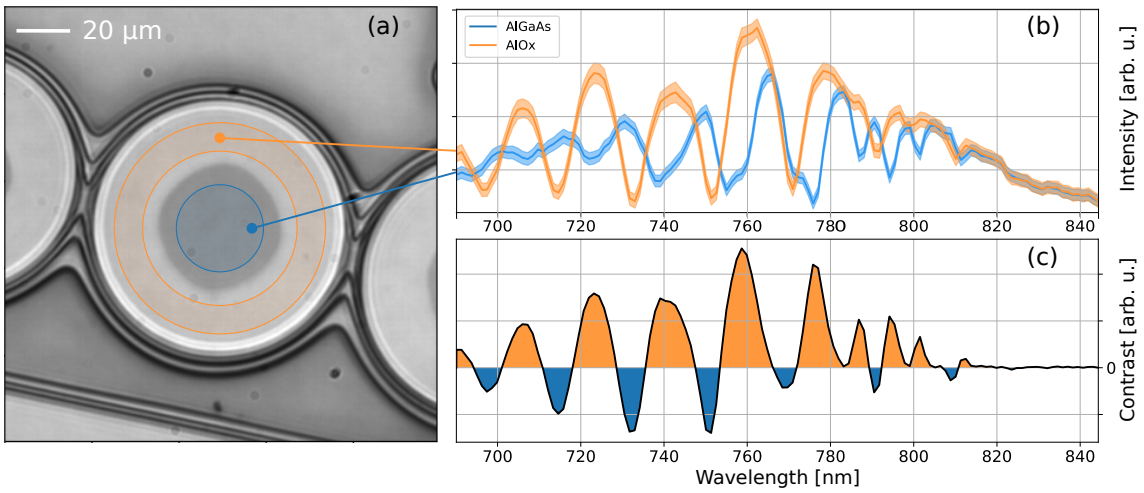

Figure 4.15: (a) Vue du dessus de l'échantillon sous illumination panchromatique avec la région de l'AlOx (orange) et la région de l'AlGaAs (bleu). (b) Moyenne de la réflectivité de chaque région (ligne centrale) entouré par la variance (zone plus claire). (c) Distribution spectrale du contraste entre les régions AlOx et AlGaAs. Figure provenant de [9].

Cette méthode de structuration du spectre d'illumination à été comparée à une illumination panchromatique, et à une illumination à spectre étroit, appelée monochromatique. Cette comparaison a été réalisée par une observation in-situ sur un VCSEL déjà oxydé et à température ambiante. Ces conditions d'observation sont appelé inspection statique. La figure 4.16 montre les résultats de détection du front d'oxydation pour les trois spectres d'illumination. La détection est effectuée en fittant une fonction d'erreur sur les segments allant du centre du mesa à son bord sur 360° tous les 2°. Les figures 4.16g, 4.16h, et 4.16i montrent que l'anisotropie de l'oxydation latérale, caractérisée par la présence d'un grand axe et d'un petit axe à 90° l'un de l'autre, ne ressort clairement que pour l'illumination à spectre structuré. De plus, le détection du front d'oxyde est plus lisse avec cette illu-

mination, ce qui est plus représentatif de la réalité, comme le montre l'image MEB du diaphragme d'oxyde prise après gravure FIB du mesa en figure 4.17. Par ailleurs, la largeur de l'intervalle de confiance à 95% sur la détection de la position du front d'oxyde montré en 4.16i est la plus faible des trois illuminations. L'illumination à spectre structuré permet d'obtenir un compromis entre une illumination panchromatique puissante permettant des acquisitions d'images rapides mais avec peu de contraste, et une illumination monochromatique très contrastée mais dont les images sont altérées par le speckle induit par la cohérence de la source laser et le spectre étroit.

L'illumination structurée permet donc, dans le cas de l'inspection statique, d'améliorer la précision de la détection de l'oxyde ainsi que la robustesse de cette détection par l'apport d'une grande liberté dans le choix du spectre d'illumination. Les prochains travaux viseront l'implémentation de ce système pour un monitoring en temps réel à haute température, où d'autres méthodes d'optimisation des spectres d'illumination tel que la PCA (Principal Component Analysis) pourront être évaluées. Enfin, la gamme spectrale du SWIR (Short Wave Infrared) est très prometteuse pour l'amélioration de la détection du diaphragme d'oxyde, puisqu'elle se situe hors de la plage d'absorption du DBR supérieur, et hors de la plage de haute réflectivité de ce DBR pour les VCSELs standards émettant à 850 nm, 940 nm et 1300 nm. Jusqu'à très récemment, l'exploitation de cette plage spectrale était limitée par la faible résolution spatiale des capteurs d'images dédiés. Cependant, de nouveaux capteurs à haute résolution spatiale de technologie CMOS pourraient aujourd'hui permettre d'exploiter facilement cette fenêtre spectrale.

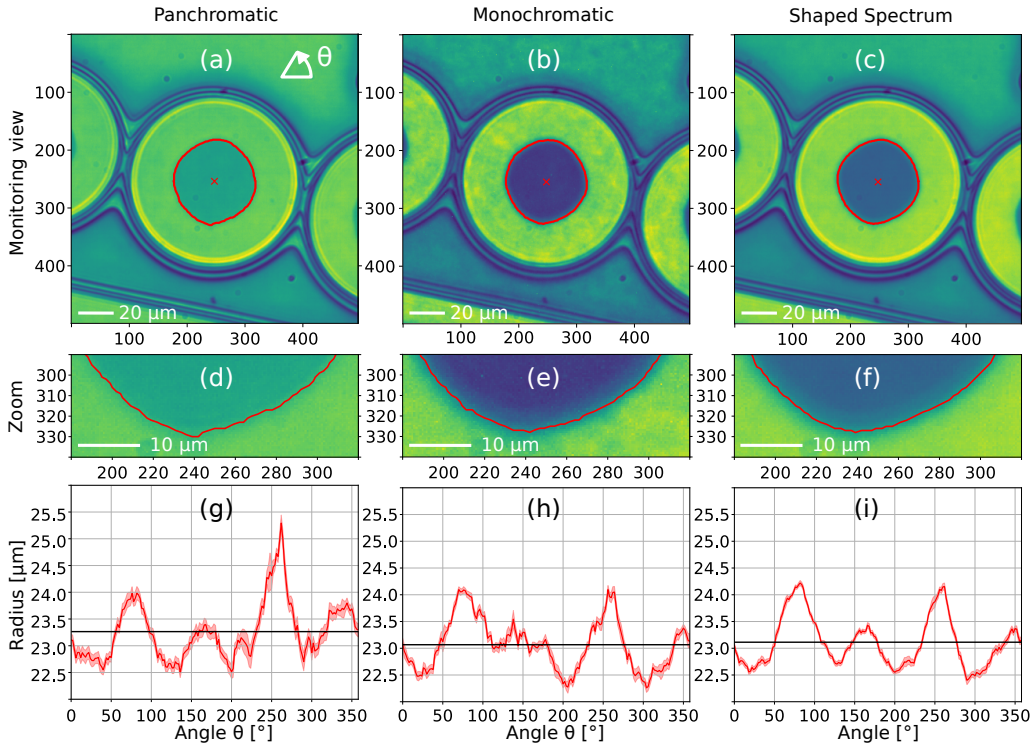

Figure 4.16: Détection du front d'oxydation pour les trois spectres d'illumination: panchromatique [(a), (d), (g)], monochromatique [(b), (e), (h)], et structuré [(c), (f), (i)]. A partir des vues [(a)-(c)] un fonction d'erreur a été fittée pour déterminer la position du front d'oxyde (ligne rouge), présentée en coordonnées polaires en [(g)-(i)]. La largeur de l'intervalle de confiance à 95% sur la détection de cette position par le fit est montrée par la zone rouge claire. Le rayon moyen détecté est représenté par la ligne noire. Figure provenant de [9].

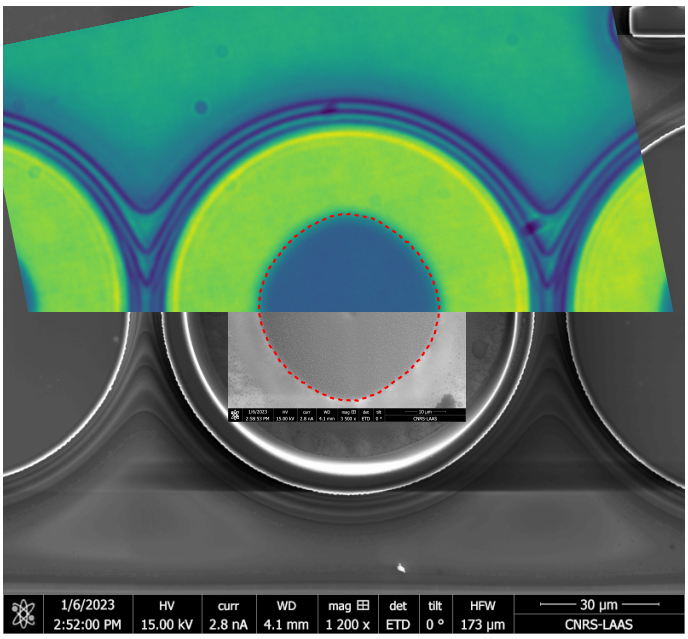

Figure 4.17: Image composite dont la composition du haut vers le bas est la suivante: la vue obtenue en inspection in-situ sous illumination structurée, l'image MEB à fort grossissement de la gravure FIB révélant le diaphragme d'oxyde, l'image MEB à faible grossissement de la gravure FIB révélant le diaphragme d'oxyde. La ligne rouge en pointillée représente le front d'oxyde détecté sous illumination structurée. Figure provenant de [9].

4.5 Conclusions et perspectives

Ce travail est une contribution à deux axes d'amélioration des performances des VCSELs, dans le contexte d'une augmentation rapide de la demande en VCSELs, et de la diversification de leurs applications et de leur cahier des charges. Les VCSELs de forte puissance et les VCSELs monomodes sont deux parties importantes de cette demande, et sont associés aux deux défis considérés dans ce travail. Le premier est la limitation de l'augmentation de la surface active pour les VCSELs standards, qui empêche l'augmentation de leur puissance d'émission. Le second est la difficulté du contrôle précis de la taille et de la forme du diaphragme dans la fabrication des VCSELs à diaphragme d'oxyde, pourtant cruciaux pour leurs performances électro-optiques, en particulier lorsque le fonctionnement monomode est visé.

Dans les VCSELs à diaphragme d'oxyde, l'injection du courant dans la structure de fait par un contact métallique de forme annulaire pour empêcher le métal de bloquer l'émission laser. L'emploi de cette technique fait que le courant est principalement injecté sur les bords du diaphragme d'oxyde lorsque son diamètre devient important, ce qui laisse une grande partie de la zone active inutilisée dans le processus d'amplification. Dans ce travail, la voie de recherche suivie pour uniformiser l'injection du courant sur de grandes zones actives est le remplacement du contact supérieur annulaire par un contact plein constitué d'une électrode transparente. Ce travail se concentre spécifiquement sur une nouvelle électrode transparente, introduite dans l'article [2] en 2020 par Tomasz Czyszanowski et al. qui consiste en une combinaison d'un réseau sub-longueur d'onde unidimensionnel en semi-conducteur entrelacé avec un autre réseau du même type en métal. Cette électrode, appelé SMDSG, pour Semiconductor-Metal Deep-Subwavelength Grating, a la propriété d'être hautement transparente sur une région spectrale relativement large pour une polarisation transverse électrique (TE) ou transverse magnétique (TM), tout en tirant parti des excellentes propriétés électriques d'un contact métallique. La gamme spectrale de haute transmission est accordable en optimisant les dimensions du réseau. Dans le cas d'une haute transmission de la polarisation TE, les lignes métalliques sont localisées dans les rainures du réseau semi-conducteur, tandis qu'elles sont situées au sommet des dents de semi-conducteur pour la haute transmission de la polarisation TM. Entre les deux configurations de SMDSG, le mécanisme de transmission est différent, ce qui engendre des différences entre leurs dimensions optimales et leurs signatures spectrales.

Ce travail démontre la fabrication, ainsi que la haute transmission et les excellentes propriétés électriques des deux configurations de SMDSG fabriquées, composées de GaAs et de contacts métalliques à base d'or. Les dimensions de ces SMDSGs fabriqués et caractérisés ont été optimisées pour une haute transmission dans le proche infrarouge, et plus spécifiquement à 940 nm en incidence normale. C'est la première démonstration de SMDSGs à haute transmission dans cette gamme spectrale. Les paramètres d'optimisation sont la périodicité du réseau et le facteur de remplissage, ainsi que la hauteur des dents de semiconducteur, tandis que la hauteur des lignes métalliques a été fixée. Pour cette plage spectrale, la périodicité requise du réseau était comprise entre 100 et 220 nm, en fonction de la configuration du SMDSG fabriqué et de la composition du contact métallique. Les procédés de fabrication des SMDSGs pour la haute transmission des polarisations TE et TM ont été développés, ce qui implique l'utilisation de techniques de nanostructuration et l'auto-alignement du réseau de semiconducteur et du réseau métallique. Des SMDSGs avec des contacts métalliques fait de Au et de TiAu ont été fabriqués, car la composition TiAu est généralement utilisée pour les contacts ohmiques sur du GaAs dopé p, dans les VCSELs ou d'autres dispositifs à base de GaAs. Pour les deux compositions de contact,

et pour les deux configurations de SMDSG, une transmission supérieure à 80% a été mesurée en considérant la polarisation adéquate entre 900 et 985 nm, ce qui est supérieur à la transmission de Fresnel à l'interface entre le GaAs et l'air. En ce qui concerne la caractérisation des propriétés électriques, la conduction latérale du courant a été quantifiée par la mesure d'une résistance de couche mince de $1,4 \pm 0,1\Omega.sq^{-1}$ en considérant des lignes métalliques d'or de 48 nm d'épaisseur. Il s'agit d'un excellent résultat pour des nanofils métalliques, qui est au moins dix fois plus faible que pour les autres electrodes transparentes implémentées dans les VCSELs jusqu'à présent. La résistance spécifique de contact, qui permet de quantifier l'efficacité de l'injection verticale du courant, n'a pas pu être mesurée par manque de temps, même si les informations pour effectuer cette mesure se trouvent dans ce manuscrit. Cependant, puisque ce travail prouve que les deux configurations de SMDSG offrent la possibilité d'utiliser le contact ohmique standard TiAu/p-GaAs, une injection verticale efficace du courant est attendue.

Ces résultats montrent que l'emploi des SMDSGs comme électrode supérieure dans les VCSELs est très prometteur pour l'obtention de plus forte puissances d'émission dans le proche infrarouge. Néanmoins, dans le cas de dispositifs basés sur une cavité résonnante comme les VCSELs, l'utilisation de SMDSGs optimisés en transmission pour une polarisation donnée conduit à ce que l'autre polarisation soit principalement réfléchie. Il en résulte un gain net plus élevé pour cette polarisation réfléchie, ce qui dégrade le rendement du VCSEL. Une meilleure façon d'utiliser les SMDSGs pourrait être de maximiser la réflectivité d'une polarisation tout en minimisant l'absorption pour assurer une transmission efficace lorsque le mode n'est pas réfléchi. Du travail doit être fait dans ce sens pour démontrer l'emploi de SMDSGs dans des VCSELs de forte puissance. Néanmoins, les SMDSGs fabriqués dans le cadre de ce travail constituent des solutions de contact électrique pour des dispositifs optoélectroniques sans cavité résonante, tels que les LEDs à émission par la surface ou les photodétecteurs, qui pourraient bénéficier de l'adaptation d'impédance optique entre le semi-conducteur et l'air offerte par les SMDSGs.

Le deuxième axe d'amélioration des performances des VCSELs visé dans ce travail concerne les VCSELs à diaphragme d'oxyde. La forme et la dimension de l'ouverture de l'oxyde définissent la distribution modale de l'émission. Généralement, un petit diamètre d'ouverture inférieur à 5 µm permet une émission monomode. Pour le contrôle de ce diaphragme, des techniques de monitoring optique du procédé d'oxydation thermique par voie humide sont utilisées. En particulier, le groupe photonique du laboratoire LAAS-CNRS a développé une illumination à bande spectrale étroite couplée à un système d'imagerie par réflectométrie placé au-dessus d'un four d'oxydation comportant un hublot pour la visualisation [3]. Il permet de sélectionner la bande spectrale d'illumination qui donne la meilleure discernabilité entre le matériau oxydé et le matériau non oxydé pour un empilement VCSEL donné. Cependant, cette discernabilité peut être faible car la fine couche d'AlGaAs à oxyder est enfouie sous le miroir de Bragg supérieur du VCSEL. Lors du procédé d'oxydation, la queue d'absorption du miroir de Bragg est décalée vers le rouge par la haute température, ce qui réduit considérablement le contraste pour les longueurs d'onde du visible. Cette gamme spectrale est utilisée pour l'illumination, car elle est compatible avec l'utilisation de caméras CMOS, dont la résolution spatiale est élevée. Le contraste à haute température dans cette gamme dépend également de l'empilement VCSEL, et la détection du diaphragme d'oxyde peut devenir très difficile dans certains cas, comme l'ont signalé certains industriels. De plus, la gamme de haute réflectivité du miroir de Bragg supérieur empêche l'observation dans la gamme spectrale du proche infrarouge pour des VCSELs émettant dans celle-ci. Malgré la discernabilité théorique élevée de l'oxyde dans le SWIR (Short Wave Infrared), les caméras à haute résolution spatiale faisaient défaut

dans cette gamme de longueurs d'onde jusqu'à très récemment. Le petit diamètre visé dans la fabrication de VCSELs monomodes oblige à l'utilisation d'un capteur avec une bonne résolution spatiale.

Dans ce travail, il a été décidé de développer une technique d'illumination qui maximise l'exploitation de l'information spectrale dans le visible, afin de conserver l'avantage de l'utilisation de composants optiques conventionnels, dont la caméra CMOS. Une source structurable spectralement a été développée et implémentée comme source d'illumination dans le système d'imagerie par réflectométrie. Sa gamme spectrale modifiable donne la possibilité de s'adapter aux caractéristiques spectrales de l'empilement VCSEL observé. Cette source, composée principalement d'un laser supercontinuum et d'une matrice de micromiroirs (DMD), permet d'effectuer une acquisition rapide du cube de données hyperspectrales par balayage spectrale multiplexé, ainsi que de structurer le spectre d'illumination avec une résolution spectrale inférieure à 1 nm sur une fenêtre de 150 nm de large. Les informations spatiales et spectrales contenues dans le cube de données sont utilisées pour pondérer les bandes spectrales afin de maximiser la discernabilité entre le matériau oxydé et le matériau non oxydé. Dans ce travail, les pondérations sont basées simplement sur la distribution spectrale du contraste entre les matériaux à distinguer. Une comparaison entre trois types d'illumination pour la détection du diaphragme d'oxyde a été réalisée dans le cadre d'une inspection statique in situ à température ambiante d'un VCSEL déjà oxydé. L'avantage de l'illumination structurée a été démontrée par rapport à une illumination à bande spectrale étroite et à une lumière blanche. Elle permet une détection plus robuste et plus précise du diaphragme, grâce à un compromis entre les images à fort contraste mais altérées par le speckle d'une illumination à bande spectrale étroite, et le fort signal, et donc l'acquisition rapide, lorsqu'une illumination en lumière blanche est utilisée.

Cette technique est compatible avec un monitoring en temps réel, compte tenu des temps d'intégration raisonnablement courts qui peuvent être obtenus. Les travaux futurs consistent à l'implémenter pour un suivi dynamique du front d'oxydation à haute température. De plus, des techniques de traitement plus avancées des informations contenues dans le cube hyperspectral pourraient être employées afin d'optimiser la discernabilité entre deux ou plusieurs zones, améliorant ainsi le monitoring. La plage spectrale du SWIR a été mentionnée comme étant très intéressante pour la détection du front d'oxydation. L'arrivée récente sur le marché de caméras CMOS à résolution spatiale élevée pour le SWIR pourrait permettre d'exploiter facilement cette plage spectrale, en utilisant la technique de l'illumination structurée ou une illumination à bande spectrale étroite pour un système optique plus simple. Enfin, l'utilisation des informations spatiales et spectrales en réflectivité pour le façonnage d'un spectre d'illumination optimisant la discernabilité entre plusieurs zones de la scène observée pourrait être intéressante pour d'autres étapes de mise en forme et de caractérisation des semi-conducteurs.

En conclusion, ce travail apporte de nouvelles possibilités pour l'amélioration des performances des VCSELs, en termes de puissance d'émission et de précision du contrôle du diaphragme d'oxyde, en réponse au contexte applicatif diversifié vers lequel le marché du VCSEL évolue rapidement.

Bibliographie

[1] B. D. Padullaparthi, J. A. Tatum, and K. Iga, *VCSEL Industry: Communication and Sensing*. Wiley : IEEE Press, 2022.

[2] T. Czyszanowski, A. K. Sokól, M. Dems, and M. Wasiak, "Transparent Electrode Employing Deep– Subwavelength Monolithic High-Contrast Grating Integrated with Metal," *Optics Express*, vol. 28, no. 19, p. 28383, 2020.

[3] G. Almuneau, R. Bossuyt, P. Collière, L. Bouscayrol, M. Condé, I. Suarez, V. Bardinal, and C. Fontaine, "Real-Time in situ Monitoring of Wet Thermal Oxidation for Precise Confinement in VCSELs," *Semiconductor Science and Technology*, vol. 23, no. 10, p. 105021, 2008.

[4] M. Morales-Masis, S. De Wolf, R. Woods-Robinson, J. W. Ager, and C. Ballif, "Transparent Electrodes for Efficient Optoelectronics," *Advanced Electronic Materials*, vol. 3, no. 5, p. 1600529, 2017.

[5] C. Chua, R. Thornton, D. Treat, V. Yang, and C. Dunnrowicz, "Indium Tin Oxide Transparent Electrodes for Broad-Area Top-Emitting Vertical-Cavity Lasers Fabricated Using a Single Lithography Step," *IEEE Photonics Technology Letters*, vol. 9, no. 5, pp. 551–553, 1997.

[6] L. Jie, X. Chen, X. Meng, W. Jun, and M. M. Ming, "The Effect of Graphene for Large Aperture Vertical Cavity Surface Emitting Laser," in *International Photonics and OptoElectronics Meetings*, p. OF5A.1, OSA, 2014.

[7] H. Ding, H. Li, B. Guan, and L. Liu, "Research on Graphene as Transparent Electrode of VCSEL Arrays," in *2021 4th International Conference on Electron Device and Mechanical Engineering*, (Guangzhou, China), pp. 130–134, IEEE, 2021.

[8] X. Guo, L. Shi, C. Li, J. Dong, B. Liu, S. Hu, and Y. He, "Research of the Use of Silver Nanowires as a Current Spreading Layer on Vertical-Cavity Surface-Emitting Lasers," *Chinese Physics B*, vol. 25, no. 11, p. 114208, 2016.

[9] N. Monvoisin, E. Hemsley, L. Laplanche, G. Almuneau, S. Calvez, and A. Monmayrant, "Spectrally-Shaped Illumination for Improved Optical Inspection of Lateral III-V-semiconductor Oxidation," *Optics Express*, vol. 31, no. 8, p. 12955, 2023.

APPENDIX A

Tomasz Czyszanowski, Adam K. Sokół, et al., "Transparent electrode employing deep–subwavelength monolithic high-contrast grating integrated with metal", Optics Express, 2020

Research Article | Vol. 28, No. 19 / 14 September 2020 / Optics Express 28383

Optics EXPRESS

Transparent electrode employing deep–subwavelength monolithic high-contrast grating integrated with metal

TOMASZ CZYSZANOWSKI,* ADAM K. SOKÓŁ, MACIEJ DEMS, AND MICHAŁ WASIAK

Photonics Group, Institute of Physics, Lodz University of Technology, 219 Wólczańska St., 90-924 Łódź, Poland
tomasz.czyszanowski@p.lodz.pl

Abstract: This paper demonstrates designs of transparent electrodes for polarized light based on semiconductor deep-subwavelength monolithic high-contrast gratings integrated with metal (metalMHCG). We provide theoretical background explaining the phenomena of high transmittance in the gratings and investigate their optimal parameters, which enable above 95% transmittance for sheet resistance of 2 ΩSq^{-1} and over 90% transmittance for extremely small sheet resistance of 0.04 ΩSq^{-1} in a broad spectral range below the semiconductor band-gap. The analysis is based on our fully vectorial optical model, which has been verified previously via comparison with the experimental characteristics of similar structures. The transparent electrodes can be realized in any high refractive index material used in optoelectronics and designed for light in spectral ranges starting from ultra-violet with no upper limit for the wavelength of the electromagnetic waves. They not only enable lateral transport of electrons but can also be used as an electric contact for injecting current into a semiconductor.

1. Introduction

The transmission of electromagnetic radiation in the wavelength spectrum from ultraviolet to infrared, from the air through a highly conductive surface to a semiconductor medium (for detectors) or in the opposite direction (for emitters), is of increasing scientific and commercial interest. This is due to rising demand for a wide range of products, from low-current consumer electronics such as touch screens and interactive electronics [1–4] to high-performance devices such as concentrator photovoltaic devices [5–8], light emitting diodes [9] and surface emitting lasers [10,11]. Typically, industrial-scale production of such devices uses indium tin oxide (ITO) for the transparent electrodes. This compound is characterized by significant electrical conductivity and high transparency in the visible range of the optical spectrum. However, the disadvantages of ITO include high cost, brittleness, large absorption in the near and far infrared ranges [12], recycling difficulties and the scarcity of indium [4,13]. An alternative solution is offered by meta-structures, in the form of periodic metal grids or irregular metal nanowire networks [14]. The pitch of such periodic structures or the average distance between their nanowires is larger than the wavelength, and their thickness is minimized to reduce interaction with the electromagnetic field. As well as by absorption and reflection, the transmission is additionally deteriorated by scattering and diffraction. The transmission of the thin ITO, thin metal plates, metal grids, or nanowires, is thus not greater than the transmission through the flat interface between the device and the air. Therefore, meta-structures are used mostly as electrodes implemented on low refractive index glass or polymers, where current is conducted along the surface.

In order to allow current to flow between the electrode and the device, the electrode must be in contact with the semiconductor, which is usually of high refractive index. In this case, the

#400489 https://doi.org/10.1364/OE.400489
Journal © 2020 Received 18 Jun 2020; revised 19 Aug 2020; accepted 19 Aug 2020; published 9 Sep 2020

Optics EXPRESS

electrodes implemented at the semiconductor enable transmission of about 70%, according to the Fresnel equation. The reflection can be reduced by deposition of antireflecting coating however its sheet resistance is at the level of 20-100 Ω/Sq due to sparse distribution of metal fingers [15].

Another group of transparent electrodes are one-dimensional metal periodic gratings that enable lower sheet resistance and significantly higher transmission on the cost of polarization selectivity. The polarization dependent electrodes use densely distributed, subwavelength striped periodic metallic structures, known as plasmonic gratings. These exploit plasmonic effects to enhance light transmission of transverse magnetic (TM) polarization, for which magnetic field of the electromagnetic wave is parallel to the metal stripes [16–21]. In the case of orthogonal transverse electric (TE) polarization, transmission in the plasmonic gratings is significantly suppressed. Plasmonic transmission in the infrared region ($\lambda > 7$ μm) is most efficient in the case of silver, gold, aluminum, and copper structures, due to the large ratio between their imaginary and real refractive indexes compared to other metals. This ratio enables transmission levels of 90%, but reduces in the near-infrared and visible range of the spectrum, contributing to significantly lower transmittance for green and blue. The advantage of this type of structure is the dense distribution of the metal stripes, which enables lower sheet resistance in comparison to metal grids or metal nanowires. A disadvantage is polarization selectivity, which only enables high transmittance of polarization perpendicular to the metal stripes.

Until now, there have been no designs for transparent electrodes with sheet resistance at levels below 10 ΩSq^{-1} that allow for nearly 100% transmission of polarized light in a wide spectrum of electromagnetic waves, from the visible to the infrared region. Similarly, there are no designs with significantly lower sheet resistance of 0.1 ΩSq^{-1} that enable above 90% transmittance of polarized light. This work describes structures of transparent electrodes which allow these ambitious parameters to be achieved.

In recent theoretical works, we presented a highly reflective monolithic high contrast grating (MHCG) [22] the effectiveness of which has been confirmed in a number of experimental demonstrations [23–25]. MHCG is a special case of high contrast grating (HCG) [26] that concept was broadly used in many applications as broadband reflectors [27], filters [28] or lenses [29]. We also proposed an original approach to current injection, based on the use of an MHCG integrated with metal stripes as the conducting mirror, which enables above 98% power reflectance [30]. The period (L) of a typical highly reflecting or transmitting (M)HCG ranges from λ/n to λ, where λ is the wavelength and n the refractive index of the semiconductor grating. In this range of periods, high reflection and high transmission are possible, due to interference between at least two modes propagating in the plane of the grating [26]. However, their spectra are narrow. In gratings of a smaller period ($L < \lambda/n$), referred to as deep-subwavelength gratings (DSGs), only one mode propagates. In this case, high reflectivity is excluded due to the lack of interference between the modes in the grating [26], but broad spectral transmission is possible. The nature of transmission in a DSG is different from that in the two-mode regime. To a certain extent, it can be explained according to homogenization [31] or metamaterial theory [32], according to which the DSG can be replaced with a uniform anisotropic slab that gives standard Fabry-Perot resonances, and hence provides the condition for perfect transmission [33].

In what follows, we show that a deep-subwavelength MHCG integrated with metal (metalMHCG), enables nearly 100% transmittance of the polarized electromagnetic field and high electrical conductivity. We show that the distribution of light in metalMHCGs is not a plane wave and can be structurized to reduce the absorption or reflection of light. In particular, we demonstrate that despite the presence of metal the parameters of an metalMHCG can be tuned to achieve almost 100% transmission and investigate the optical and electrical properties of the gratings. In section 2, we present the details of metalMHCG designs and provide a brief discussion of our numerical model. In sections 3-5, we illustrate optical phenomena supporting high transmittance in two configurations of the metalMHCG. In section 6, we investigate the influence of the metal

Research Article | Vol. 28, No. 19 / 14 September 2020 / Optics Express 28385
Optics EXPRESS

geometry and material parameters of the metalMHCGs on optical transmittance. Finally, in section 7 we analyze the electrical properties of the gratings.

2. Structure and model

The metalMHCG used in the calculations consists of an infinitely thick, monolithic undoped semiconductor layer with etched stripes on the surface. The undoped semiconductor enables us to assume a lack of free-carrier absorption in calculations. Two design variants are considered. In the first, (B) metal stripes are deposited on the bottom of the grooves between the semiconductor stripes (Fig. 1(a)). In the second, (T) metal stripes are deposited on top of the semiconductor stripes (Fig. 1(b)). An MHCG grating composed of an undoped monolithic semiconductor and a plasmonic grating composed of densely distributed metal stripes implemented on an undoped semiconductor substrate (Au-grating) are used as references. The thickness of the air above all the gratings is assumed to be infinite. In the calculations, we consider a single period of the gratings with periodic boundary conditions, which elongates the grating to infinity in the lateral direction. The parameters of the metalMHCG are as follows: L – period of the grating; H – height of the semiconductor stripe; H_m – thickness of the metal stripe; F – the duty cycle, as the ratio of the width (a) over the period (L) of the semiconductor stripe. The parameters L, F, H of the MHCG are defined identically. In the case of the Au grating, L is also the period of the grating, while F and H are the duty cycle and the height of the metal stripes, respectively. Unless stated otherwise, we assume GaAs as semiconductor material and gold as the metal, a wavelength of 1 μm and a metal stripe thickness (H_m) of 50 nm. The refractive index of the semiconductor is assigned by n_s and that of the metal by n_m. For a wavelength of 1 μm, the refractive indexes of GaAs and Au are 3.5 and 0.15–6.6i, respectively. In general, a metalMHCG can be composed of any semiconductors and dielectric materials that are of acceptably low absorption.

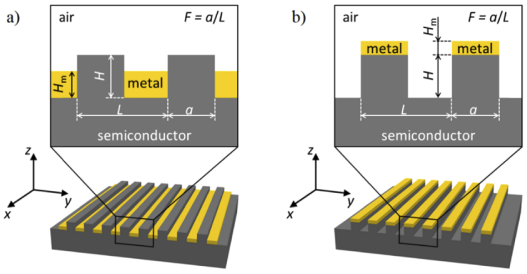

Fig. 1. a) B configuration of the metalMHCG structure, composed of semiconductor bars implemented on a substrate of the same material and metal stripes implemented between the semiconductor bars; b) T configuration with metal stripes implemented on top of the semiconductor bars. The geometrical parameters of the metalMHCG and the coordinate system are defined in the figure.

To determine the optical transmittance through the gratings, we use the plane-wave reflection transformation method (PWRTM) [34], which is a fully vectorial optical model. Because of the periodicity of the gratings, the optical field of the propagating electromagnetic wave can be expressed in the form of Bloch waves:

$$\Psi(y) = e^{ik_y y} f(y), \tag{1}$$

where $f(y)$ is a periodic function with the same the period as the gratings (L) and k_y is the lateral component of the wavevector, ranging from $-\pi/L$ to π/L. The model has been shown to have high reliability by comparison with experimental results [23,25]. In the analysis, we consider TE polarization, for which the electric field is parallel to the gratings stripes, and TM

Optics EXPRESS

polarization perpendicular to the gratings. B-TE, B-TM, T-TE and T-TM refer to metalMHCG configurations through which a given light polarization is transmitted. For example, B-TE stands for a B configuration through which TE light polarization is transmitted. The same applies to the MHCG grating. Figure 2(a) illustrates the numerical convergence of transmission, calculated by PWRTM as a function of the number of plane waves for exemplary B-TE and T-TM structures with the following respective parameters: $L = 226$ nm, $H = 87$ nm and $L = 167$ nm, $H = 47$ nm. In both cases, $F = 0.5$ and $H_m = 50$ nm. The results show that using more than 60 plane waves for the TE polarization and over 600 for the TM polarization does not modify the calculated transmission by more than 10^{-5}. These numbers of plane waves are therefore used in the analysis. The convergence for the TM polarization requires larger number of plane-waves with respect to TE polarization although PWRTM is enhanced by the inverse rule [35,36]. The discrepancy in the convergence is mainly attributed to the electric field distribution of TM polarization that reveals abrupt features at the metal interfaces as shown later in Fig. 5.

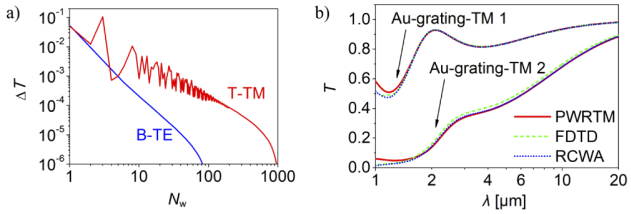

Fig. 2. a) Absolute value difference between transmittances calculated for 2000 plane waves and given numbers of planewaves (N_w) for B-TE (blue line) and T-TM (red line) configurations, b) transmittance calculated by FDTD (dashed line), RCWA (dotted line) and PWRTM (solid line) for a gold grating implemented on top of a substrate with a refractive index of 1.45 and the following parameters: $L = 300$ nm, $a = 200$ nm (Au-grating-TM 1) and $L = 300$ nm, $a = 285$ nm (Au-grating-TM 2).

Figure 2(b) reveals very close consistency between the transmission spectrum calculated by PWRTM, the finite-difference time-domain method (FDTD) and rigorous coupled-wave analysis (RCWA) for two gratings, composed of gold stripes implemented on a substrate with a refractive index of 1.75 [22] (Au-grating-TM 1 and 2) illuminated by the normal incidence of TM polarization. The spectrum calculated by FDTD is reproduced from the results presented in [17]. The RCWA spectrum is calculated using an algorithm developed by Zhang's group [37] using 30 diffraction orders. The consistency between PWRTM and other methods used in the analysis of subwavelength gratings in the past, in addition to the experimental verification of our model in [23,25], strengthens the reliability of the results presented in the current paper.

3. Transmission mechanism of MHCG

Figure 3 shows transmission maps of the reference MHCGs and for metalMHCGs in the domain of the period and etching depth. Figure 3(a) presents the transmission of an MHCG for TE polarization (MHCG-TE). The pattern of the transmission map of the MHCG is very close to that of a HCG suspended in the air [26], although MHCG grating modes are leaky [38]. The region in which more than one mode exists in the grating is distinguished by a typical pattern of low and high transmission regions (checkboard pattern). This indicates interference effects between the modes propagating in the grating. In the deep subwavelength regime, $L/\lambda < 1/n_s$, only one grating mode exists and the pattern of transmission bands reaching nearly 100% resembles the Fabry-Perot (FP) mechanism. This suggests that the MHCG behaves as a quasi-uniform layer.

Figure 3(b) depicts TM polarized light transmission through an MHCG (MHCG-TM). It shows very similar behavior to MHCG-TE, despite the slightly different arrangement of high and low

Research Article | Vol. 28, No. 19 / 14 September 2020 / Optics Express 28387
Optics EXPRESS

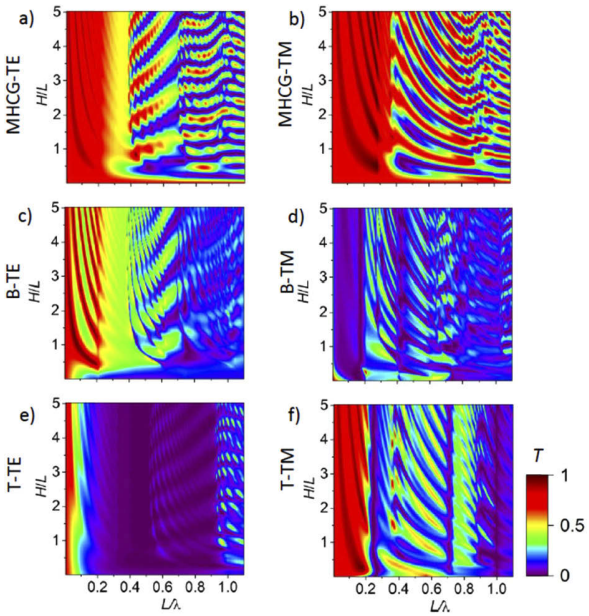

Fig. 3. Maps of transmittance in the domain of inverse wavelength and grating height for $F = 0.5$. Maps in the first row correspond to MHCG gratings. The second and third rows correspond to metalMHCGs in B and T configurations. Maps designations do not appear in the order in which they are discussed in the text to facilitate visual comparison.

transmission regions in the multi-mode regime with respect to TE polarization. In the single mode-regime, however, high transmission bands are arranged in a manner which suggests the same FP mechanism as in MHCG-TE.

4. Transmission mechanisms of B configuration

Figure 3(c) presents the transmission of TE polarized light through the B design (B-TE), which has the same parameters as the MHCG in Fig. 3(a) except for 50 nm gold stripes implemented on the bottom of the grooves between the semiconductor stripes. Despite the use of metal in the metalMHCG, nearly 100% transmission bands are preserved in the single mode regime ($L/\lambda < 1/n_s$), indicating the possibility of nearly total transmission through the grating with metallization. The B-TE design will be one of two transmitting designs considered in this paper. Between the high transmission bands of B-TE, the transmission value is noticeably reduced in comparison to MHCG-TE, mainly due to the absorption of light by the metal. The influence of metal absorption is also noticeable in the multi-mode regime, where high transmission regions are absent. However, the checkboard pattern is similar to the one visible in Fig. 3(a), suggesting that the transmission mechanism in B-TE is similar to that for MHCG-TE, but deteriorated by the absorption introduced by the metal. Figure 3(d) illustrates the transmission of TM polarized light through the B grating (B-TM). In this design, TM transmission is significantly reduced by strong absorption of light by the metal.

Figure 4(a) presents the transmission of the zeroth diffraction order and the reflection of all diffraction orders for B_{op}-TE in the plane of L/λ and $Lk_x/2\pi$, where λ is the incident wavelength and k_x the lateral component of the wave vector. The picture is nearly antisymmetric, suggesting that absorption caused by the metal is almost eliminated. Additional proof of this supposition is provided by the map of absorbance (Fig. 4(b)), which is defined in the model as $A = 1 - T -$

Optics EXPRESS

R, where T – optical power transmittance, R – optical power reflectivity. Noticeable absorption occurs in the single mode region ($L/\lambda < 0.2$) if the incident angles are in proximity to the light-line. The B_{op}-TE for $L/\lambda = 0.23$ enables transmission of 0.964, assisted by total optical power reflection of $5{\cdot}10^{-4}$ and absorption of 0.035 at $k_x = 0$.

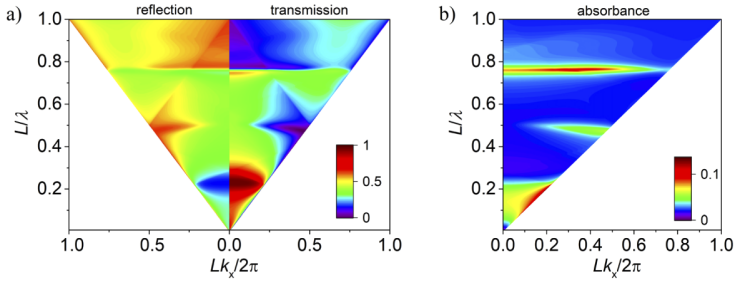

Fig. 4. Dispersion diagrams of the B_{op}-TE configuration for a) optical power reflection (left panel) and transmission (right panel), and b) absorbance.

To analyze the transmission mechanism in B-TE, we select design enabling maximal transmittance and the smallest semiconductor stripe height (H). The optimal B_{op}-TE design is defined by the following parameters: $L/\lambda = 0.22$, $F = 0.5$, $H/L = 0.4$, $H_m/L = 0.22$.

Figure 5 presents intensity of light in proximity to a single grating stripe, incident from the substrate side for selected L of B_{op}-TE. In this case, large transmission is enabled by the fact that light propagating predominantly through the semiconductor stripes, bypassing the metal and hence eliminating light absorption by the metal. This mechanism is possible due to light funneling through the semiconductor stripes, which typically occurs when TE polarized light propagates through an MHCG and is additionally enhanced by lateral confinement if metal has a low value for the real part of the metal refractive index. The L/λ range of large transmission is limited by the occurrence of a second mode in the grating above Ln_s/λ ($L/\lambda = 0.3$ in Fig. 4), which deteriorates broadband transmission in the short wavelength range. Large transmission is still possible in this regime, as shown by the yellow-orange regions in Fig. 3(c). However, their spectra are very narrow, as a consequence of grating modes interference. On the other hand, TM light transmission is significantly impeded in this design. Enhanced transmission (ET) by a periodic array of slits in the metal takes place only for TM polarization [39], due to two interacting mechanisms [40]. These mechanisms are coupling of the incident plane wave with cavity resonances (CRs) located inside low refractive index (e.g. air) slits and excitation of the coupled surface plasmons (SPs) on both surfaces of the metal grating. In the B_{op}-TE configuration, the regions between the metal stripes are filled with high refractive index material,

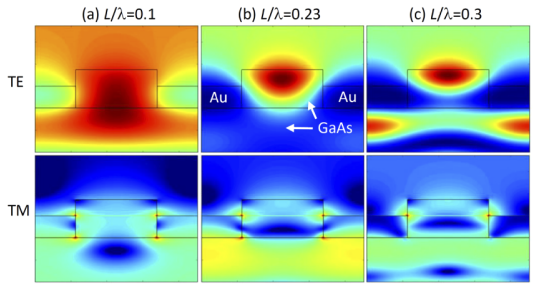

Fig. 5. Distributions of optical field intensity within a single period of optimal B design at three different wavelengths (in columns), illuminated by TE and TM polarizations (in rows).

Research Article | Vol. 28, No. 19 / 14 September 2020 / Optics Express 28389
Optics EXPRESS

which deteriorates the cavity resonances. In the far infra-red region, metals prohibit penetration by light, so the appearance of SPs is not related to enhanced light absorption. In the near infrared and visible spectral ranges, which are our focus here, SPs are associated with notable penetration of the optical field into the metal, which deteriorates both the CR and the SPs (Fig. 5, TM polarization). This contributes to large optical absorption, which severely reduces transmittance.

5. Transmission mechanisms of T configuration

Figure 3(f) refers to the T-TM configuration with the same semiconductor grating as MHCG analyzed in Fig. 3(b), but with 50 nm thick gold stripes implemented on top of the semiconductor stripes. T-TM also preserves high transmission bands and will be the second design considered in this paper. The transmission between the highest transmission bands is significantly higher in comparison to B-TE. In T-TM, nearly 0 transmission vertical lines appear in the multimode region and on the border between the single mode and multimode regions. This indicates a different transmission mechanism than that which governs transmission through B-TE. As in the case of B-TE, there is reduced transmission in the multi-mode region, which is caused by the absorption of light by the metal. Transmission of orthogonal polarization (TE) is strongly suppressed, except in the region $L/\lambda < 0.05$ where it may be significant. This case, however, will be excluded from further consideration, due to the very small structure periods required.

To analyze the transmission mechanism in T-TM, we select designs enabling maximal transmittance, the smallest semiconductor stripe height (H) and the same amount of metal as in B_{op}-TE design. The optimal T_{op}-TM design is defined by: $L/\lambda = 0.17$, $F = 0.5$, $H/L = 0.28$, $H_m/L = 0.3$.

As shown in Fig. 3, the transmission mechanism in T_{op}-TM is different from that which occurs for B_{op}-TE. It is mainly dominated by the formation of SPs, which as will be discussed in the following sections has an ambiguous influence on the transmission mechanism. Figure 6 combines transmission and reflection maps in the plane (λ, k_x) for T_{op}-TM (Fig. 6(a)) and the Au-grating-TM (Fig. 6(c)). Large transmissions are located in the long-wave region (single mode regime) in both configurations and are limited by regions of nearly 0 transmission from the short wavelength side. As shown in [40], the creation of SPs enables ET. On the other hand, a symptom of SP is the high density of light at the interface of the metal, which in turn enhances absorption. Hence, in Fig. 6(d) we use absorption to visualize SPs in the Au-grating-TM. We calculate absorption in the case of very narrow slits ($F = 0.99$, which does not affect the spectral position of SP), to reduce the influence of CRs on the image. The SP of the longest wavelength for $k_x = 0$ shown in the map coincides very well with first order SP calculated by the following simplified formula [41]:

$$\frac{L}{\lambda} = \sqrt{\frac{\varepsilon_m + \varepsilon_d}{\varepsilon_m \varepsilon_d}}, \tag{2}$$

which equals 0.24. ε_m and ε_d are the dielectric constants of the metal and the semiconductor, respectively. High absorption in T_{op}-TM (Fig. 6(b)) also occurs in proximity to this wavelength, suggesting that the mechanism of SP creation limits the T_{op}-TM transmission band from the side of short wavelengths, due to increased penetration of the metal by light.

When $k_x \neq 0$, broadband high transmission arises close to the light line ($\lambda = 2\pi/k_x$) in T_{op}-TM, as a symptom of a plasmonic mechanism known as plasmonic Brewster transmission [42]. This additionally confirms the plasmonic character of the transmission in T-TM. The transmission and reflection map for the Au-grating-TM (Fig. 6(c)) shows complex interplay between the surface modes (tilted lines of low transmission) and cavity modes (horizontal regions of high transmission), which challenges simple interpretation [38]. In the case of T_{op}-TM, the semiconductor grating modes are an additional factor that should be taken into account when interpreting the transmission mechanism in the multi-mode regime, but lies beyond the scope of this work. For determination of the transmittance mechanism in the single-mode regime in

Optics EXPRESS

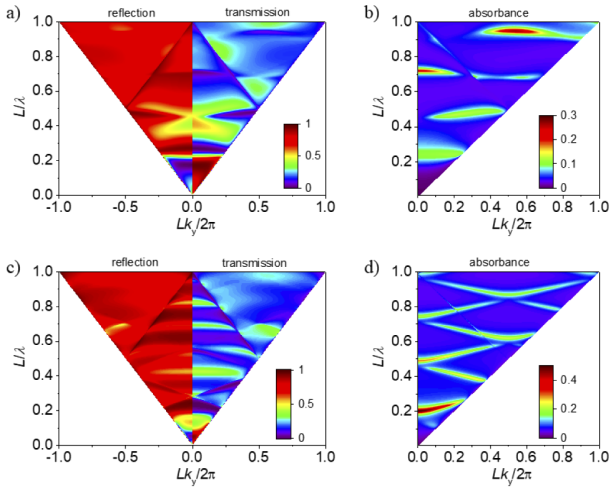

Fig. 6. Dispersion diagrams of the T_{op}-TM configuration a-b) and Au-grating-TM c-d) for optical power reflection (left panel) and transmission (right panel) a), c) and absorbance b), d). The parameters of the Au-grating-TM in c) are as follows: $L/\lambda = 0.05$, $H/L = 3.22$, $F = 0.58$ and in d) differ with respect to F that equals 0.99.

T_{op}-TM, two mechanisms are important: the reduced absorption in T_{op}-TM with respect to the Au-grating-TM (compare Figs. 6(b) and 6(d)) and the appearance of a first order SP which limits the transmission spectrum from the side of short wavelengths.

The first mechanism can be understood by visualization of the propagating light intensity in T_{op}-TM, as shown in Fig. 7 in proximity to a single stripe of the grating. An MHCG illuminated by TM polarized light typically confines light between the stripes [43], and the same applies in the case of the T_{op}-TM. The T_{op}-TM configuration that enables maximal transmission is illustrated in Fig. 7(a) TM. Due to the presence of a semiconductor stripe below the metal, light is confined between the stripes supporting CR. This reduces the amount of light that is typically involved in the creation of SP at the bottom metal interface in the case of pure metal gratings (see the light intensity spikes at the corners of the metal stripe in Fig. 8). In T_{op}-TM, at a wavelength of $L/\lambda = 0.28$, which is close to the first SP in the Au-grating-TM, SP appears at the bottom metal interface and CR is eliminated (Fig. 7(b) TM). These mechanisms are responsible for the nearly 0 transmission. In this case, 90% of the optical energy is reflected by the grating, as confirmed by the optical field distribution, in which the minimum of the standing plane-wave is visible as a blue horizontal line below the grating. At shorter wavelengths, the two-mode regime begins in a non-plane-wave distribution of light below the grating, as visualized in Fig. 7(c) TM. At $L/\lambda = 0.4$, corresponding to the second transmission maximum in T_{op}-TM, the creation of SP at the bottom metal interface occurs together with CR. None of these processes predominate as explicitly as in the previous situation, so transmission reaches a low value of 0.6. The very low transmission in the T_{op}-TE configuration corresponds to the confinement of TE polarized light in the semiconductor stripes, which is then reflected by the metal implemented on top of the grating (Fig. 7 TE). The T_{op}-TM for $L/\lambda = 0.17$ enables a level of transmission of 0.961, accompanied by total optical power reflection of 0.033 and absorption of 0.043.

A significant difference between the B_{op}-TE and T_{op}-TM constructions is the optimal period, which in the case of B_{op}-TE is 35% larger with respect to T_{op}-TM, enabling easier processing of real-world transparent electrodes. For the purposes of comparison one can notice, that the period of the optimal Au-grating is $L/\lambda = 0.05$, which is more than four times smaller than the period of B_{op}-TE and three times smaller than that of T_{op}-TM.

Research Article | Vol. 28, No. 19 / 14 September 2020 / Optics Express 28391
Optics EXPRESS

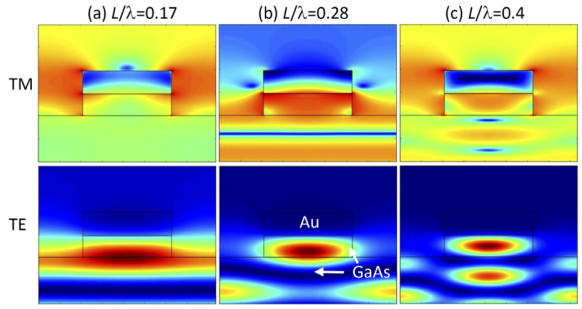

Fig. 7. Distributions of optical field intensity within a single period of T_{op} at three different wavelengths (in columns) illuminated by TM and TE polarizations (in rows).

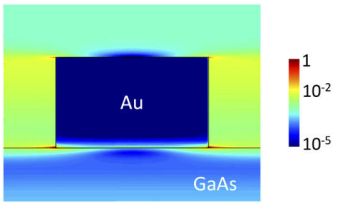

Fig. 8. Distributions of optical field intensity within a single period of the Au-grating illuminated by TM polarization. Grating parameters: $L/\lambda = 0.05$, $H/L = 3.22$, $F = 0.58$.

6. Influence of metal thickness

The thickness of the metal stripes is an important design parameter, which should allow for sufficiently high transmission, on one hand, and acceptably high current conductivity, on the other. In this section, we present the dependence of optical power transmittance for B-TE and T-TM as a function of metal stripe thickness H_m and duty cycle F. The maps become difficult to interpret if H_m is represented as a relative value with respect to L. Hence, in the analysis illustrated in Fig. 9, we assume that the wavelength of incident light is 1 μm, while the thickness of the metal stripes ranges from 0 to a few microns. Each point in the maps for a given F and H_m was determined by searching the transmission maxima in the L and H domain, which ranges from 50 nm to 300 nm for L and from 0 to 1 μm for H. If the transmissions of a multiple maxima differ by not more than 0.1%, then the one with the smallest H is chosen. Therefore, each point in the maps is for a different set of L and H parameters.

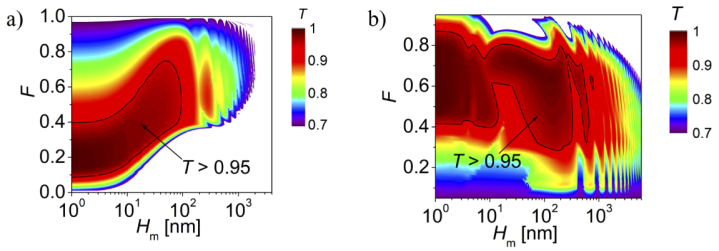

Fig. 9. Maps of transmittance in the domain of the duty cycle (F) and thickness of the metal stripes (H_m) for B-TE a) and T-TM b) configurations. In the area indicated by the black line transmission exceeds 0.95.

Optics EXPRESS

In the case of B-TE (Fig. 9(a)), metal stripes with thicknesses of less than 100 nm are located in the node position of the optical field in the grating, which reduces interaction between the metal and the optical field. This facilitates transmittance at a level of over 0.95. If the thickness of the metal is increased, the optical field penetrates to a greater extent, contributing to enhanced absorption and lower transmission, reaching a level of 0.7 for an Au thickness of 2 μm. The region of very high transmittance, above 0.95, occurs for F from 0.2 to 0.4 for small H_m and shifts to a larger F ranging from 0.4 to 0.6 for H_m, approaching 100 nm. When F is in a range from 0.2 to 0.4, this enables perfect antireflection by the MHCG, hence very high transmittance of B-TE in the case of small H_m. Larger F is preferential in the case of larger H_m, since the presence of thick metal stripes enables more efficient confinement of light in the semiconductor stripes and more light is funneled through the wide semiconductor stripes.

Figure 9(b) illustrates the influence of metal thickness on transmission in the T-TM configuration. In this construction, due to the mechanism described above, metal as thick as 0.7 μm still enables transmittance at a level of 0.95. High transmission occurs for larger F with respect to B-TE, which is mainly due to CR. The grating period of highly transmittive B-TE configurations with thick metal stripes is typically 200 nm, while the grating period of T-TM is very low, at 50 nm (see Fig. S1 inSupplement 1). This is the bottom limit for the period analyzed here. Such a small period is also preferable in the case of the Au-grating-TM, which suggests that the mechanism of transmission is the same in both designs.

7. Influence of refractive indices

In this section, we analyze the optical power transmittance through B-TE and T-TM when the refractive indices of metalMHCG are varied. Modifying the refractive index of a semiconductor and/or metal imposes different conditions for the optimal geometrical parameters allowing maximal transmittance. Hence, all figures presented in this section are composed of points that result from the search for the transmission maximum in the domain of L and H in the ranges of 50 nm $< L <$ 300 nm and $0 < H <$ 1 μm. The grating duty cycle is kept constant at 0.5, which enables fair comparison between B-TE and T-TM, since the optimization procedure may converge to configurations of extremely high or low F values, thereby eliminating metal from the grating.

Figure 10 shows maps of transmission through B-TE (Fig. 10(a)) and T-TM (Fig. 10(b)) in the domain of the complex refractive index ($n_r - in_i$) of the metal stripes, while the refractive index of the semiconductor is kept constant and equals 3.5. The open circles represent the refractive indices of specific metals at a wavelength of 1 μm. Black curves represent the refractive indices of gold and silver as they change with the wavelength in the range from 270 nm to 2 μm [44]. These curves are used for illustrative purposes only, since the dispersion of the refractive index of the semiconductor is not taken into account in this figure and corresponds to the refractive index of GaAs at a wavelength of 1 μm.

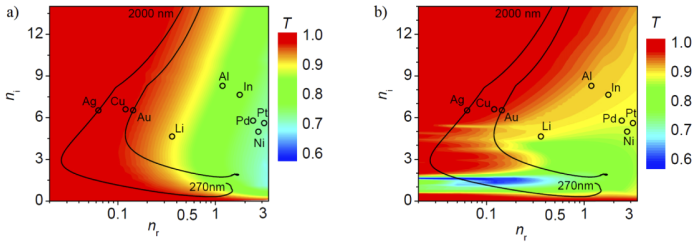

Fig. 10. Power transmittance of B-TE a) and T-TM b) as a function of the real (n_r) and imaginary (n_i) parts of the metal refractive index. Refractive indices of selected metals are indicated by circles. Solid lines show the dispersion of gold and silver in a range from 270 to 2000nm [45].

Research Article | Vol. 28, No. 19 / 14 September 2020 / Optics Express 28393
Optics EXPRESS

In the case of B-TE (Fig. 10(a)), the increase in the real part of the refractive index (n_r) of the metal deteriorates transmittance, since it enables greater penetration of the metal by light, inducing high absorption. The change in the imaginary part of the refractive index (n_i) of the metal causes two opposite processes, which explain the existence of a transmission minimum for $n_i = 3$. These are the reduction of absorption with decreasing n_i and more efficient confinement of light in the semiconductor stripes if n_i is large. Referring to real metals, above 90% transmission (Fig. 10(a), orange-red region) corresponds to silver, as well as to gold in a broad spectral range starting from blue light. The same refers to Cu, although for clarity the function of the Cu refractive index is not shown. The refractive index dispersions of other metals, for example aluminum and platinum, which are also not shown in Fig. 10(a), reach the red region of high transmission for wavelengths longer than 3 μm, because their n_i becomes much larger than n_r in that spectral range. Figure 10(b) illustrates an analogous transmission map for T-TM. The main difference with respect to B-TE concerns the lower transmission in the range of n_i from 0.5 to 6. In this range, CR (explained in section 3) is assisted by strong absorption, which can be reduced if n_i increases with respect to n_r. This range of $n_{i,}$ where transmission is deteriorated, corresponds to $n_{i,}$ of gold and silver from UV to visible light.

Figure 11 illustrates the influence of the real refractive index of the semiconductor grating (n_s) on transmission, while the refractive index of the metal is kept constant and equals 0.15–6.6i. T-TM and B-TE reach their transmission maxima for n_s slightly below 2. The maximum is present due to two counteracting processes. The first relates to the reduction of reflection at the interface between the semiconductor and air by lowering n_s. The second is related to the improvement of waveguiding through the stripes in B-TE and more efficient CR in T-TM by increasing n_s. When the refractive index of the semiconductor decreases below 1.5, waveguiding and CR become less efficient and transmission reduces in B-TE and T-TM for F, which is kept constant ($F = 0.5$). However, if F can be arbitrarily chosen then high transmission is achieved in designs with a small volume of metal for $n_s < 1.5$ (large F in B-TE and small F in T-TM). The refractive index contrast between the semiconductor and air becomes small and transmission through the semiconductor-air interface becomes high. Structurization of the interface does not improve transmission.

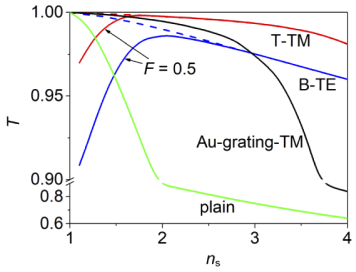

Fig. 11. Transmittance of B-TE (red), T-TM (blue), Au-grating-TM (black) and plain semiconductor surfaces (green) as a function of the refractive index of the semiconductor material. Solid lines for B-TE and T-TM represent optimal designs for $F = 0.5$, while dashed lines show optimal designs for arbitrary F, $H_m = 50$ nm and $\lambda = 1$ μm.

When B-TE and T-TM are compared with an Au-grating-TM, the Au-grating-TM can be seen to have a smaller transmission than T-TM in the whole range of refractive indices and smaller than B-TE for refractive indices larger than 3. Transmission through the flat interface between the semiconductor layer and air is shown as a green line in Fig. 11, which is the upper limit for all transparent electrodes that rely on reduced interaction with light (ITO, nanowires, metal grids). This can be considered to be competitive with respect to B-TE and T-TM only for low refractive index materials ($n_s < 1.5$).

Optics EXPRESS

These results show that metalMHCG can be considered as an attractive alternative to currently used transparent electrodes, if implemented on the surface of high refractive index materials used widely in photonic devices operating in the optical spectrum from ultraviolet to infrared, such as Si, InP, GaAs, GaP, GaN and AlN. Figure S2(a) in Supplement 1 illustrates the refractive index dispersion of these semiconductors in a wavelength range from the absorption edge to 2 μm. Figure S2(b) in Supplement 1 illustrates the analogous dispersions of gold and silver. The transmittance of optimal configurations of B-TE and T-TM designed for wavelengths in the broad spectral range are presented in Fig. 12. These wavelengths ranges are limited by the semiconductor band-gaps from the short-wavelength side. Both B-TE and T-TM are constructed of 50 nm thick gold (solid curves) or silver (dashed curves) stripes. The results show that B-TE realized by a combination of appropriate materials enables above 95% transmission in the spectral range from UV to infrared. This is superior with respect to T-TM (as Fig. 10 suggests), for which transmittance in the UV range reduces to below 90%. Semiconductors of lower refractive index enable higher transmission, as Fig. 11 confirms. Metal stripes of thickness $H_m = 50$ nm become thick enough to induce significant absorption at short wavelengths, hence in the case of $\lambda < 400$ nm transmission above 90% can be achieved by configurations with 20 nm thick silver stripes. The T-TM configuration provides higher transmittance, approaching 1 in the IR range, and the influence of the refractive index of the semiconductors on transmittance is rather marginal. Transmittance spectra of three selected metalMHCGs designed at the wavelengths of 380 nm, 660 nm and 1550 nm are presented in Fig. 13. More examples are illustrated in Figs. S3 and S4 in Supplement 1.

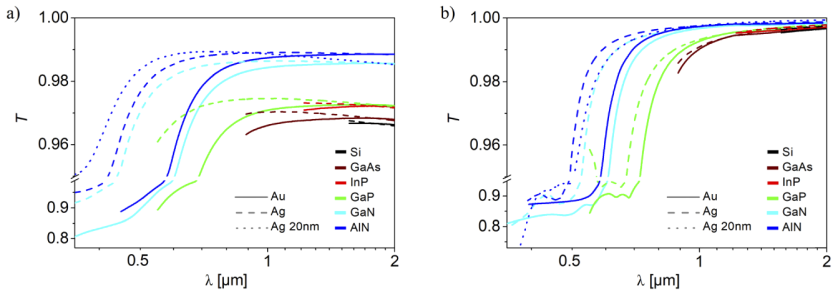

Fig. 12. Power transmittance versus wavelength for B-TE a) and T-TM b) composed of selected semiconductors with gold stripes (solid curves) and silver stripes (dashed lines).

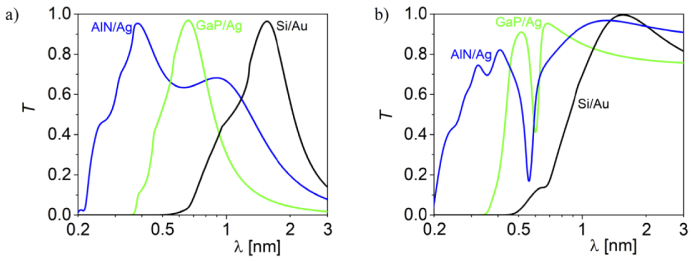

Fig. 13. Transmittance spectra of selected B-TE a) and T-TM b) configurations designed at the wavelengths of 380 nm (AlN grating with Ag stripes, blue), 660 nm (GaP grating with Ag stripes, green) and 1550 nm (Si grating with Au stripes, black). Construction details of the designs are given in Tab. S1 and S3 in Supplement 1.

Research Article | Vol. 28, No. 19 / 14 September 2020 / Optics Express 28395
Optics EXPRESS

8. Electrical properties

An efficient transparent electrode is expected to have transmittance approaching to 1 and as low as possible sheet resistance (R_s), enabling current flow through the electrode. Sheet resistance can be determined according to the formula

$$R_s^{-1} = \sigma H_m F_m, \tag{3}$$

where σ is the electrical conductivity of the metal and F_m is the duty cycle of the metal. Here, $F_m = 1 - F$ for B-TE and $F_m = F$ for T-TM. In the designs considered in this section, the electrical conductivity of gold is 10^7 S/m, which is four times smaller with respect to its bulk conductivity [45]. This is due to the nanometer scale of the metal stripe cross-section, which reduces electrical conductivity as metal corrugation deteriorates the transport of electrons. Figure 14 summarizes the data calculated in Fig. 9, plotting maximal optical transmission versus sheet resistance for B-TE and T-TM configurations. Figure 14 also shows the transmittance relation for the Au-grating-TM, which was found based on the results presented in Fig. S5 in Supplement 1. The transmittance of ITO films in the visible range, of silver nanowires, graphene films and other transmitting electrodes, are not shown, since their transmittance is below 70% for high refractive index materials and their sheet resistance is above 10 ΩSq^{-1} [45]. B-TE and T-TM reach very similar transmittance in the range of sheet resistance, above 10 ΩSq^{-1}, which corresponds to 100 nm thick metal stripes. In that range, the Au-grating-TM reveals low transmittance, since CR does not occur for such low metal stripes at a wavelength of 1 μm. For higher metal stripes and hence lower sheet resistance, T-TM reaches larger transmittance with respect to B-TE. However, it occurs for small grating periods of 50 nm in the case of T-TM, while the period of B-TE that enables sheet resistance below 1 ΩSq^{-1} is 200 nm at a wavelength of 1 μm.

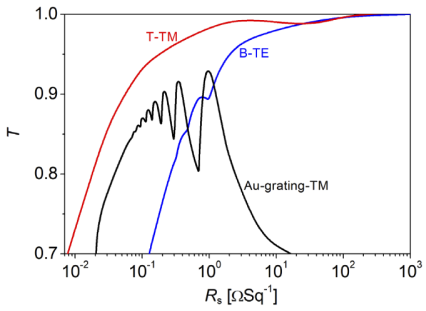

Fig. 14. Transmittance as a function of sheet resistance for B-TE (blue), T-TM (red) and the Au-grating-TM (black) calculated for $\lambda = 1$ μm.

9. Conclusions

This paper has proposed two designs for new transparent electrodes in which metal stripes are implemented in a deep-subwavelength monolithic high-contrast grating. By conducting a numerical analysis, we showed that a construction in which metal stripes are implemented between semiconductor stripes (B-TE) enables nearly 100% transmission of transverse electric (TE) polarization. The main mechanism responsible for such high transmittance is the funneling of light through the semiconductor stripes, which reduces the interaction of light with the metal, and thereby prevents strong light absorption. The second design, in which metal stripes are implemented on top of semiconductor stripes (T-TM), also enables nearly 100% transmittance for transverse magnetic (TM) polarization. In this design, the well-known effect of plasmonic assisted transmittance is enhanced by the elimination of surface plasmon creation at the bottom surface of

Optics EXPRESS

the metal stripe, which deteriorates transmittance in the case of purely metal gratings. Different mechanisms govern transmittance in each design, inducing their different properties. In B-TE, the elimination of light-metal interaction enables above 90% transmittance in the ultra-violet region, which is significantly deteriorated in T-TM. However, T-TM relies on strong light-metal interaction, which enables thick metal implementation and so very low sheet resistance. Although the transmittance mechanism in T-TM is very similar to extraordinary transmittance in metal gratings it enables the use of a larger grating period, although this is still half that enabled by the B-TE design. The period of both designs can be scaled with the wavelength. For example, high transmitting B-TE requires periods above 150 nm and an etching depth of 70 nm at a wavelength of 600 nm, which can be facilitated by contemporary electrolitography or nanoimprint technology. Despite the differences between the two designs, unlike existing transparent electrodes which are implemented on low refractive index materials both can be implemented on the surface of high refractive index semiconductors, enabling not only horizontal electron transport but also injection of current into the semiconductor. B-TE and T-TM offer the prospect of record >95% transmittance for sheet resistance of 2 ΩSq^{-1} while T-TM offers >90% transmittance for extremely small sheet resistance of 0.04 ΩSq^{-1}.

Funding

Narodowe Centrum Badań i Rozwoju (NCBR) and Science Engineering and Research Council (SERC) (project HybNanoSens no. DZP/POL-SINIV/283/2017); Narodowe Centrum Nauki (OPUS 018/29/B/ST7/01927).

Disclosures

The authors declare no conflicts of interest.

See Supplement 1 for supporting content.

References

1. E. Fortunato, D. Ginley, H. Hosono, and D. C. Pain, "Transparent conducting oxides for photovoltaics," MRS Bull. **32**(3), 242–247 (2007).
2. D. J. Lipomi, M. Vosgueritchian, B. C.-K. Tee, S. L. Hellstrom, J. A. Lee, C. H. Fox, and Z. Bao, "Skin-like pressure and strain sensors based on transparency elastic films of carbon nanotubes," Nat. Nanotechnol. **6**(12), 788–792 (2011).
3. H. Peng, W. Dang, J. Cao, Y. Chen, D. Wu, W. Zheng, H. Li, Z.-X. Shen, and Z. Liu, "Topological insulator nanostructures for near-infrared transparent flexible electrodes," Nat. Chem. **4**(4), 281–286 (2012).
4. A. Kumar and C. W. Zhou, "The race to replace tin-doped indium oxide: which material will win?" ACS Nano **4**(1), 11–14 (2010).
5. Z. Wu, Z. Chen, X. Du, J. M. Logan, J. Sippel, M. Nikolou, K. Kamaras, J. R. Reynolds, D. B. Tanner, A. F. Hebard, and A. G. Rinzler, "Transparent, conductive carbon nanotube films," Science **305**(5688), 1273–1276 (2004).
6. M. Zhang, S. L. Fang, A. A. Zakhidov, S. B. Lee, A. E. Aliev, C. D. Williams, K. R. Atkinson, and R. H. Baughman, "Strong, transparent, multifunctional, carbon nanotube sheets," Science **309**(5738), 1215–1219 (2005).
7. M. G. Kang and L. J. Guo, "Nanoimprinted semitransparent metal electrodes and their application in organic light-emitting diodes," Adv. Mater. **19**(10), 1391–1396 (2007).
8. S. R. Forrest, "The path to ubiquitous and low-cost organic electronic appliances on plastic," Nature **428**(6986), 911–918 (2004).
9. G. Liang, Z. Liu, F. Mo, Z. Tang, H. Li, Z. Wang, V. Sarangi, A. Pramanick, J. Fanand, and C. Zhi, "Self-healable electroluminescent devices," Light: Sci. Appl. **7**(1), 102 (2018).
10. T. C. Lu, C. C. Kao, H. C. Kuo, G. S. Huang, and S. C. Wang, "CW lasing of current injection blue GaN-based vertical cavity surface emitting laser," Appl. Phys. Lett. **92**(14), 141102 (2008).
11. T.-C. Lu, S.-W. Chen, T.-T. Wu, P.-M. Tu, C.-K. Chen, C.-H. Chen, Z.-Y. Li, H.-C. Kuo, and S.-C. Wang, "Continuous wave operation of current injected GaN vertical cavity surface emitting lasers at room temperature," Appl. Phys. Lett. **97**(7), 071114 (2010).

Research Article | Vol. 28, No. 19 / 14 September 2020 / *Optics Express* 28397

Optics EXPRESS

12. T. A. König, P. A. Ledin, J. Kerszulis, M. A. Mahmoud, M. A. El-Sayed, J. R. Reynolds, and V. V. Tsukruk, "Electrically tunable plasmonic behavior of nanocube-polymer nanomaterials induced by a redox-active electrochromic polymer," ACS Nano **8**(6), 6182–6192 (2014).
13. R. B. H. Tahar, T. Ban, Y. Ohya, and Y. Takahashi, "Tin doped indium oxide thin films: electrical properties," J. Appl. Phys. **83**(5), 2631–2645 (1998).
14. Y.-J. Moon, S.-W. Kim, H. S. An, J.-Y. Na, Y.-B. Kim, J.-H. Kim, J.-U. Park, and S.-K. Kim, "Engineered unidirectional scattering in metal wire networks for ultrahigh glass-like transparency," ACS Photonics **5**(11), 4270–4276 (2018).
15. S. M. Ahmad, C. S. Leong, K. Sopian, and S. H. Zaidi, "Role of firing temperature, sheet resistance, and contact area in contact formation on screen-printed metal contact of silicon solar cell," J. Electron. Mater. **47**(3), 2120–2134 (2018).
16. J. van de Grop, P. Spinelli, and A. Polman, "Transparent conducting silver nanowire networks," Nano Lett. **12**(6), 3138–3144 (2012).
17. G. Subramania, S. Foteinopoulou, and I. Brener, "Nonresonant broadband funneling of light via ultrasubwavelength channels," Phys. Rev. Lett. **107**(16), 163902 (2011).
18. H. A. Atwater and A. Polman, "Plasmonics for improved photovoltaic devices," Nat. Mater. **9**(3), 205–213 (2010).
19. K. R. Catchpole and A. Polman, "Are negative index materials achievable with surface plasmon waveguides? A case study of three plasmonic geometries," Opt. Express **16**(23), 19001–19017 (2008).
20. P. B. Catrysse and S. Fan, "Nanopatterned metallic films for use as transparent conductive electrodes in optoelectronic devices," Nano Lett. **10**(8), 2944–2949 (2010).
21. J. N. Munday and H. A. Atwater, "Large integrated absorption enhancement in plasmonic solar cells by combining metallic gratings and antireflection coatings," Nano Lett. **11**(6), 2195–2201 (2011).
22. M. Gębski, M. Dems, A. Szerling, M. Motyka, L. Marona, R. Kruszka, D. Urbańczyk, M. Walczakowski, N. Pałka, A. Wójcik-Jedlińska, Q. J. Wang, D. H. Zhang, M. Bugajski, M. Wasiak, and T. Czyszanowski, "Monolithic high-index contrast grating: a material independent high-reflectance VCSEL mirror," Opt. Express **23**(9), 11674–11686 (2015).
23. M. Marciniak, M. Gębski, M. Dems, E. Haglund, A. Larsson, M. Riaziat, J. A. Lott, and T. Czyszanowski, "Optimal parameters of monolithic high contrast grating mirrors," Opt. Lett. **41**(15), 3495–3498 (2016).
24. S. Kim, Z. Wang, S. Brodbeck, C. Schneider, S. Höfling, and H. Deng, "Monolithic high-contrast grating based polariton laser," ACS Photonics **6**(1), 18–22 (2019).
25. M. Gebski, J. A. Lott, and T. Czyszanowski, "Electrically injected VCSEL with a composite DBR and MHCG reflector," Opt. Express **27**(5), 7139–7146 (2019).
26. C. Chang-Hasnain and W. Yang, "High-contrast gratings for integrated optoelectronics," Adv. Opt. Photonics **4**(3), 379–440 (2012).
27. Gyeong Cheol Park, Alireza Taghizadeh, and Il-Sug Chung, "Hybrid grating reflectors: Origin of ultrabroad stopband," Appl. Phys. Lett. **108**(14), 141108 (2016).
28. Martin Scherr, Michael Barrow, and Jamie Phillips, "Long-wavelength infrared transmission filters via two-step subwavelength dielectric gratings," Opt. Lett. **42**(3), 518–521 (2017).
29. D. Fattal, J. Li, Z. Peng, M. Fiorentino, and R. G. Beausolei, "Flat dielectric grating reflectors with focusing abilities," Nat. Photonics **4**(7), 466–470 (2010).
30. T. Czyszanowski, M. Gebski, M. Dems, M. Wasiak, R. P. Sarzala, and K. Panajotov, "Subwavelength grating as both emission mirror and electrical contact for VCSELs in any material system," Sci. Rep. **7**(1), 40348 (2017).
31. A. Bensoussan, J. L. Lions, and G. Papanicolaou, *Asymptotic analysis for periodic structures*, (North-Holland, 1978).
32. J. Li, L. Fok, X. Yin, G. Bartal, and X. Zhang, "Experimental demonstration of an acoustic magnifying hyperlens," Nat. Mater. **8**(12), 931–934 (2009).
33. A. Maurel, S. Felix, and J.-F. Mercier, "Enhanced transmission through gratings: Structural and geometrical effects," Phys. Rev. B **88**(11), 115416 (2013).
34. M. Dems, "Modelling of high-contrast grating mirrors. The impact of imperfections on their performance in VCSELs," Opto-Electron. Rev. **19**(3), 340–345 (2011).
35. P. Lalanne and G. M. Morris, "Highly improved convergence of the coupled-wave method for TM polarization," J. Opt. Soc. Am. A **13**(4), 779 (1996).
36. L. Li, "Use of Fourier series in the analysis of discontinuous periodic structures," J. Opt. Soc. Am. A **13**(9), 1870 (1996).
37. Nanoscale Thermal Radiation Laboratory, Georgia Institute of Technology, http://zhang-nano.gatech.edu/Rad_Pro.htm, access date: 20.04.2019
38. M. Dems, "Monolithic High-Contrast Gratings: why do they not scatter light?" J. Lightwave Technol. **35**(2), 159–165 (2017).
39. T. W. Ebbesen, H. J. Lezec, H. F. Ghaemi, T. Thio, and P. A. Wolff, "Extraordinary optical transmission through sub-wavelength hole arrays," Nature **391**(6668), 667–669 (1998).
40. J. A. Porto, F. J. Garcia-Vidal, and J. B. Pendry, "Transmission resonances on metallic gratings with very narrow slits," Phys. Rev. Lett. **83**(14), 2845–2848 (1999).
41. H. F. Ghaemi, T. Thio, D. E. Grupp, T. W. Ebbesen, and H. J. Lezec, "Surface plasmons enhance optical transmission through subwavelength holes," Phys. Rev. B **58**(11), 6779–6782 (1998).
42. A. Alu, G. D'Aguanno, N. Mattiucci, and M. J. Bloemer, "Plasmonic Brewster angle: broadband extraordinary transmission through optical gratings," Phys. Rev. Lett. **106**(12), 123902 (2011).

Optics EXPRESS

43. T. Czyszanowski, S. Grzempa, M. Dems, and W. Nakwaski, "Quantum-cascade vertical-cavity surface-emitting laser integrated with monolithic high-contrast grating," Proc. SPIE **10552**, 1055208 (2018).
44. D. Rioux, S. Vallières, S. Besner, P. Muñoz, E. Mazur, and M. Meunier, "An analytic model for the dielectric function of Au, Ag, and their alloys," Adv. Opt. Mater. **2**(2), 176–182 (2014).
45. K. Ellmer, "Past achievements and future challenges in the development of optically transparent electrodes," Nat. Photonics **6**(12), 809–817 (2012).

APPENDIX B

Spectrally-shaped source design and modelling

This appendix presents the design and the modelling of the spectrally-shaped source. This work has been realized by Elizabeth Hemsley, PDRA in the group.

Contents

B.1 Presentation of the supercontinuum laser source 164
B.2 Dimensioning of spectral dispersion subsystem 164
B.3 DMD diffraction modelling 166
B.4 Collection subsystem efficiency calculations 166
B.5 Fiber coupling subsystem 167

B.1 Presentation of the supercontinuum laser source

The supercontinuum laser source that is used is a SuperK compact from NKT photonics that emits an unpolarized Gaussian beam whose spectrum covers the 450-2400 nm wavelength range, as presented in figure B.1.

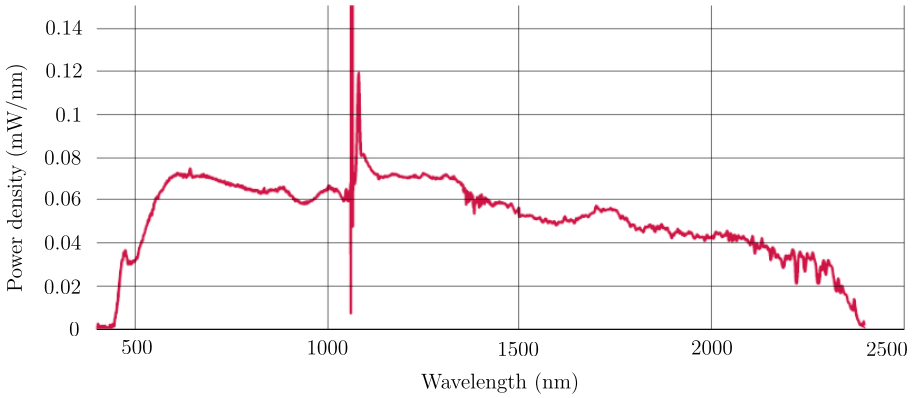

Figure B.1: SuperK compact laser spectral density mW/nm versus wavelength © https://www.nktphotonics.com

The laser power is attenuated to eye-safe level using a $OD = 1.7$ neutral density filter combination F1. F2 filter corresponds to a combination of longpass and highpass filters (Thorlabs DMLP650 and DMSP900), that enable to keep the NIR spectral window of interest, defined from 650 to 900 nm.

B.2 Dimensioning of spectral dispersion subsystem

The beam is dispersed by a holographic transmission grating (G1) with 600-lines/mm (Wasatch photonics WP-600/600-25.4) and focused on the DMD using a cylindrical lens (L1) with focal length f = 50 mm (Thorlabs LJ1821L1-B). Figure B.2 shows that the shape of the spectral range depends on the grating dispersion, the focal length F_1 of the lens L1 and the lateral extension D of the DMD. The equation for the transmission grating we use is :

$$d \times [\sin(\theta_d) - \sin(\theta_i)] = m\lambda \tag{B.1}$$

where d is the groove spacing, θ_i and θ_d respectively the incidence and diffracted angles, m the diffraction order and λ the wavelength. Here we have $d = 1000\mu m/600 \sim 1.67\,\mu$m and we consider the diffraction order $m = -1$. During the initial alignment, the grating is used at normal incidence ($\theta_i = 0$) and the lens L1 is oriented such that the wavelength $\lambda_0 = 770\,$nm is imaged at the centre of the DMD. At the output of the grating, the optical axis of the system is thus rotated by an angle:

$$\theta_{d0} = \arcsin(m\lambda_0/d) \sim -34.75^\circ \tag{B.2}$$

Around this central direction, the lens of focal length $F_1 = 50\,$mm, and the DMD of lateral extent $D = 4.864\,$mm collects light over an half angle of :

$$\Delta\theta = \arctan\left(\frac{D}{2F_1}\right) \sim 2.78^\circ \tag{B.3}$$

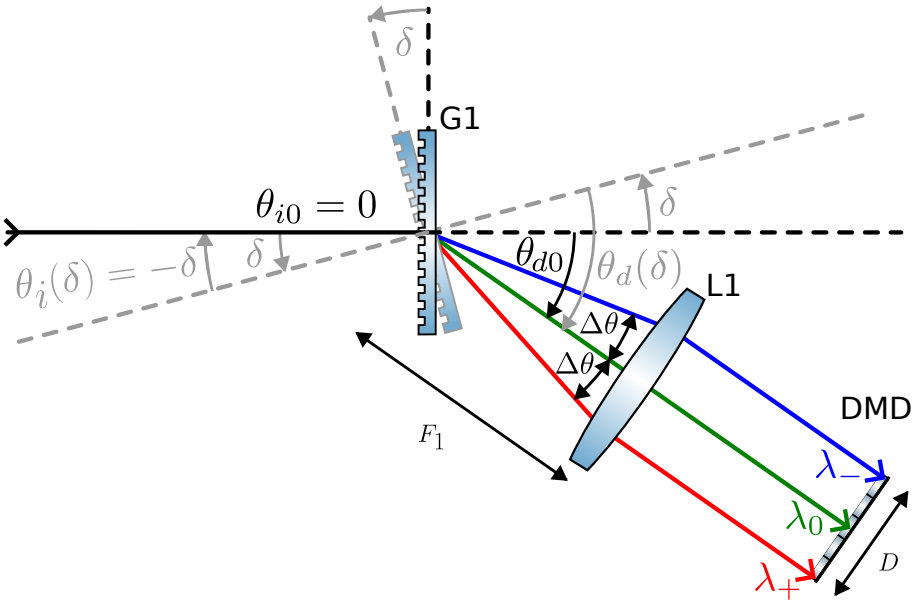

Figure B.2: Spectral range schematic: the DMD extension D and lens focal length F_1 sets the spectral range that can be shaped. This range is tuned by rotating the grating by an angle δ.

The two extreme wavelengths λ_+ and λ_- defining the spectral range covered by the DMD are thus :

$$\lambda_\pm = d/m \times \sin(\theta_{d0} \mp \Delta\theta) \tag{B.4}$$
$$\lambda_- \sim 697\,\text{nm} \tag{B.5}$$
$$\lambda_+ \sim 841\,\text{nm} \tag{B.6}$$

giving a spectral range of :

$$\Delta\lambda = |\lambda_+ - \lambda_-| \sim 144\,\text{nm} \tag{B.7}$$

Starting from this initial setting, this spectral range is then fine tuned by rotating the grating by an angle δ (figure B.2). This tuning results in a incident angle $\theta_i = -\delta$ and a diffraction angle $\theta_d = \theta_{d0} - \delta$ from which we can calculate the new extreme wavelengths :

$$\lambda_\pm(\delta) = d/m \times [\sin(\theta_{d0} - \delta \mp \Delta\theta) + \sin(\delta)] \tag{B.8}$$

The figure B.3 shows the evolution of the central wavelength together with the two extreme ones as a function of the orientation δ of the grating for two intial central wavelengths $\lambda_0 \sim 650\,\text{nm}$ and $\lambda_0 \sim 950\,\text{nm}$. This allows to reach further in the infrared, which is useful to adapt the monitoring of the oxidation to the reflectance of the specific vertical layerstack and to allow for aperture detection at greater depths by overcoming high-temperature-induced material absorption limitations.

The Julia code to reproduce these results is available at `https://gitlab.laas.fr/nmonvoisin/scubed_project/-/tree/main/scubed_modelling/spectral_range`.

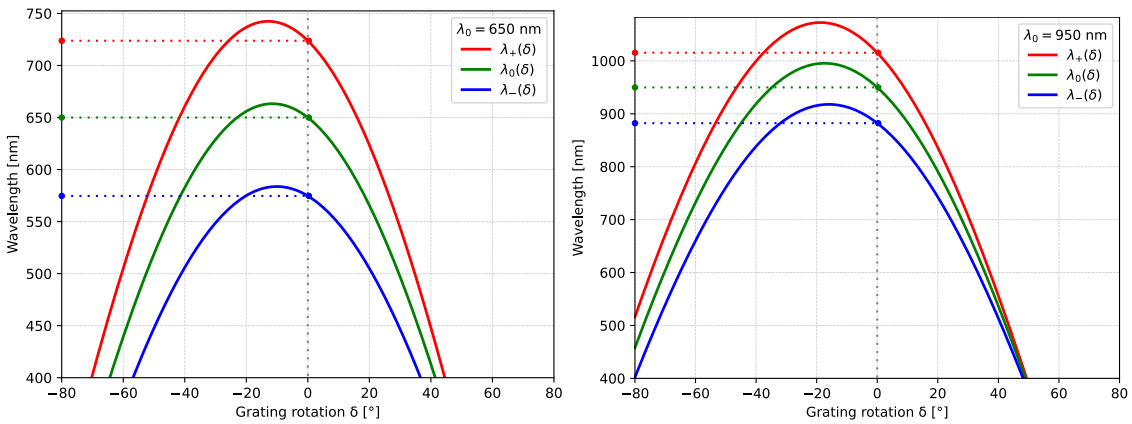

Figure B.3: Tuning of the spectral range covered by the DMD: maximal (red), central (green) and minimal (blue) wavelengths covered by the DMD as a function of the rotation δ of the grating for an initial central wavelength of $\lambda_0 \sim 650\,\text{nm}$ (left) and $\lambda_0 \sim 950\,\text{nm}$ (right).

B.3 DMD diffraction modelling

The DMD is inherently a blazed grating that induces 2D diffraction patterns on the light transmitted along its ON and OFF directions. To take this effect into account, Elizabeth Hemsley and Antoine Monmayrant have developed a model following the theory proposed in [1, 2, 3], using a Python code that is available at `https://gitlab.laas.fr/nmonvoisin/scubed_project/-/tree/main/scubed_modelling/diffraction`. This is a simplified model but it allows to take into account the diffraction induced by the base periodicity of the micro-mirrors in the DMD, the diffusion envelop due to the particular shape and phase function of the tilted micro-mirror, the angular spectrum of the incident light and the angular collection by the lens L2 after the DMD.

B.4 Collection subsystem efficiency calculations

The light filtered by the DMD is collected using a spherical lens (L2) with focal length $f = 100\,\text{mm}$ (Thorlabs AC508-100-B-ML) and a large numerical aperture to capture the many diffraction orders emitted from the DMD. Indeed, using the DMD diffraction model, it is possible to calculate the direction and the intensity of the different orders diffracted by the DMD, and how efficiently they are collected by the collecting lens. The figure B.4 shows the collected diffracted orders as a function of the x and y angles from the normal of the DMD, for the smaller, central and larger wavelengths addressed by the DMD (respectively in red, green and blue), together with the apparent collection angle of L2 and the direction corresponding to the optical axis after the DMD (dotted lines). This figure shows that for each wavelength, several diffraction orders are collected. Moreover, these orders span a wide range of angles, both vertically and horizontally, which justifies the use of a high-NA spherical lens for collection.

In addition, by integration of the intensity of all the collected orders as a function of the wavelength, the transmission through the DMD and collecting lens L2 is calculated, as shown in figure B.5. As one can see, a larger lens L2 offers both higher transmission and lower spectral distortion.

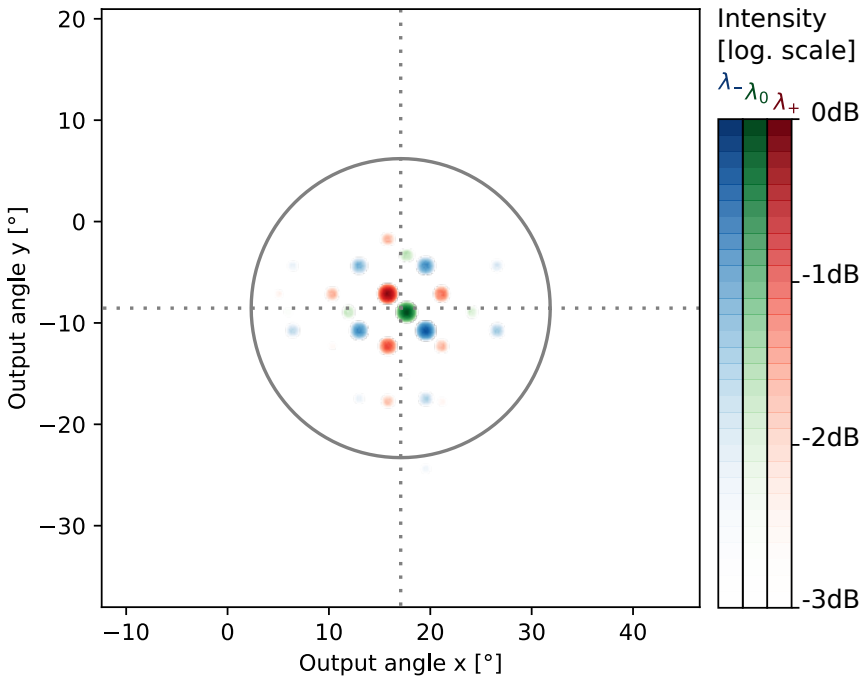

Figure B.4: DMD diffracted orders as collected by the lens L2 for the smaller (red), central (green) and larger wavelengths (blue) addressed by the DMD. The apparent collection angle of L2 is the gray circle, while the dotted gray lines indicate of the optical axis.

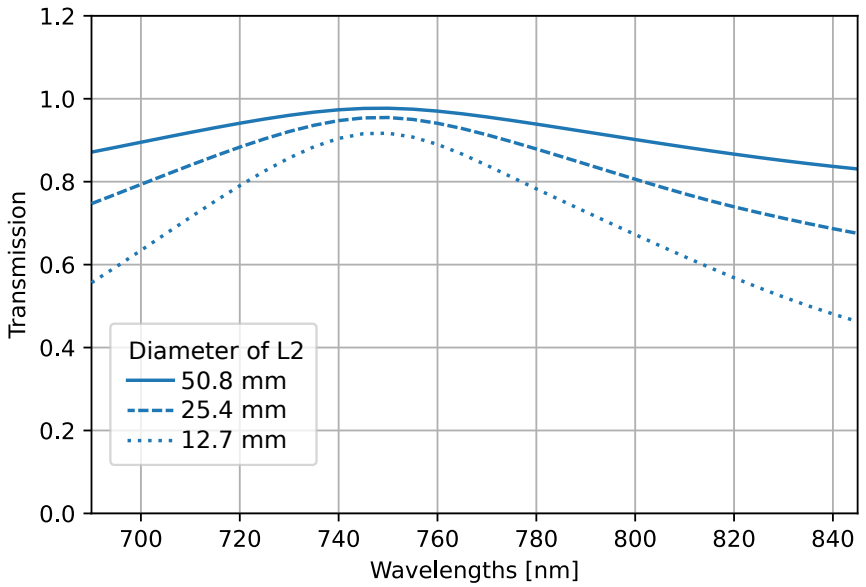

Figure B.5: DMD transmission as a function of the diameter of the collecting lens L2.

B.5 Fiber coupling subsystem

The dispersed wavelengths are recombined using a second transmission grating (G2) with 300 lines/mm (Thorlabs GTI50-03A), and coupled into a multimode fibre (Thorlabs M107L02, core size 1.5 mm and $NA = 0.5$) using a collimation package (L3, F230SMA-850). The 300 lines/mm grating is chosen to allow a lens with a longer focal length (100 mm rather than 50 mm) to collect the light reflected from the DMD. The longer focal length is much easier to fit into the system and align, as space is limited around the DMD (see Figure 4.14a).

Bibliography

[1] X. Chen, B.-b. Yan, F.-j. Song, Y.-q. Wang, F. Xiao, and K. Alameh, "Diffraction of Digital Micromirror Device Gratings and Its Effect on Properties of Tunable Fiber Lasers," *Applied Optics*, vol. 51, no. 30, p. 7214, 2012.

[2] A. Sandmeyer, M. Lachetta, H. Sandmeyer, W. Hübner, T. Huser, and M. Müller, "DMD-based Super-Resolution Structured Illumination Microscopy Visualizes Live Cell Dynamics at High Speed and Low Cost," tech. rep., Biophysics, 2019.

[3] L. McMackin, M. A. Herman, and T. Weston, "Design of a Multi-Spectral Imager Built Using the Compressive Sensing Single-Pixel Camera Architecture," in *SPIE OPTO*, p. 97610G, 2016.